# UNIVERSITY OF SOUTHAMPTON

# FACULTY OF ENGINEERING AND APPLIED SCIENCE

# SCHOOL OF ENGINEERING SCIENCES

# MATERIALS RESEARCH GROUP

Thesis submitted for the degree of Doctor of Philosophy

## MATERIAL CHARACTERISATION AND MODELLING OF FATIGUE INITIATION IN ALUMINIUM BASED PLAIN BEARING MATERIALS

by Jian Liu

March 2005

UNIVERSITY OF SOUTHAMPTON

ABSTRACT

FACULTY OF ENGINEERING AND APPLIED SCIENCE

SCHOOL OF ENGINEERING SCIENCES

ENGINEERING MATERIALS RESEARCH GROUP

**Doctor of Philosophy**

**MATERIAL CHARACTERISATION AND MODELLING OF FATIGUE INITIATION IN ALUMINIUM BASED PLAIN BEARING MATERIALS**

by Jian Liu

Aluminium based plain bearings used in small automotive engines typically comprise a number of layers of different materials. As the service loadings for plain bearings become more severe, it is important that a bearing can provide a long operating lifetime at an economic cost. The fatigue performance of these roll-bonded bearings has been found to be strongly dependent on relative layer properties and the micro-mechanics of the Al lining. It is therefore necessary to be able to determine accurately the material properties of each layer for understanding plain bearing failures and to identify the role of the Al lining microstructure on fatigue initiation, with an aim of optimising the design and manufacture of the roll-bonded system as a whole. These roll-bonded bearings, manufactured by Dana Glacier Vandervell Bearings (UK), are typical shell bearings, constructed in two parts or half-shells, which are clamped together within a housing to support the rotating journal. Each half shell comprises a thin layer of a complex Al-Sn based lining material, roll-bonded to a steel-backing layer via a thin layer of aluminium foil. This thesis first presents the results of a three-year research program characterising the elasto-plastic material properties of the thin Al-Sn based alloy linings used in modern plain journal bearings applications. Then it presents work on the investigation of the effect of microstructure (particularly particle distributions) on fatigue initiation behaviour in linings.

For material characterisation of thin lining layers for which the stress strain data cannot be obtained through traditional tensile tests, a methodology was proposed involving a combination of different experimental and numerical techniques: Vickers micro-hardness test, FEM, adaptive numerical modelling and genetic algorithms. In this methodology a stress-strain curve that could give an identical load-indentation curve from FE modelling as the experimentally obtained load-indentation curve from Vickers micro-hardness tests was taken to be a good approximation of the property of that material. Adaptive numerical modelling and genetic algorithms were used to perform the iterations and optimisations to identify such a stress-strain curve. The generic nature of the procedure of this methodology allows it to be extended to other materials, rather than just Al linings.

FE models of the microstructure and classification approaches using adaptive numerical modelling techniques were applied to investigate the effect of critical microstructure parameters, i.e., particle distributions, on initiation behaviour in Al linings. In the FE modelling (using materials models obtained from the material characterisation procedure detailed earlier) the maximum plastic shear strain and hydrostatic stress were adopted as possible initiation criteria. Microstructure features revealed by an in-house tessellation program on fatigued linings were compared with FEM results. FE modelling of the real microstructure shows correlation between crack initiation sites and the high local stress/strain initiation criteria. The classification models on the preferential crack initiation particles observed experimentally provided possible predictions of microstructural sites most likely to initiate failure.

## ACKNOWLEDGEMENTS

# CHAPTER 1  Introduction

## 1.1  Background

Plain bearings have been widely used in the automotive industry for many years; there have been significant developments in both the overall bearing design and the constitution of the lining material over this time. However, industry keeps pursuing the goal of a higher power output while reducing the weight of engines, which leads to increasing service loading stresses for plain bearings. As the service conditions for bearings become more severe, it is important that a bearing can provide a long operating lifetime at an economic cost. To achieve this, it is necessary to investigate the fatigue failure of a bearing and the loading conditions which cause such failure by both experimental and modelling methods.

A common modern automotive bearing design usually comprises three layers as shown in Figure 1-1: an aluminium alloy lining, a steel backing layer, and a thin aluminium foil interlayer. In the last few years many aspects of the bearing design have been investigated and their influence on overall fatigue performance identified[1].

Hard Steel backing

Pure Al interlayer

Multi phase Al alloy lining material
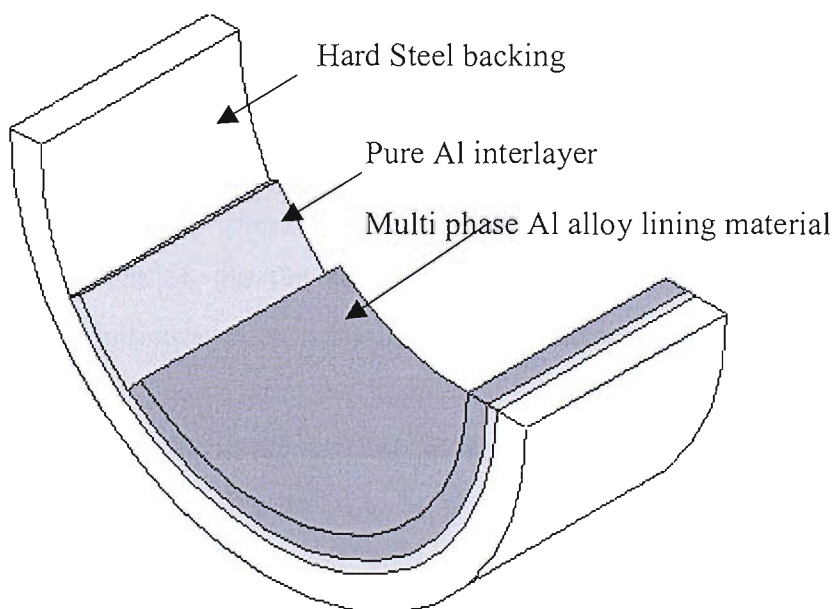
Figure 1-1    Half shell schematic of plain bearing[2]

These aspects include the bearing lining thickness and properties, microstructure of the lining material, housing compliance, oil cooling holes and grooves, bearing clearance and fluid film thickness, overall bearing shape, and operating environments. Among these aspects, the microstructure of the lining is of special interest. A typical lining material comprises an aluminium matrix containing tin, silicon, lead or other elements depending on differing designs and purposes. Usually the alloying additions give rise to coarse or fine secondary phases which may either strengthen the matrix (for harder phases) or give greater conformability in the case of oil film loss (for softer phases). When bearings are under loads that may finally lead to failure, the development of stresses and strains in local regions of the lining material is strongly dependent on bearing architecture, local microstructure and material properties. A major possible mode of bearing fatigue occurs when cracks initiate from the lining surface and then penetrate through the lining material. It is widely believed that the surface cracks are introduced due to the presence of circumferential stresses in the lining material[3]. Previous fatigue crack initiation studies on bearings AS15[1] and AS124[1] have shown that the favoured sites for crack initiation in those materials are at particle/matrix interfaces in the microstructure and along slip bands within the aluminium grains.

The bearing AS1241 considered in an earlier research programme in Southampton University[4] was produced by Dana Glacier Vandervell, which is a leading manufacturing company producing various bearing designs for the automotive industry. The lining aluminium alloy of AS1241 is a thin layer of Al-12Sn-4Si-1Cu alloy (element % by weight). The microstructure of this lining can be seen in the micrograph of Figure 1-2. In simple three point bending fatigue tests (as illustrated in Figure 1-3) carried out on the flat strip which is produced just prior to bearing forming, the crack initiation sites were found to be associated with the interfaces between Si secondary phases and the surrounding matrix. Initiation was usually observed at large Si particles in the AS1241 lining alloy. The very early fatigue crack growth was seen to occur both parallel to as well as normal to the nominal applied loading, indicating a complex local stress state. Tessellation approaches and microstructure modelling results showed that a reasonable correlation existed between points of predicted high shear strain within the aluminium matrix and fatigue initiation sites[4].

Rolling direction
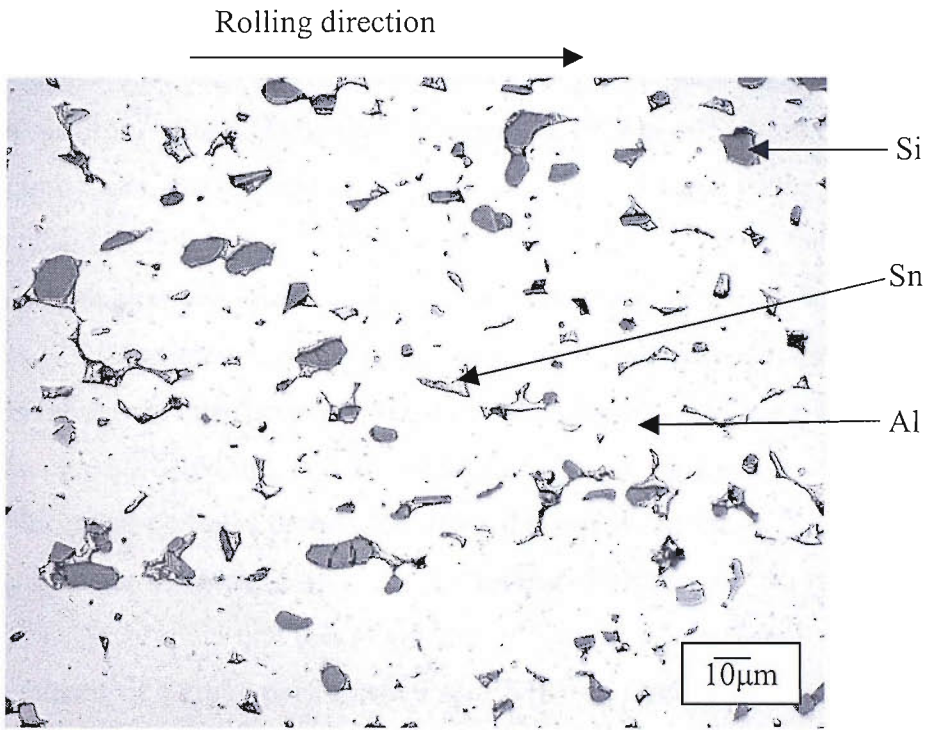


Figure 1-2    AS1241 optical micrograph showing typical microstructure[4]
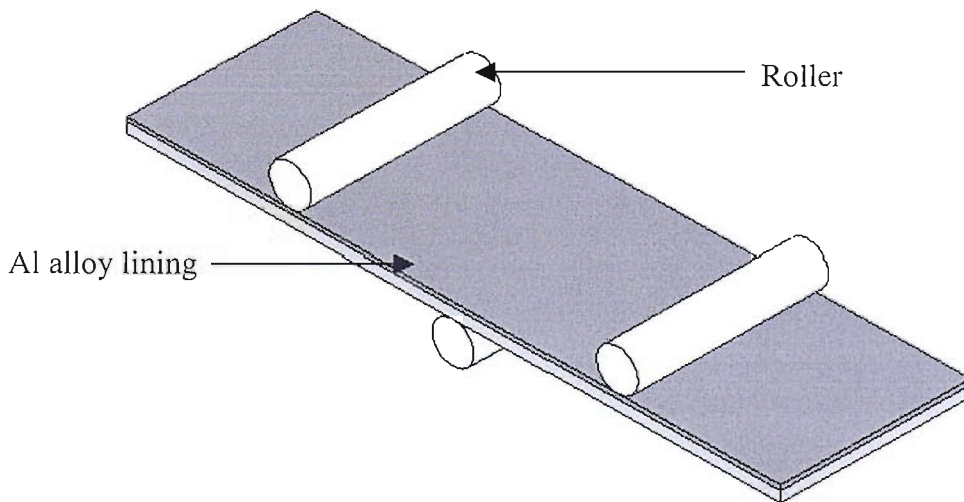


Figure 1-3    Three point bending test[4]

Hard Si inclusions are present only in some bearings. There are other modern designs of bearings containing only soft particles (e.g. Sn) exhibiting differing local elasto-plastic responses. One such bearing design has been produced, designated AS16, with a lining of Al-20Sn-1Cu-0.25Mn alloy (element % by weight) which has a different microstructure from that of AS1241 (see Figure 1-4). Similar three point bending fatigue tests and tessellation approaches have been applied to AS16 flat strips[5]. It has been observed that fatigue initiation sites occur at the Sn-matrix interface, particularly around large Sn particles. Certain other features of the Sn particles (assessed by tessellation measures) have been examined through classification approaches based on adaptive numerical modelling, and are believed to have strong effects on preferential crack initiation and particles de-bonding from the matrix. In the AS16 lining, the Sn distribution has an alignment due to the rolling direction of the manufacturing process. It has been noted that this alignment of Sn to the local tensile axis seems to be a determinant of fatigue performance of AS16[2]. A more detailed review of this approach is discussed in Chapter 3.
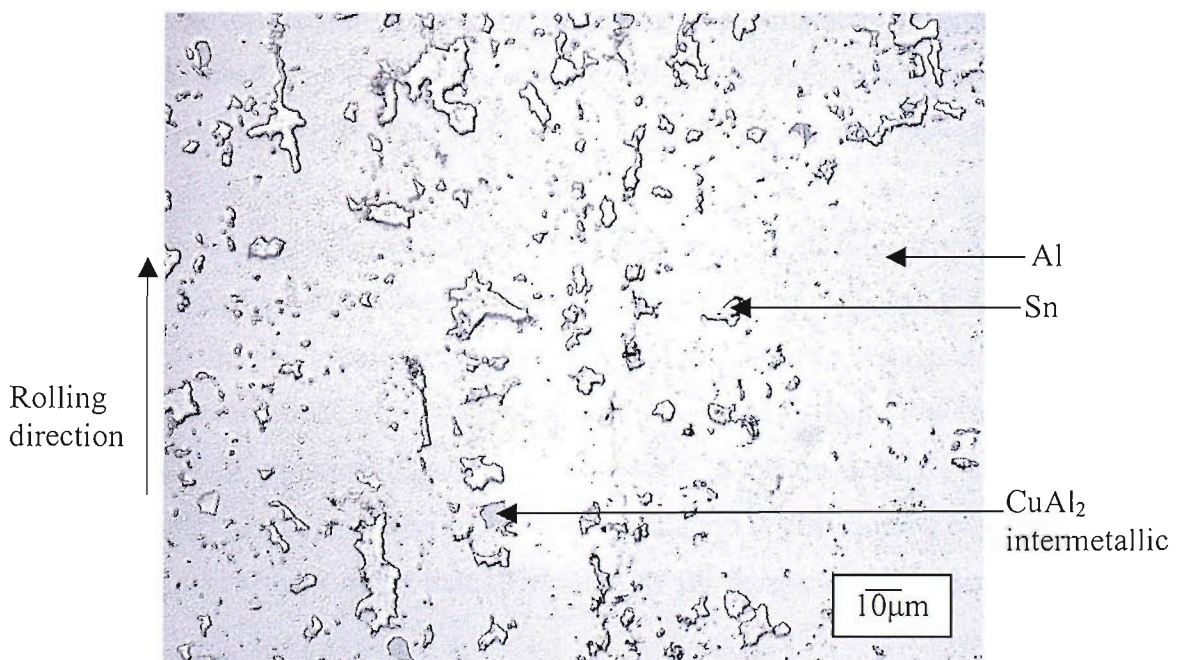


Figure 1-4    AS16 optical micrograph showing typical microstructure[5]

Analysis of the effect of lining microstructure on bearing fatigue behaviour needs to be performed more systematically using idealised microstructures to investigate the effect of particle alignment and distribution and thus allow an optimised

microstructure to be specified. The effect of key microstructure parameters could be more clearly observed and assessed through Finite Element Modelling (FEM). For instance, an FEM investigation of stress and strain distribution around combinations of circular or elliptical particles with varying material properties may identify the critical features affecting fatigue initiation.

The safe operating life of engineering components is always emphasised in industrial applications. Total-life approaches[6] and damage tolerant approaches have been proposed and developed for characterising fatigue phenomena. While a total-life approach characterises catastrophic failure preceded by initiation and a considerable amount of stable crack growth, the damage tolerant methodology focuses on the growth behaviour of individual cracks. The stress-life approach and the strain-life approach are often considered among total-life approaches, depending on either maximum loading stress or strain range being related to the fatigue lifetime of a component. In the bearing projects, recently carried out in the University of Southampton[4, 5], total-life approaches have been principally employed. In contrast, the damage tolerant approach is applied through either energy methods or more advanced fracture mechanics-based techniques which define the driving force to propagate an individual fatigue crack, allowing crack propagation behaviour to be characterised.

It is of course important to predict accurately the critical values of stress and strain developing in components whichever approach is adopted. Due to the geometric complexity of the bearing design and the high loads applied causing elasto-plastic deformation, predictions are usually obtained by FEM, which requires reliable material model information. Hence it is necessary to obtain accurate stress-strain relations for all layers of the bearings. Such information is also needed for all phases of a complex microstructure so that FEM analysis for fatigue crack initiation can be performed.

## 1.2 Objectives and methodology

As part of an extensive research programme on bearing fatigue, carried out at University of Southampton, the present research aims to use modelling methods

firstly to characterise bearing materials, then to investigate the fatigue crack initiation behaviour of the lining material and, in particular, the effect of microstructure on this behaviour. Experimental data from a parallel project investigating the fatigue behaviour of AS16[5] have been made available for this work.

The work is thus carried out in two stages. First, it is necessary to determine the overall material properties of the lining for use in modelling in order to identify accurately the stress and strain fields in the surface region where crack initiation has been observed. However, a complex rolling and heat treatment procedure is used to produce the final bearing; hence the properties of the lining are no longer the same as those of the original alloy billet and may vary spatially. This makes the elastic-plastic properties of thin layers hard to assess experimentally using the traditional tensile test method so an alternative technique needs to be adopted. The first objective of this research programme is therefore the development of a versatile and reliable characterisation method yielding such material properties via micro-hardness test data. This is achieved through the following steps:

- Generation of high-quality indentation data from relevant materials (so called "control materials") with known elasto-plastic properties.

- Development of a reliable Finite Element (FE) indentation model, to enable the production of numerous load-indentation diagonal size curves corresponding to rational ranges of aluminium alloy elasto-plastic properties. The FE analysis is verified by applying it to the control materials.

- Application of an Adaptive Numerical Modelling (ANM) technique, to generate an approximate relation between indentation diagonal size and material properties based on a large database of stress-strain curves and the corresponding indentation data.

- Application of an optimization algorithm, to identify the best approximation for the stress-strain curve for an alloy material with a given, experimentally obtained, load-indentation diagonal size curve.

- Demonstration of the use of the characterization results in generating stress-life and strain-life curves from three-point fatigue tests on flat strips with the bearing layer architecture.

The second important modelling objective in this work is a numerical investigation of possible fatigue crack initiation sites in the bearing lining based on Finite Element Analysis (FEA) with the elasto-plastic characterization results as material input. Strategies for two-dimensional analysis of the multi-phase microstructure of bearing linings are developed. Fatigue initiation criteria are adopted and applied to the stress and strain predictions. Modelling in this part of the project comprises the following steps:

- Validation of FEM through comparison with appropriate elastic analytical approaches in the case of a single inclusion.

- Analysis of idealized microstructures with well defined geometric characteristics, that is, regular patterns of the critical secondary-phase particles.

- Analysis of the real microstructure of lining materials combined with advanced image analysis tessellation techniques to verify the importance of certain micro-structural features in encouraging crack initiation. This task involves the comparison of experimental information on initiation sites with the respective indications from the predicted stress and strain distributions.

- Classification with geometric information on initiating and non-initiating particles to identify a number of microstructure parameters and their combination that are important to crack initiation.

## 1.3   Literature review

The industrial relevance and scope of this research programme prompted literature background reading in four areas: causes of bearing fatigue failure, material elasto-plastic characterisation using pyramidal or conical indenters, fatigue initiation criteria in multi-phase materials and FE micro-structure analyses.

### 1.3.1   Bearing fatigue review

The failure of plain bearings is mainly caused by fatigue or seizure. Fatigue loads are obtained from both inertia and firing loads. The fatigue life of the bearing is of course

mostly related to the load applied on the bearing. Although it is assumed by most of the existing theories that the load transmitted through the oil film is smoothly distributed over the bearing, this load can by no means be considered continuous over the whole lining surface. It is generally agreed that discontinuous oil film islands moving around the lining surface generate varying stresses[7]. Taking account of the fact that the bearing system is not rigid and local deformation of the bearing as well as possible dynamic distortion of the crank shaft and bearing housing may occur, the true stress experienced by the lining surface is difficult to determine. This variation is expected to specify the stress range causing fatigue in the lining material.

Despite this lack of precise stress field data, many aspects of the bearing design have been empirically investigated and the influence of these on overall fatigue performance assessed.

### 1.3.1.1   Effect of the lining thickness

From industrial experience many workers reported that decreasing the lining thickness has the effect of increasing the overall fatigue strength of a bearing. Love *et al*[8] suggested that as the lining thickness is decreased, it is easier to transfer load to the harder backing materials so that the ratio of the stress distribution between the lining and backing approaches the ratio between their elastic moduli. This helps to increase the effective load bearing capacity hence the overall fatigue strength increases as well. From this hypothesis it would be expected that if the ratio of elastic moduli between the backing and lining is high and the ratio of their thickness has the same value, the fatigue life of the bearing could be optimised. However, after extensive experiments using bearings with different soft and hard combinations of the lining and backing, Duckworth and Walter[9] indicated that there was no obvious relationship between the elastic moduli ratio and increased fatigue strength when the thickness of the lining was reduced. It was the increased cyclic yield stress after a reduction in lining thickness that contributed to the rise in fatigue resistance.

### 1.3.1.2 Effect of the housing rigidity

Blount[10] observed that the fatigue life of a bearing is influenced directly by the rigidity of the bearing housing. His experiments showed that the tested bearings in a rigid housing have higher fatigue strength than those in a less rigid housing. This was attributed to the additional bending stress to the bearing caused by the housing and shell flexing. Blount also indicated that if the bearing shell thickness was increased without significantly increasing the combined housing-shell rigidity, the fatigue life of the bearing would be reduced, which was possibly because the thicker bearing was poorly fitting with rigid shells, hence leading to premature failure. He thus suggested that the optimum fatigue life could be achieved with a thin bearing shell thickness within a very rigid housing. This is however contrary to current trends in engine component design.

### 1.3.1.3 Effect of the microstructure in bearing lining fatigue

As already mentioned, the microstructure of the bearing lining material plays an important role in determining the fatigue resistance of the journal bearing. Previous investigations have provided evidence supporting this view. Blount[10] pointed out that the white metal bearings with a coarse, statically cast microstructure had a shorter fatigue life than bearings with a finer, strip cast microstructure. It was also observed by Sakamoto *et al*[11] that the fatigue strength of a bearing could be increased by refining the microstructure of the lining alloy when they examined the Al-Zn-Si alloys.

Romer[12] investigated the effect of tin particle's size on the fatigue strength of AS15 (an Al-Sn alloy). For material from various production processes in the as received condition, no significant difference was observed in the bearing fatigue tests with changed tin particle sizes. However, the deterioration of the bond layer which occurred during the heat treatment process was found to be associated with the reduction in fatigue strength in the bearing fatigue tests.

An extensive study of fatigue crack propagation in Al-Sn bearing alloys was performed by Rusby[13,14]. The results showed that at high R ratios, the existence of the tin addition helps to increase the fatigue crack propagation rate, while at R=0.1, higher threshold stress intensity factors were observed with alloys containing larger amounts of tin. Considering premature crack closure at low R ratios and crack deflection during propagation, this contradiction was explained by arguing that at low R ratios the fatigue crack propagation rates and threshold values were more dependent on the morphology of the tin phase than its volume fraction. Rusby also pointed out that the decohesion observed along the Al-Sn interfaces was probably the result of hydrogen embrittlement which could arise from the interaction of the moisture in the laboratory air and the freshly created metal at the tip of the fatigue crack.

The fatigue properties of the multi-layered AS1241 bearings were investigated in a previous research project at the University of Southampton[4]. As mentioned earlier, this plain bearing comprises three layers: a multiphase Al-Si-Sn lining, a hard steel, and a soft pure Al interlayer to bond the two layers together. The lining exhibited complex fatigue behaviour including events like multiple crack initiations and highly microstructurally dependent crack growth. The locations of fatigue initiation were found associated with the interface between Si secondary phases and the matrix in the lining materials. Data-driven techniques such as ANM based classification were used to investigate the effect of key microstructure parameters on the preferential location of fatigue initiation sites[15]. It was found, for instance, that large Si particles are more likely to cause initiation compared with other particles.

A subsequent project carried out in the University of Southampton in parallel with the present research investigated AS16 bearings with an Al-Sn-Cu lining alloy[5] different in various respects from AS1241. Similar techniques were employed to investigate the fatigue behaviour. Fatigue crack initiation was found to occur at Sn/matrix interface, particularly around particles of high aspect ratio and aligned perpendicular to the global tensile load[5]. In the absence of Si, large Sn particles were also found to be the likely cause of fatigue crack initiation. A more detailed assessment of these data-driven classification approaches applied to these two systems is given in Chapter 3, where the previous findings are compared with new findings on a complementary data-set.

### 1.3.2   Material characterisation

One of the important mechanical properties characterising a material's resistance to localised plastic deformation (e.g., a small dent or a scratch) is hardness. Quantitative hardness techniques use a small indenter which is forced into the surface of a material to be tested, under controlled conditions of load and rate of application. By measuring the depth or size of resulting indentation, a relative (i.e. comparison between hard indenter and tested material) hardness number will be obtained. Hardness tests can be classified as Rockwell hardness tests, Brinell hardness tests, Knoop hardness tests and Vickers hardness tests according to the different shape of indenters. Among these techniques, Knoop and Vickers use a diamond indenter of pyramid geometry with different shape and angles; the Brinell uses a spherical indenter of steel, and Rockwell uses a diamond cone indenter or a steel sphere. Details of different hardness testing techniques are given in Appendix A.

There has been a long history of experimental and analytical studies on the relation between indentation data and elasto-plastic parameters. Tabor's[16] work with spherical indenters was among the most prominent early contributions. More recently, the emphasis of such investigations has shifted to the systematic use of the finite element method[17,18,19,20]. Attempts have been made to determine the elasto-plastic parameters from the combination of FEM and load-depth results obtained from nano-indentation tests[21,22]. Considerable work has been done with spherical indenters but it is not reviewed here since a Vickers indenter was used in the present investigation.

Zeng *et al*[23] provided a general approach to determine the mechanical properties of brittle materials by analysing the experimentally obtained loading cycles of indentation load-depth (*P-h*) results for Vickers indentation. The elastic modulus was estimated from the unloading curve. Based on the model $P=Ch^2$ for the loading curve, relationships for yield stress, hardness, strain hardening factor and the contact area were given in a series of formulae.

Similar approaches have been applied extensively to metals and alloys. Most authors[17,24,25] examine carefully the complete loading and unloading *P-h* curve from

either spherical or cone nano-hardness indenters, and derive their own equations between mechanical properties and experimentally measured factors such as hardness and contact area. Combined with the flow stress state obtained from FEM analysis, various mechanical properties are calculated. Particularly, Lamagnere[25] investigated the nano-indentation application to bearing steels and demonstrated the ability to derive the Young's modulus from the loading and unloading *P-h* curve using a Berkovitch indenter, which is a pyramidal diamond with a triangular basis. FEM was used to estimate the possible deviation of Young's modulus due to inclusions in the steel. This large Young's modulus mismatch between the matrix and the inclusion explained qualitatively the observation reported in previous publications[26] that these inclusions are harmful to the fatigue life of bearing steels.

Giannakopoulos and Suresh[27] gave a detailed step-by-step approach for estimating local and bulk mechanical properties of materials through sharp indentation tests adopting both a displacement approach and an energy approach and analysing the area under *P-h* curve. Mechanical properties such as Young's modulus, compressive yield strength, strain hardening exponent, strength at a plastic strain of 0.29 and hardness could be estimated through continuous indentation. This approach is suitable for Vickers, Berkovich or conical indenter (whose apex angle is the same as that of Vickers or Berkovich). The validity of this method has been examined on a broad range of homogeneous materials[28]. The sensitivity of this method for both the forward problem (to predict *P-h* curve from known material elasto-plastic properties) and the reverse problem (to estimate material elasto-plastic properties from the experimentally measured loading and unloading *P-h* curve) has been examined. The uniqueness of relating the *P-h* response to material compressive stress-strain behaviour has been addressed in their research. It is reported that a good prediction of $E$, $\sigma_y$, and $\sigma_{0.29}$ (that is, stress corresponding to a characteristic strain of 0.29) was obtained but the authors were unable to distinguish the different stress-strain behaviour between two materials with identical $E$, $\sigma_y$, and $\sigma_{0.29}$ but different stress-strain behaviour between $\sigma_y$, and $\sigma_{0.29}$. Dao *et al*[29] from the same group investigated large deformation finite element studies using dimensional analysis on instrumented sharp indentation. A set of dimensionless functions was established to characterise instrumented sharp indentation. By assessing the performance of their approach with various metals and

alloys, their proposed forward (loading) algorithm was found to work well and robustly, while the reverse (unloading) algorithm was less effective in predicting yield strength. It is notable that in this paper, it was mentioned that the plastic properties of materials extracted from instrumented indentation were very sensitive to even small variations in the *P-h* curves.

ANM techniques (such as the one described in Section 1.5 of this thesis) have been applied to interpolate between FEM predictions[30,31] recently because ANM offered the advantage of obtaining optimum correlation between material properties and indentation data with considerably reduced computing effort.

Most of the techniques for predicting elasto-plastic parameters found in the literature are based on the analysis of the loading-depth and unloading-depth curves, and are therefore different from the approach adopted in this project. It seems that no previous attempt has been made to extract elasto-plastic information from the varying load-indentation size curve obtained from interrupted micro-hardness tests (a far simpler test than an instrumented hardness test). The full investigation of this possibility is discussed in Chapter 2.

### 1.3.3   Fatigue crack initiation

The initiation of fatigue cracks is often of interest in the literature concerned with investigation and improvement of material performance. Fatigue initiation is usually associated with the existence of microscopic flaws, e.g., in materials at grain boundaries, twin boundaries, inclusions, microstructural and compositional inhomogeneities, and stress concentrations.

Three types of crack initiation have been observed in ductile solids as described in the study by Yates[32]

1) Cracks developed directly from persistent slip bands (PSBs), which are planes of discontinuity with abrupt difference in the density and distribution of dislocations on both sides.

2) Cracks initiated along a twin grain boundary. This kind of initiation is less common than the previous one. Kim and Laird[33] noted that this initiation occurs if: (a) the grain boundaries separate highly misoriented grains; (b) the active slip system of at least one of the grains is directed at the intersections of the boundary with the specimen surface, and (c) the traces of the high angle grain boundaries in the free surface make a large angle (30°-90°) with the tensile stress axis.

3) Cracks initiated in grains that showed no evidence of slip bands.

Yates *et al* indicated that although the initiation mechanisms are different, all slip-band cracks initiated at 45° to the principal axis in a relatively large grain. However, in the current project, crack initiations at or around secondary phases within the lining material occur preferentially and the role of secondary phase distribution appears to be more relevant.

For materials containing particles/secondary phases, the fracture of brittle particles and debonding at matrix-particle interfaces are two common failure mechanisms. Most of the particle fracture phenomena are observed with hard brittle particles. In Gross-Weege's research[34], a common tool steel CAE-D3 and a high speed steel (ASP30) were investigated as representative of general discontinuously reinforced composites. Hard phases of $M_7C_3$ exist in different arrangements within the ductile matrix. Experimental observation revealed that two different damage mechanisms exist, i. e., cleavage of big particles, and interfacial failure for small annealed carbides and spherical hard phases. Consequently, FE simulation of crack initiation was performed in the hard two-phase materials. A critical normal stress was used as the criterion for interfacial cracking. If the normal stress at the interface reached that critical value, debonding was introduced to simulate the interfacial failure between the hard phase and metal matrix in the FEM. Similarly, an analogous criterion was applied for simulating hard particle fracture. In the FE modelling, the interfaces between the particles and the matrix were assumed to be perfectly bonded unless failure according to the adopted criterion occurred.

Similar phenomena of particle fracture have been observed and investigated using the finite element method[35,36,37]. In Moorthy's study[35], a ductile elastic-plastic Al-3.5%

Cu matrix material containing elastic brittle SiC inclusions was analysed. The model assumes that a crack is initiated once the maximum principal stress in the particles exceeds a critical failure stress. The orientation of the crack is taken normal to the maximum principal stress direction. The FEM analysis by Gall *et al*[36] considered Si particles embedded in Al-1%Si matrix and used the maximum tensile principal stress in Si particles as their fracture criterion for the study of stress distributions near damaged Si particle clusters.
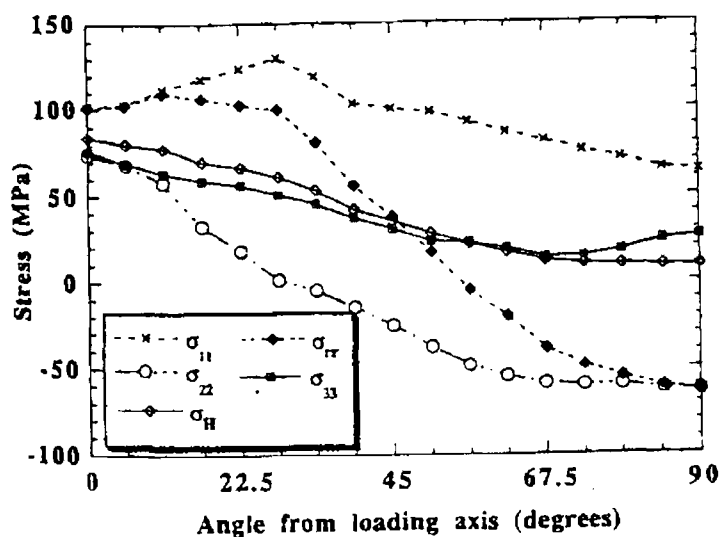


Figure 1-5    Predicted stress components in the matrix at the interface around a spherical particle, as a function of the angular divergence from the loading direction with an applied load of 100 MPa for Al/Al$_2$O$_3$ MMC[40]

Another important type of failure in materials containing particles and secondary phases is the interfacial debonding due to the formation and growth of voids at interfaces[38,39,40,41,42]. A continuum model for void nucleation by inclusion debonding was proposed by Needleman[38]. In this model rigid spherical inclusions in an isotropically hardening elastic-viscoplastic matrix were analyzed. A cohesive zone interface was considered in the model and it was suggested that hydrostatic stresses play an important role in the void nucleation process. Experiments carried out by Whitehouse *et al*[39] on Al metal matrix composites reinforced by Al$_2$O$_3$ were aimed at investigating void nucleation under tensile tests. The Al$_2$O$_3$ reinforcements had different shapes: spherical, angular, and fibres with an aspect ratio around 5. Void

formation was found most likely to happen at the interface when the reinforcement is elongated along the loading direction. Subsequent FEM in their research indicated that, for spherical particles, the maximum of the hydrostatic stress around a particle occurs at the pole relative to loading direction, where the observed void nucleation forms. However, the measured maximum normal interfacial stress happens at points with an angle off axis (as shown in Figure 1-5). FEM analysis to assess the effect of reinforcement aspect ratio and angularity also confirmed that the void would be nucleated at the position of the highest hydrostatic stress. The effect of hydrostatic stress in the Al matrix on debonding of particles was also reported by Soppa *et al*[42] in their investigation of an Al/Al$_2$O$_3$ composite. A void nucleation study on a SAE4330 modified steel containing 0.040 wt pct Ti by Shabrov *et al*[43] examined various void nucleation criteria and found that a combination of the hydrostatic tension and a effective stress were well correlated with the onset of nucleation. This compares with the use of a critical normal stress as a criterion for decohesion between a hard phase and metal matrix suggested by some researchers[34,44].

### 1.3.4   Micro-mechanical modelling

It has been demonstrated by many researchers that microstructure-based FEM under prescribed far field loading can provide important information on the local stress and strain fields. Most of these micromechanical analyses employ methods of continuum mechanics to deduce the overall behaviour of multiphase material from the material behaviour of the individual components and from the constituents' arrangement. The most straightforward application of these studies is material characterisation, which in this project will be achieved from information derived from hardness tests. However, the ability to describe highly localised stress and strain fields from micromechanical modelling is of interest here to evaluate the relationship between microstructure and fatigue crack initiation in multi-phase microstructures.

Homogenization and localization are two important features of continuum mechanics. Characterisation of inhomogeneous materials usually involves the process of applying homogenization, while to investigate local behaviour involves application of localization. For regions of materials that do not have significant gradients in

macroscopic stress, strain and composition, the microscale strain and stress fields ($\varepsilon(x)$, $\sigma(x)$) and the macroscale responses ($\langle\varepsilon\rangle$, $\langle\sigma\rangle$) have the following relations[45]:

$$\varepsilon(x) = \mathbf{A}(x)\, \langle\varepsilon\rangle$$

$$\sigma(x) = \mathbf{B}(x)\, \langle\sigma\rangle$$

where $\mathbf{A}(x)$ and $\mathbf{B}(x)$ are called mechanical strain and stress concentration tensors. Use of such a process to obtain microscale information from macroscale responses is called localization. The opposite process, homogenization, could be described by the following relations:

$$\langle\varepsilon\rangle = \frac{1}{\Omega_S} \int_{\Omega_S} \varepsilon(x)\, d\Omega$$

$$\langle\sigma\rangle = \frac{1}{\Omega_S} \int_{\Omega_S} \sigma(x)\, d\Omega$$

where $\Omega_S$ is the volume of the region of interest.

One important part of homogenization and localization methods is to find a reference volume's responses to link the local behaviour and the prescribed mechanical loads (typically far field stresses or far field strains) or changes due to temperature. Since the analysis of realistic phase distributions for a sufficiently large volume of materials requires very high computational capabilities, the following approximations have been developed to describe inhomogeneous materials in micromechanical modelling: Mean Field Approaches (MFAs), Periodic Microfield Approaches (PMAs) or Unit Cell Methods, and Embedded Cell Approaches (ECAs).

Most of the MFAs to describe multiphase materials are based on the work of Eshelby[46]. The case of a sub-region which no longer fits its previous space due to shape or size change in homogenous material was considered by Eshelby. For an elastic inclusion in an infinite matrix subjected to a uniform strain $\varepsilon_I$, the uniform strain $\varepsilon_c$ in the constrained inclusion is given by the following expression

$$\varepsilon_c = \mathbf{S}\varepsilon_I$$

where $\mathbf{S}$ is the Eshelby tensor. It is especially useful to model the stress fields within a typical matrix-inclusion composite. More complex MFAs such as Mori-Tanaka methods[47] and self-consistent schemes[48] have been developed to expand this approach.

In Periodic Microfield Approaches (PMAs) or Unit Cell Methods the real inhomogeneous material is approximated by creating a model material with a spatially periodic phase arrangement. The corresponding periodic microfields can be obtained by analyzing unit cells (which describe microgeometries ranging from rather simplistic to highly complex depending on the analysis requirement) by exact or numerical methods. The analysis may be limited to a single cell without losing much information. Unit cell methods are typically used for performing material characterization of inhomogeneous materials, but they can also be used as micromechanically based constitutive models.

Recent examples of applying Unit Cell methods to two-dimensional micromechanical modelling for material characterisation can be found in the literature. Al-Abbasi and Nemes[49,50] developed such a model to investigate the effect of particle size variation and volume fraction on the predicted stress strain curves of dual phase steels. A typical unit cell containing one or two Martensite particles in a Ferrite matrix was modelled in this analysis. Nygards[51] established a two-dimensional micromechanical model to simulate the overall properties of two-phase ferritic/pearlitic steel. A typical microstructure of grains was obtained from microscopy and then modelled by the Voronoi algorithm. The representative periodic cell was modelled around 50 grains with periodic boundary conditions applied. The results obtained from the ABAQUS FE model showed good agreement with experimental results at high strain levels along the stress strain curve, but less agreement around the yield point. However, the feature of periodic boundary conditions in this micromechanical modelling enables the investigation of material behaviour under biaxial loading.

Steglich[52] generated a 3D unit cell micromechanical model on $Al/Al_3Ti$ composites to provide the overall mechanical properties for a mesomechanical modelling analysis. A hexagonal cell containing one particle was modelled and symmetry conditions were applied. By simulating a precracked or a perfect particle, the lower and upper bound of mesoscopic stress strain curve could be obtained for mesomechanical damage analysis. Similar work on a 3D unit cell model for a unidirectional fibre metal matrix composite was presented in Aghdam's work[53] to investigate the effect of interface damage on the predicted stress strain curve.

Another important application of Unit Cell Methods is to study the initiation of damage at the microscale because of their high resolution of the microfields. They can give detailed information on the local stress and strain fields of a given unit cell, but they tend to be computationally expensive and are less suited for investigating phenomena such as the interaction of microscopic cracks due to the periodic requirement. Examples of applying unit cell methods in 3D micromechanical modelling for local stress or damage analysis can be found in the literature[54,55,56].

The representative unit cell for modelling needs to be carefully selected when the micromechanical details are of concern. Wilkins and Shen[57] investigated the stress enhancement in inclusions by developing a unit cell model for SiC particulate reinforced aluminum matrix composites. Two kinds of unit cells were considered in their micromechanical modelling. The simplistic model simulated an axisymmetric unit cell containing a large inclusion and Al/SiC "matrix", in which the Al/SiC mixture was treated as homogeneous. In the refined model, the SiC phase was separated out as small discrete particles in Al/SiC mixture. Both models give good prediction of stress enhancement around the inclusion that is consistent with the measured propensity of fatigue crack initiation when elasticity dominates. When plasticity dominates, only the refined model could capture the observed trend in experiments.

Unit cell methods can be used for simulated microstructure[35] or actual microstructure[58] to investigate particle damage or initiation by selecting a proper representative material element in a micromechanical model. Microstructure features such as particle size, clustering and shape could be linked to material failure in a more straightforward way in these analyse. Brockenborough[58] reported that large hard particles have a greater probability of failure than smaller particles at the same stress level, and in addition, clustered hard particles tend to crack. Similar results were also reported by Moorthy[35].

Generally ECAs use a core region that contains a discrete phase arrangement similar to a unit cell. Instead of applying periodic boundary conditions, the core region is surrounded by a large outer region material of bulk material property, which serves to transfer far field loads or displacement to the core (as shown in Figure 1-6). The

material properties of this outer region do not need to be accurate at the first stage of material characterisation; they can be determined self-consistently or quasi-self-consistently from the behaviour of the core. ECAs are very well suited for studying regions of special interest, e.g. crack tips and their neighbourhood in inhomogeneous materials. Like PMAs, embedded cell approaches can resolve local stress and strain fields in the core region at high detail, but do not have a limit on periodic boundary conditions.

Far field loading

Core region. Matrix and particles modelled separately -discrete material properties assigned to each phase

Embedding region. Homogeneous material – bulk material properties
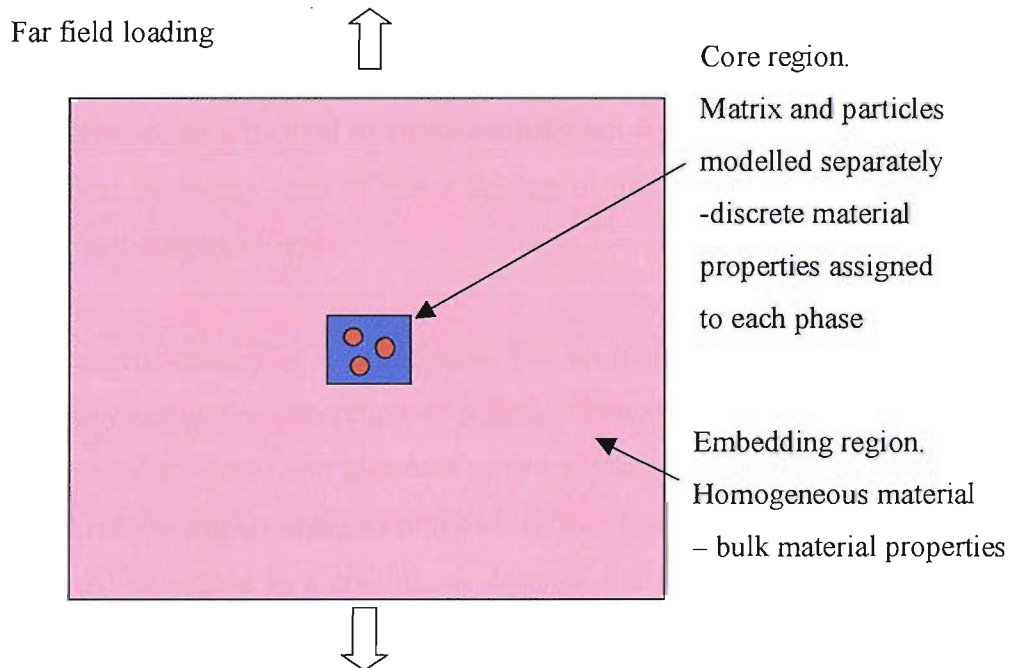
Figure 1-6    Embedded cell model geometry

Dong *et al*[59] developed a self-consistent embedded cell model to calculate the stress strain curves for a particle reinforced Ag-58vol.%Ni composite and for a transversely loaded uniaxially fibre reinforced Al-46vol.%B composite. Good agreement was obtained between experiment and calculation results. It was suggested that the outer region should be made at least approximately 25 times the area of the core to eliminate the influence of the outer region geometry boundary condition on the embedded core region. Farrissey[60] calculated the stress strain curve of a 58 vol% martensite-austenite composite using different analytical and finite element models, among which the 3D embedded cell model was found to have the closest result to experimental one while requiring only a reasonable computational time. An example

of applying the embedded cell model incorporating local damage behaviour was reported by Aktaa[61]. The obtained effective Young's modulus and yield stress were in good agreement with theoretical and experimental results.

## 1.4  Introduction to finite element method

The finite element method is a numerical procedure for solving a group of differential equations governing the behaviour of structures and continua in cases it is too complicated to be solved satisfactorily by classical analytical methods. The finite element method originated as a method of stress analysis but it has also been used to solve various physical problems such as those arising in heat transfer, fluid flow, lubrication, electric and magnetic fields.

The basic finite element strategy is discretization. For an identified linear problem with known necessary input, the generation of a finite element model relies on the problem domain being discretized into elements joined at the nodes. Both nodes and elements are numbered for further analysis purpose. Unlike a classical approach, that is, solving differential equations in a continuous domain, the finite element method generates relations for each element rather than the whole domain. For each node the nodal degrees of freedom (DOFs) are specified. They form vectors for a single element or for the whole structure. Then relations are established between the various internal element variables such as rotations, stresses, strains, bending moments and the vector of DOFs. They lead to a group of linear equations between the nodal forces, and the nodal DOFs. All the equations for elements together contribute to the equations for the whole problem domain, leading to a global matrix equation between the global force vector (usually consisting of known applied forces and unknown reactions), and the DOFs of the whole domain. The coefficient matrix in this equation is known as the global stiffness matrix. By applying boundary conditions, this global equation can be reduced to a form only consisting of the free DOFs and known external forces, which can be solved using established algorithms. The nodal DOFs are then determined and then used to determine the internal variables for each or any chosen element.

Non-linear behaviour arises from a number of causes, which can be grouped into three basic types: changing status, geometric nonlinearities, and material nonlinearities. The non-linear behaviour in this project is mainly due to material nonlinearities (elasto-plastic behaviour). Unlike a linear problem where the stiffness matrix is constant, the stiffness matrix of elasto-plastic analysis changes with load. One common method to solve an elasto-plastic problem is to apply the load incrementally over several load steps. Within each load step, the problem is assumed linear. Many iterative methods such as Newton-Raphson method, Quasi-Newton method, have been developed for updating the solution matrix in non-linear problems.

In this project the finite element analyses are performed using ANSYS61[62], which is a general purpose finite element modelling package for numerically solving a wide variety of mechanical problems including: static/dynamic structural analysis (both linear and non-linear), heat transfer and fluid problems, as well as acoustic and electromagnetic problems. A typical ANSYS program has three analysis stages: (a) building the model, (b) applying loads (and boundary conditions), and obtain the solution, and (c) review the results. These stages correspond to the three basic processors available in ANSYS: Preprocessor, Solution, and Postprocessor. The Preprocessor is used to build model, which includes the element types, material properties, model geometry, and mesh control. Solution processor is used to specify loads and boundary conditions and to perform the calculations. Several methods are available in ANSYS program to solve the equations. The Postprocessor is used to review the FEM results obtained by Solution processor. It provides various ways to illustrate the results such as contour plots, tables, and graphs.

## 1.5 SUPANOVA

SUPANOVA is an adaptive numerical modelling technique applied to both the material characterisation and microstructure problems for regression and classification purposes, respectively.

Adaptive numerical methods generate approximate multi-dimensional relations through interpolations between a sufficiently large number of datasets. A dataset

consisting of inputs, $x_1$, $x_2...x_n$, which are believed to contribute to an output $y$, can be assessed by many possible regression approaches. Purely adaptive numeric methods will search for non-linear relationships for the mapping between $x_1$, $x_2...x_n => y$ without needing any specification of the form of the relationship. These methods (e.g. neural networks) may be considered as statistical, or machine learning techniques, and are many and varied and new ones are being developed continuously. They can be of considerable help in the analysis of complex problems, where a detailed understanding has not yet been reached, by supplying specific (though often highly complex) mathematical equations linking, for instance, material property inputs to respective hardness indentations and thus allowing predictions. ANMs provide powerful empirical tools for modelling non-linear datasets that are not fully understood or are not amenable to exact analytical solution. Examples of ANMs applied to Al alloy property modelling have been reported in the literature[63,64,65].

Support vector machines (SVMs) are often used in ANMs for many regression and classification problems[66]. They provide a mechanism for choosing optimal model complexity for limited data, thus accurately achieve regression and classifying behaviour. SVMs make use of kernels which are functions that provide a method of dealing with non-linear algorithms by enabling computations to be done in the input space as opposed to the potentially high dimensional feature space. Unlike more recent advanced "hybrid models" which combine neuro-fuzzy with physically based modelling to aid interpretation[67], SVMs are essentially complex "black-box" predictive models (as are many neural networks such as the Bayesian MLP[65] etc.) that sacrifice the direct interpretability of a model in order to obtain a high regression accuracy or classification rate. They are thus referred to as having a lack of transparency, i.e. they can produce very accurate models, but the relationship between inputs and outputs is difficult to visualise when assessing the physical relationships. The models are therefore difficult to validate and have very little value for understanding the physical meaning of the complex system. It is important to increase the "transparency" of these "black box" models to visualise underlying relationships between inputs and outputs for more scientific interpretation and model validation.

Transparency can be introduced by the use of the SUpport vector Parsimonious ANOVA (SUPANOVA[68]) framework, where an Analysis Of Variance (ANOVA[69]) functional decomposition of the form:

$$f(x) = f_0 + \sum_{i=1}^{N} f_i(x_i) + \sum_{i=1}^{N} \sum_{j=i+1}^{N} f_{i,j}(x_i, x_j) + \ldots + f_{1,2,\ldots,N}(x)$$

is used within the kernel. This representation is based on the concept that any high dimensional SVM function ($f(x)$ say) may be broken down into a subset of terms, where $f_0$ is the bias (constant term), $N$ represents the number of input parameters and other terms are all possible univariates, bivariates, trivariates, etc., functional combinations of the input parameters. By breaking down the whole model into sub-functions, the influence of each input parameter on the output is relatively easy to understand. Rather than using all the sub-functions, the SUPANOVA techniques choose a sparse representation of these terms to give maximum transparency without sacrificing predictive accuracy.

## 1.6    Structure of thesis

Chapter 2 lays out the details of combining the load-indentation data from micro hardness tests, finite element modelling and adaptive numerical modelling to determine material properties in the individual bearing lining layers. Both methodology and application are discussed for these approaches.

FEM analysis to identify the effect of microstructure on fatigue initiation behaviour has been presented in Chapter 3. Tessellation of the secondary phase distribution has been combined with ANM classification approaches to predict initiation sites based on new, previously unanalysed experimental observations. FEM analysis has been performed on both particle distributions from the lining material of AS16 flat strip and corresponding equivalent idealized particle distributions to assess early fatigue initiation sites and to establish the initiation mechanism. Developing such an approach will allow the successful fatigue initiation assessment of simulated particle distributions allowing optimized fatigue resistant microstructures to be identified.

Chapter 4 draws together the overall thesis findings and outlines areas of future work.

[1] A.C. Hollis, Fatigue of journal bearings, T&N Technology LTD confidential report, (1992)

[2] M.C. Mwanza, M.R. Joyce, K.K. Lee, S. Syngellakis and P.A.S. Reed, Microstructural characterisation of fatigue crack initiation in Al-based plain bearing alloys, Int. J. Fatigue, Vol. 25, September-November, pp. 1135-1145, (2003)

[3] H. Bahai, T&N Technology LTD confidential report, (1997)

[4] M.R. Joyce, Fatigue of aluminium linings in plain automotive bearings, PhD Thesis, University of Southampton, (2000)

[5] M.C. Mwanza, Microstructural modelling of fatigue in novel plain bearing designs, PhD Thesis, University of Southampton, (2004)

[6] A. Wholer, Versuche uber die festigkeit der eisenbahnwagenachsen. zeitschrift fur bauwesen. Vol. 10, (1860), English summary, Engineering Vol. 4, pp. 160-161, (1867)

[7] N. Glyde, Fatigure fracture in Babbitt lined journal bearings, PhD Thesis, Technical University of Denmark, Copenhagen, (1969)

[8] P.P. Love, P.G. Forrester and A.E. Burke, Functions of materials in bearing operation, Proc. Inst. Mech. Engrs., Automobile Div. No. 2, (1953-54)

[9] W.E. Duckworth and G.H. Walter, Fatigue of plain Bearings, Int. Conf. on Fatigue of Metals, I. Mech. E., pp. 585-592, (1956)

[10] E.A. Blount, Design factors influencing the fatigue resistance of connecting-cod big-end bearings, Proc. I. Mech. E., Vol. 175, pp. 513-527, (1961)

[11] M. Sakamoto, Y. Ogita, Y. Sato and T. Tanaka, Development of new Aluminium – Zinc-Silicon bearings for heavy load applications in uprated engines, SAE paper 900124, (1990)

[12] H.F. Romer, The effect of tin particles size on the fatigue strength and surface properties of AS15, Report no.514, AE No. 114/072/69, (1969)

[13] A.K. Busby and J.W. Martin, Fatigue crack propagation in Al-Sn bearing alloys, Mater Sci Tech, Vol. 5, pp. 689-698, (1989)

[14] A.K. Busby, J.W. Martin and N.J.H. Holroyd, Environmental embrittlement of Al-Sn alloys and its implication for fatigue crack growth, Mater Sci Tech, Vol. 4, pp. 518-523, (1988)

[15] M.R. Joyce, K.K. Lee, S. Syngellakis and P.A.S. Reed, Quantitative assessment of preferential fatigue initiation sites in a multiphase aluminium alloy, Fatigue Fract Eng M, Vol. 27, pp. 1025-1036, (2004)

[16] D. Tabor: The hardness of Metals (Clarendon Press, Oxford, 1951).

[17] S. Jayaraman, G.T. Hahn, W.C. Oliver, C.A. Rubin and P.C. Bastias, Determination of monotonic stress-strain curve of hard materials from ultra-low-load indentation tests, Int J Solids Structures, Vol. 35, pp. 365-381, (1998)

[18] B. Taljat, T. Zacharia and F. Kosel, New analytical procedure to determine stress-strain curve from spherical indentation data, Int J Solids Structures, Vol. 35, pp. 4411-4426, (1998)

[19] A.K. Bhattacharya and W.D. Nix, Analysis of elastic and plastic-deformation associated with indentation testing of thin-films on substrates, Int J Solids Structures, Vol. 24, pp. 1287-1298, (1988)

[20] A.K. Bhattacharya and W.D. Nix, Finite-element analysis of cone indentation, Int J Solids Structures, Vol. 27, pp. 1047-1058, (1991)

[21] A. Nayebi, R. El Abdi, O. Bartier and G. Mauvoisin, New procedure to determine steel mechanical parameters from the spherical indentation technique, Mech Mater, Vol. 34, pp. 243-254, (2002)

[22] K. Zeng, A.E. Giannakopoulos and D.J. Rowcliffe, Vickers indentations in glass-II: comparison of finite element analysis and experiments, Acta Metall Mater, Vol. 43, pp. 1945-1954, (1995)

[23] K. Zeng, E. Soderlund, A.E. Giannakopoulos and D.J. Rowcliffe, Controlled indentation: A general approach to determine mechanical properties of brittle materials, Acta Mater, Vol. 44, pp. 1127-1141, (1996)

[24] K. Zeng and C. –h Chiu, An analysis of load-penetration curves from instrumented indentation, Acta Mater. Vol. 49, pp. 3539-3551, (2001)

[25] P. Lamagnere, D. Girodin, P. Meynaud, F. Vergne and A. Vincent, Study of elasto-plastic properties of microheterogeneities by means of nano-indentation measurements: application to bearing steels, Mat Sci Eng A-Struct, Vol. 215, pp. 134-142, (1996)

[26] R. Osterlund, O. Vingsbo, L. Vincent and P. Guiraldenq, Butterflies in fatigued ball bearings-formation mechanisms and structure, Scand J Metall, Vol. 11, (1982)

[27] A.E. Giannakopoulos and S. Suresh, Determination of elastoplastic properties by instrumented sharp indentation, Scripta Mater, Vol. 40, pp. 1191-1198, (1999)

[28] T.A. Venkatesh, K.J. Van Vliet, A.E. Giannakopoulos and S. Suresh, Determination of elasto-plastic properties by instrumented sharp indentation: guidelines for property extraction, Scripta Mater, Vol. 42, pp. 833-839, (2000)

[29] M. Dao, N. Chollacoop, K.J. Van Vliet, T.A. Venkatesh and S. Suresh, Computational modelling of the forward and reverse problems in instrumented sharp indentation, Acta Mater, Vol. 49, pp. 3899-3918, (2001)

[30] A. Muliana, R. Steward, R.M. Haj-Ali and A. Saxena, Artificial neural network and finite element modelling of nanoindentation tests, Metall Mater Trans A, Vol. 33, pp. 1939-1947, (2002)

[31] N. Huber, W.D. Nix and H. Gao, Identification of elastic-plastic material parameters from pyramidal indentation of thin films, P Roy Soc Lond A Mat, Vol. 458, pp. 1593-1620, (2002)

[32] J.R. Yates, W. Zhang and K.J. Miller, The initiation and propagation behaviour of short fatigue cracks in Waspaloy subjected to bending, Fatigue Fract Eng M, Vol. 16, pp. 351-362, (1993)

[33] W.H. Kim and C.Laird, Crack nucleation and stage I propogation in high strain fatigue-2. Mechanism. Acta Metall, Vol. 26, pp. 789-799, (1978)

[34] A. Gross-Weege, D. Weichert and C. Broeckmann, Finite element simulation of crack initiation in hard two-phase materials, Comp Mater Sci, Vol. 5, pp. 126-142, (1996)

[35] S. Moorthy and S. Ghosh, Particle cracking in discretely reinforced materials with the Voronoi Cell finite element model, Int J Plasticity, Vol. 14, pp. 805-827, (1998)

[36] K. Gall, M. Horstemeyer, D.L. McDowell and J. Fan, Finite element analysis of the stress distributions near damaged Si particle clusters in cast Al-Si alloys, Mech Mater, Vol. 32, pp. 277-301, (2000)

[37] D.L. McDowell, K. Gall, M.F. Horstemeyer and J. Fan, Microstructure-based fatigue modelling of cast A356-T6 alloy, Eng Fract Mech, Vol. 70, pp. 49-80, (2003)

[38] A. Needleman, A continuum model for void nucleation by inclusion debonding, J Appl Mech-T ASME, Vol. 54, pp. 525-531, (1987)

[39] A.F. Whitehouse and T.W. Clyne, Critical stress criteria for interfacial cavitation in MMCs, Acta Metall Mater, Vol. 43, pp. 2107-2114, (1995)

[40] Y. Liu, Y. Tanaka and C. Masuda, Effect of Interfacial debonding and sliding on matrix crack initiation during isothermal fatigue of SCS-6/Ti-15-3 composites, Metall Mater Trans A, Vol. 31, pp. 2637-2645, (2000)

[41] K. Gall, N. Yang, M. Horstemeyer, D.L. McDowell and J. Fan, The debonding and fracture of Si particles during the fatigue of a cast Al-Si alloy, Metall Mater Trans A, Vol. 30, pp. 3079-3088, (1999)

[42] E. Soppa, S. Schmauder, G. Fisher, J. Brollo and U. Weber, Deformation and damage in Al/Al$_2$O$_3$, Comp Mater Sci, Vol. 28, pp. 574-586, (2003)

[43] M.N. Shabrov, E. Sylven, S. Kim, D.H. Sherman, L.Chuzhoy, C.L. Briant and A. Needleman, Void nucleation by inclusion cracking, Metall Mater Trans A, Vol. 35A, pp. 1745-1755, (2004)

[44] A. Gross-Weege and D. Weichert, Micromechanical modelling of crack initiation in hard two-phase materials, J Mater Process Tech, Vol. 56, pp. 482-491, (1996)

[45] R. Hill, Elastic properties of reinforced solids: some theoretical principles, J Mech Phys Sol, Vol. 11, pp. 357-372, (1963)

[46] J.D. Eshelby, The determination of the elastic field of an ellipsoidal inclusion and related problems, P Roy Soc Lond, Vol. A241, pp. 376-396, (1957)

[47] T. Mori and K. Tanaka, Average stress in the matrix and average elastic energy of materials with misfitting inclusions, Acta Metall., Vol. 21, pp. 571-574, (1973)

[48] R. Hill, A self consistent mechanics of composite materials, J Mech Phys Sol, Vol. 13, pp. 213-222, (1965)

[49] F.M. Al-Abbasi and J.A. Nemes, Micromechanical modelling of the effect of particle size difference in dual phase steels, Int J Solids Structures, Vol. 40, pp. 3379-3391, (2003)

[50] F.M. Al-Abbasi and J.A. Nemes, Micromechanical modelling of dual phase steels, Int J Mech Sci, Vol. 45, pp. 1449-1465, (2003)

[51] M. Nygards and P. Gudmundson, Micromechanical modelling of ferritic/pearlitic steel, Mat Sci Eng A-Struct, Vol. 325, pp. 435-443, (2002)

[52] D. Steglich, T. Siegmund and W. Brocks, Micromechanical modelling of damage due to particle cracking in reinforced metals, Comp Mater Sci, Vol. 16, pp. 404-413, (1999)

[53] M.M. Aghdam and S.R. Falahatgar, Micromechanical modelling of interface damage of metal matrix composite subjected to transverse loading, Compos Struct, Vol. 66, pp. 415-420, (2004)

[54] J. A. Sherwood and H.M. Quimby, Micromechanical modelling of damage growth in titanium based metal-matrix composites, Comput Struct, Vol. 56, pp. 505-514, (1995)

[55] H. Ismar, F. Schroter and F. Streicher, Modelling and numerical simulation of the mechanical behaviour of woven Sic/Sic regarding a three-dimensional unit cell, Comp Mater Sci, Vol. 19, pp. 320-328, (2000)

[56] A. Eckschlager, W. Han and H.J. Bohm, A unit cell model for brittle fracture of particles embedded in a ductile matrix, Comp Mater Sci, Vol. 25, pp. 85-91, (2004)

[57] T. Wikins and Y. Shen, Stress enhancement at inclusion particles in aluminium matrix composites: computational modelling and implications, Comp Mater Sci, Vol. 22, pp. 291-299, (2001)

[58] J.R. Brockenbrough, W.H. Hunt and O. Richmond, A reinforced material model using actual microstructural geometry, Scripta Metall Mater, Vol. 27, pp. 385-390, (1992)

[59] M. Dong and S. Schmauder, Modelling of metal matrix composites by a self-consistent embedded cell model, Acta Mater. Vol. 44, pp. 2465-2478, (1996)

[60] L. Farrissey, S. Schmauder, M. Dong, E. Soppa, M.H. Poech and P. McHugh, Investigation of the strengthening of particulate reinforced composites using different analytical and finite element models, Comp Mater Sci, Vol. 15, pp. 1-10, (1999)

[61] J. Aktaa, H. Kiewel and J. Turki, Modelling of the influence of damage on the deformation behaviour by a self-consistent embedded cell model, Comp Mater Sci, Vol. 12, pp. 64-72, (1998)

[62] ANSYS 6.1, SAS IP, Inc., Canonsburg, PA, (2001)

[63] O.P. Femminella, M.J. Starink, M. Brown, I. Sinclair, C.J. Harris and P.A.S. Reed, Data pre-processing/model initialisation in neurofuzzy modelling of structure-property relationships in Al-Zn-Mg-Cu alloys, ISIJ Int, Vol. 39, pp.1027-1037, (1999)

[64] M.J. Starink, I. Sinclair, P.A.S. Reed and P.J. Gregson, Predicting the structural performance of heat-treatable Al-alloys, Mater Sci Forum Vol. 331-3, pp.97-110, (2000)

[65] S. Christensen, J.S. Kandola, O. Femminella, S.R. Gunn, P.A.S. Reed and I. Sinclair, Adaptive numerical modelling of commercial aluminium plate performance. Aluminium alloys: Their physical and mechanical properties, Mater Sci Forum, Vol. 331-3, pp. 533-538, (2000)

[66] C. Burges, A tutorial on support vector machines: Data mining and knowledge discovery 2, pp. 121-167, (1998)

[67] Q. Zhu, M.F. Abbod, J. Talamantes-Silva, C.M. Sellars, D.A. Linkens and J.H. Beynon, Hybrid modelling of Al-Mg alloys during thermomechanical processing in terms of physically-based neuro-fuzzy and finite element models, Acta Mater, Vol 51, pp 5051-5062 (2003)

[68] S.R. Gunn and M. Brown, SUPANOVA - a sparse, transparent modelling approach. Proc. IEEE International Workshop on Neural Networks for Signal Processing, (Edited by Y.H. Hu, J. Larsen, E. Wilson and S. Douglas), pp. 21-30, IEEE, Piscataway, NJ, USA, (1999)

[69] J.H. Friedman: The Annals of Statistics, Vol. 19, pp.1-141, (1999)

# CHAPTER 2  Characterisation of Bearing Lining Alloys

## 2.1  Introduction

Since the elastic-plastic properties of the lining material have a strong influence on the fatigue lifetime of the bearing and the development of local non-uniform stress and strain fields within the lining alloy layer, it is important to have reliable values of these properties for future modelling use. Tensile tests can sometimes be carried out to obtain the appropriate stress-strain curves of bearing materials such as those of the steel backing, which can be extracted from flat bearing strips before being formed into half-shells, or of monolithic sheets of lining material produced in a similar way to the layered systems, or for cast samples of pure metals, which form secondary phases in the lining alloy.

However, the bonded lining and curved bearing components cannot be characterised using tensile test procedures. In bearing linings, a complex rolling and heat treatment procedure is used to produce the final bearing so that the properties of the lining are no longer the same as those of the original alloy billet and may vary spatially (i.e. through thickness). Thus, it is necessary for the elasto-plastic properties of such thin layers to be assessed experimentally using alternative means to the traditional tensile test method. As a first step towards developing a general methodology, micro-hardness tests were undertaken as the basis for evaluating material properties. A standard Vickers hardness test cannot be easily applied to the lining layer because of its low thickness. However, micro-hardness tests allow the measurement of hardness within less than a mm of material thickness (e.g. bearing lining $\sim$ 0.5 mm). Typical micro-hardness indents may vary between 0.01 mm and 0.2 mm in an Al alloy over a load range 10 $\sim$ 1000 grams. Micro-hardness indent size variation with load may give some insight into the elastic-plastic properties of such thin layers. The aim of the work presented in this chapter is to establish a method for determining elastic-plastic material properties from simple, non-instrumented micro-hardness tests.

## 2.2   Methodology

The methodology given here involves a combination of different experimental and numerical techniques: Vickers micro-hardness test, FEM, adaptive numerical modelling and genetic algorithms.

The Vickers micro-hardness testing technique uses a square-based diamond pyramid as an indenter. The actual parameters measured during tests for the elasto-plastic property prediction are the diagonal size of the permanent indentation and the corresponding applied load so that experimental force-indentation size relations can be plotted. The indentation process was simulated by finite element modelling with an elasto-plastic material input characterised by a few key parameters: Young's modulus, elastic limit, 0.2% proof stress, strain hardening coefficient and exponent. Rather than being extracted from a rigorous theoretical analysis of the micro-hardness test results, here this elasto-plastic information for a new material will be identified as that producing the same load-indentation curve in FEM as the experimental one. This problem can therefore only be solved through an iterative scheme within an optimization algorithm. Since however repeated FEM simulation of indentations would have made the application of the iterative method practically impossible (too time-consuming), adaptive numerical modelling approaches were introduced into the characterisation process for estimating (effectively, interpolating) indentation behaviour from a given set of material data and FE cases.

Initially, both micro-hardness tests and subsequent FE analysis were carried out on aluminium alloys with known elasto-plastic properties so that the FE model could be validated. Once the reliability of the FE predictions was established, an expanded database of force-indentation size curves was generated by running the FE model with a realistic range of values for the key elasto-plastic properties mentioned above. This larger database has been used in an adaptive numerical modelling scheme to derive a generic approximate model for the indent size as a function of load, elastic limit, yield strength, as well as strain hardening coefficient and exponent for aluminium alloys. The generated adaptive numerical model was subsequently used to interpolate between the time-intensive FE results. Based on iterative application of the most

appropriate adaptive numerical model and a Genetic Algorithm (GA) program which was able to locate the optimum solution in a given solution space, the elastic limit, yield strength and strain hardening exponent for a given material can be determined from the experimental micro hardness force-indentation size curves. A flowchart of the overall methodology is shown in Figure 2-1.
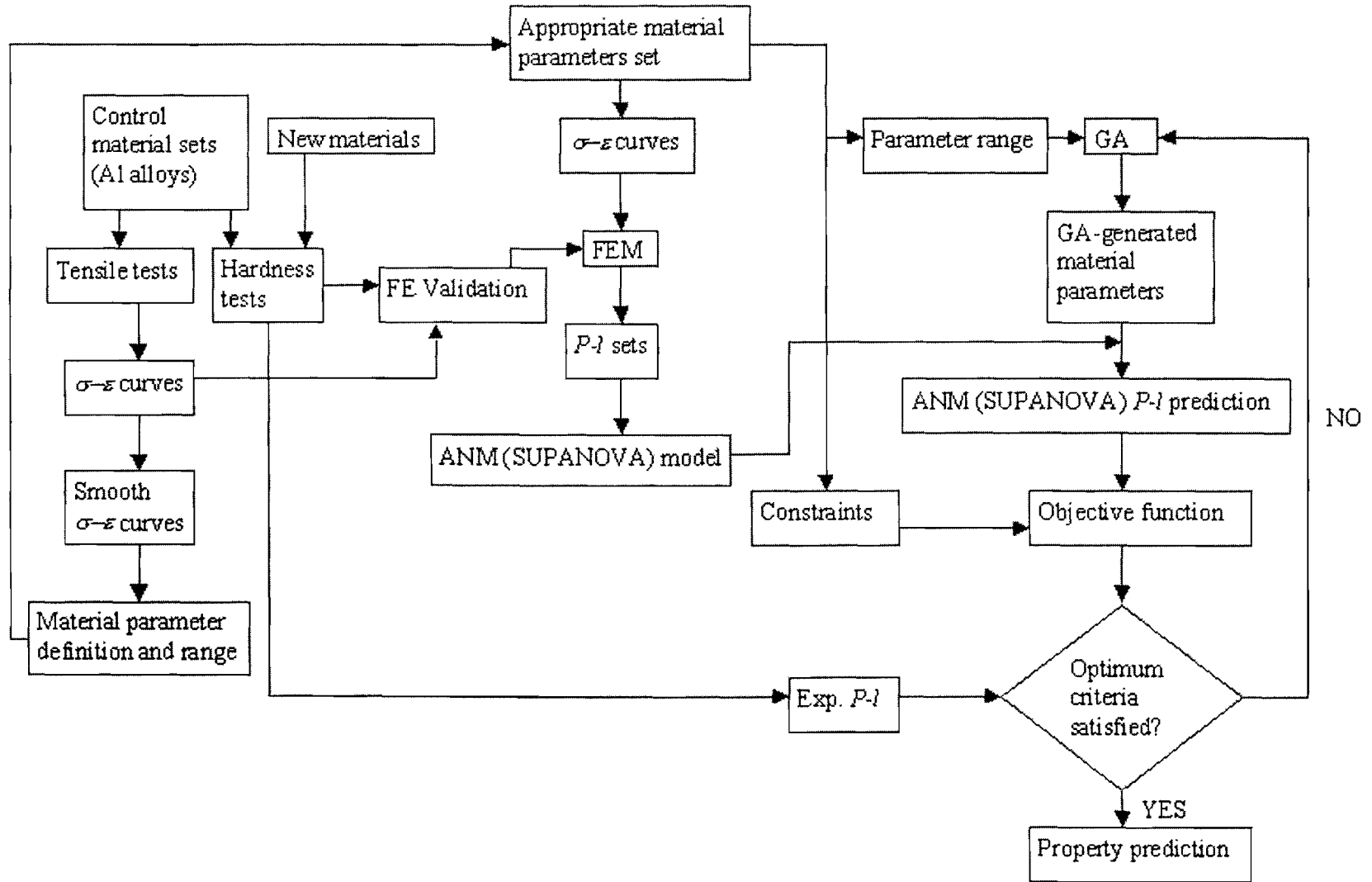
Figure 2-1　Flowchart of material characterisation procedure

## 2.3   Experimental results

### 2.3.1   Control materials

The term "control materials" is applied here to some Al alloys, available within the Southampton Materials group, with known elasto-plastic properties obtained from prior tensile tests. Initially, micro-hardness tests and FE modelling were carried out for these materials. The experimental load-indentation curves obtained were compared with the corresponding FEM results so that the reliability of the FE model could be established. The stress-strain curves of control materials also helped to define the ranges of critical parameters required to characterise the elasto-plastic behaviour of aluminium alloys.

The first among the control materials used was a monolithic bearing lining labelled by its manufacturers as AS1241. This is an Al alloy with Si and Sn as its main alloying elements. The remaining four control materials were commercial Al alloys known as: RTWQ and VQ1B, two differing extrusion batches of a 6082 Al alloy, as well as B1Q2 and B1Q3, two differing extrusion batches of a 2014A Al alloy. The compositions of the control materials are given in Table 2–1. Unfortunately the composition of 2014A alloy was not available, but it was suggested to be similar to commercial alloys with the ranges of element content as listed in Table 2–1.

**Table 2–1 Composition of control materials**

| Al alloy | Elements (in wt%) | | | | | | | |
|---|---|---|---|---|---|---|---|---|
| | Sn | Si | Cu | Mn | Fe | Mg | Other | Al |
| AS1241 | 12 | 4 | 1 | nominal | nominal | nominal | nominal | Balance |
| 6082 | 0 | 1.01 | 0.026 | 0.44 | 0.19 | 0.68 | 0.006 Cr, 0.02 Zn, 0.001 B, 0.009 Ti, | Balance |
| 2014A | 0.05 max | 0.50-0.90 | 3.9-5.0 | 0.4-1.2 | 0.50 max | 0.2-0.8 | 0.10 Cr, 0.2 max Zn, 0.2 max Ti+Zr, 0.2 max Ni, 0.05 max Pb | Balance |

An experimental stress-strain curve of AS1241 alloy was provided by the sponsors of this research programme[1]. Tensile tests for the other four materials were performed by a fellow researcher in the University of Southampton[2] on an Instron 1196 machine at room temperature. The samples had a gauge length of 25 mm and a 5 mm diameter. The stress-strain curves obtained directly from tensile tests are nominal stress-engineering strain curves and are shown in Figure 2-2.
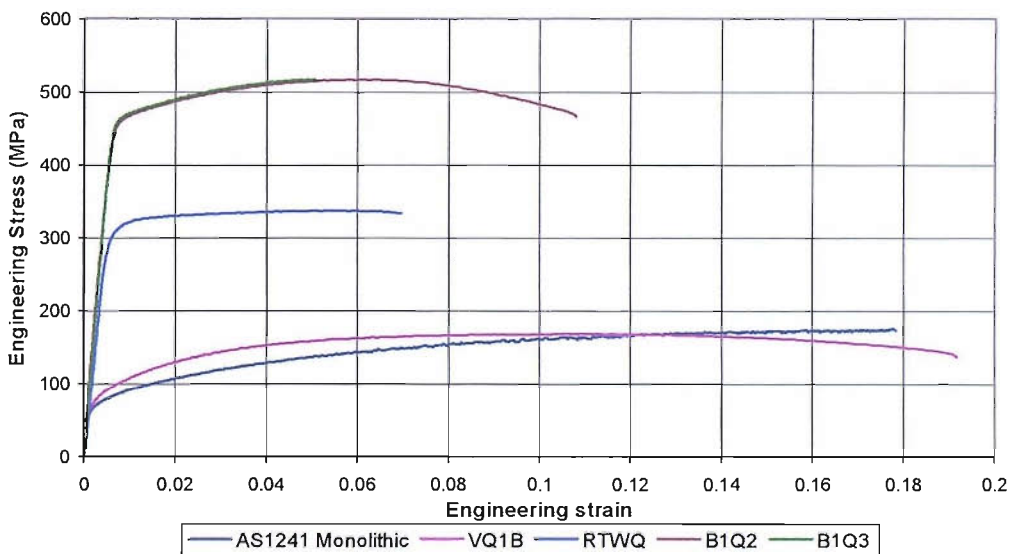


Figure 2-2    Nominal stress – engineering strain curves of control materials

However, a nominal stress-engineering strain curve does not represent the real stress-strain relationship during large elasto-plastic deformation which is essential to a large strain finite element analysis. For this reason, the nominal stress-engineering strain curve curves are converted into relations between true stress $\sigma$ and logarithmic strain $\varepsilon$ using the following equations:

$$\sigma = \sigma_n (1 + \varepsilon_n) \tag{2.1}$$

$$\varepsilon = \ln(1 + \varepsilon_n) \tag{2.2}$$

where $\sigma_n$ and $\varepsilon_n$ are the nominal stress and engineering strain respectively.

Before a $\sigma$-$\varepsilon$ curve could be used in a finite element analysis, a smoothing procedure needs to be applied to the raw data to ensure the feasibility and convergence of the

elasto-plastic indentation analysis. This process also generates the various parameters characterising elasto-plastic behaviour and was performed in the following steps:

1. For the elastic part of each curve, the proportional limit (assumed to be identical to the elastic limit) was identified and the Young's modulus $E$ was calculated. The elastic part of the curve was then replaced by a straight line through the proportional limit with a gradient equal to the Young's modulus.
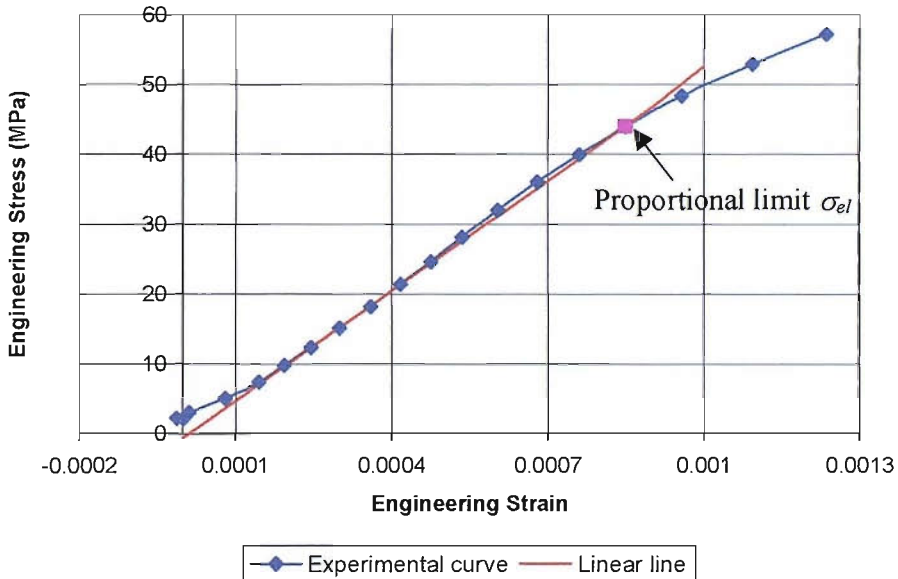


Figure 2-3    Linear part of the VQ1B $\sigma$-$\varepsilon$ curve

An example of this procedure is shown in Figure 2-3. The red straight line

$$\sigma = 53052\varepsilon - 0.5521 \qquad (MPa)$$

that defines the proportional limit $\sigma_{el}$, replaced the elastic part of experimentally obtained stress strain curve of VQ1B.

2. When tensile tests are performed, the records of load and elongation at beginning of tests are often inaccurate due to slack in the loading chain or gaps between the specimen and holding system, etc. Due to experimental errors, the intersection between the straight line representing elastic behaviour and the $\varepsilon$ axis is not always at the origin (as in Figure 2-3). A "shift" of the whole curve along the strain direction needs to be performed while keeping the stress at each point unchanged.

3. The $\sigma_n$-$\varepsilon_n$ curve is converted into $\sigma$-$\varepsilon$ curve using (2.1) and (2.2).

4. Since the experimental results consist of hundreds of stress and strain points and the material property input for FE has a limitation of 100 points, a proportion of data in the plastic region should be removed. One in five or ten points, depending on the total number of points, are retained to ensure that the selected points are evenly distributed along the whole curve.

5. Meanwhile, to ensure that the FE analysis can converge, the data should be carefully selected so that the final curve for the FE input file is smooth, i.e., its gradient is monotonically decreasing. This work to achieve this is mainly done manually. An example of selected points from part of a $\sigma$-$\varepsilon$ curve is given in Figure 2-4, in which the new curve through the selected points has a monotonically decreasing gradient.
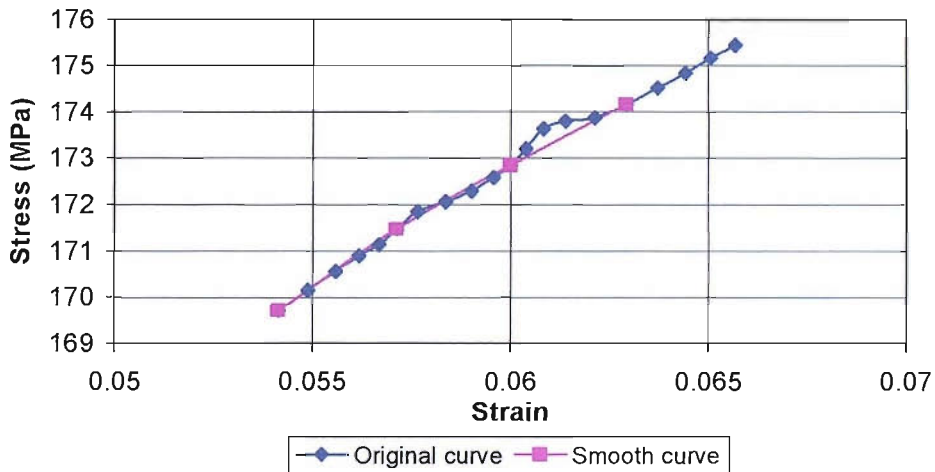


Figure 2-4    Example of point selection for a smooth $\sigma$-$\varepsilon$ curve

6. The useful part of the stress-strain curves obtained from the tensile tests ends at the point where necking of the specimen begins; as indicated in Figure 2-2, this corresponds to a strain value of up to 15%. However, in indentations, high compressive plastic strains develop under the indenter, well beyond 15%. Ideally compressive tests should be performed to obtain extended stress-strain relationships. Due to the difficulty of performing reliable compressive tests, the tensile stress-strain curve is extended by adopting an exponential model

$$\sigma = A\varepsilon^n \qquad (2.3)$$

for representing the plastic part. The parameters $A$ and $n$ of the exponential model are obtained by fitting (2.3) to the plastic region of the $\sigma$-$\varepsilon$ curve. If good exponential fitting to the curve between the 0.2% yield point $\sigma_{0.2}$ and necking point could not be achieved, the advanced part of the curve for best fitting was identified and the whole curve extended using the exponential model to a reasonably high strain value.

**Table 2–2 Stress-strain curve parameters of control materials**

| Control materials | $E$ (GPa) | $\sigma_{el}$ (MPa) | $\sigma_{0.2}$ (MPa) | $A$ (MPa) | $n$ |
|---|---|---|---|---|---|
| AS1241 | 60 | 45 | 73 | 357 | 0.2993 |
| VQ1B | 53 | 44 | 84 | 391 | 0.2769 |
| RTWQ | 65 | 242 | 312 | 421 | 0.0575 |
| B1Q2 | 75 | 355 | 463 | 716 | 0.0933 |
| B1Q3 | 75 | 360 | 469 | 723 | 0.0947 |

The final $\sigma$-$\varepsilon$ curves of all control materials are shown in Figure 2-5. The dashed lines indicate their exponential extensions. Table 2–2 lists the key parameters of the stress-strain curves of the control materials.
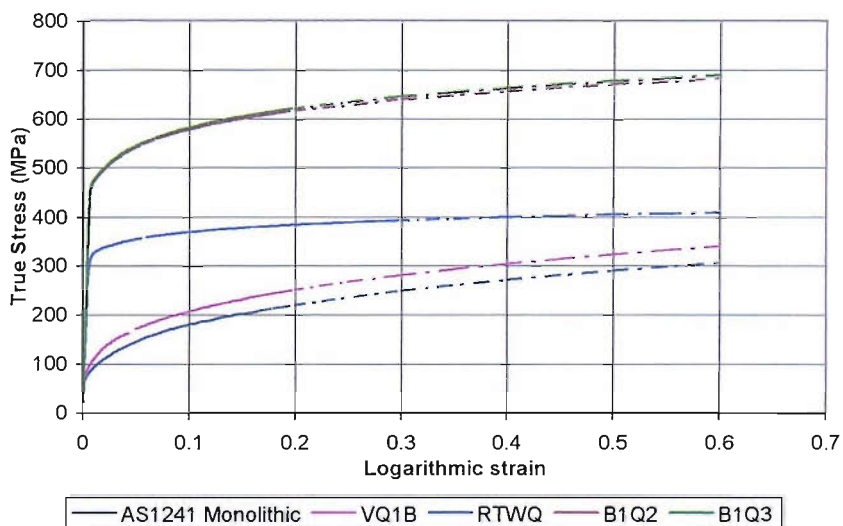


Figure 2-5     True stress – logarithmic strain curves for control materials

## 2.3.2   Hardness tests

Hardness is defined as a measure of a material's resistance to surface penetration by an indentation when it is subject to an applied local force. Since the local deformation is largely dependent on the plastic flow, hardness is related to plastic flow resistance. Nowadays the hardness test is widely used to examine the mechanical behaviour of a metal. Hardness tests are performed more frequently than any other mechanical tests for the following advantages[3]:

1. They are simple, inexpensive and do not need a special specimen to be prepared. In order to do a micro-hardness test, only very simple polishing is required.
2. The test is non-destructive. The specimen is neither fractured nor excessively deformed. The only deformation of the specimen is a small indentation.
3. Other mechanical properties often may be estimated from hardness data.

The indenter is usually made from a very hard material such as diamond. When performing a hardness test, the indenter is forced into the surface of the metal to be tested, and then the depth or size of the indentation is measured. This value is related to a hardness number, which is an established mechanical property of the material.

The Vickers micro-hardness technique was used to determine the material properties in this project because its small size is more suitable to the thin layer of bearings. The Vickers hardness test uses a square-based diamond pyramid as an indenter. It has been pointed out[3] that as a result of the geometric similarity of the Vickers indents, the variation of the developing plastic strain with applied load is small and, therefore, the degree of strain hardening would not be easily detected. This problem can be overcome through the use of a spherical indenter, but a pyramidal indentation has the advantage of its size being accurately measured and little affected by pile-up which is expected to be significant for soft aluminium alloys.

The micro-hardness tests were carried out using a Matsuzawa micro-hardness machine. A dwell time of 15 seconds for loading was set to ensure that the indenter

sits in the material long enough to achieve consistent results. The applied loads in the performed micro-hardness test are 10, 25, 50, 100, 200, 300, 500, and 1000 grams. For 6082 and 2014A alloys, the hardness tests were performed on cross-sections perpendicular to their tensile test directions. For the AS1241 alloy, the hardness tests were done on cross-sections LS and ST as shown in Figure 2-6 of the bearing and flat sheet linings as well as the control material, AS1241 monolithic alloy.
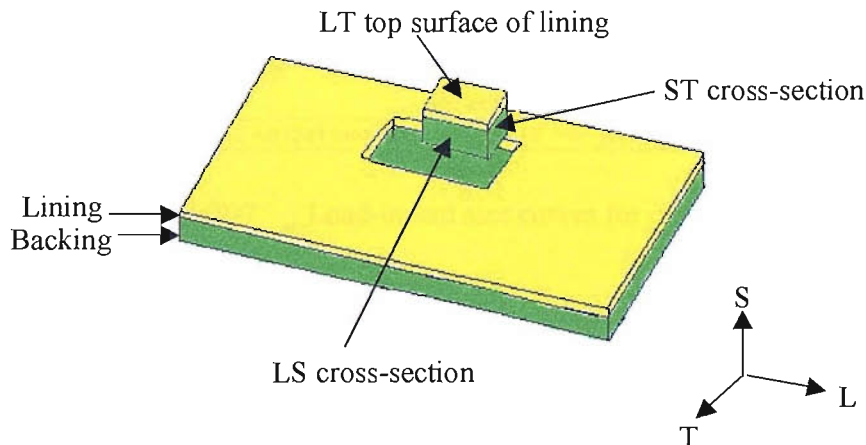
Figure 2-6    AS1241 flat strip specimen, showing hardness test direction

The Vickers hardness number is given by the load divided by the indented surface area. Since the indented area is relatively small compared to the indented areas associated with other types of hardness measurements, careful surface polishing is required before doing a Vickers indentation. The polishing work for these hardness tests was performed by a fellow researcher associated with the current bearing fatigue project. The actual parameter measured during tests is the diagonal size of the indentation instead of the contact area, and then the relationship between the diagonal size and the corresponding applied load was plotted.

A total of 40 indents (5 readings per load) were made across the surface on each of the samples of control materials (along the tensile test direction for VQ1B, RTWQ, B1Q2 and B1Q3, and cross section for lining materials). The measured load-average indent size curves with error bars are shown in Figure 2-7. The hardness experimental results and standard deviation are also given in Table 2–3.
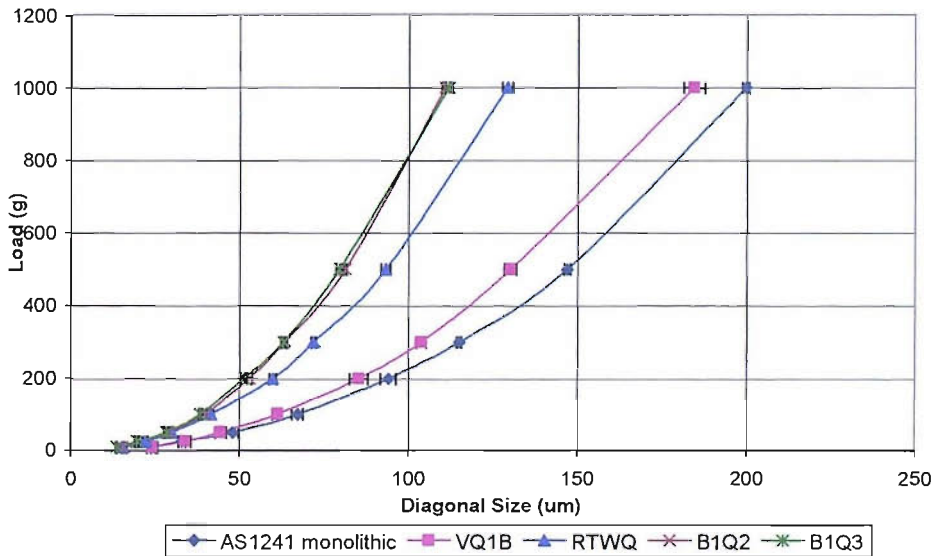
Figure 2-7      Load-indent size curves for control materials

It can be seen that the B1Q3 is slightly harder than B1Q2, and both of them are harder than other control materials. AS1241 monolithic is the softest material. The results of hardness tests are consistent with the relative trends of the $\sigma$-$\varepsilon$ curves shown in Figure 2-2.

**Table 2–3 Vickers Micro-hardness Test Results**

| Load (g) | Diagonal Size ($\mu$m) | | | | |
|---|---|---|---|---|---|
| | AS1241 Monolithic | VQ1B | RTWQ | B1Q2 | B1Q3 |
| 10 | 24.4±0.7 | 24.2±1.6 | 15.5±0.4 | 15.2±1.4 | 13.6±0.2 |
| 25 | 32.9±1.0 | 33.9±1.7 | 22.1±0.8 | 19.6±0.6 | 19.6±0.5 |
| 50 | 47.9±1.9 | 44.4±1.6 | 29.8±0.6 | 28.9±0.6 | 28.3±0.7 |
| 100 | 67.2±1.7 | 61.2±1.4 | 41.5±0.8 | 39.7±0.7 | 38.3±0.3 |
| 200 | 94.1±2.3 | 85.3±2.7 | 59.8±1.0 | 53.0±0.8 | 51.4±0.9 |
| 300 | 115.1±0.7 | 103.8±1.4 | 72.0±0.6 | 63.4±0.9 | 63.0±0.6 |
| 500 | 146.9±0.9 | 130.2±1.8 | 93.3±1.3 | 81.3±0.4 | 79.5±0.8 |
| 1000 | 199.8±1.0 | 184.5±3.1 | 129.2±1.5 | 110.8±1.1 | 111.8±1.0 |

Hardness tests were also performed on various other bearing lining materials for which stress-strain data were not available. These test results are listed in Table 2–4. They were used in Section 2.6 for the elasto-plastic characterisation of these linings. The data for AS16 bearing lining and HVOF lining were actually produced in a parallel research programme[4].

**Table 2–4 Vickers Micro-hardness test results of linings**

| Load (g) | Diagonal Size (μm) | | | | |
|---|---|---|---|---|---|
| | AS1241 Flat Strip | AS1241 Bearing | AS16 Flat Strip | AS16 Bearing | HVOF |
| 10 | 25.3±1.1 | 19.3±1.1 | 23.3±1.3 | 19.1±0.9 | 20.4±1.4 |
| 25 | 32.6±1.3 | 27.2±0.6 | 34.2±1.6 | 30.8±3.0 | 30.9±0.9 |
| 50 | 45.8±1.2 | 39.6±1.4 | 44.7±1.1 | 43.4±3.6 | 42.2±1.4 |
| 100 | 64.5±0.7 | 57.3±1.5 | 61.7±1.0 | 61.4±5.6 | 59.4±2.0 |
| 200 | 90.8±1.7 | 79.0±1.5 | 87.5±0.7 | 84.2±0.9 | 86.4±0.8 |
| 300 | 112.7±1.0 | 97.2±3.6 | 106.6±1.7 | 103.2±1.5 | 104.3±5.1 |
| 500 | 141.9±0.5 | 127.7±2.8 | 135.6±0.4 | 132.3±2.3 | 132.4±1.2 |
| 1000 | 189.6±3.7 | 173.7±6.4 | 187.6±1.0 | 182.7±2.7 | 192.0±5.9 |

## 2.4   FE modelling

The objective of this FE modelling was to simulate accurately the micro-hardness process so that reliable load-indentation size relations could be generated. Initially, the analysis was applied to materials with known stress-strain behaviour in order to establish the reliability of the model, which was then to be used to generate force-indentation size curves for a range of artificial material stress-strain curves. Thus a large database of force-indentation curves corresponding to a relevant range of elastic-plastic properties was obtained and subsequently used for the generation of the SUPANOVA indentation size-load/material parameters model. This analysis was performed using ANSYS 6.1[5], a general purpose FEM package.

## 2.4.1 Three-dimensional model

Initially, a three-dimensional (3D) Vickers model was developed in order to represent the geometry precisely in the simulation of the indentation process. Assuming a perfect square-based pyramid indenter, the geometry of the process is symmetric with respect to four vertical planes. Applying these symmetry conditions in the modelling, only one-eighth of the specimen and indenter is required to be modelled.

### 2.4.1.1 Model geometry

The specimen was modelled as a prismatic block with a 1×1 mm plan view and 0.5 mm depth. Referring to Table 2–3 and Table 2–4, the indentation diagonal sizes reached in tests do not exceed 200 μm, which corresponds to an indentation size of 141 μm and depth of 14.3 μm. The chosen size of the block was therefore rational since stresses and displacements away from the zone of contact were expected to be negligible while the size of the FE model was kept as small as possible. The diamond indenter was assumed rigid because of its high stiffness relative to that of the specimen. The validity of this assumption was later tested with the axi-symmetric (conical) indenter model. Thus, only the face of the rigid indenter in direct contact with the specimen needs to be modelled, which can be represented in ANSYS as a plane. The model geometry is shown in Figure 2-8. Since ANSYS performs all the calculations without units, it is important to define a consistent unit system throughout the modelling. It was decided to use mm for length and N for force.
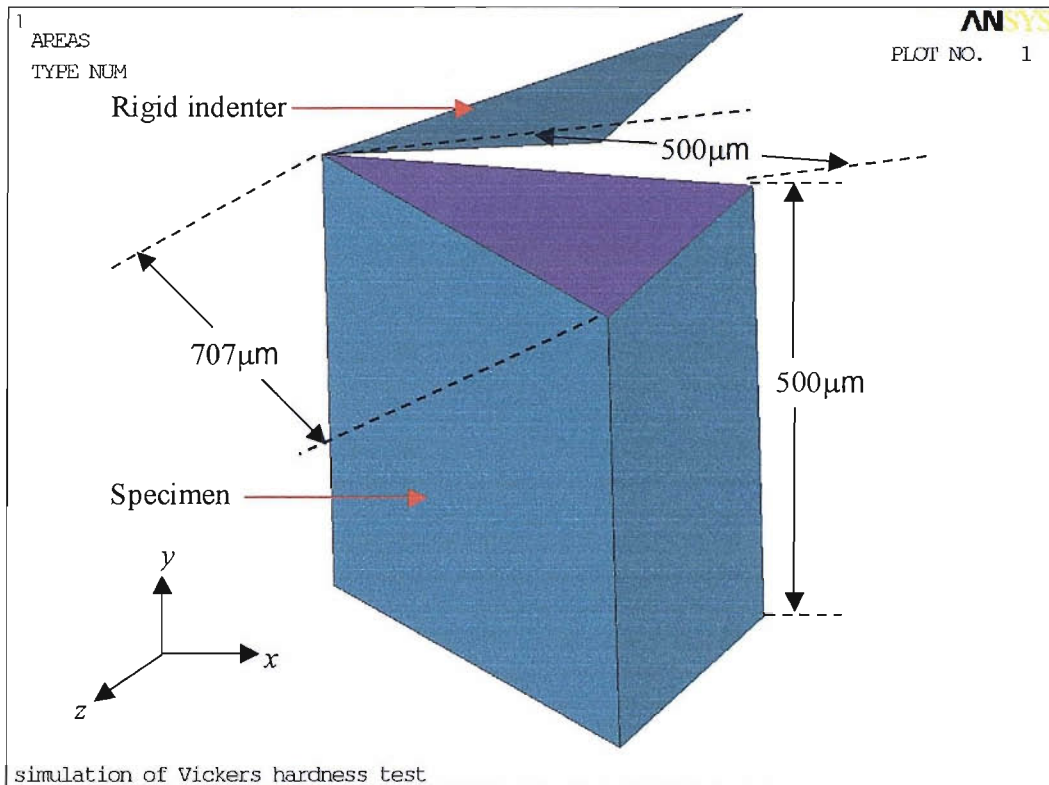
Figure 2-8     Geometry of three-dimensional FE model

## 2.4.1.2   Elements

The bulk of the specimen was modelled with SOLID45, which is an eight-node three-dimensional hexahedral element for solid structural elasto-plastic analysis. ANSYS has various special elements designed for contact problems. For a 3D rigid indentation simulation, the appropriate combination of contact elements, corresponding to SOLID45, are TARGE170 and CONTA173. This contact pair allows contact between two surfaces and one of them can be rigid. Here TARGE 170 was used to simulate the contacting face of the rigid indenter, which was meshed to several elements to improve computational efficiency. The top surface of the specimen was modelled with the 4-node CONTA173 forming a two-dimensional mesh, which perfectly matches the underlying top surface of the specimen solid element mesh. It is worth noting that the TARGE170-CONTA173 combination can also be used with SOLID185, while the contact pair TARGE170-CONTA174 is combined with the 20-node brick elements SOLID95 and SOLID186. These options

45

were subsequently tried but they did not provide results of higher accuracy than those obtained with the original element choices.
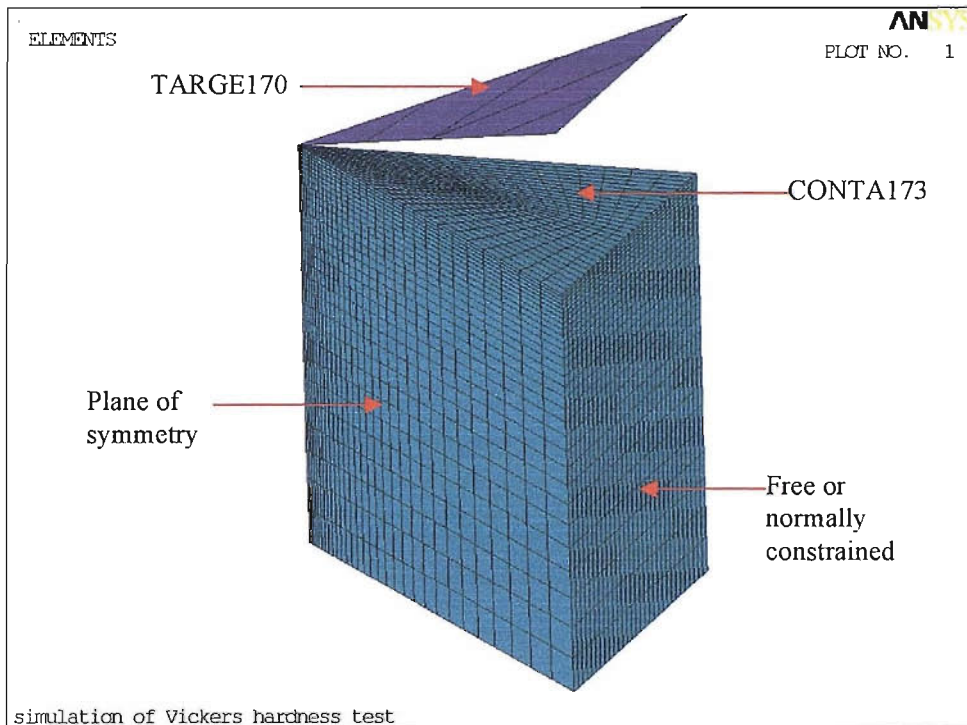


Figure 2-9    3D Model

In ANSYS the properties of a contact pair, such as TARGE169-CONTA171 or TARGE170-CONTA173, is controlled by a common set of real parameters. Most parameters of the set can be left with their default values but two of them are important and their effect needs to be assessed carefully. These are FKN, the normal contact stiffness factor and FTOLN, a tolerance factor. Improper values for those parameters will cause either too much artificial penetration or convergence problems.

### 2.4.1.3   Material properties

During hardness tests, the metal will have both elastic and plastic deformation. After the load is removed, there is a slight elastic recovery from the total deformation in that part of the specimen. Since the whole physical process is non-linear, this requires additional consideration in modelling. To represent such elastic and also plastic strain

hardening behaviour, the complete stress-strain curve of the metal is required as a material properties input. As pointed out in Section 2.3, this curve is typically obtained from standard tensile tests. The non-linear material behaviour can be incorporated into an ANSYS analysis if an appropriate element is used. Here the Multilinear Isotropic (MISO) hardening model is used to perform the large strain deformation as recommended by the ANSYS user manual and this model allows the full stress-strain curve as input without losing information. It is actually a multilinear curve which contains no more than 100 different stress-strain points selected from the stress strain curve of material. The Poisson's ratio (usually assumed to be 0.33) is also required. The contact pair was not ascribed by any material properties although it is possible to enter the maximum contact friction as a real constant TAUMAX. Sliding will occur if the friction stress reaches the value of TAUMAX. In this modelling the default value of $10^{14}$ MPa was taken for TAUMAX.

### 2.4.1.4  Meshing

During the hardness test, the bulk of the specimen will not deform significantly. Thus the mesh was designed so that only the part underneath the tip of the indenter was refined to obtain smooth and accurate results. The rest of the specimen was meshed with larger elements since the corresponding results have little influence on the accuracy of the model. The meshing was performed within the ANSYS pre-processor. The presented results were obtained with the mesh shown in Figure 2-9. In this mesh the specimen has 12000 solid elements (SOLID45) and the contact surface has 300 contact elements (CONTA173) overlaid on the solid elements of the specimen surface.

### 2.4.1.5  Boundary and loading conditions

The model represents one-eighth of the real object. Symmetry boundary conditions were applied on the sides of the model, which lie on the symmetry planes. The bottom of the specimen was constrained in the $y$-direction since it cannot move vertically during experiments. As mentioned earlier, the lateral faces of the specimen are at a

sufficient distance from the indenter tip for the boundary conditions there not to have any significant effect on the prediction of indentation. FEM analyses were performed with both free and normally constrained lateral surfaces and the corresponding indentation results were almost identical. In hardness tests different force loads are applied during the indentation giving rise to a displacement (indentation depth) after loading and unloading. However, it is only possible to apply displacement load using element Targe170. Therefore, displacement load was applied to the indenter in the modelling, and the resultant force experienced by the specimen was calculated as the sum of the contact forces developing in contact elements multiplied by 8.

As mentioned before, after removing the indenter there will be a slight elastic recovery of the deformation. So the imposed displacement at maximum force cannot be used as the displacement corresponding to that measured during hardness tests. The depth of the indentation after unloading needs to be obtained. Then the corresponding diagonal size can be calculated.

## 2.4.2   Axi-symmetric conical indenter model

### 2.4.2.1   Assumptions

In the axi-symmetric model, the rigid indenter was represented by a cone instead of the actual square-based diamond pyramid. To achieve the same indentation effect, the corner angle $\alpha_1$ of the cone is calculated based on the assumption that the projected contact areas should be the same when the cone indenter produces the same indentation depth as the square-based diamond pyramid indenter.
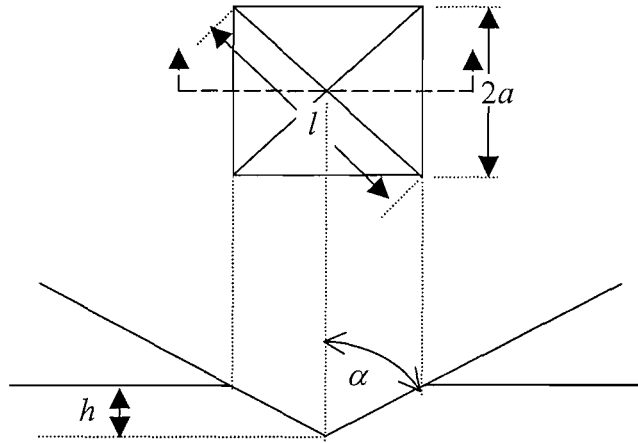
Figure 2-10     Axi-symmetric modelling schematic diagram

The geometric parameters of the square-based diamond pyramid geometry are defined in Figure 2-10. If $r$ represents the radius of the cone projected contact area, then according to the above assumption,

$$\pi r^2 = 4a^2 \tag{2.4}$$

and

$$h = r \cot \alpha_1 = a \cot \alpha \tag{2.5}$$

where $\alpha$ is the half-angle of the pyramid indenter tip. From the equations above, it is clear that $\alpha_1$ satisfies:

$$\tan \alpha_1 = \frac{2}{\sqrt{\pi}} \tan \alpha \tag{2.6}$$

In the FE modelling, the value $\alpha_1 = 70.3^o$ was used since $\alpha = 68^o$ in the actual Vickers hardness indenter. The diagonal size $l$ can be found directly from the indentation depth using

$$l = 2\sqrt{2} h \tan \alpha \tag{2.7}$$

### 2.4.2.2   Model geometry

The specimen was modelled as a cylindrical block of radius 0.4 mm and depth 0.4 mm. The choice of these dimensions is justified by the same arguments as those applied to the 3D model. Due to the fact that an axi-symmetric approach was adopted,

only half of the section by a plane through the axis of symmetry is required to be modelled; the model exists only in the positive $x$ region and the axis of rotation symmetry is the $y$-axis. A rigid line was used to represent the face of the rigid cone indenter in the axi-symmetric situation while a deformable indenter was represented as a triangle. The specimen was represented by a solid rectangle. The model geometry and dimensions are shown in Figure 2-11.
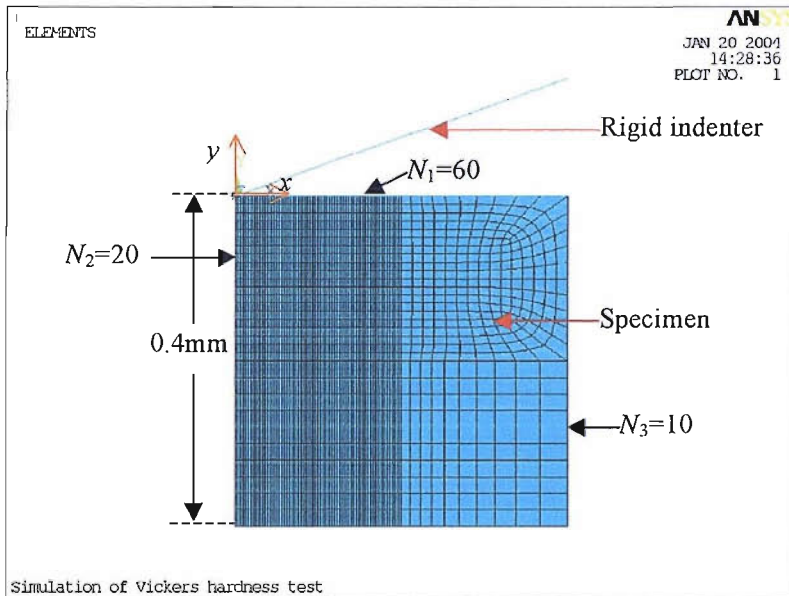


Figure 2-11     Axi-symmetric model with rigid indenter

### 2.4.2.3   Elements and mesh
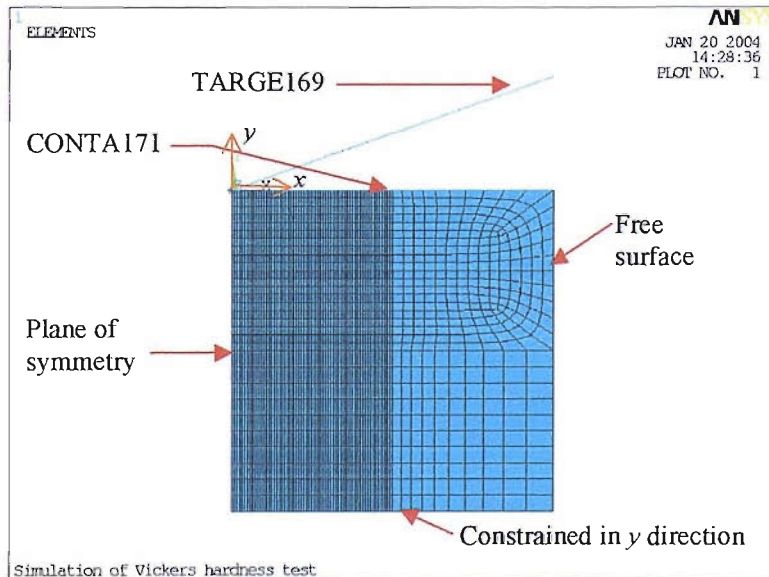


Figure 2-12     Boundary conditions of axi-symmetric model with rigid indenter

The bulk of the specimen was modelled using PLANE42, which is a four-node, two dimensional solid element. The key option 3 was set to 1 to allow this element to be used in an axi-symmetric analysis. A typical mesh of the axi-symmetric model with rigid indenter is shown in Figure 2-12. The specimen is divided into four areas and each of them is meshed with different size elements. The area underneath the indenter has a very fine mesh and the remaining areas have a relatively coarse mesh. Parameters $N_1$, $N_2$ and $N_3$, defined in Figure 2-12, represent the number of divisions along the edges of each area. The mesh could be easily controlled by changing those parameters in the ANSYS batch file. In Figure 2-12, the mesh consists of 2150 solid elements corresponding to $N_1 = 60$, $N_2 = 20$ and $N_3 = 10$. The appropriate contact element pair to be used with PLANE42 in the axi-symmetric model is TARGE169-CONTA171. The rigid indenter is represented by a single TARGE169 element. There are 70 2-node contact elements (CONTA171) along the upper edge of the specimen. The properties of this contact pair are entered in a similar way as those of the TARGE170-CONTA173 combination. It should be noted that TARGE169-CONTA171 can also be used with PLANE182, an element suitable for nearly incompressible materials. Another available contact pair is TARGE169-CONTA172, which is combined with mid-side node elements PLANE82 and PLANE183. These three alternative combinations were tried but did not prove more reliable than the original choice.
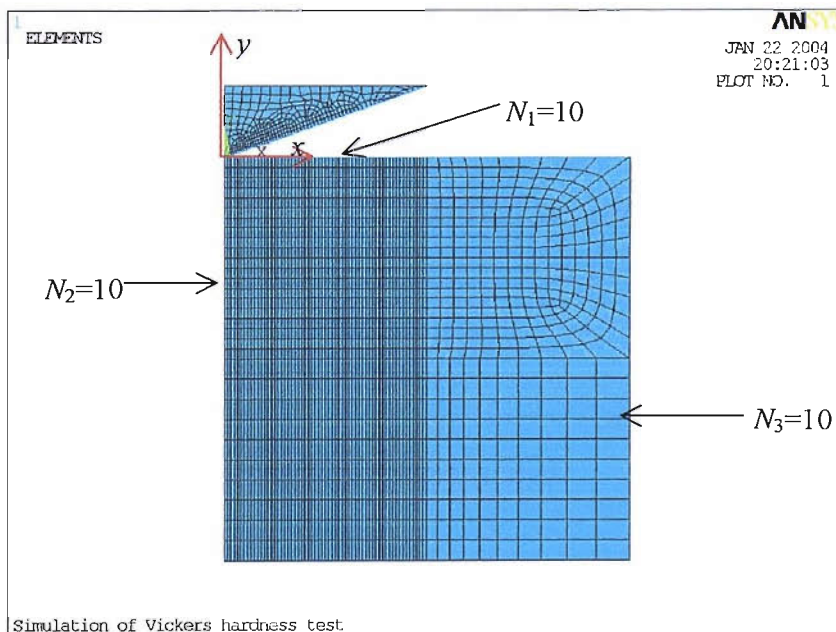


Figure 2-13     Mesh of the axi-symmetric model with deformable indenter

Figure 2-13 shows a typical mesh of the axi-symmetric model with a deformable indenter. The deformable indenter is simulated as diamond material. Its Young's modulus is taken as 1035 GPa and Poisson's ratio 0.1 to represent a very hard indenter. The specimen has the same number of solid elements and contact elements as the model with rigid indenter shown in Figure 2-11. The deformable indenter has 293 solid elements and the target surface is overlaid by 60 target elements (TARGE169).

### 2.4.2.4   Boundary and loading conditions

Since the model is axi-symmetric and the $y$-axis is the axis of symmetry, all the nodes along the $y$-axis have to be constrained in the $x$-direction. The bottom of the model was constrained in the $y$-direction so that it would simulate the support in the $y$-direction in the experiment. Assuming that the lateral surface of the specimen is either free or radially constrained did not make any difference to the indentation results. As discussed in the previous section, displacement load was applied to the indenter in the modelling, and the resultant force experienced by the specimen was calculated as the sum of the contact forces developing in contact elements. The axi-symmetric ANSYS analysis computes these forces, so that the contact force obtained corresponds to the load experienced by the whole indenter in a hardness test.

As mentioned before, after removing the indenter, there will be a slight elastic recovery of the deformation, which is deducted from the total deformation. Thus only the depth of the permanent (plastic) indentation is used for calculating the diagonal size that corresponds to maximum load.

### 2.4.3   Comparison of the various modelling schemes

### 2.4.3.1   Force and displacement

Referring to the orientation of the FE models in Figure 2-8, Figure 2-11, and Figure 2-13, the $y$-component of the contact element force was identified before the indenter was removed from the specimen. Then the sum of such forces over all contact elements was calculated as the total force applied by the indenter (multiplied by 8 in

the case of the 3D model). The indenter was removed to allow for the elastic recovery. The deepest position of the node underneath the indenter tip after recovery was measured as the depth of the indentation. Then the corresponding diagonal size was calculated from (2.7). The load-diagonal size curve is thus obtained as the FEM result.

### 2.4.3.2   Numerical error at indenter tip

It was noted that the load-indentation results from both the 3D and the axi-symmetric models did not generate smooth curves when plotted. This suggests that some numerical error might exist when the residual indentation depth is measured from the specimen profile after unloading. If there is no numerical error when a displacement load is applied on the indenter, the following relationship must be satisfied

$$h_{tip} = h_{maxf} \qquad\qquad (2.8)$$

where $h_{tip}$ is the displacement of the indenter tip and $h_{maxf}$ is the displacement of the specimen node underneath the indenter tip at maximum displacement load. In the modelling, $h_{maxf}$ is taken as the indentation depth before elastic recovery. The residual indentation depth $h_{maxr}$ is obtained by measuring the displacement of the same node after removing the indenter.
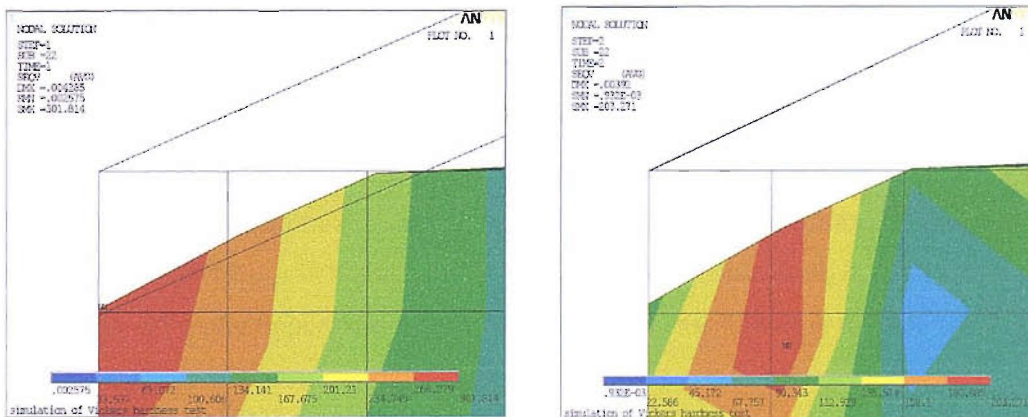


a) At full load (*P*=22.92g)                    b) After unloading

Figure 2-14     Residual von Mises stress from the 3D model

53

a) At full load (*P*=25.44g)          b) After unloading
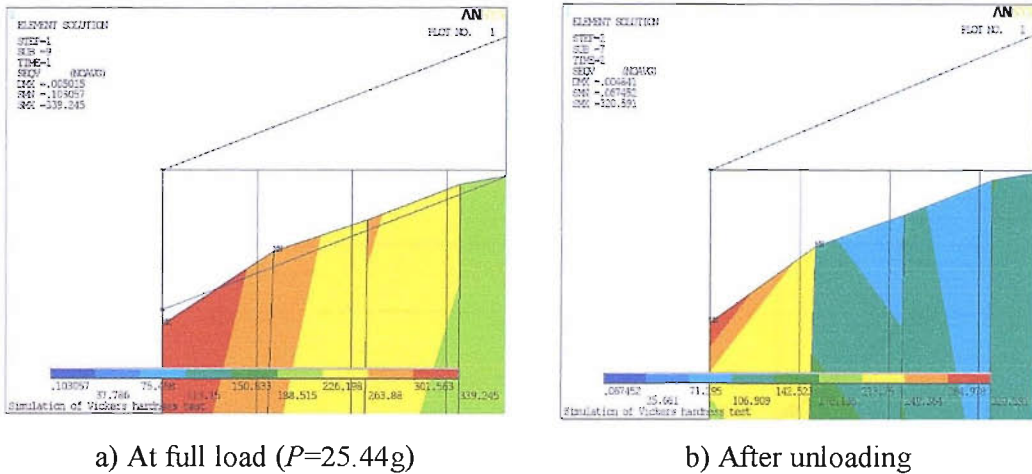
Figure 2-15      Residual von Mises stress from the axi-symmetric model

Enlarged plots of the predicted profile geometry of both the indenter and specimen at maximum indentation load and at full elastic recovery are shown in Figure 2-14 and Figure 2-15 for the 3D and axi-symmetric indentation models, respectively. It can be clearly seen in these figures that $h_{tip}$ is different from $h_{maxf}$ due to the local distortion of the solid elements in contact and the inherent error tolerance in contact analyses. This distortion persists after elastic recovery.

In an attempt to solve this problem, it is assumed that the distortion of the contact profile at maximum indentation remains the same as that at full load after removing the indenter. Thus, a numerical error

$$h_{error} = h_{maxf} - h_{tip} \tag{2.9}$$

is introduced, which is used to correct the residual indentation depth according to:

$$h_{maxrc} = h_{maxr} - h_{error} = h_{maxr} - (h_{maxf} - h_{tip}) \tag{2.10}$$

With this correction, smooth load-diagonal size curves were consistently obtained. It may be noted that $h_{error}$ is negative, that is, $h_{maxr}$ is underestimated, in the case of the 3D model, while the opposite is true in the case of the axisymmetric model.

### 2.4.3.3   3D versus axi-symmetric modelling

Since the control material VQ1B gives the closest $\sigma$-$\varepsilon$ curve to that of AS1241 alloy of interest, both the 3D model and the axi-symmetric model were applied to VQ1B

using the known true stress-logarithmic strain curve described in Section 2.3.1. Both FEM results obtained using meshes described in Figure 2-9 and Figure 2-12 as well as the respective experimental results are shown in Figure 2-16.
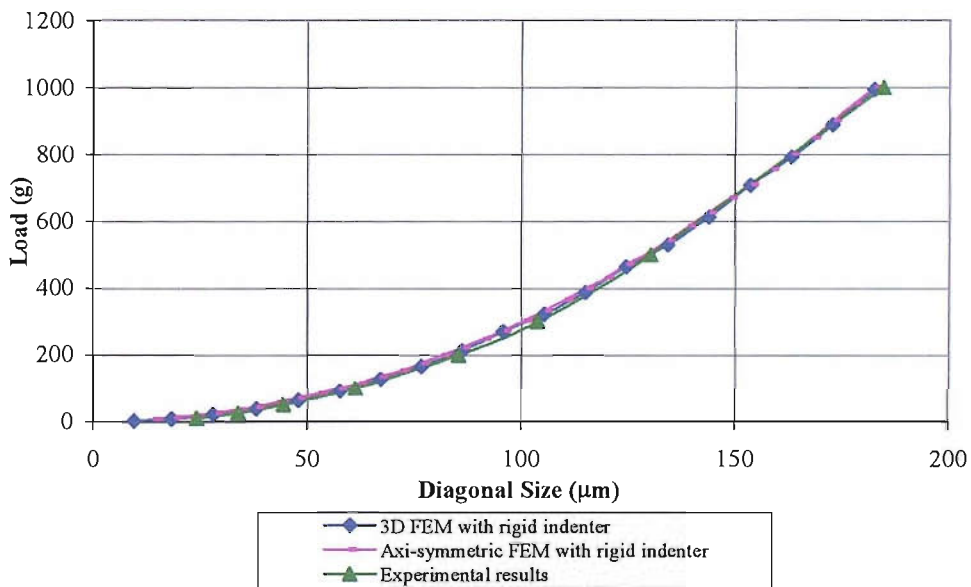


Figure 2-16    3D versus axi-symmetric results with rigid indenter for VQ1B

From Figure 2-16 it can be seen that both 3D model and axi-symmetric model are in good agreement with the experimental result. However, a much larger number of solid and contact elements would have been required in the 3D model to achieve the same degree of refinement as that of the axi-symmetric model. To obtain approximately 20 points of the *P-l* curve from the 3D FE model in Figure 2-16 using an Intel P4 computing node, it takes approximately 70 hours, while to obtain the corresponding results from the axi-symmetric FE model takes around 6 hours. Thus considering the obvious advantage of the axi-symmetric model in significantly reducing the computational time, it is preferable to use this rather than the 3D model.

### 2.4.3.4   Rigid versus deformable indenter

The FE indentation analysis was again applied with the material properties of VQ1B and the results for both rigid and deformable indenters from the axi-symmetric model are given in Figure 2-17, which shows that the two models gave almost the same

results. Since the rigid indenter model is simpler than the deformable indenter model and requires less computational time, the former model is applied in further FE work.
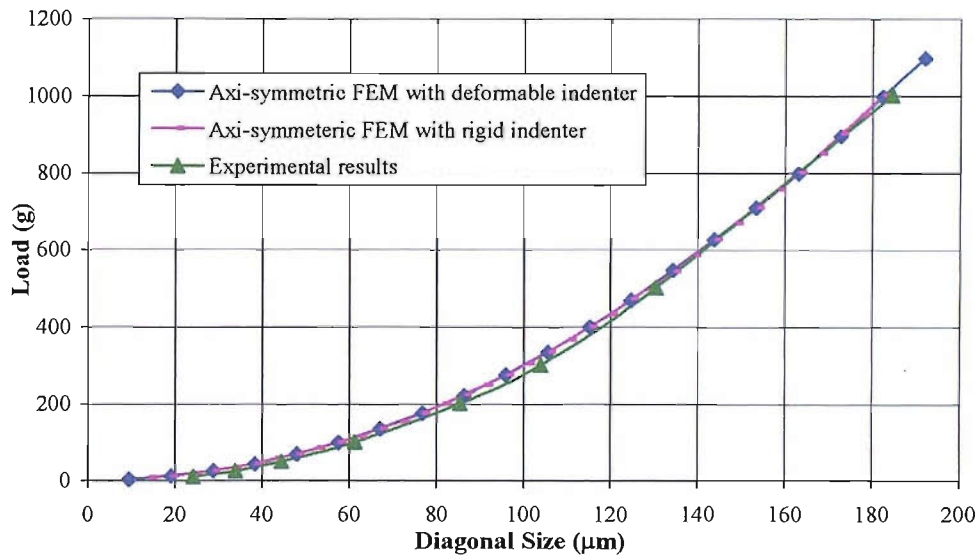


Figure 2-17    Rigid versus deformable indenter results from the axi-symmetric model for VQ1B

## 2.4.4    Assessment of the axi-symmetric model

## 2.4.4.1    Effect of normal contact stiffness

As mentioned previously, the normal contact stiffness, represented by the factor FKN in ANSYS, is one of the real constants that needs to be selected carefully to ensure that the analysis converges and the contact process is simulated accurately. The recommended range of this value is 0.01-10, with a default of 1.0. A smaller value of FKN facilitates convergence but generates additional artificial penetration. It is suggested that the default value be used if the model is subjected to deformation involving volume change. This can be updated automatically by the program depending on the material property. When plasticity is defined in the underlying elements, the contact normal stiffness can be reduced by a factor of 100.

In order to ensure that the effect of FKN on the indentation results is indeed negligible and, possibly, identify an optimum value, the axi-symmetric FEM analysis was performed with FKN equal to 0.5, 0.8, 1, 2 and 3. The default values of all other real

56

constants were used. Figure 2-18 shows the axi-symmetric FEM results as well as the experimental indentation result for control material VQ1B.
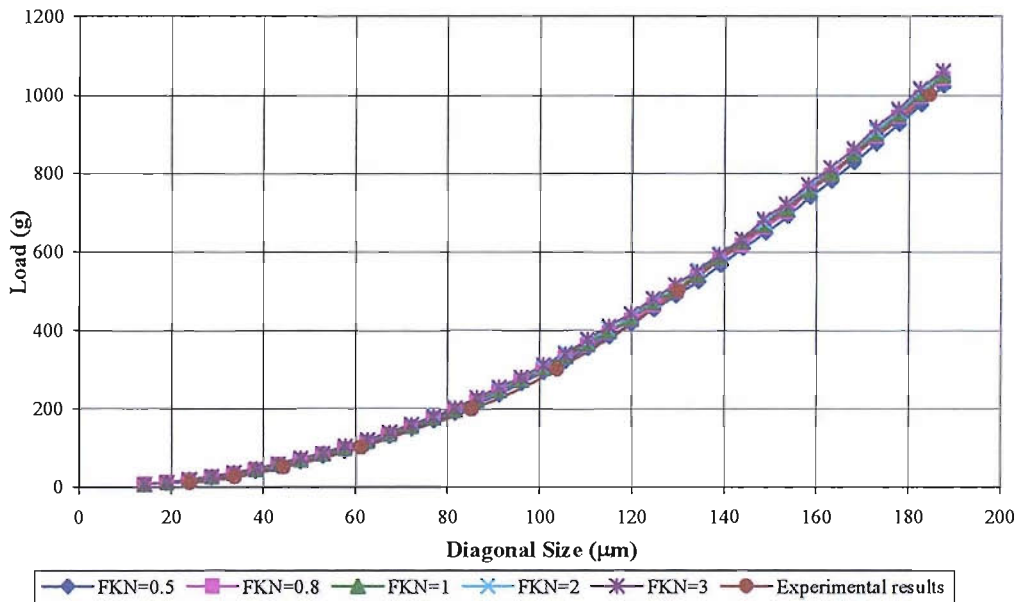


Figure 2-18    FEM results with different FKN for VQ1B

In all cases, the results were similar to the experimental ones with negligible differences. As expected, the model with a high FKN value appears slightly harder than that with a low value. It was thus decided to use the default FKN value of 1 in the subsequent analyses.

### 2.4.4.2   Effect of tolerance factor

Another important real constant in contact analyses is FTOLN, which is used to define a tolerance factor to be applied in the direction of the surface normal. This factor should be less than 1.0 (usually set less than 0.2), with a default of 0.1, and is based on the thickness of the element. If this factor is too large, too much artificial penetration may occur, and if it is too small, it is difficult for the contact problem to converge. Values of 0.2, 0.15, 0.1, 0.08, 0.05 and 0.01 were tried in the axi-symmetric FEM analysis while all other real constants remained at their default values. The

respective axi-symmetric FEM results and the experimental indentation results for VQ1B are shown in Figure 2-19.
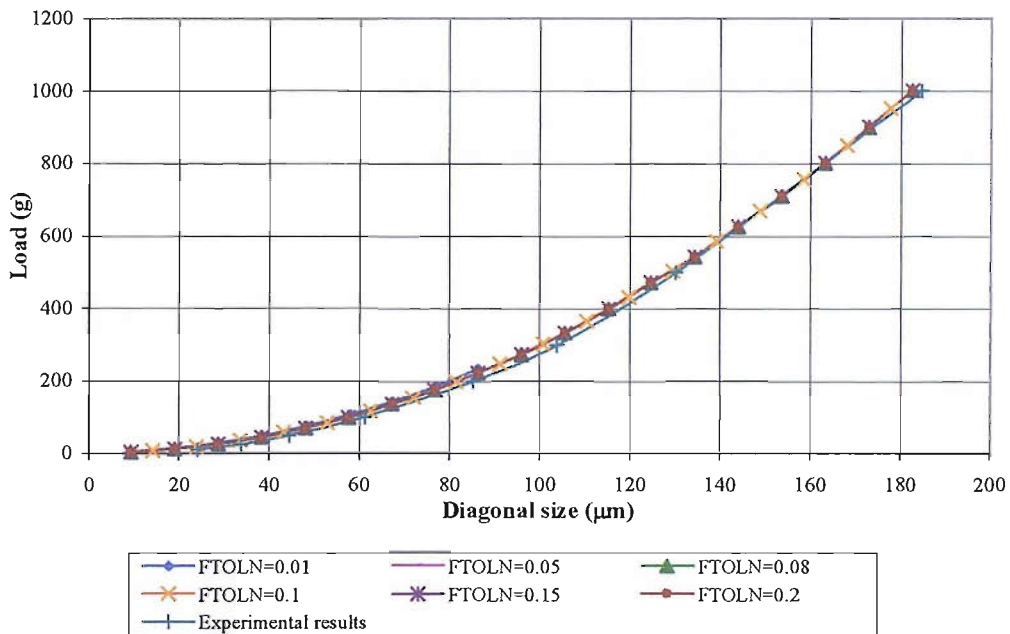


Figure 2-19    FEM results with different FTOLN (curves FTOLN=0.05, 0.08, 0.1, 0.15, 0.2 overlap each other)

It can be seen that varying the value of FTOLN between 0.01 and 0.2 has almost no effect on the FEM results. However, when FTOLN equals 0.01, the analysis experienced serious converging problems and stopped at a load of around 250 g. As a consequence, the default value of FTOLN was chosen for further analysis.

### 2.4.4.3   Model size

For building an efficient FE program, the chosen model size was much smaller than that of the specimens. The tested specimens for VQ1B, RTWQ, B1Q2, and B1Q3 were semi-cylindrical with a base radius of 5 mm and a depth of 10 mm. That for monolithic AS1241 was a rectangular block with dimensions 1 mm × 15 mm × 10 mm, with the hardness tests performed on the narrow 1 mm × 15 mm area. Artificial boundary conditions were applied to the boundaries of the model and this might have

affected the accuracy of the output. In order to assess the sensitivity of the results to model size variations, the initial dimensions of the model were changed uniformly by about ±20% while keeping the element sizes more or less constant. It should be noted here that, in the indentation tests on VQ1B (one of the softest alloys of the control materials), the diagonal size at maximum load (1000 g) was approximately 185 μm. The corresponding maximum radius of the projected contact area for an equivalent conical indenter in FEM is, according to equations (2.5) and (2.7), approximately 74 μm, that is, approximately a quarter of the minimum model size adopted. Thus the minimum model size is still big enough for a reasonably accurate FE analysis. The details of the three models are listed in Table 2–5. The corresponding results for VQ1B are shown in Figure 2-20. No significant variation in the result is observed, thus the original choice of the model size was accepted as rational.

**Table 2–5 FEM matrix for VQ1B to investigate model size effect**

| VQ1B | Model size (μm) | $N_1$ | $N_2$ | $N_3$ | Element size (μm) | Number of elements |
|---|---|---|---|---|---|---|
| FEM 1 | 400 | 60 | 20 | 10 | 3.33 | 2220 |
| FEM 2 | 500 | 75 | 25 | 12 | 3.33 | 3220 |
| FEM 3 | 600 | 90 | 30 | 15 | 3.33 | 4696 |
| FEM 4 | 800 | 120 | 60 | 30 | 3.33 | 8740 |
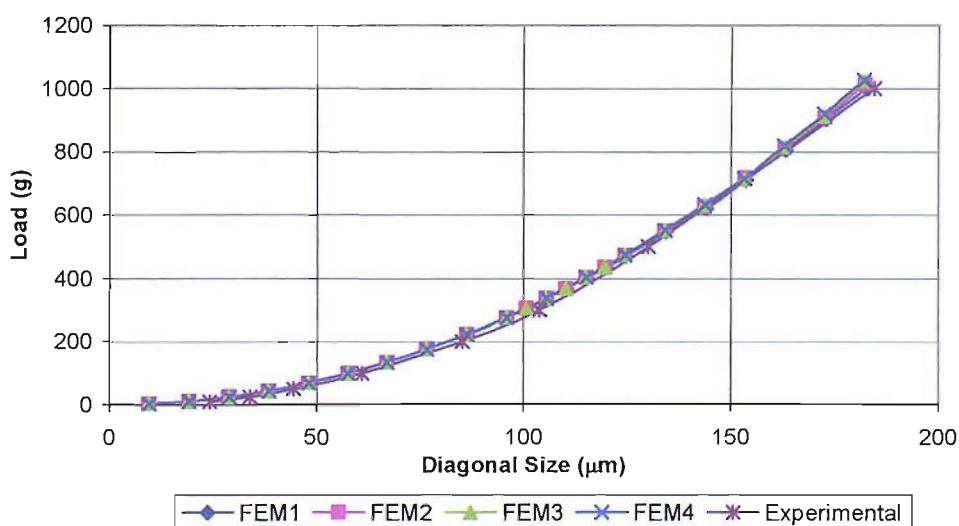


Figure 2-20    FEM results with different model sizes (material VQ1B)

## 2.4.4.4   Element size

The element size plays an important role in FEM. A coarse mesh with large element size requires less computing time but may give poor results. A fine mesh increases the accuracy of FEM results at the expense of computational efficiency. When the element size is too small, the numerical error due to increased size of the problem also compromises accuracy.

Table 2–6 presents a matrix of subdivisions for the same model size to investigate the effect of element size and distribution on the performance of the axi-symmetric model. The change of element size is achieved by means of refining the mesh. The FEM results for control material VQ1B are shown in Figure 2-21. It is noted that reducing the element size or increasing further the number of elements does not bring the FEM results closer to the experimental *P-l* curve. Therefore the mesh shown in Figure 2-11 is adopted in all subsequent analyses.

**Table 2–6 FEM matrix to investigate elements size effect**

| Model | Model size ($\mu$m) | $N_1$ | $N_2$ | $N_3$ | Element size ($\mu$m) | Number of elements |
|---|---|---|---|---|---|---|
| FEM 1 | 400 | 60 | 20 | 10 | 3.33 | 2220 |
| FEM 2 | 400 | 75 | 25 | 12 | 2.67 | 3222 |
| FEM 3 | 400 | 90 | 30 | 15 | 2.22 | 4696 |
| FEM 4 | 400 | 120 | 40 | 20 | 1.67 | 8742 |
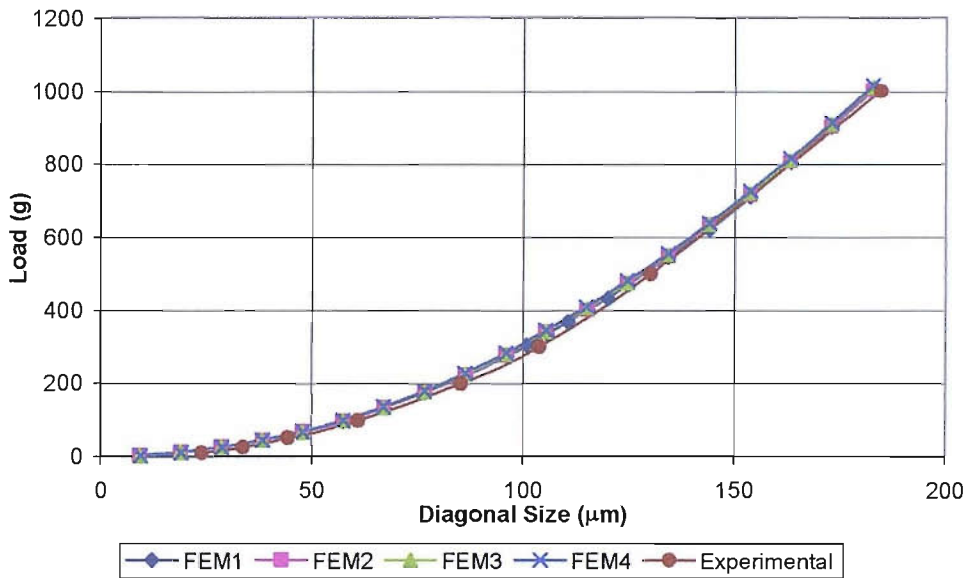
Figure 2-21    FEM results with different element sizes (material VQ1B)


## 2.4.5    Further comparisons with experimental results


Following all the investigations described in the previous section, the axi-symmetric modelling with a rigid indenter seems to give very good predictions of residual indentation sizes when applied to material VQ1B. In order to confirm its accuracy, the same indentation modelling was applied to the other four control materials, namely monolithic AS1241, RTWQ, B1Q2, and B1Q3. The corresponding results are shown in Figure 2-22, Figure 2-23, Figure 2-24 and Figure 2-25 respectively. The values of FKN, FTOLN, as well as the model size and element size were the same as those established as reliable when applied to VQ1B (refer to Figure 2-11 for the adopted mesh).
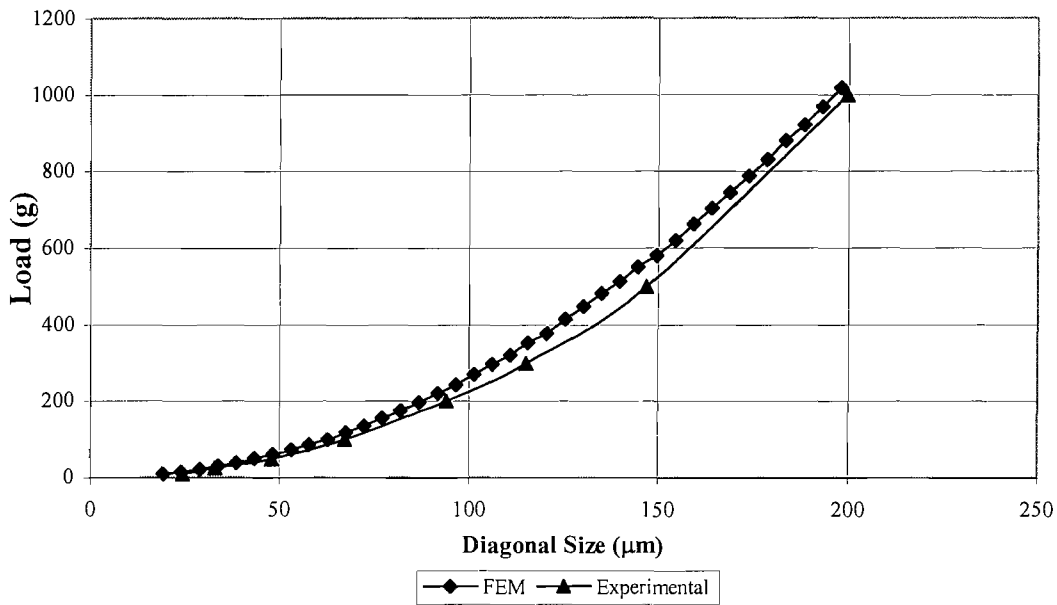
Figure 2-22    Axi-symmetric modelling results versus experimental results for monolithic AS1241

It is seen in Figure 2-22 that the axi-symmetric modelling results are reasonably close to the experimental indentation results for monolithic AS1241. The agreement at low loads and high loads is better than for the middle load range. It is worth noting that the material input to the FEM analysis was provided by the project sponsors, it was therefore obtained from a different batch of lining material than that used for the Southampton hardness tests. This might explain the small discrepancy between numerical and experimental results.
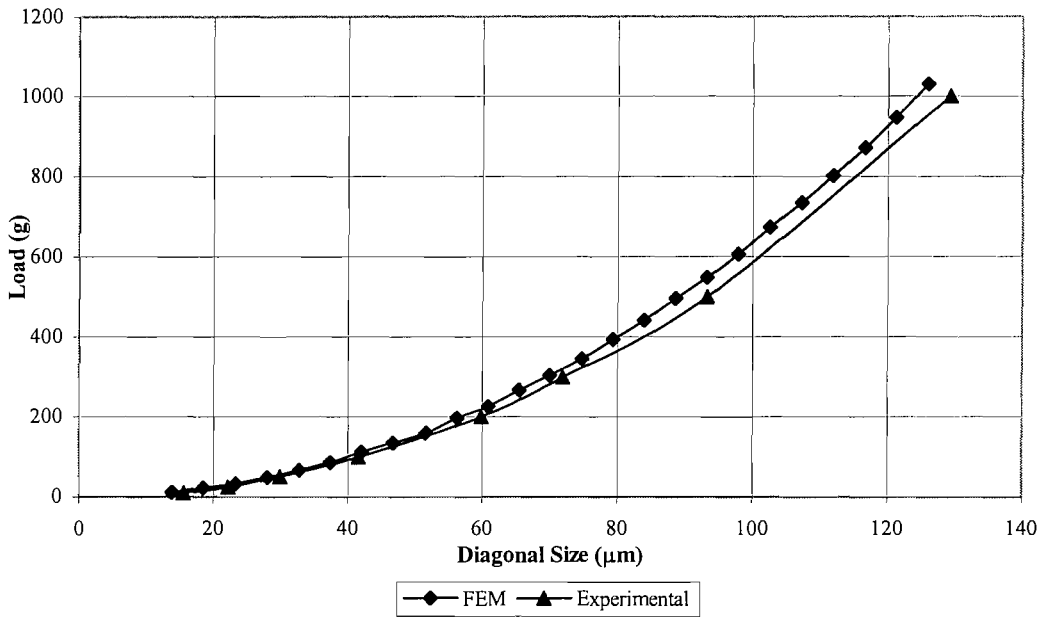
Figure 2-23    Axi-symmetric modelling results versus experimental results for RTWQ
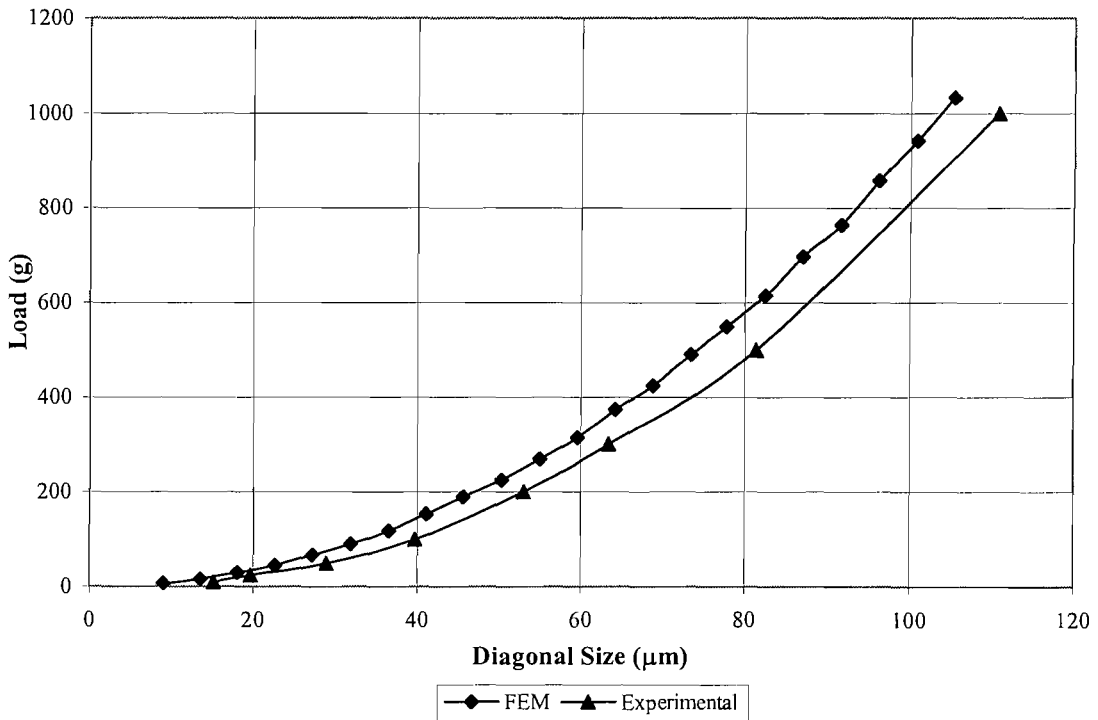


Figure 2-24    Axi-symmetric modelling results versus experimental results for B1Q2
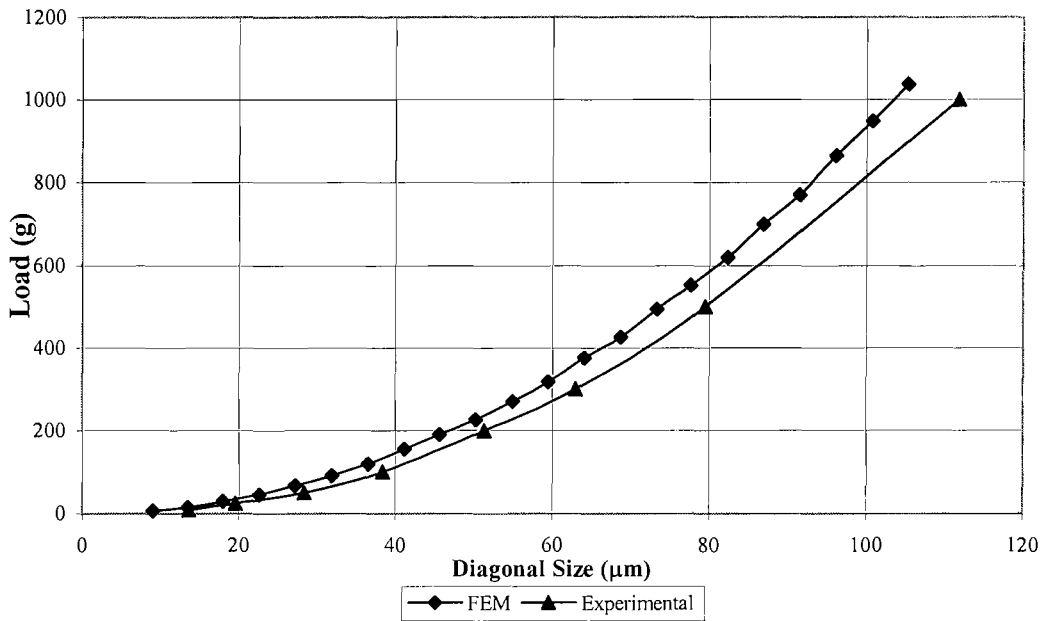
Figure 2-25    Axi-symmetric modelling results versus experimental results for B1Q3

The FEM results for RTWQ, B1Q2, and B1Q3 are not as close to the respective experimental results as those for VQ1B and monolithic AS1241. It was initially thought that this discrepancy might be due to the higher hardness of these materials compared to that of monolithic AS1241 and VQ1B (see Figure 2-7). In order to investigate this possibility, the FEM analysis was applied to these alloys with the same variations of model and element size (see Figure 2-26 and Figure 2-27) as well as values for FKN and FTOLN as those considered for VQ1B. However, the indentation predictions were proved to be insensitive to such variations for all three materials. The axi-symmetric model was thus accepted as robust and the difference between FEM predictions and experimental results was attributed to potential inconsistency between material FEM input and hardness measurements.
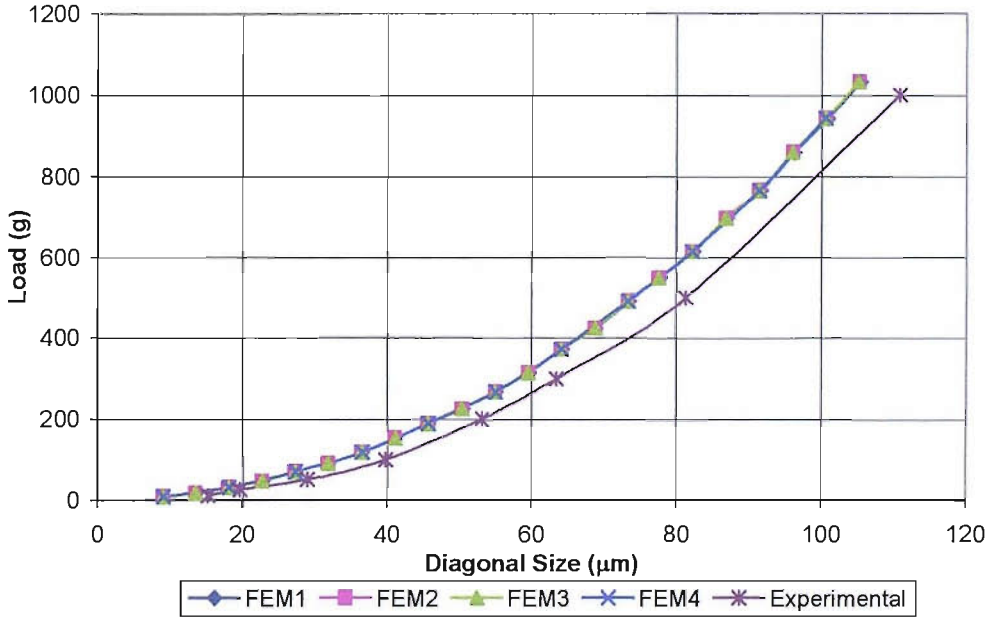
Figure 2-26    FEM results with different model sizes (material B1Q2)
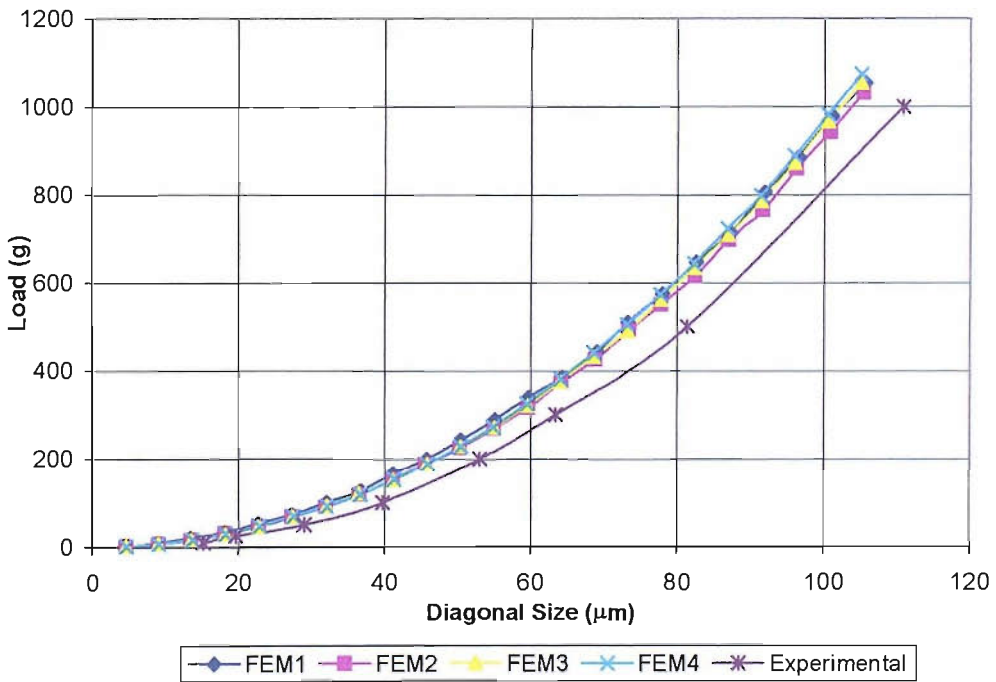


Figure 2-27    FEM results with different element sizes (material B1Q2)

This project will focus on soft materials such as the linings of AS1241 and AS16 bearings and flat strips and HVOF Al-Sn systems, which are similar in hardness to VQ1B and monolithic AS1241. Since the axi-symmetric model was shown to exhibit good prediction ability with materials properties lying in the range of interest, it should be sufficient for the subsequent modelling of similarly soft lining materials, which are considered in the material characterisation process.

## 2.5   Adaptive numerical modelling

It is evident from the FE results presented in the previous section that there is an implicit relation between the elasto-plastic material input and the load-indentation size ($P$-$l$) output. Thus, if the FE analysis with an assumed $\sigma$-$\varepsilon$ curve for a material of interest could produce the same $P$-$l$ curve as that obtained from experiments, the assumed elasto-plastic properties could be considered as an accurate characterisation of this material. It is however impossible to guess correctly the material input that would result in satisfactory agreement between FE and experimental $P$-$l$ curves and thus deduce directly the elasto-plastic properties of an alloy. The only way to achieve a solution of the inverse problem is by iterations, that is, by varying the material parameters, represented by a vector **x**, until the best analytical-experimental $P$-$l$ fit is produced.

However, the FE analysis of indentation is time consuming. It is evident that, for the iterative characterisation process to work, there is a need for a much faster analytical tool for the prediction of the $P$-$l$ curve for any material input. This can be achieved via adaptive numerical modelling (ANM). In this regression problem, the SUPANOVA technique is used to give maximum transparency without sacrificing predictive accuracy. The general features of SUPANOVA are presented in Chapter 1, Section 1.5.

## 2.5.1 Artificial stress-strain curves set

An essential requirement of ANM techniques is well-distributed and plentiful data – allowing the "best fit" to the data to be obtained unambiguously. Unfortunately, with experimental work, obtaining sufficient well-distributed data may be a lengthy and expensive process, and this was the case in the current work. Limited confidence in the available experimental $\sigma$-$\varepsilon$ data was another adverse factor. Consequently, the use of FE for the supply of data not only greatly enlarged the available data set but also meant that gaps in the input data space, not covered by the experimental data could be filled by suitable choices of the properties of the simulated materials. A large database of *P-l* curves was thus generated by running the FE model for a wide range of elasto-plastic properties and the applicability of the ensuing models was increased.

## 2.5.1.1 Material parameters definition and range

For validation purposes in the last section, the initial FE models were using digitised experimental true stress-logarithmic strain curves, extended to higher strains using the exponential strain hardening model. For developing the SUPANOVA models however, the elasto-plastic behaviour needs to be described in terms of a finite number of property values, which can yield smooth artificial stress-strain curves representing as closely as possible the true stress-logarithmic strain curves. Variation of these properties can then generate, through FE analysis, a large database of load-indentation curves.
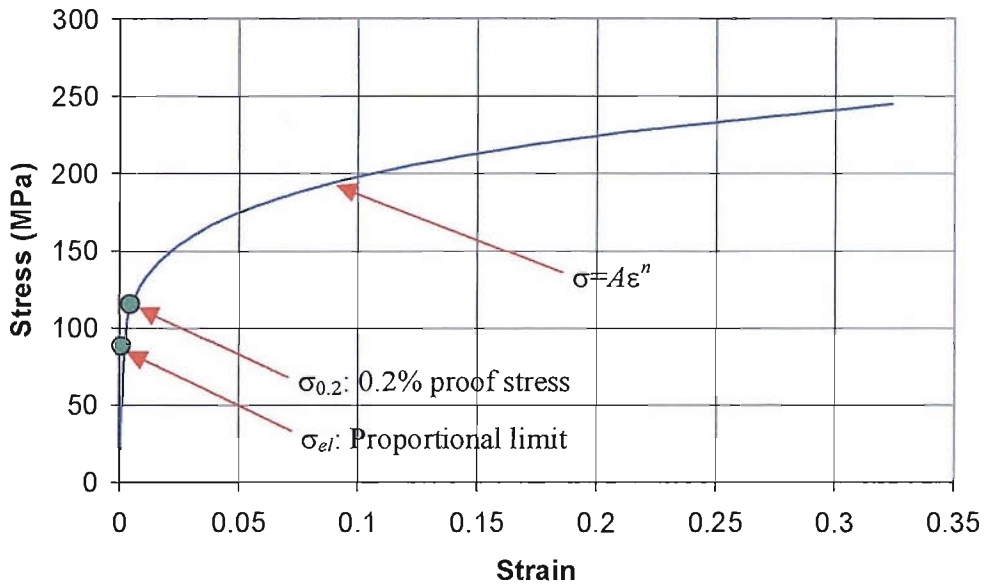
Figure 2-28    A typical artificial stress-strain curve

Figure 2-28 shows a typical artificial stress-strain curve generated from a limited number of parameters ($E$, $\sigma_{el}$, $\sigma_{0.2}$, $A$, and $n$) as defined in Section 2.3.1. Each artificial curve comprises three parts: a straight line with gradient $E$ describing the elastic part up to proportional limit $\sigma_{el}$, the post yield strain hardening model describing behaviour beyond the point of 0.2% proof stress $\sigma_{0.2}$, and a suitably chosen smooth line joining the two parts.

The points ($\sigma_{el}$, $\varepsilon_{el}$), ($\sigma_{0.2}$, $\varepsilon_{0.2}$) can be joined by a cubic curve that provides continuity of gradient at the two ends, that is, with gradients equal to $E$ and $An\varepsilon^{n-1}$ at $\varepsilon_{el}$ and $\varepsilon_{0.2}$, respectively. When this choice was applied to some of the real stress-strain curves shown in Figure 2-5, it produced non-monotonically increasing gradient and had therefore to be abandoned. An alternative choice was the cubic-spline with known curvatures at the two ends, in the present case 0 at ($\sigma_{el}$, $\varepsilon_{el}$) and

$$\sigma_{0.2}'' = An(n-1)\varepsilon_{0.2}^{n-2} \tag{2.11}$$

at ($\sigma_{0.2}, \varepsilon_{0.2}$). The resulting equation for the interpolation function is

$$\sigma = f_1\sigma_{el} + f_2\sigma_{0.2} + f_3\sigma_{0.2}'' \tag{2.12}$$

where

68

$$f_1 = \frac{\varepsilon_{0.2} - \varepsilon}{\varepsilon_{0.2} - \varepsilon_{el}}$$

$$f_2 = \frac{\varepsilon - \varepsilon_{el}}{\varepsilon_{0.2} - \varepsilon_{el}}$$

$$f_3 = \frac{1}{6}(f_2^3 - f_2)(\varepsilon_{0.2} - \varepsilon_{el})^2$$

The third term on the right-hand side of (2.14) was found to have a small influence and as a consequence the curve represented by (2.14) appears as almost a straight line. The most generally applicable solution was to adopt a parabolic curve for joining points ($\sigma_{el}$, $\varepsilon_{el}$) and ($\sigma_{0.2}$, $\varepsilon_{0.2}$) with gradient continuity only at ($\sigma_{0.2}$, $\varepsilon_{0.2}$).

Table 2–2 shows considerable variation in the experimental Young's modulus, *E*, for the control materials which can be partly attributed to experimental error. FE indentation analyses indicated however that this variation has negligible effect on the predicted *P-l* curves; thus, it is not expected to affect significantly also the experimental indentation data for aluminium alloys. An example is shown in Figure 2-29, which gives the FEM results for an adjusted experimental stress strain curve of VQ1B with a Young's modulus of 70 GPa and the original one with 53.12 GPa.
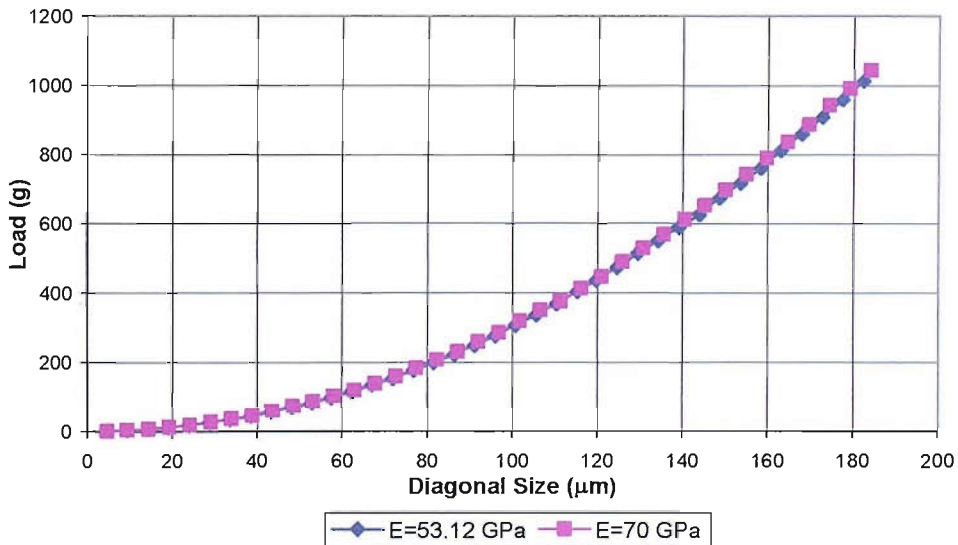


Figure 2-29    FEM results of VQ1B with different Young's modulus

For this reason, the Young's modulus was taken equal to an average value of 70 GPa in all artificial stress-strain curves. Then such a curve can be represented by a parameter set consisting of $\sigma_{el}$, $\sigma_{0.2}$, $A$, and $n$. However, independently varying all four input parameters is not appropriate since the continuity of the stress-strain curves means that they are correlated. In order to obtain a continuous and piece-wise smooth artificial curve, certain relations have to be satisfied by the material parameter values leading to rational choices for their ranges.

Ideally, the curve represented by the strain hardening model, (2.3), should pass through the point $(\sigma_{0.2}, \varepsilon_{0.2})$ where

$$\varepsilon_{0.2} = 0.002 + \frac{\sigma_{0.2}}{E} \qquad (2.13)$$

This continuity condition gives the relation

$$\sigma_{0.2} = A \left( 0.002 + \frac{\sigma_{0.2}}{E} \right)^{n} \qquad (2.14)$$

therefore $A$ can be determined from $\sigma_{0.2}$ and $n$. A set of artificial stress-strain curves can thus be generated by assigning random values to $\sigma_{el}$, $\sigma_{0.2}$ and $n$. The ANM model is built with the material property vector $\mathbf{x}$ consisting of these three parameters.

In order to specify constraints on the material property vector $\mathbf{x}$, it is useful to consider realistic values of the gradient of the exponential curve represented by (2.3) at $\varepsilon_{0.2}$ given by

$$E_2 = \frac{d\sigma}{d\varepsilon} (\varepsilon = \varepsilon_{0.2}) = An\varepsilon^{n-1} \qquad (2.15)$$

as well as the gradient of the straight line joining $(\sigma_{el}, \varepsilon_{el})$ and $(\sigma_{0.2}, \varepsilon_{0.2})$

$$E_1 = \frac{\sigma_{0.2} - \sigma_{el}}{\varepsilon_{0.2} - \varepsilon_{el}} \qquad (2.16)$$

where

$$\varepsilon_{el} = \frac{\sigma_{el}}{E} \qquad (2.17)$$

Referring to Table 2–2, it may be noted that the material parameters for the control materials are within the following ranges:

$$40 < \sigma_{el} < 360 \ (\text{MPa}) \qquad (2.18)$$

$$70 < \sigma_{0.2} < 470 \ (\text{MPa}) \tag{2.19}$$

$$0.05 < n < 0.3 \tag{2.20}$$

The corresponding range for the strain hardening coefficient is, approximately,

$$350 < A < 730 \ (\text{MPa}) \tag{2.21}$$

The experimental data were also found to satisfy the conditions

$$0 < E_2 \,/\, E_1 < 0.55 \tag{2.22}$$

$$0.15 < E_1 \,/\, E < 0.45 \tag{2.23}$$

The randomly chosen artificial data are required to lie within the above ranges as well as to satisfy the following constraints:

$$E_2 < E_1 < E \tag{2.24}$$

$$\sigma_{el} < \sigma_{0.2} \tag{2.25}$$

A MATLAB program was written to generate rational random values that satisfy all the conditions listed above. In MATLAB, function *rand*() produces a random value $\lambda$ from a uniform distribution in the interval $(0,1)$. Then material parameter $x_i$ ($x_1 = \sigma_{el}$, $x_2 = \sigma_{0.2}$, $x_3 = n$) is calculated from the following equation:

$$x_i = \lambda \ (x_{imax} - x_{imin}) + x_{imin} \tag{2.26}$$

where $x_{imax}$ and $x_{imin}$ are the extreme values adopted for that parameter given by (2.18)-(2.20). Each material combination of values thus generated is stored if it satisfies all the constraints mentioned above, otherwise it is discarded and the subroutine generates new values for testing. Digitised versions of the generated smooth stress-strain curves, each consisting of around 80 points for all three parts, are used as inputs to the FE indentation analysis.

Based on the values listed in Table 2–2, new parameters were determined for each stress strain curve of control materials. The idealised stress-strain curves of control materials could then be represented by the parameters shown in Table 2–7.

**Table 2–7 Parameters representing the idealised stress-strain curves of control materials**

| Control material | $E$ (GPa) | $\sigma_{el}$ (MPa) | $\sigma_{0.2}$ (MPa) | $A$ (MPa) | $n$ |
|---|---|---|---|---|---|
| AS1241 | 70 | 45.42 | 61.95 | 356.64 | 0.2993 |
| VQ1B | 70 | 43.98 | 84.25 | 338.20 | 0.242 |
| RTWQ | 70 | 241.85 | 312.33 | 417.37 | 0.0575 |
| B1Q2 | 70 | 354.49 | 458.91 | 715.56 | 0.0933 |
| B1Q3 | 70 | 359.25 | 462.4 | 720.50 | 0.0933 |

A comparistion of the idealised and original $\sigma$-$\varepsilon$ curves is given in Figure 2-30.
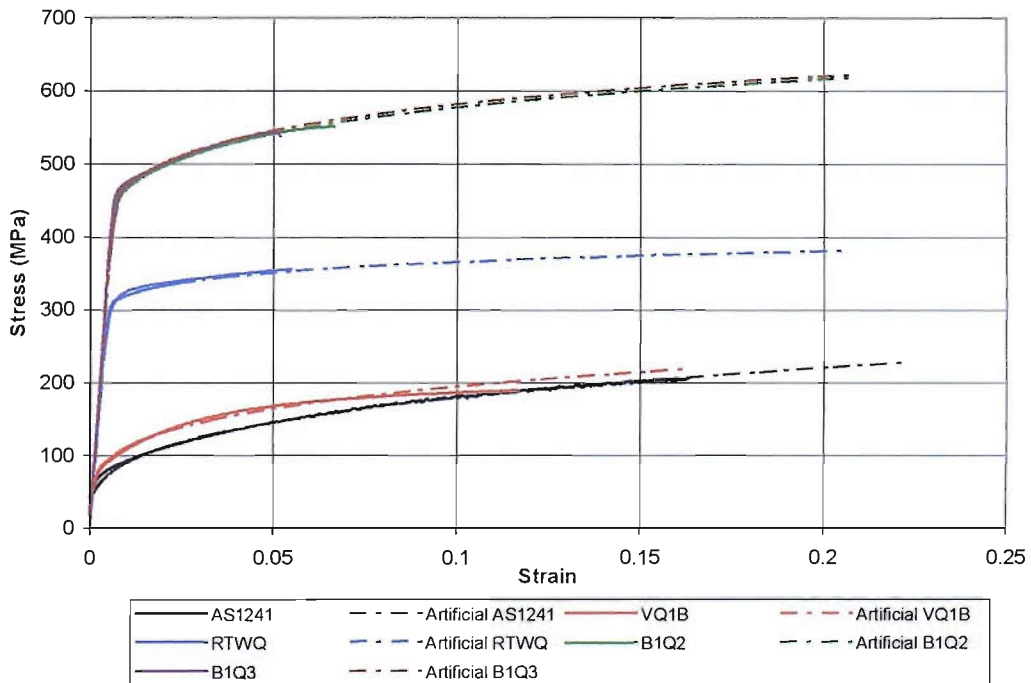


Figure 2-30    Original and idealised $\sigma$-$\varepsilon$ curves of control materials

The corresponding FEM indentation results are shown in Figure 2-31. It can be seen that for each control material, the FEM results of both curves are almost identical. This indicates that the idealised true stress – logarithmic strain curve can be treated as a reasonable substitute of the original $\sigma$-$\varepsilon$ curve.
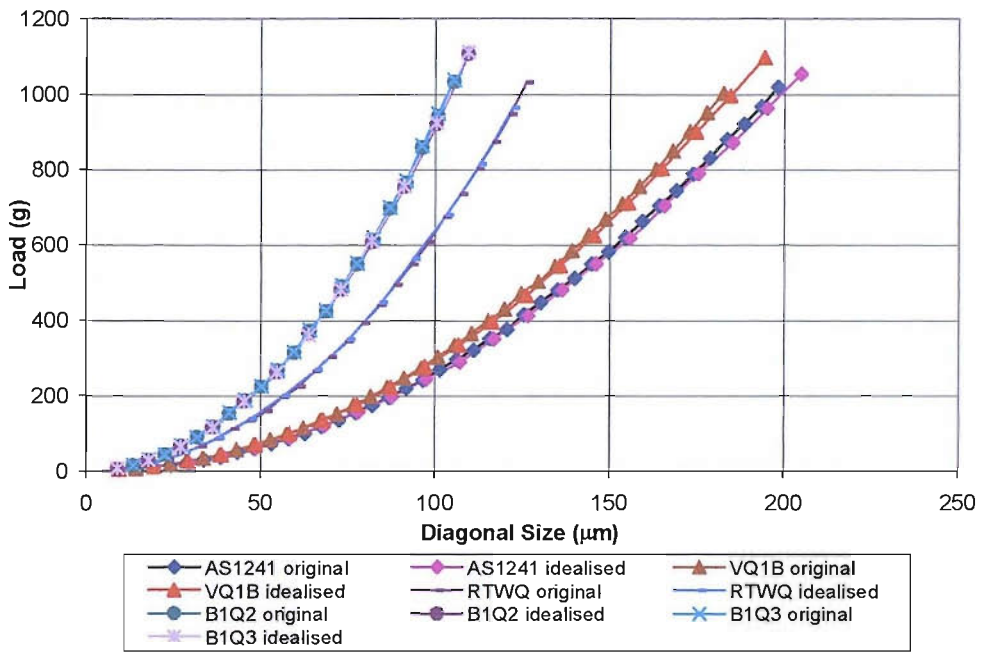
Figure 2-31    FEM results of original and idealised σ-ε curves for control materials

A total of 150 material property vectors **x** satisfying the above constraints were randomly generated. Figure 2-32, Figure 2-33 and Figure 2-34 show the distribution of these variables.
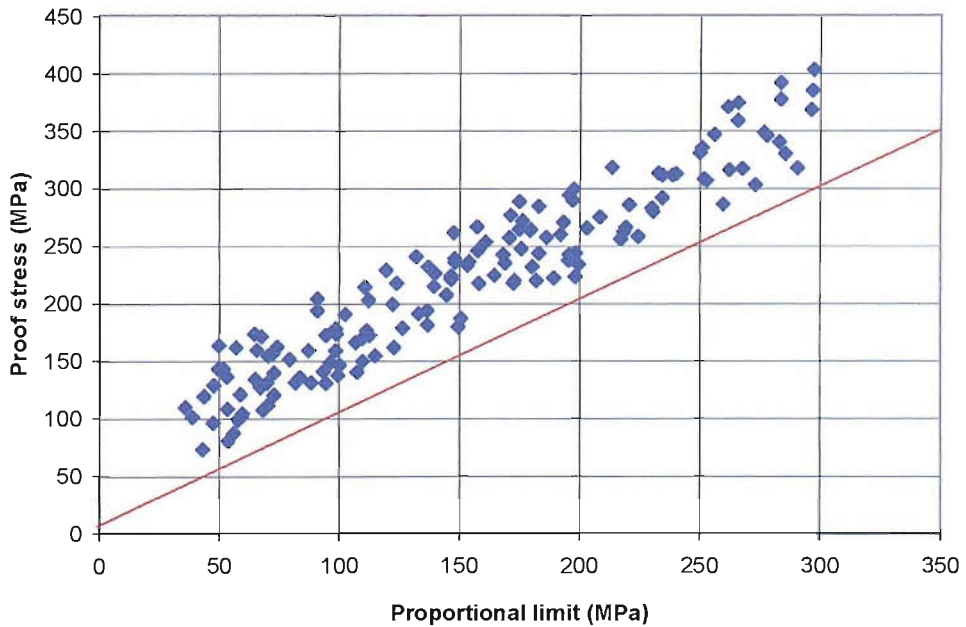


Figure 2-32    Input space of $\sigma_{el}$ and $\sigma_{0.2}$
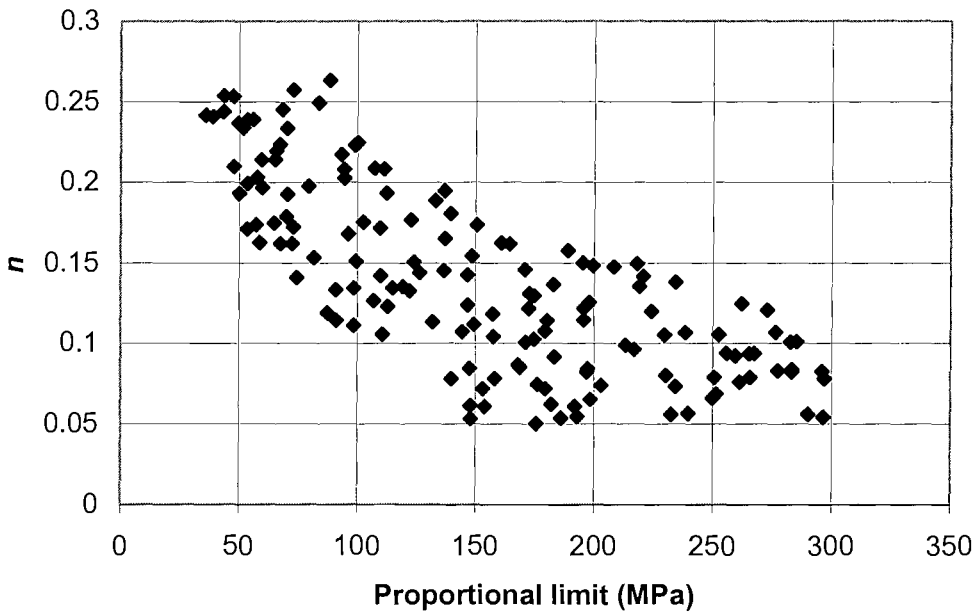
Figure 2-33    Input space of $\sigma_{el}$ and $n$
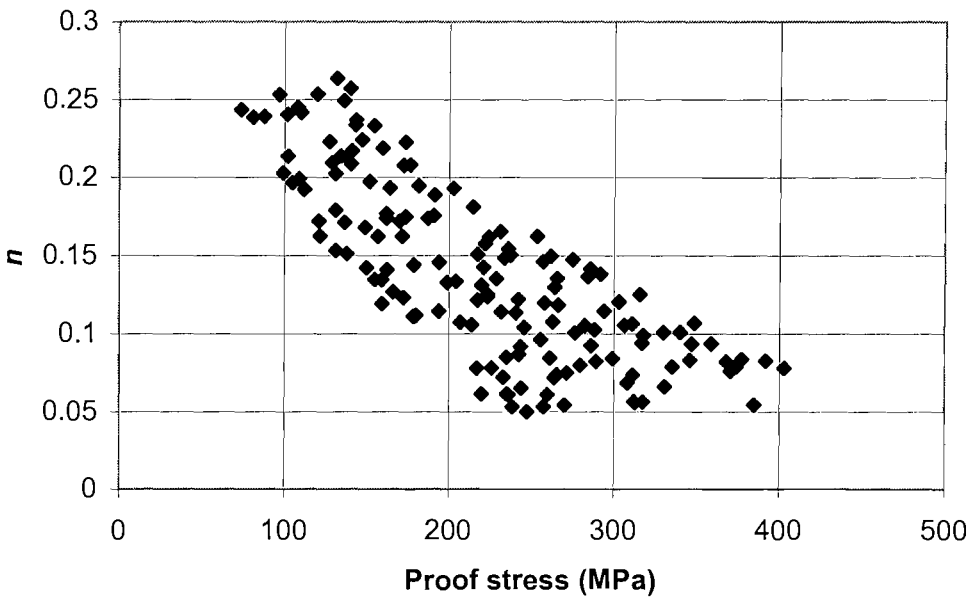


Figure 2-34    Input space of $\sigma_{0.2}$ and $n$

The randomly generated parameters are not distributed uniformly in the input space due to the applied constraints. However, it can be seen from the graphs above that there is considerable spread within their range, which is important for the success of the adaptive neural network modelling.

FEM analysis produced the respective *P-l* curves for all the 150 artificial elasto-plastic data. The predicted distinct values of micro-hardness indentation diagonal size *l* for each simulation were arranged into a vector array *l* which can be considered as a function of the respective array of loads **P** as well as the vector of elasto-plastic properties **x**.

## 2.5.2 SUPANOVA models

Due to the dearth of reliable experimental data, only results from FEM were included here in the dataset produced for SUPANOVA modelling. Each dataline includes four inputs ($P$, $x_1 = \sigma_{el}$, $x_2 = \sigma_{0.2}$, $x_3 = n$) and one output ($l$). In each SUPANOVA model, 90% of the data was used for training to define the model and 10% of data was reserved as "unseen" or test data to assess the performance of the model. The training and testing data were randomly selected 10 times to assess the effect of data sampling on the models produced. Predictions presented here are therefore averages of the 10 models produced by the 10 data sampling runs. Consistency of input selection by the sparse ANOVA representation of SUPANOVA was also assessed as it revealed the stability of the modelling process.

Sub-sets of $K$ material arrays $\mathbf{x}^{(k)}$, ($k = 1, \ldots, K$) among the 150 initially selected, together with their respective simulated indentation records $l_k = l(\mathbf{P}_k, \mathbf{x}^{(k)})$ are used as training data to generate a SUPANOVA model $l^S = l^S(\mathbf{P}, \mathbf{x})$ for predicting indentation size for any given load and material array.

The first SUPANOVA model (SA1) used a set of $K = 30$ "training data" combinations of material arrays and their corresponding indentation records. A SUPANOVA model with a combination of univariate, bivariate and trivariate functions of input variables was produced.

The accuracy of the predictions of this model was assessed by evaluating the root mean square (rms) error for each particular indentation record $k$:

$$(\text{rms})^{(k)} = \sqrt{\frac{1}{M}\sum_{i=1}^{M}[l^S(P_i, \mathbf{x}^{(k)}) - l(P_i, \mathbf{x}^{(k)})]^2} \qquad (2.27)$$

where *M* is the number of respective load levels.

Table B-1 in Appendix B gives the rms error for each artificial material A($k$) ($k$ = 1, ..., 30) together with the corresponding property vectors $\mathbf{x}^{(k)}$ themselves.

It can be seen that the rms error was found to range from 0.4668 µm to 1.686 µm over the set of training data and the average is 1.001 µm. Considering that the average indentation size was around 75 µm (take material A2 as an example), this variation was not considered significant.

The consistency of the SUPANOVA performance was examined by selecting another set of 30 training data from the 150 initially generated to obtain a second SUPANOVA model (SA2). Table B-2 in Appendix B gives the rms error for each *x* in SA2.

For SA2 the rms error ranges from 0.709 µm to 2.534 µm over the set of training data and the average is 1.197 µm. Compared with SA1, SA2 gives a higher individual rms error for its training data but a similar average value as SA1.

Since the bearing lining materials of interest in the present project are expected to lie within the softer part of the initially considered range, it was decided to develop an additional SUPANOVA model with a set of material property data within the following, narrower ranges:

$$35 < \sigma_{el} < 200 \text{ (MPa)} \tag{2.28}$$

$$65 < \sigma_{0.2} < 300 \text{ (MPa)} \tag{2.29}$$

$$300 < A < 450 \text{ (MPa)} \tag{2.30}$$

$$0.08 < n < 0.3 \tag{2.31}$$

$$0.1 < E_2 / E_1 < 0.55 \tag{2.32}$$

$$0.15 < E_1 / E < 0.45 \tag{2.33}$$

Also, for the individual gradients, the following ranges were adopted based again on the experimental evidence from the softer control materials:

$$12{,}000 < E_1 < 30{,}000 \quad \text{(MPa)} \tag{2.34}$$

$$2{,}500 < E_2 < 6{,}500 \quad \text{(MPa)} \tag{2.35}$$

These new limits removed the uncertainty regarding the ability of the developed FEM program to predict accurately the indentation behaviour of harder alloys, that is, those with higher elastic limit and 0.2% proof stress.

The new SUPANOVA (SA3) model was based on a set of 31 training data sets ($K$=31) in order to generate reliable approximate relations between indentation and material parameters. The data were selected from the 150 initially generated data so that they satisfy the modified ranges given by (2.28) – (2.35).

Table B-3 in Appendix B gives the rms error for each $\mathbf{x}^{(k)}$ in SA3 as well as the corresponding property sets. The error range is from 0.7660 μm to 1.9612 μm and its average value is 1.1057 μm. Again this is consistent with average errors of SA1 and SA2.

A further SUPANOVA (SA4) was built which consists of the data sets used in SA3 and 7 additional data sets that satisfy the same constraints as SA3. This gives a total of 38 training data sets ($K$=38) in this model. The purpose of building this model was to investigate the effect of increasing data sets on the performance of SUPANOVA model.

Table B-4 in Appendix B gives the rms error for each $\mathbf{x}^{(k)}$ in SA4 as well as the corresponding property sets. The error range is from 0.706 μm to 1.772 μm and its average value is 1.040 μm. Both the error range and its average value are better for SA4 than for SA3.

Considering the post-yield behaviour of the materials of interest and that the reliability of FEM appears to be good within the respective narrow range of properties, SA4 was chosen for approximation modelling in the characterisation process.

The consistency of all possible univariate, bivariate and trivariate terms in the four SUPONOVA models is given in Table 2-8.

**Table 2–8 Consistency of SUPANOVA models**

| Input | | Model | | | |
|---|---|---|---|---|---|
| | | SA1 | SA2 | SA3 | SA4 |
| Univariate terms | $\sigma_{el}$ | - | - | - | - |
| | $\sigma_{0.2}$ | 100% | 40% | 100% | 100% |
| | $n$ | 100% | - | 100% | 100% |
| | $P$ | 100% | 100% | 100% | 100% |
| Bivariate terms | $\sigma_{el}$ & $\sigma_{0.2}$ | - | - | - | - |
| | $\sigma_{el}$ & $n$ | - | - | - | - |
| | $\sigma_{el}$ & $P$ | 30% | 100% | - | - |
| | $\sigma_{0.2}$ & $n$ | - | 90% | - | - |
| | $\sigma_{0.2}$ & $P$ | 100% | 100% | 100% | 100% |
| | $n$ & $P$ | 100% | 100% | 100% | 100% |
| Trivariate terms | $\sigma_{el}$ & $\sigma_{0.2}$ & $n$ | - | - | - | - |
| | $\sigma_{el}$ & $\sigma_{0.2}$ & $P$ | 100% | 100% | - | - |
| | $\sigma_{el}$ & $n$ & $P$ | - | 90% | - | - |
| | $\sigma_{0.2}$ & $n$ & $P$ | 100% | 100% | 100% | 100% |

It can be seen that some terms such as $\sigma_{el}$, $\sigma_{el}$ & $\sigma_{0.2}$, $\sigma_{el}$ & $n$, and $\sigma_{el}$ & $\sigma_{0.2}$ & $n$ are not selected by any of the SUPONOVA models. Terms involving $P$, $\sigma_{0.2}$ & $P$, $n$ & $P$ and $\sigma_{0.2}$ & $n$ & $P$ are important in all four models and were picked up by each of the ten runs of SUPONOVA model. Because SA3 and SA4 are based on almost the same data sets, they picked up the same components in their predictions.

Figure 2-35 shows the prediction accuracies of SA4.
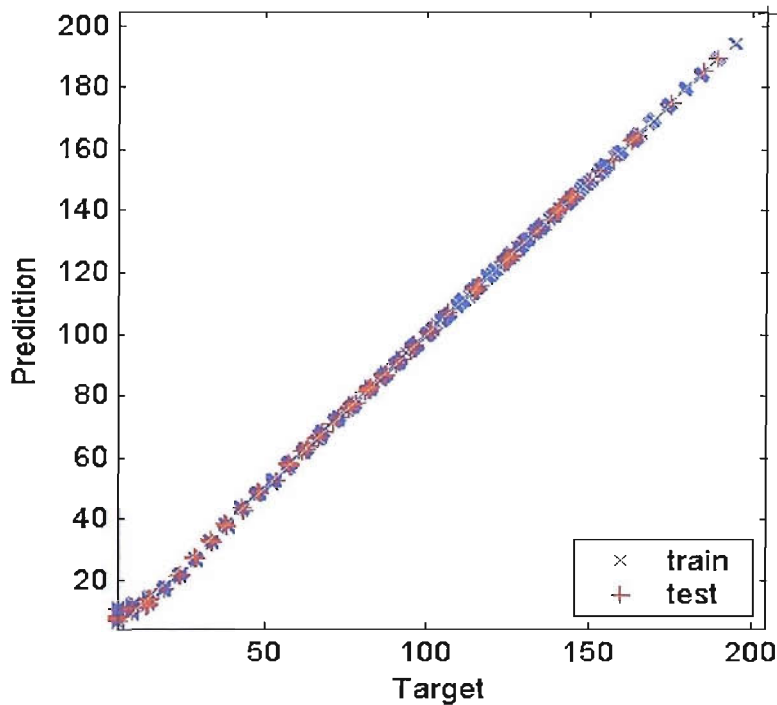
Figure 2-35    Target vs prediction of SA1

Both target and prediction in this plot means the output (here the indentation size) of SUPANOVA models. The "Target" of each point is indentation size of the datalines in the input file. The "Prediction" is the predicted indentation size. The "train" data are datalines used to construct the SUPANOVA model, while the "test" data represent the remaining datalines of the input file. It can be seen that the prediction accuracy is quite satisfactory for most of the range of indentation size. However, relatively large error occurs at low indentation size (implying low load) for both train and test data. This is believed to be the result of high relative error in FEM results at low load level.

Referring to Table 2-8, all 10 models of SA4 picked up the univariate terms for $\sigma_{0.2}$, $n$ and $P$, the bivariate terms for the combinations $\sigma_{0.2}$ & $P$ and $n$ & $P$, and the trivariate term $P$ and $\sigma_{0.2}$ & $n$. It implies that these parameters and combination of parameters are consistently important in the SUPANOVA model for predicting the indentation size.

Figures 2-36, 2-37 and 2-38 show the general forms of the relationships found between inputs and output in the SUPANOVA model.



(a)

(b)

(c)
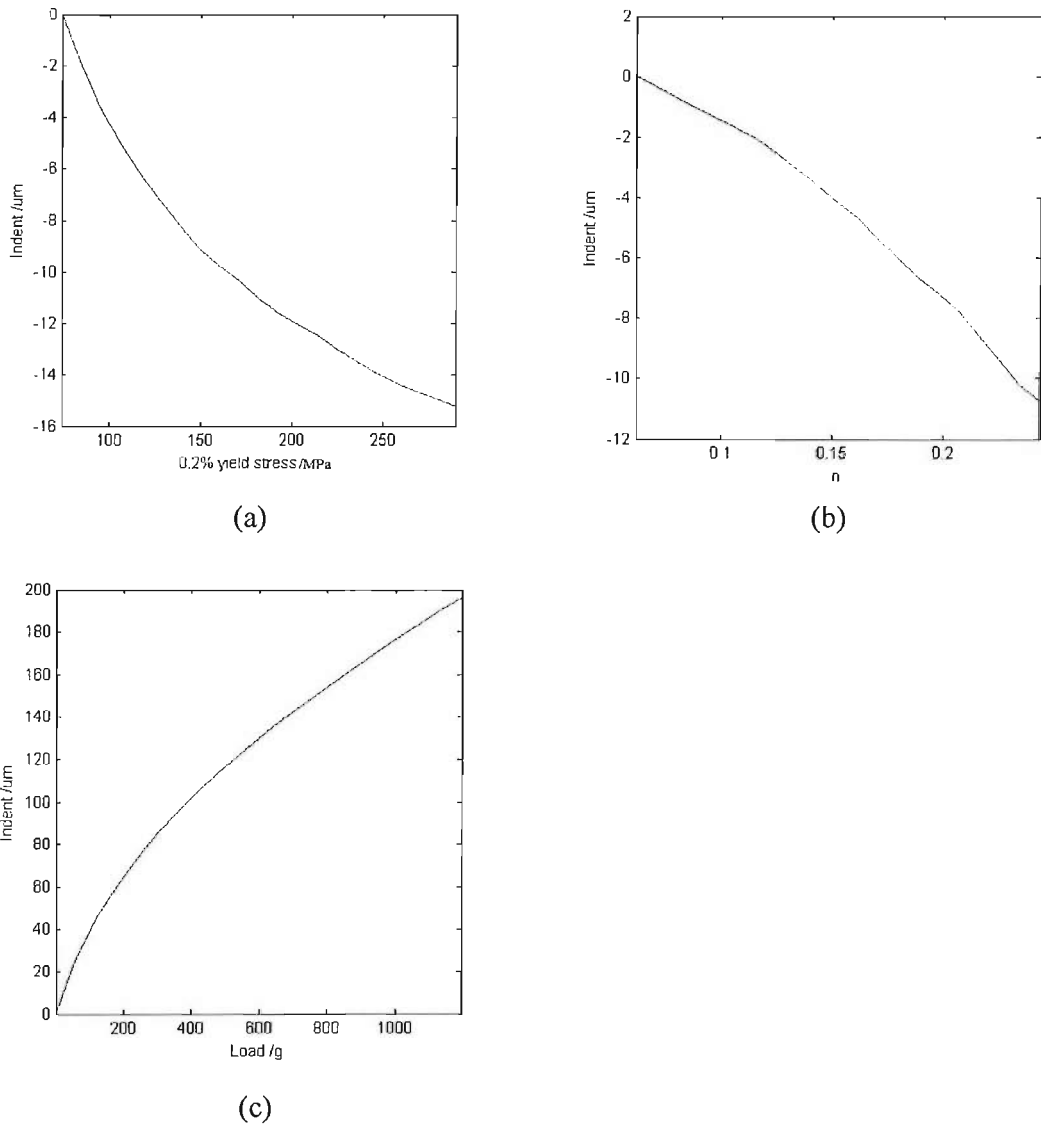
Figure 2-36     Selected univariate terms by SUPANOVA for SA4
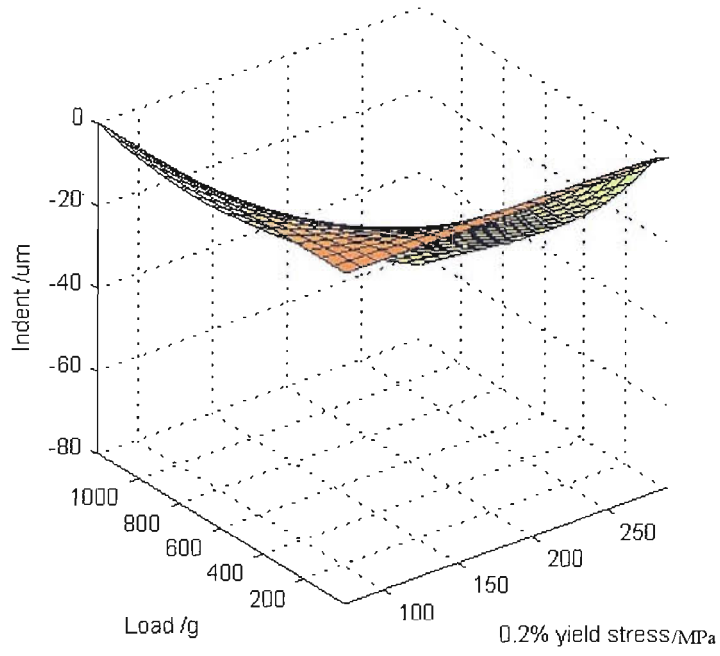
(a)
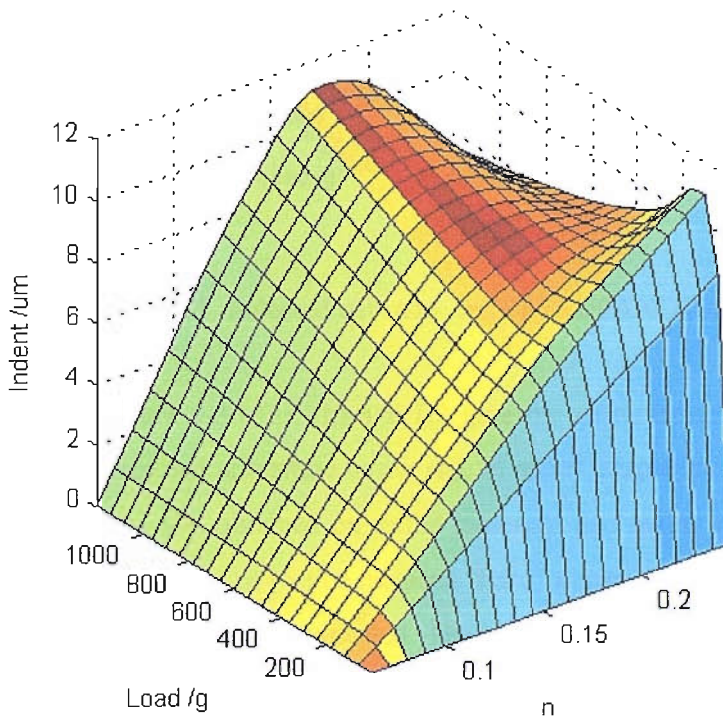


(b)

Figure 2-37    Selected bivariate terms by SUPANOVA
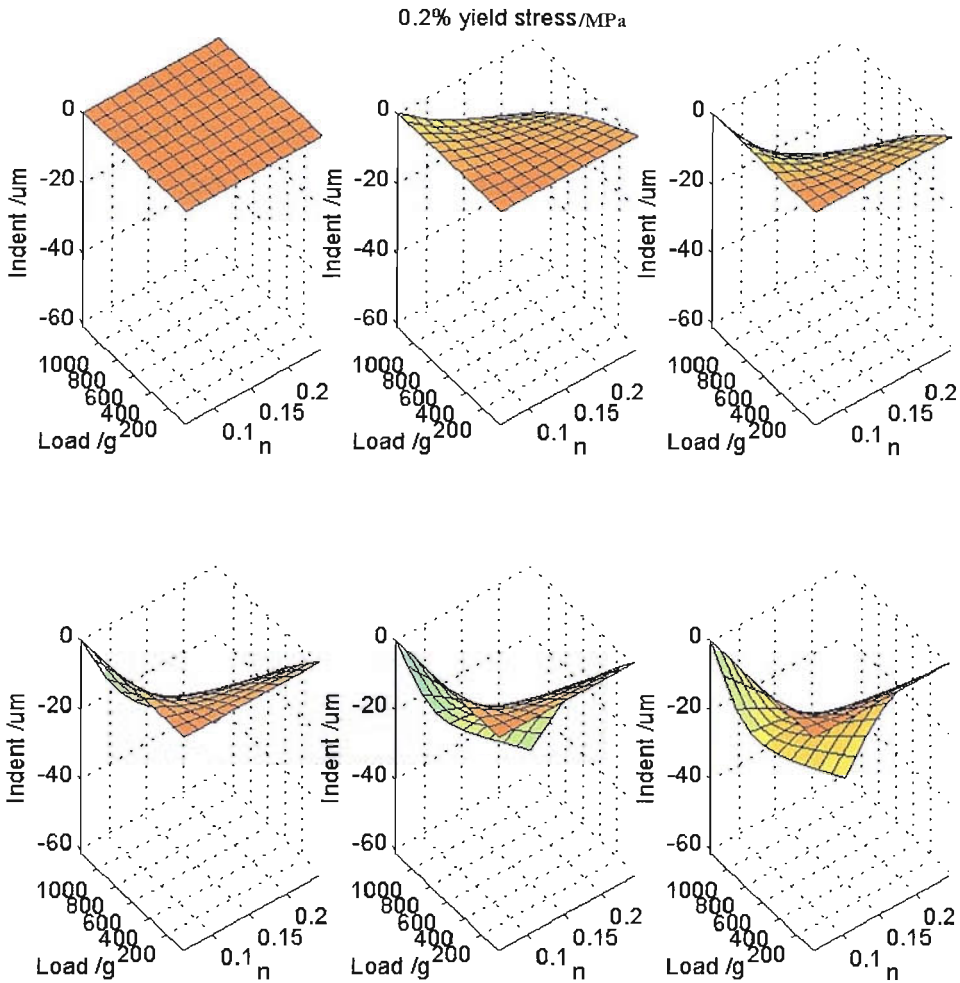
Figure 2-38    Selected trivariate term by SUPANOVA

The plots shown in Figure 2-36 (a), (b) and (c) give the relationships between the predicted indentation size and univariate terms $\sigma_{0.2}$, $n$, and $P$, respectively. When $n$ or $\sigma_{0.2}$ increases, the indent size obtained on tested materials decreases. This is easy to understand because a large $n$ or $\sigma_{0.2}$ value means a "hard" material. The effect of $P$ on indent size as shown above is also as expected. The higher the load applied, the larger the indent size obtained.

In Figure 2-37 (a), for a given $\sigma_{0.2}$, indent size appears to drop as load increases. This appears to be odd but has to be considered in the context of the overall model as a "correction" of the univariate term prediction.

In Figure 2-37 (b), the anomaly occurs at low load values, for which indent size increases for all $n$. The sudden dropping down at low load level could be a result of high relative error in FEM calculation when low load is applied so that the variation is not smooth. Indent size appears to increase for $0.05<n<0.175$, but this behaviour has to be considered together with that of Figure 2-36 (b) and Figure 2-38, which show the opposite trend. One possible explanation for the contradiction between Figure 2-36 (b) and Figure 2-37 (b) may be the constrained data set used to build SUPANOVA model. It is noted from Figure 2-33 and Figure 2-34 for the produced artificial data, high $n$ is correlated to low $\sigma_{el}$ and $\sigma_{0.2}$, due to the constraints applied. As a result, for artificial $\sigma$-$\varepsilon$ curves with high $n$ value, the obtained indent sizes at a certain load might be higher than artificial $\sigma$-$\varepsilon$ curves with a relative lower $n$ but higher $\sigma_{el}$ and $\sigma_{0.2}$.
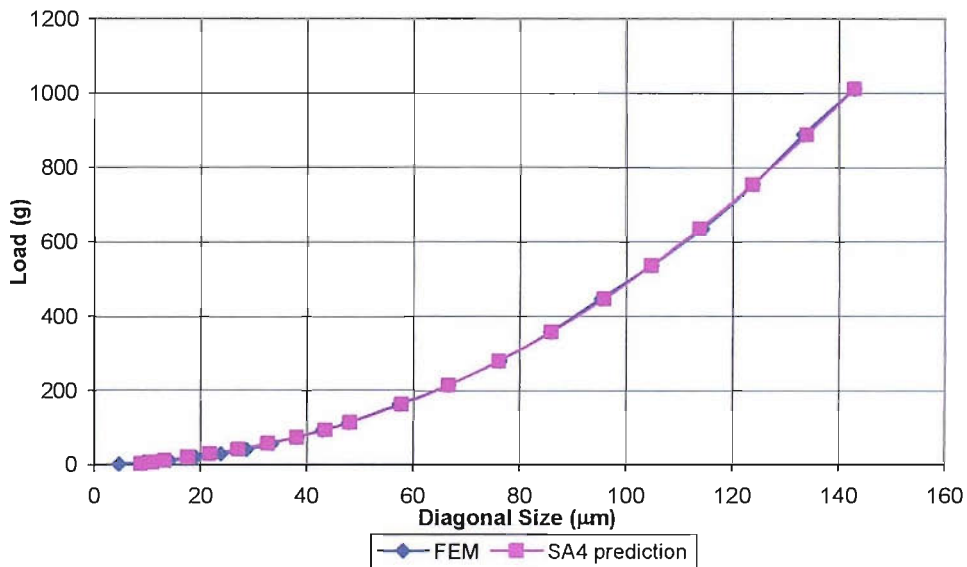


Figure 2-39     The SUPANOVA prediction of a training data

Figure 2-39 shows a typical indentation prediction of SA4 for a training data set (B11) for which the rms error equals 1.1375 µm. Figure 2-40 shows an indentation prediction of SA4 for a non-training data set for which the rms error equals 0.7577 µm. Both SUPANOVA predictions give high accuracy at high load levels. The error mainly occurs at low load level. Considering that the numerical error correction in FEM is more significant relative to the indent depth at low load level, the error in the

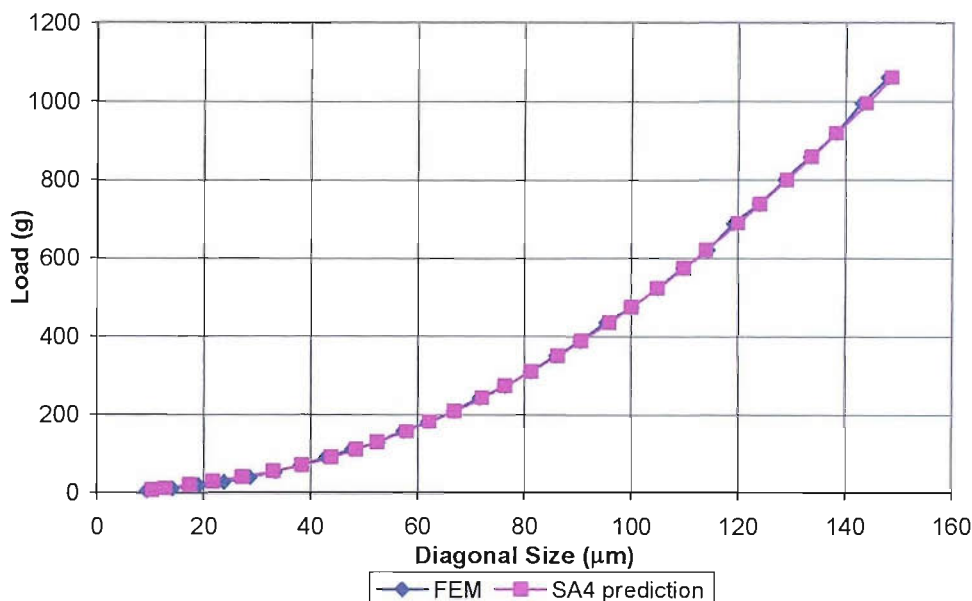present SUPANOVA model can be attributed to the inaccuracy of respective low load-level inputs.



Figure 2-40    The SUPANOVA prediction of a non-training data

Nevertheless, the SA4 exhibits good overall prediction ability. Since SA4 satisfies the finally adopted constraints and has a better performance than SA3 in terms of the average rms error, SA4 was selected for further approximation of the indent size – material properties relation in the next optimisation step.

## 2.6   Optimisation

### 2.6.1   Definition of problem

For any given material, the relationship between load $P$ and indentation size $l$ can be obtained experimentally through hardness tests. In the previous sections, it was shown that $l$ can be calculated either by FEM analysis or SUPANOVA modelling if the material parameter vector $\mathbf{x}$ is given. This relationship is described as:

$$l = l(P, \mathbf{x})$$

The aim of this project is to identify the stress-strain behaviour of a material of interest through Vickers hardness tests. Thus it is a problem of how to determine $\mathbf{x}$

from a given experimental record $l(P)$. Since the function $l = l(P, \mathbf{x})$ is not explicit, the solution $\mathbf{x} = \mathbf{x}(l,P)$ cannot be directly obtained. However, this inversion can be stated as an optimisation problem. It has been shown that FEM analysis can provide the indentation size for a given load if the stress-strain behaviour of the material is known. For a particular material parameter array $\mathbf{x}_j$, FEM yields $l_j=l(P,\mathbf{x}_j)$. By minimising the difference between $l_j$ obtained from FEM and $l$ obtained from experiments, a good approximation for $\mathbf{x}$ could be found. However, this process needs repeated calculations of $l_j = l(P,\mathbf{x}_j)$ for each update $\mathbf{x}_j$. While FEM indentation analysis is usually time consuming, the SUPANOVA model allows fast prediction of $l_j$ with satisfactory accuracy. The application of SUPANOVA model to the present problem enables the optimisation process.

For the characterisation of a particular material, $l^h(P)$ is first obtained from hardness tests. For any chosen $\mathbf{x}^{(j)}$, SUPANOVA provides $l^S=l^S(P_i, \mathbf{x}^{(j)})$ where $P_i$ is a fixed set of $M = 8$ loads applied by the available Vickers micro-hardness tester with the specific values of 10, 25, 50 100, 200, 300, 500 and 1000 grams. The root mean square (rms) error

$$(\text{rms})^{(j)} = \sqrt{\frac{1}{M} \sum_{i=1}^{M} [l^h(P_i) - l^S(P_i, \mathbf{x}^{(j)})]^2} \qquad (2.36)$$

is adopted as a measure of the difference between $l^h$ and $l^S$ over the complete loading range. All $\mathbf{x}^{(j)}$ should satisfy the constraints described in the previous section. $\mathbf{x}^{op}$ is determined by minimising the value of rms. It is believed to be the best approximation of $\mathbf{x}$, which represents the stress-strain behaviour of the material of interest.

### 2.6.2 Genetic Algorithm

A Genetic Algorithm (GA) was chosen for performing the required optimisation work. Genetic algorithms have been used to solve difficult problems when the objective functions are complex, implicit functions of their arguments lacking continuity and differentiability. In GAs each vector of input space is described as an individual. A group of individuals comprises a population. GAs maintain and manipulate a family of population of solutions through a "survival of the fittest"

strategy. These algorithms search the solution space of objective functions while evaluating the simulated solution obtained for individuals. Those individuals of any population that tend to give best solution have more chance to survive to the next generation thus the performance of successive generations is improved. Genetic algorithms allow mutation, crossover and selection operations applied to individuals to ensure that all regions of solution space should be explored and the promising areas are not omitted. Genetic algorithms have shown a strong ability to find optimisation results for nonlinear problems.

A GA optimisation toolbox[6] for Matlab was used for the present function optimization. The essential inputs required for this toolbox are parameter spaces, the objective function and the constraints. In this problem, the parameter spaces are the ranges specified for the property parameters constituting array $\mathbf{x}$. The objective function here is the rms error function defined by (2.36).

Given a set of discrete indentation inputs $l^h(\mathbf{P}, \mathbf{x})$, which can be either true experimental records from a material with still unknown properties $\mathbf{x}$ or simulations generated by FEM analysis for validation purposes, the GA works with successive guesses $\mathbf{x}^{(j)}$ for which SUPANOVA generates predictions $l^S(\mathbf{P}, \mathbf{x}^{(j)})$ so that the rms error is continuously evaluated and eventually minimised. The optimisation algorithm accounts for the constraints by adding a penalty term if a particular guess violates them. For example, for a guess of $\sigma_{el}$, which should satisfy condition (2.28), a penalty term of the form:

$$P\sigma_{el} = (\frac{\sigma_{el} - 200}{200})^2 \text{ if } \sigma_{el} \text{ is greater than 200 MPa,}$$

or

$$P\sigma_{el} = (\frac{35 - \sigma_{el}}{35})^2 \text{ if } \sigma_{el} \text{ is smaller than 35 MPa,}$$

or

$$P\sigma_{el} = 0 \text{ if } \sigma_{el} \text{ is in the specified range}$$

will be added to the rms error. The flowchart of the optimisation process is included in the overall characterisation flowchart shown in Figure 2-1.

### 2.6.3   Validation results

1)      Training data of SA4

The characterisation process was initially applied to materials with known properties in order to assess its performance. Such materials were either simulated, contributing to the FE database, or experimentally tested in both tension and hardness.

Table 2–9 shows optimisation results with a selection of simulated indentations among the training data records for validation purposes. The rms errors of the SUPANOVA predictions based on the optimisation result $x^{op}$ and the initial material input $x$ to the FE simulation are listed. The actual $x^{op}$ values can be obtained by referring to Table B-4 in Appendix B. The latter error should ideally have been very close to zero since $x$ belongs to the training data set. This however does not happen due to the SUPANOVA using subsets of training data to generate a number of models and then averaging over them. This explains why there is an rms error in the first place. The two rms errors do not coincide because of a slight tilt of the solution surface (rms) that displaces the location of its minimum thus leading to a different $x$ and the GA does not lead to the correct solution. It can be seen that rms($x^{op}$) is always less than rms($x$), which means that the GA does indeed identify the optimum solution for the objective function for the given SUPANOVA approximation $l^S(P, \mathbf{x})$.

**Table 2–9 Differences between optimisation predictions and training data**

| Material | $\sigma_{el}$ (MPa) | $\sigma_{0.2}$ (MPa) | $n$ | $rms^s_{xop} - rms^s_x$ |
|----------|---------|---------|---------|---------|
| B1 | 27.52% | 3.79% | -21.74% | -0.030 |
| B3 | -35.13% | 1.90% | -9.65% | -0.025 |
| B6 | -23.33% | 0.45% | -3.31% | -0.016 |
| B7 | -23.32% | 3.64% | -14.05% | -0.054 |
| B9 | 20.46% | 4.48% | -23.04% | -0.089 |
| B10 | 1.39% | 0.46% | -2.75% | -0.013 |
| B11 | 16.14% | 3.08% | -15.12% | -0.050 |
| B12 | 10.33% | 3.83% | -19.22% | -0.068 |
| B13 | -2.01% | -1.12% | 0.05% | -0.122 |
| B14 | -4.10% | -1.22% | -0.66% | -0.137 |
| B22 | 15.18% | -0.77% | 0.37% | -0.062 |
| B24 | -10.77% | 3.20% | -13.67% | -0.041 |
| B31 | -41.22% | 3.29% | -8.04% | -0.052 |
| B32 | -39.35% | 1.84% | -5.48% | -0.058 |
| B33 | -50.34% | 3.99% | -15.63% | -0.056 |
| B35 | -22.67% | 2.86% | -8.00% | -0.067 |
| B37 | -34.72% | 3.53% | -7.13% | -0.156 |
| B38 | -48.60% | -1.21% | 5.92% | -0.014 |

Figure 2-41 shows an example of comparison between the original true stress – logarithmic strain curve and that obtained from predicted properties.
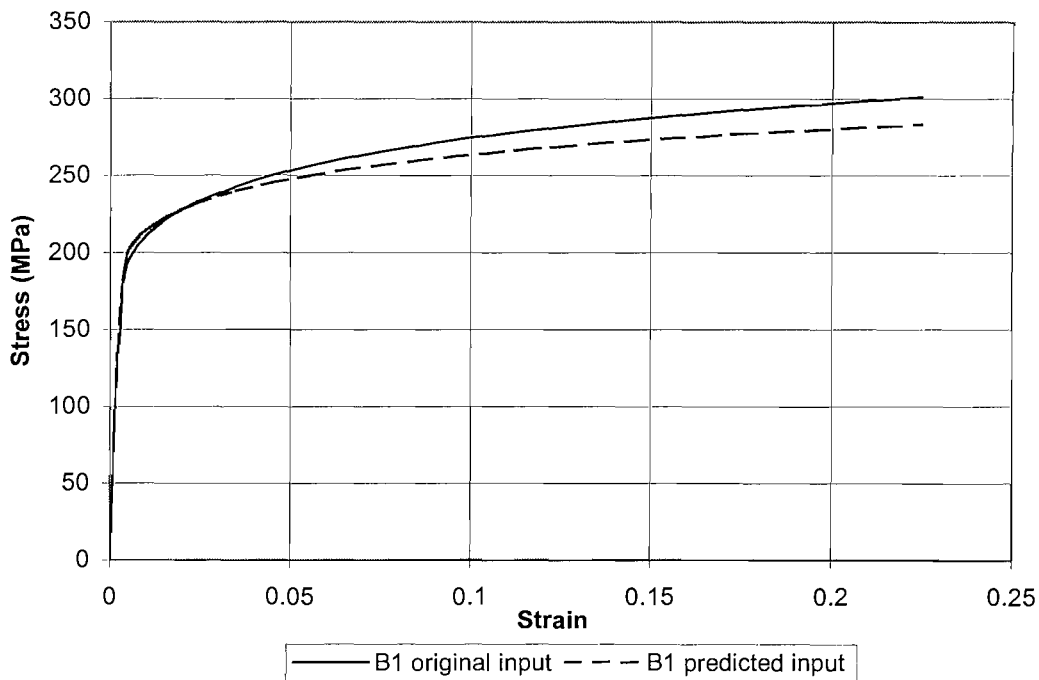


Figure 2-41     Stress-strain curves

It can be seen that the predicted curve is close to the original one, but a certain discrepancy exist which increases beyond the point where they cross over each other, indicating the difficulty to predict accurately the plastic property. Similar problem was reported by Giannakopoulos and Suresh[7].

FEM indentation analysis was performed using the predicted true stress-logarithmic strain curve for material B1. The results are plotted together with the FEM results obtained using the original values for the material properties in Figure 2-42. The agreement between two curves appears to be very good although there is a discrepancy between predicted and original $\sigma$–$\varepsilon$ curves. It confirms the observation by Dao *et al*[8] that the plastic properties of materials extracted from instrumented indentation were very sensitive to even small variations in the *P-h* curves.
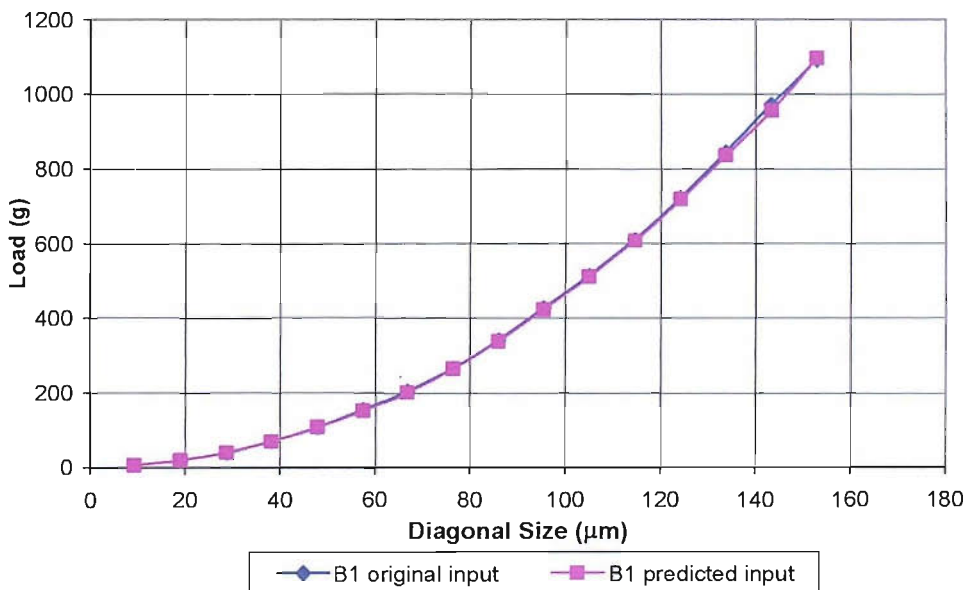


Figure 2-42    Load indent size curves by FEM

To further validate the difference between the original stress-strain curves and predicted stress-strain curves, both curves are used in the three point bending FE model of AS1241 flat strip to assess the stress and strain in lining materials. This FE model was used to provide stress and strain information at top surface of lining materials for flat strips. Details of this model are given in Appendix C.
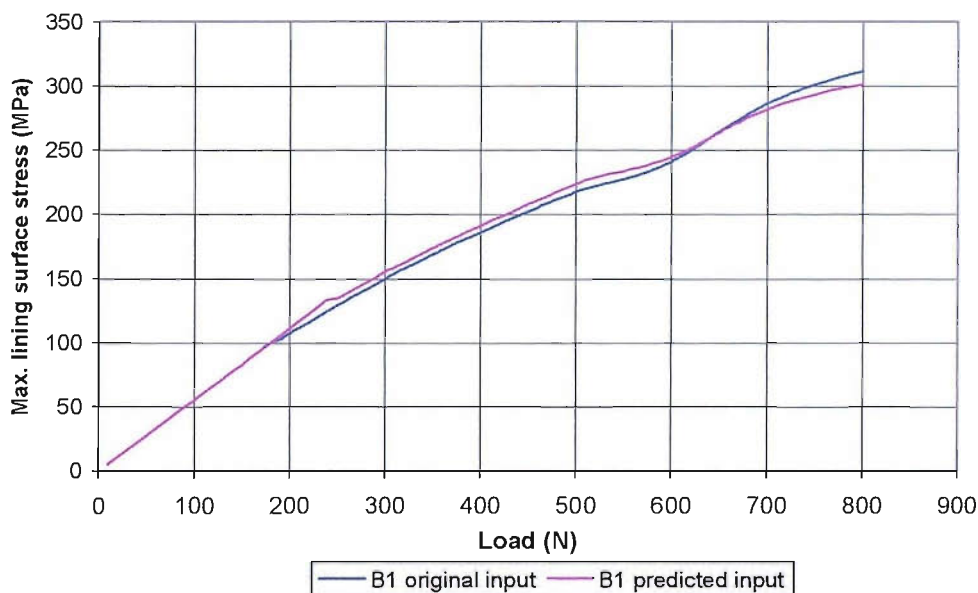
Figure 2-43    Maximum stress of lining in flat strip model by FEM
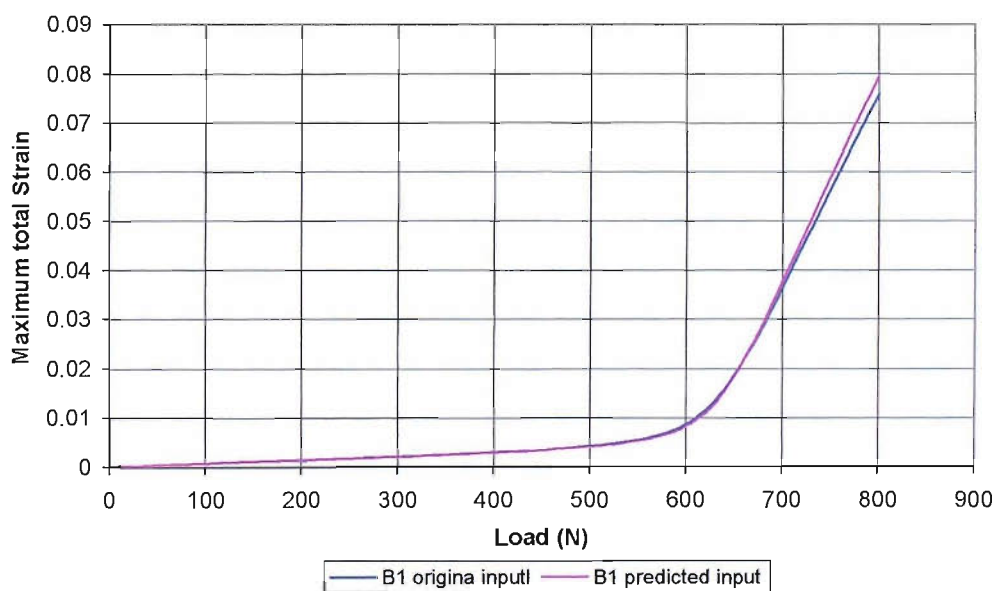


Figure 2-44    Maximum total strain of lining in flat strip model by FEM

The stress and strain responses in the lining layer are similar for both sets of materials. At low load range the stress-strain curves produce the same stress and strain behaviour. A discrepancy less than 5% exists at high load level. The estimated fatigue lifetimes of flat strip using the two $\sigma$–$\varepsilon$ curves will follow in the scatter of

90

experimental error[4], which indicates that the predicted $\sigma$–$\varepsilon$ curve can be used for the purpose of fatigue lifetime analysis without much shift from the actual results.

2) Simulated data

The artificial materials parameter sets used for validation in the previous section are also training data sets for the SUPANOVA model SA4. The optimisation process has been applied to some new, randomly chosen simulated data sets, for validating the model further, which are unknown data to the SUPANOVA model itself. The difference between optimisation predictions and original data is shown in Table 2–10.

**Table 2–10 The difference between optimisation prediction and original data for new simulated data set**

| Material | | $\sigma_{el}$ (MPa) | $\sigma_{0.2}$ (MPa) | $n$ | rms error of $l^S(P, x^{op})$ (μm) |
|---|---|---|---|---|---|
| C1 | Original | 99.6 | 200.4 | 0.085 | 0.935 |
| | Predicted | 139.3 | 188.1 | 0.115 | 0.695 |
| C2 | Original | 95.9 | 155.2 | 0.151 | 0.722 |
| | Predicted | 128.5 | 167.2 | 0.156 | 0.560 |
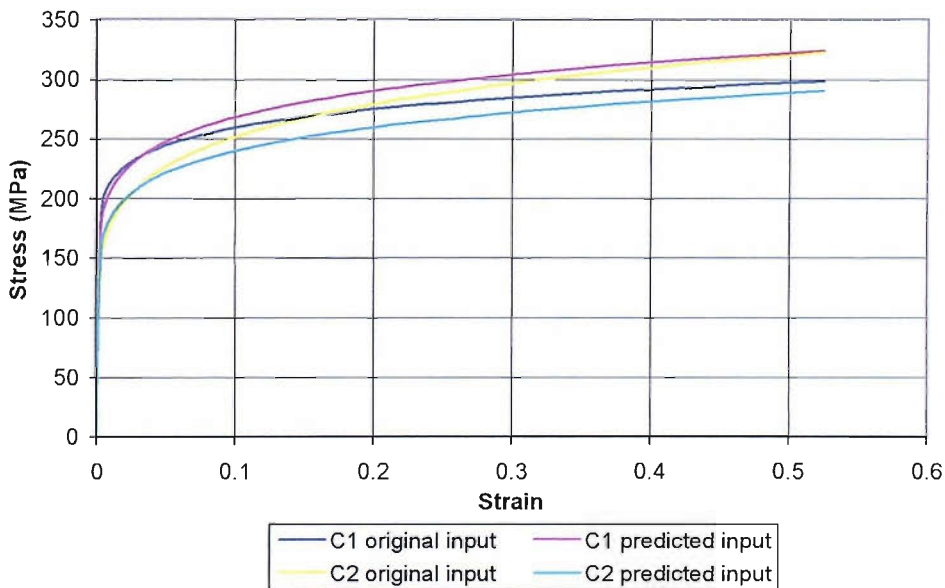


Figure 2-45     Stress-strain curves

Figure 2-45 shows the $\sigma$-$\varepsilon$ curves for original data and optimisation prediction. Again it can be seen that discrepancy exists between the test data and prediction, which becomes significant at high strains. This is mainly due to the discrepancy between the $n$ values. However, the indentation FEM plotted for both sets of curves shown in Figure 2-46 indicates that they produce very similar load-indent size curves.
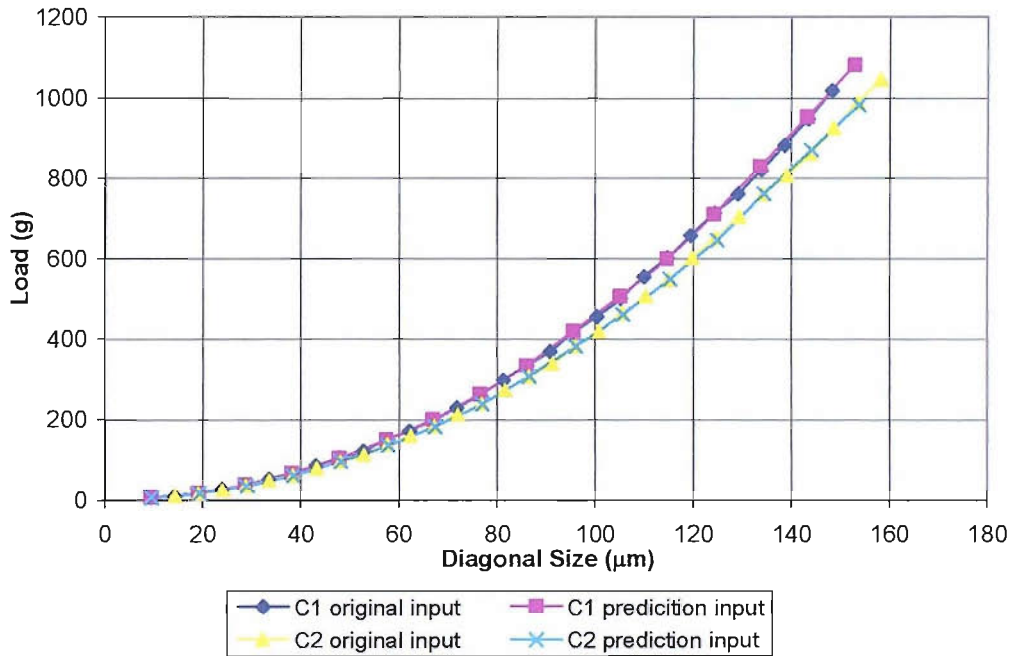


Figure 2-46    Load indent size curves obtained by FEM

Analysis was performed on the three point bending FE model of AS1241 flat strip to assess the stress and strain variations in lining using C1 and C2 original and predicted $\sigma$-$\varepsilon$ curves as material inputs for lining materials. Again Figure 2-47 and Figure 2-48 show that the original stress strain curve and the predicted one produced different maximum stress and strain but within a small range in the FEM analysis of flat strip models. It is also noted that the optimised results of stress strain curves for unknown data are consistent with the results of training data, which means the optimisation is reliable in terms of unknown data prediction.
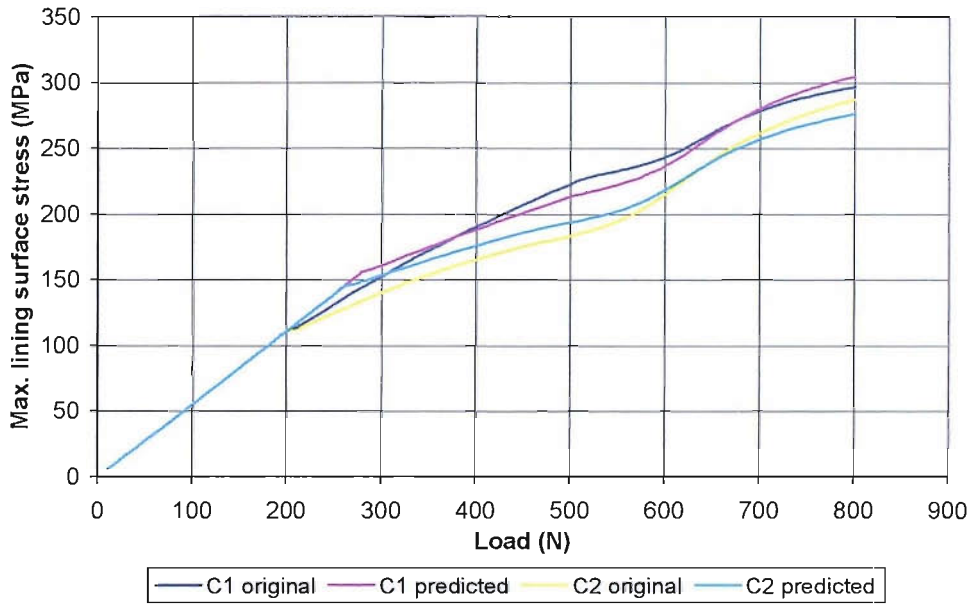
Figure 2-47    Maximum stress of lining in flat strip model
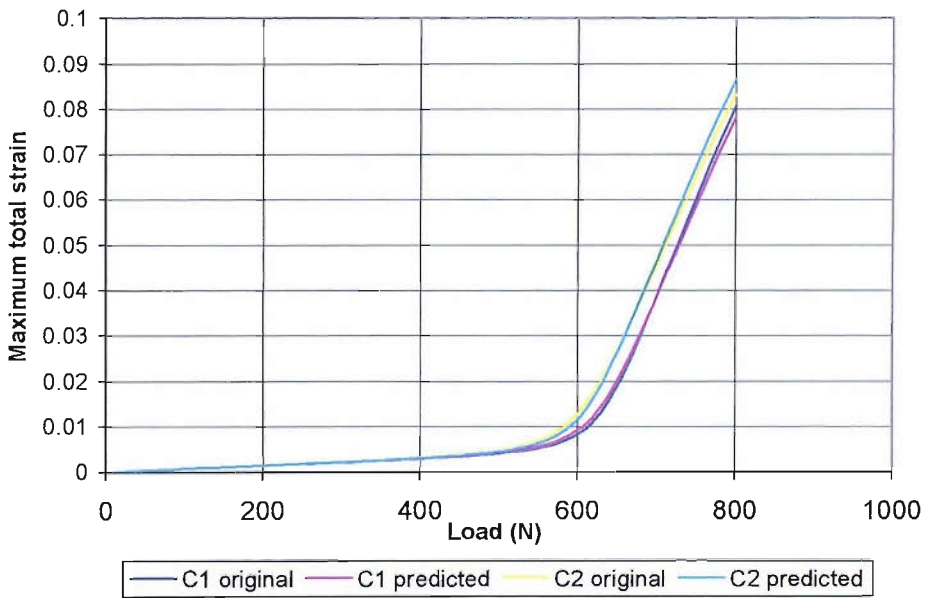


Figure 2-48    Maximum total strain of lining in flat strip model

3) Control material VQ1B

For validation purposes, the optimisation process was performed on control material VQ1B based on its load – indent size curve obtained from experimental hardness test. The difference between optimisation predictions and the idealised stress strain curve data of VQ1B is shown in Table 2–11. The predicted $\sigma$-$\varepsilon$ curve is shown in Figure 2-49 together with its idealised $\sigma$-$\varepsilon$ curve. A certain discrepancy is observed between the predicted and idealised $\sigma$-$\varepsilon$ curves.

**Table 2–11 Optimisation prediction and original data for VQ1B**

| Material | | $\sigma_{el}$ (MPa) | $\sigma_{0.2}$ (MPa) | $n$ | rms error of $l^S(P, x^{op})$ ($\mu$m) |
|---|---|---|---|---|---|
| VQ1B | Original | 44.0 | 84.3 | 0.242 | 3.7394 |
| | Predicted | 48.5 | 83.2 | 0.223 | 3.1634 |
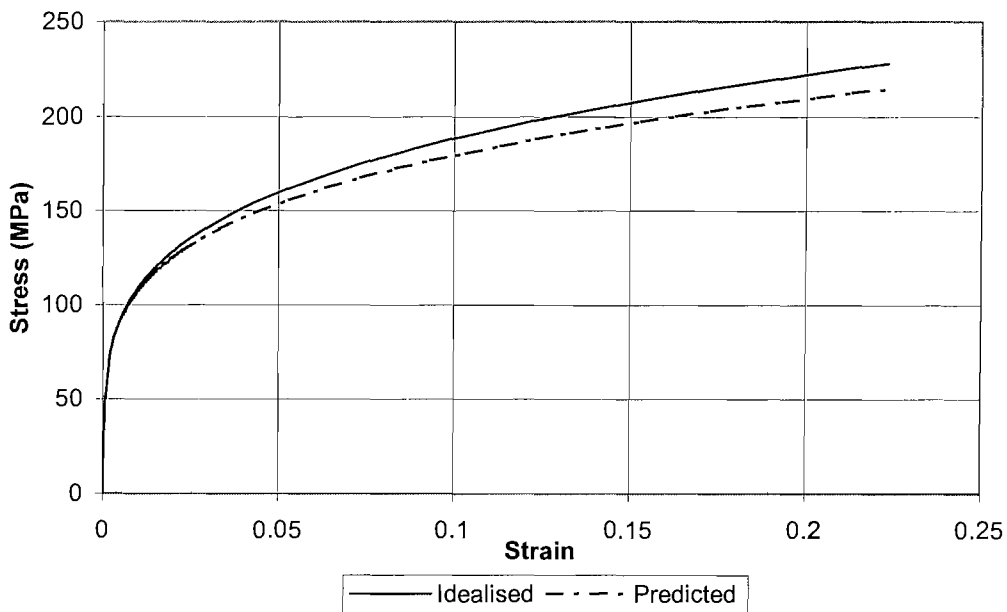


Figure 2-49    Predicted $\sigma$-$\varepsilon$ curve of VQ1B

4) Lining materials

Finally, the optimisation approach has been applied to all lining materials based the indentation results from Vickers hardness tests shown in Table 2–4 and the predictions are listed in Table 2–12.

**Table 2–12 Predicted stress-strain curve parameters of lining materials**

| Lining materials | $\sigma_{el}$ (MPa) | $\sigma_{0.2}$ (MPa) | $n$ | rms error of $l^S(P, x^{op})$ (μm) |
|---|---|---|---|---|
| AS1241 flat strip | 42.8 | 71.0 | 0.2483 | 4.9652 |
| AS1241 bearing | 36.2 | 106.2 | 0.1838 | 2.0298 |
| AS16 flat strip | 35.0 | 79.3 | 0.2308 | 3.6791 |
| AS16 bearing | 50.0 | 87.8 | 0.2146 | 2.5527 |
| HVOF | 49.6 | 79.4 | 0.2362 | 1.8783 |

Figure 2-50 shows the predicted stress-strain curves whose trend is consistent with that of the hardness results, that is, yield and strain hardening parameters increase with increased hardness. Figure 2-51 to Figure 2-53 allow a comparison between the experimental results and the indentation FEM simulation results using these predicted stress-strain curves. It can be seen that the agreement between the two sets of indentation results is satisfactory. According to the characterisation methodology described in Section 2-2, the predicted curves shown in Figure 2-50 could be taken as approximations (to a certain degree of accuracy) of the actual elasto-plastic behaviour of these materials of interest.
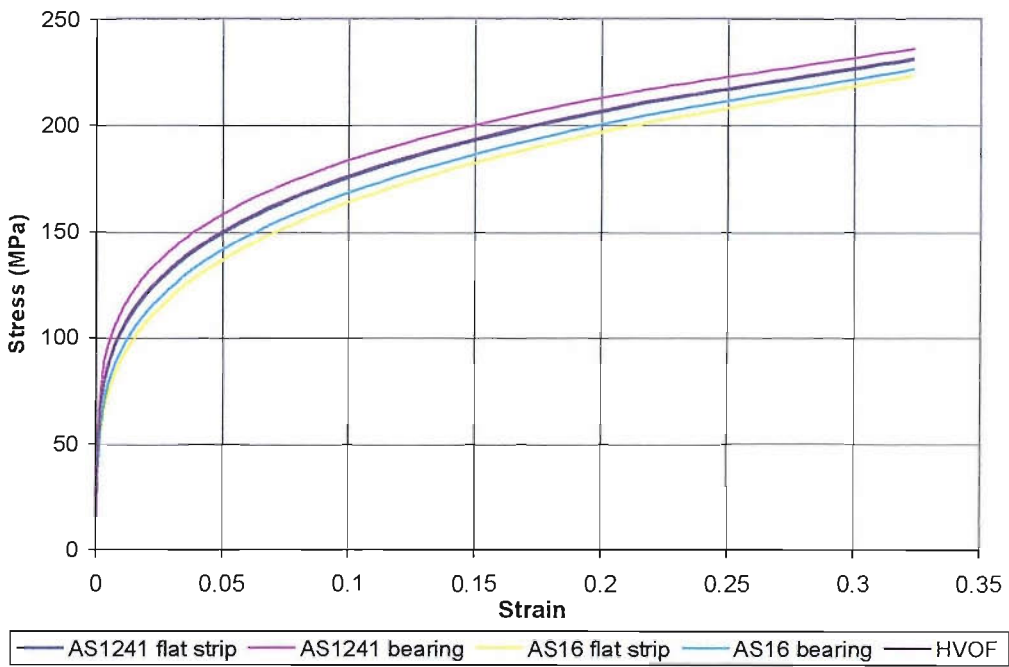
Figure 2-50    Predicted σ-ε curves of lining materials
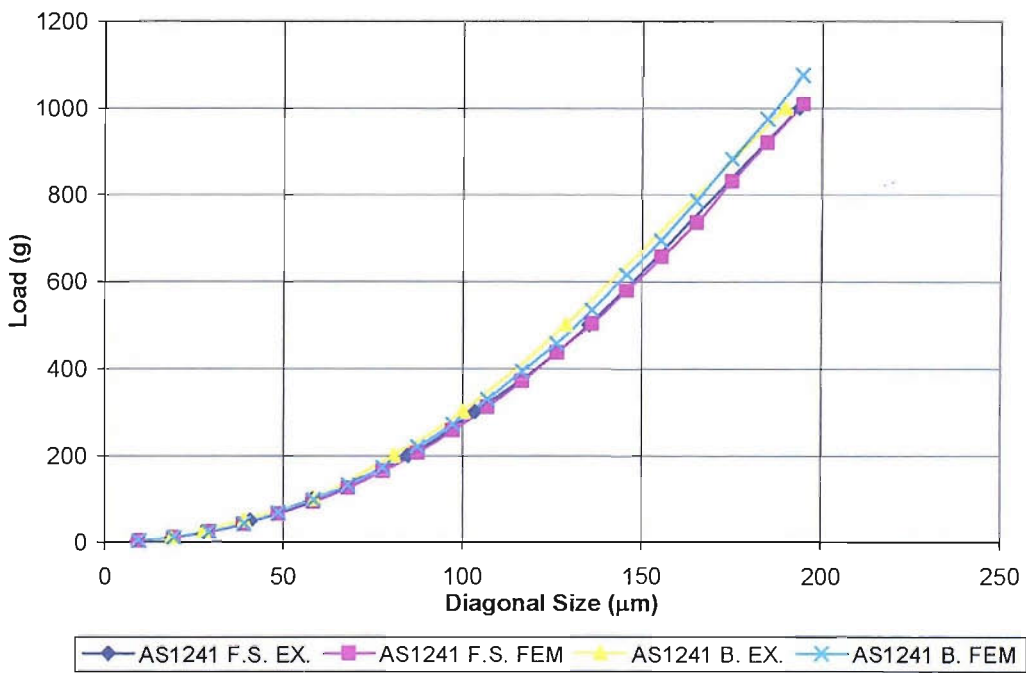


Figure 2-51    Load indent size curves
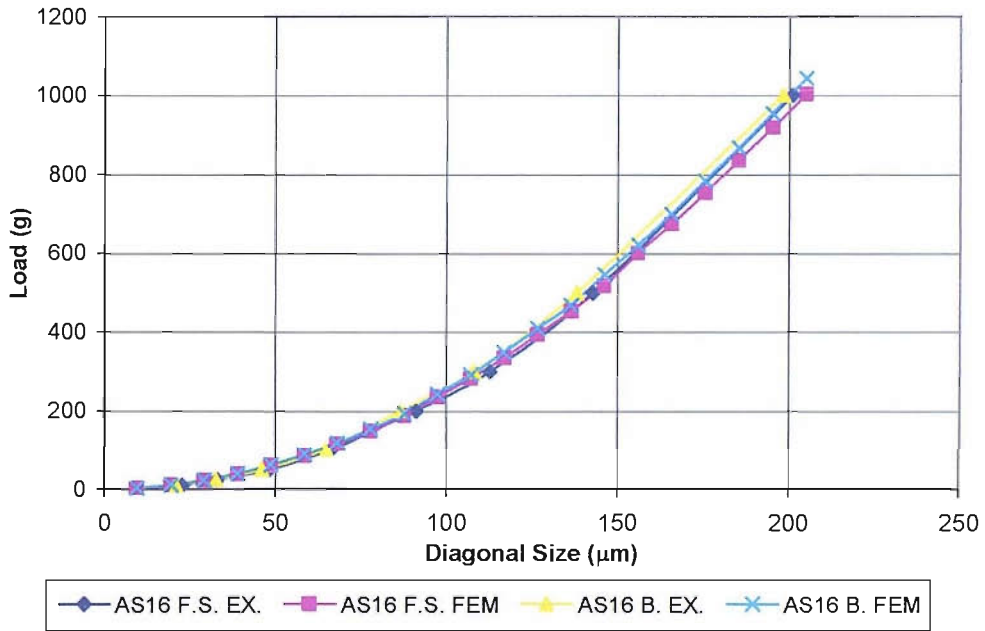
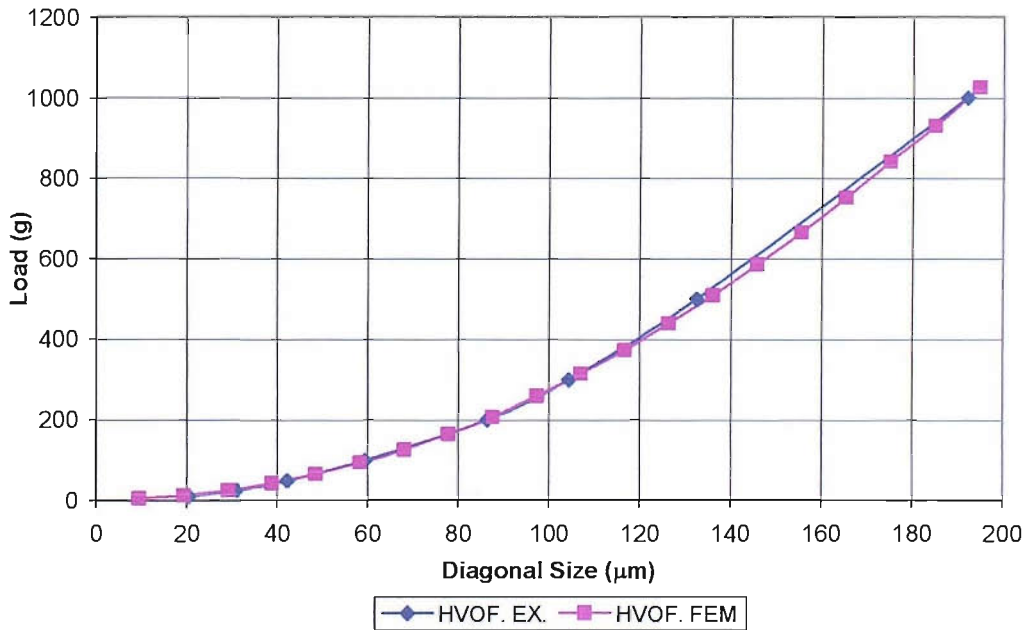Figure 2-52    Load indent size curves



Figure 2-53    Load indent size curves

## 2.7 Summary

In this chapter a characterisation methodology to obtain elasto-plastic properties of lining material from Vickers micro-hardness tests has been discussed. It aims to identify approximate estimates of stress-strain curves for materials, e.g. thin linings, upon which it is difficult to perform traditional tensile tests. In the methodology, a stress-strain curve that could give an identical load-indentation curve from FE modelling as the experimentally obtained load-indentation curve from Vickers micro-hardness tests was taken to be a good approximation of the property of that material. Numerical techniques such as adaptive numerical modelling and genetic algorithms were used in the characterisation to speed up the search process for the best-fitted curves. The methodology was applied to some materials of known elasto-plastic behaviour for validation purposes. Discrepancies within acceptable ranges exist between the predicted stress-strain curves and actual curves. As a result, the stress-strain curves of a few lining materials with unknown elasto-plastic behaviour were obtained, which will be used in flat strip and bearing modelling for fatigue analysis, and microstructure modelling to investigate initiation behaviour in the next chapter.

[1] M.R. Joyce, Fatigue of aluminium linings in plain automotive bearings, PhD Thesis, University of Southampton, U.K. 2001

[2] P. Rometsch, Private Communication, 2001

[3] W. D. Callister, Materials Science and Engineering An Introduction, fourth edition, pp. 130, New York, Chichester, Wiley, 1997

[4] M. Mwanza, Microstructural modelling of fatigue in novel plain bearing designs, PhD Thesis, University of Southampton, 2004

[5] ANSYS 6.1, SAS IP, Inc., Canonsburg, PA, 2001

[6] C. Houck, J. Joines and M. Kay, "A Genetic Algorithm for Function Optimization: A Matlab Implementation", NCSU-IE TR 95-09, 1995 http://www.ie.ncsu.edu/mirage/GAToolBox/gaot/

[7] A.E. Giannakopoulos and S. Suresh, Determination of elastoplastic properties by instrumented sharp indentation, Scripta Mater, Vol. 40, pp. 1191-1198, (1999)

[8] M. Dao, N. Chollacoop, K.J. Van Vliet, T.A. Venkatesh and S. Suresh, Computational modelling of the forward and reverse problems in instrumented sharp indentation, Acta Mater. Vol. 49, pp. 3899-3918, (2001)

# CHAPTER 3  Microstructure Modelling of the Initiation Sites

## 3.1  Introduction

This chapter aims to investigate the role of the microstructure of the lining material in controlling fatigue crack initiation with particular attention given to the AS16 lining. In Mwanza's[1] experimental work, the replica records of early fatigue tests on flat strips were collected and the initiation sites were identified under microscope. The finite body tessellation approach developed by Boselli *et al*[2] was used in Mwanza's investigation to identify the key microstructural factors that might influence the initiation behaviour. Parameters such as the secondary phase (soft Tin) shape, size and distribution were believed to play the most important role in the initiation phenomenon.

A lot of studies have been done on the effect of hard inclusions, such as Silicon particles, on the fatigue behaviour of soft aluminium matrix. Joyce's[3] and Mwanza's[1] experimental work on the AS1241 material shows that generally the points of fatigue crack initiation are associated with the decohesion of the Si at the Al matrix interface. Initiation was also observed to occasionally occur by debonding of Si/Sn interface in AS1241 lining. The results show that the larger the Si particles are, the more likely it is to initiate fatigue cracks. Gall *et al*'s[4] finite element analysis on the Si particle clusters in Al-Si alloys reveals that the particle shape and alignment are the most dominant parameters influencing initial particle fracture and debonding.

Detailed optical microscopy of polished samples of AS16 lining alloy before and during fatigue testing has been carried out[1]. A typical microstructure of AS16 is shown in Figure 3-1. It can be seen that Sn particles exist as the majority of the secondary phases in the Al matrix alloy. A small number of intermetallics which appear to be occasional darker grey phases were also observed (EDX tests performed by Mwanza[1] confirmed this material to be $CuAl_2$). Fatigue initiation was found mostly associated with the decohesion of Sn secondary phases from the Al matrix interface.
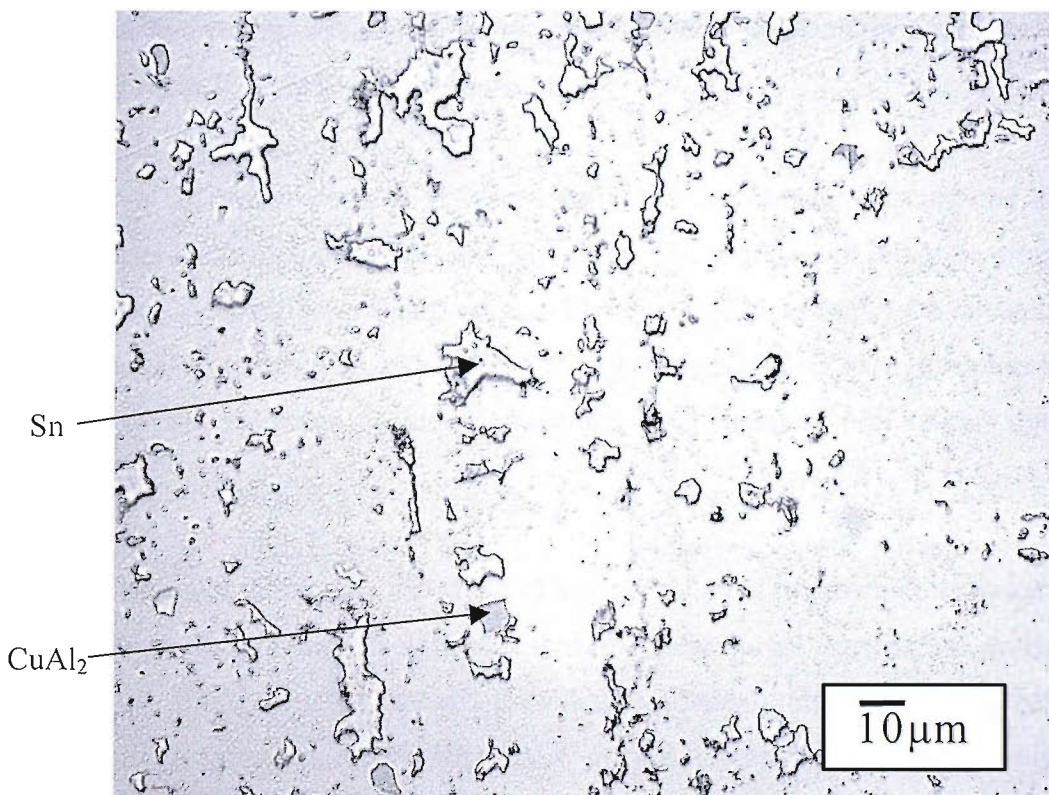
Figure 3-1     Optical micrograph showing a typical microstructure of

Al-Sn-Cu-Mn alloy (AS16)[1]

Thus, in the current project, the focus is on inclusions, which are soft, Sn, rather than hard Si, and the study of the local stress redistribution will be of interest in determining the initiation behaviour.

Finite element analysis was employed here to investigate the role of key microstructure parameters in initiation behaviour. The investigation was based on various approaches to two-dimensional microstructure modelling. To check the reliability of the developed FE models before any further analysis, the benchmark problem of a single elliptical elastic particle in an infinite plate with different elastic properties under far field load was considered for validation purposes[5,6].

Then, a two-dimensional multi-particle microstructure model was developed to investigate the effect of certain geometric parameters on initiation behaviour. This model consisted of a group of hexagonally distributed circular elasto-plastic particles within a matrix with different elasto-plastic properties. The particle-matrix area ratio and the distance between particles were the critical geometric parameters while the

maximum hydrostatic stress and the maximum plastic shear strain were adopted as possible causes for initiation behaviour.

Replicas of microstructure of flat strip linings were obtained during the fatigue experiments performed by Joyce[3] and Mwanza[1]. The preferential initiation sites were identified on these replicas. Based on such experimental record of real microstructure, it was possible to develop a local FE model which can be used to compare the location of the predicted critical stress/strain with observed preferential initiation sites.

To systematically investigate the effect of a wider range of microstructure parameters, it is useful to develop models with idealised microstructures. Tessellation analysis on images of lining microstructure provided statistical information on particle parameters. A classification SUPANOVA software[7] with information on initiating particles and non-initiating particles was used to identify a number of microstructure parameters and their combination that were important to crack initiation, and within a certain accuracy, the software could identify possible particles that are likely to crack for a given microstructure. It was then planned that the effectiveness of this approach would be examined by generating a few idealized microstructures and performing FE analyses on these microstructures. The distribution of critical stress and strain of particles and surrounding matrix would then be compared with the location of likely initiating particles predicted by the SUPANOVA software, however problems with the SUPANOVA models meant that this final stage could not be fully completed.

## 3.2   Tessellation analysis

Since the focus of the work is, on how fatigue crack initiation may be affected by critical microstructure geometric parameters, statistical analyses of the lining microstructure were necessary to investigate the initiation behaviour. Optical microscopy of polished samples (before and after fatigue testing) was obtained showing the microstructure and the secondary phases of linings. Statistical analysis was then performed on these binary images of microstructures to investigate the

distribution of secondary phases[1,3] using a statistical particle assessment based on finite body tessellation (FBT), developed by Boselli *et al*[2].

This tessellation approach provides a means of statistically characterising a multiphase microstructure by generating a series of tessellated cells surrounding each particle in the microstructure such that all points within a given cell are closer to the enclosed particle than to any other. It is capable of generating 11 types of statistical data based on secondary particle sizes, spatial distributions and near-neighbour measurements for each cell. The 11 FBT parameters are shown in Figure 3-2 and defined as following:

- *OA*: area of the object, i.e. the particle.
- *OAspRat*: aspect ratio of the object, defined as the maximum chord length divided by perpendicular width.
- *OAng*: angle of the object's longest chord with respect to the horizontal (between 0 and $\pi/2$ radians). In this study, the horizontal is set to be the tensile axis.
- *CA*: area of the cell.
- *CAspRat*: aspect ratio of the cell, defined as the maximum chord length divided by the perpendicular width.
- *CAng*: angle of the cell's longest chord with respect to the horizontal (between 0 and $\pi/2$ radians).
- *LAF*: local area fraction, that is the ratio of object to cell area multiplied by 100.
- *No. NNs*: number of near-neighbours, i.e. number of objects sharing a cell boundary with object of interest.
- $d_{min}$: nearest-neighbour distance, i.e. shortest interfacial distance with any of the near-neighbours.
- $d_{mean}$: mean near-neighbour distance, i.e. the average of shortest interfacial distances to all of the near neighbours.
- *NNAng*: nearest-neighbour angle, i.e. the angle of the line joining the centroid of the object to the centroid of the nearest neighbour, measured with respect to the horizontal (between 0 and $\pi/2$ radians).
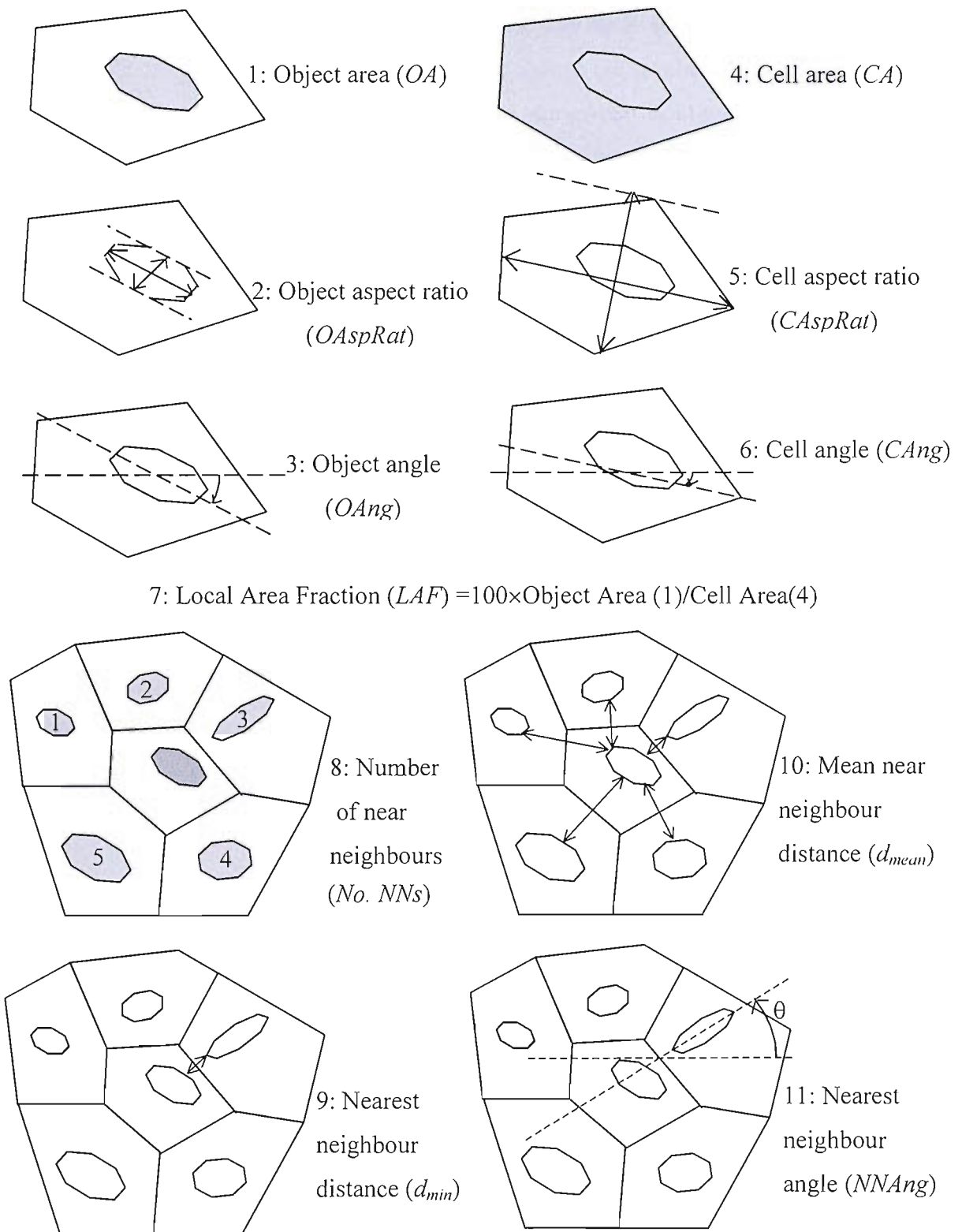
Figure 3-2     The 11 feature measurements obtained by FBT$^2$

In previous projects[8,9] detailed experimental work was done on AS1241 and AS16 alloys which are used for bearing linings. These linings are produced by continuous casting before being cut into billets, and are then extensively cold-worked to reduce their thickness. This lining is then roll-bonded to the steel backing and annealed before finally being formed into bearings.

The AS1241 and AS16 materials subjected to fatigue tests were available as both 'as-finished' half-shell roll-bonded bearings and roll-bonded flat sheets. The plain bearing is shown schematically in Figure 1-1. The flat sheets were produced by the same manufacturing process as the bearings and were in the condition immediately prior to the final bearing forming operation, so that they have similar properties to the finished bearing half shell. In the study of AS1241, the flat strips were cut perpendicular to rolling direction only, which gives the same rolling directionality as the bearing for both AS1241 and AS16. In addition to the bearings and flat strips, AS1241 monolithic lining material, a lining alloy formed through the same rolling process as bearings and flat sheet lining, but without the pure Al interlayer or steel backing attached, was also available from the previous project[3]. Fatigue tests were then performed for both bearings and flat strips in a three-point bend configuration on a digitally controlled Instron 8502 servo-hydraulic fatigue-testing machine (±50 kN load capacity)[9].

For AS16, bend bar type flat strips measuring 80 mm × 20 mm × 2 mm were cut from the flat sheet as shown in Figure 3-3 for fatigue tests. Due to the rolling directionality introduced during manufacture two types of flat strip were obtained for AS16, one cut perpendicular to rolling direction (AS16 Perp.) and one cut parallel to rolling direction (AS16 Para.). Fatigue work has previously been carried out on AS124 and AS16 lining alloys (both perpendicular alignment and parallel alignment) and investigation of preferential fatigue initiation sites was performed on AS1241 and AS16 Perp.
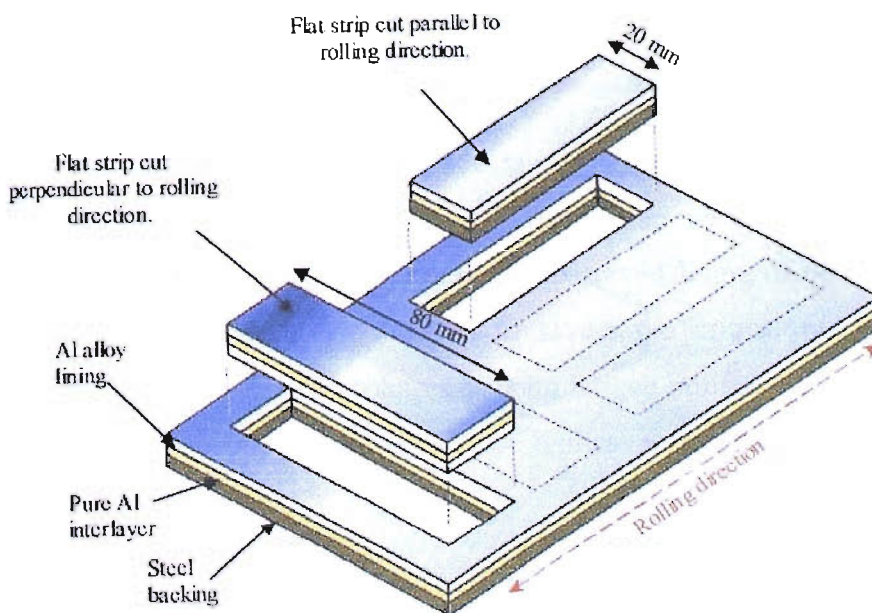
Figure 3-3    AS16 flat sheet showing bend bar type flat strips cut out perpendicular and parallel to rolling direction[1]

Figure 3-4 shows an example of Object Area (*OA*) frequency histogram for Si particles from FBT on parts of the lining microstructures of AS1241 bearing, flat strip and monolithic lining[3].
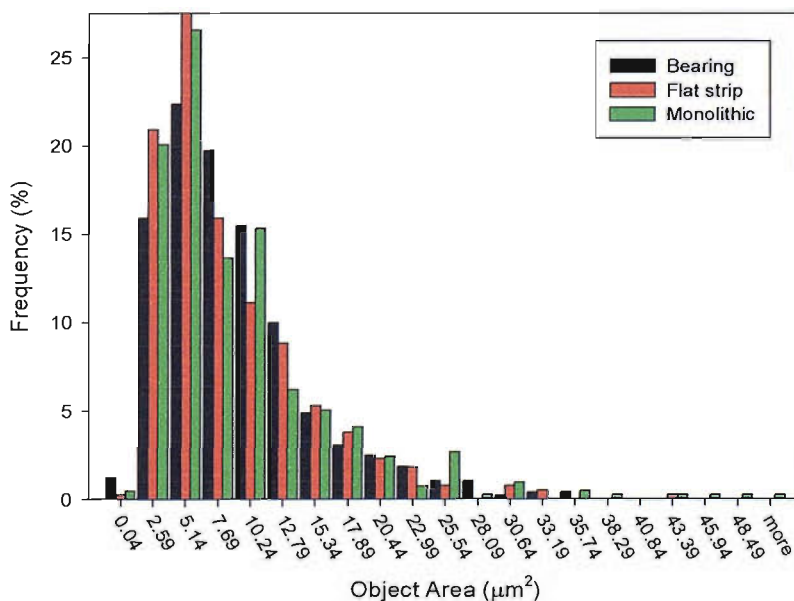


Figure 3-4    Object Area histogram for Si particles in AS1241 material systems[3]

Selected frequency histograms of other FBT parameters for Si particles in AS1241 material systems[3] are shown in Appendix D, from Figure D-1 to Figure D-3.

Using acetate replicas of the sample surface taken during fatigue tests, areas of microstructure containing crack initiation sites have been identified. Due to the difficulties of obtaining a high quality polish on the curved lining of bearings, only flat strips were used for acetate replication to assess the critical microstructure features and parameters of secondary phases causing fatigue initiation. Binary images including only Si or Sn secondary phases of these replicas were produced with a note of each individual initiation site.

The cells produced by this method have been divided into three groups according to the behaviour of the secondary phase particle in each cell.

- Initiating Cells: those cells containing a particle at which a fatigue crack initiated.

- Bordering Cells: those cells sharing a common boundary with an initiating cell (near neighbours of initiating particles).

- Background Cells: those cells neither containing nor sharing a boundary with a cell containing a fatigue crack initiation.

Figure 3-5 shows an example of Object Area (*OA*) histogram for the three groups of cells from a surface sample of AS1241 flat strip lining[3].
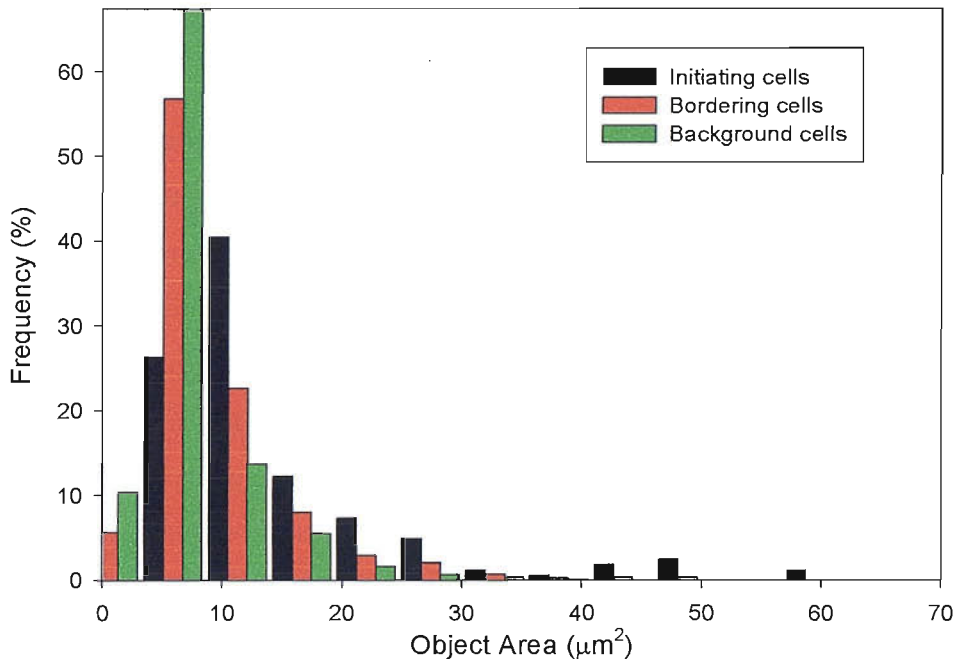
Figure 3-5     Object Area histogram for Si particles in fatigued AS1241 flat strip[3]

Histograms of other FBT parameters for Si particles in AS1241 flat strip and Sn particles in AS16 flat strip (Perp. only) could be found in Appendix D, from Figure D-4 to Figure D-10.

In this thesis, further initiation site analysis is presented on newly obtained experimental data from AS16 Para. specimen and compared with the prior analyses on AS1241 and AS16 Perp. This analysis will be presented in Section 3.6.

## 3.3   FE validation analysis

An analytical solution was found in the literature[6] for an infinite elastic plate containing an elliptical inclusion of different elastic material under constant stresses at infinity. It is shown that constant stresses will be induced in the inclusion. In this section, single particle analyses were performed with a hard inclusion and a soft inclusion in an Al matrix to establish the validity of the FE model through comparison of its predictions with exact elasticity results.

### 3.3.1 Model description

In the FE analysis of the validation problem, the infinity condition can be approximated by modelling a square plate which is significantly larger than the particle. Initially three FE models were generated in which the ratio between the length of the plate and the major axis was taken as 3, 4 and 5. All three models gave uniform stress distribution in regions away from the particle, as shown later, which indicates the selection of sizes for all three models represented satisfactorily the behaviour of the infinite plate. To have a sufficiently large model for accuracy, while retaining computational efficiency, the ratio between the length of the plate and the major axis was taken as 4. Due to the symmetry of the problem, only a quarter of the whole plate was modelled. The half-length of the plate was chosen equal to 8 mm and the major semi-axis of the elliptic particle 2 mm as shown in Figure 3-6.

For mesh selection, the convergence of the solution was examined by refining the mesh gradually. In the final FE model, each of the loaded edges of the plate has 10 divisions and the edges of the plate along the plane of symmetry have 20 divisions. The regions adjacent to the interface between the particle and surrounding matrix, where the stress and strain are of interest, were finely meshed to obtain an accurate stress distribution. Both semi-axes of the elliptical particle have 20 divisions and its perimeter has 32 divisions to generate a fine mesh within the elliptical particle and the surrounding matrix. The final chosen mesh of model is shown in Figure 3-6. The whole model is meshed with 800 8-node quadrilateral (PLANE82) elements.

For comparison purposes, both matrix and particle were assumed to behave elastically. The adopted Young's moduli of the matrix, hard particle and soft particle were 70 GNm$^{-2}$, 420 GNm$^{-2}$, and 41.4 GNm$^{-2}$ respectively. The respective Poisson's ratios were 0.33, 0.14, and 0.33.

The adopted boundary conditions are also shown in Figure 3-6. Symmetry conditions are applied to the bottom edge and the left edge of model to enable it to represent the whole plate and particle. Loading is applied via a uniform nodal traction of 1000 MPa in the $x$-direction along the right edge of plate. The top edge is assumed free. An

analysis with the top edge fixed in *y*-direction was performed but the results did not show any difference from those obtained with free top edge condition.
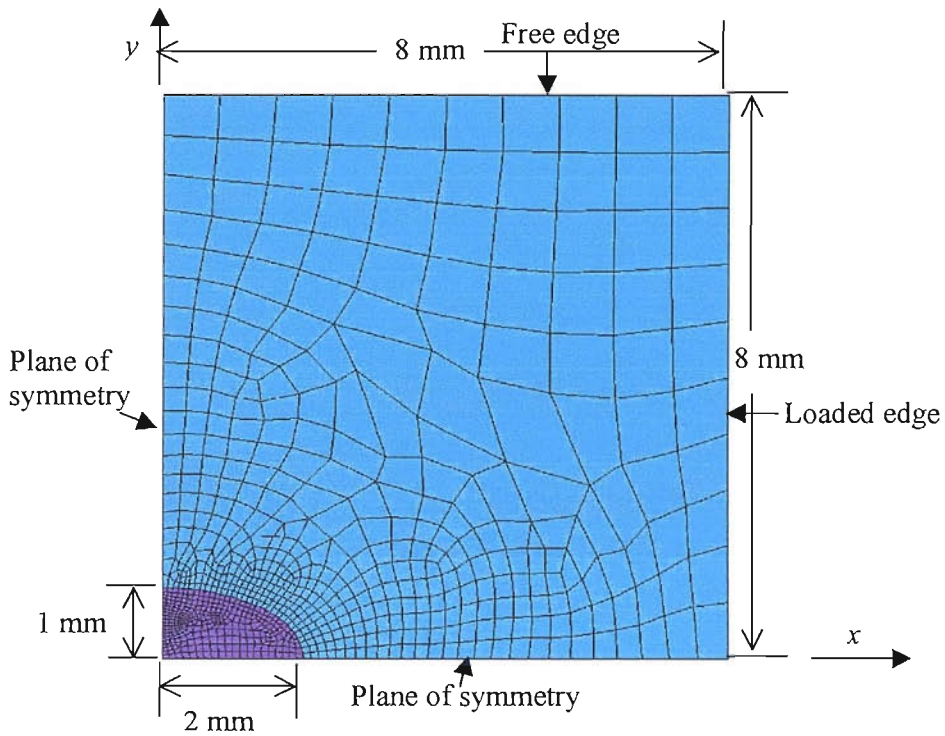


Figure 3-6    A typical mesh of single inclusion model

### 3.3.2   Hard inclusion

Results were obtained for a hard inclusion with a major semi-axis of 2 mm and a minor semi-axis *b* of 1 mm to give a ratio $c = b/a = 0.5$. Figure 3-7 shows the $\sigma_x$ distribution in both inclusion and matrix. It is noted that stresses in the inclusion are approximately uniform, which agrees with the exact analytical solution. The maximum $\sigma_x$ in the matrix was found close to the end of the major semi-axis, parallel to the tensile axis. This is also consistent with the analytical solution.
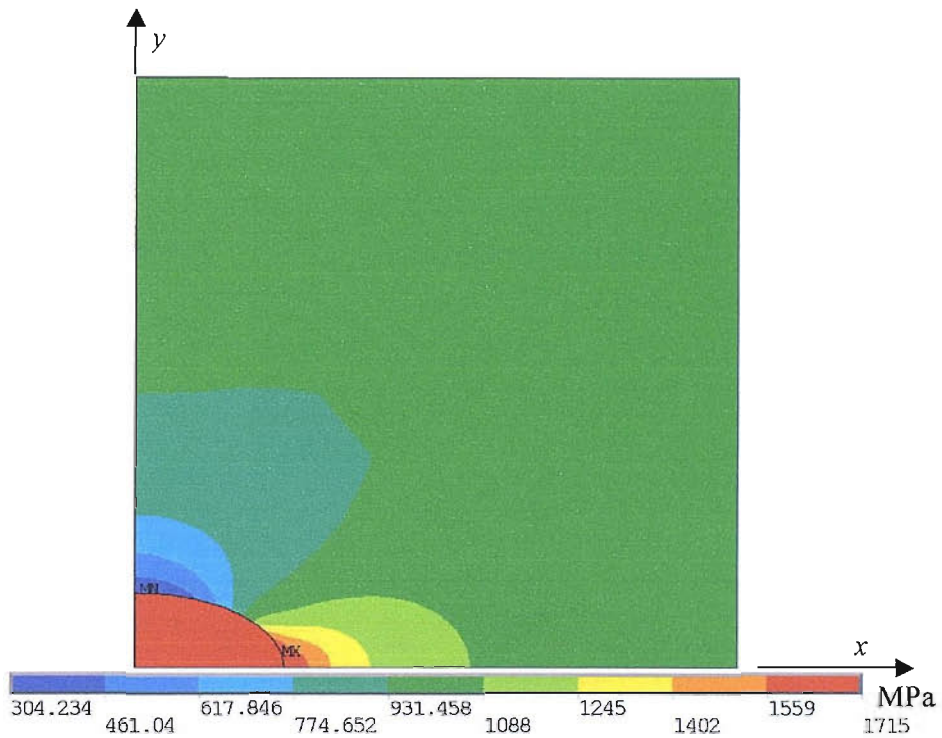
Figure 3-7    $\sigma_x$ distribution in both inclusion and matrix under uniform tension in
*x*-direction

The stresses in the matrix along its interface with the inclusion were compared with the corresponding exact theoretical results. It can be seen in Figure 3-8 that the FEM results are in good agreement with theoretical results with a maximum error of –4.02% for $\sigma_x$ at the point around 10° to tensile axis. Since a uniform mesh was used along the matrix/particle interface, it is expected that the error between FEM results and exact theoretical results could be reduced by further refining the mesh in the high stress region.
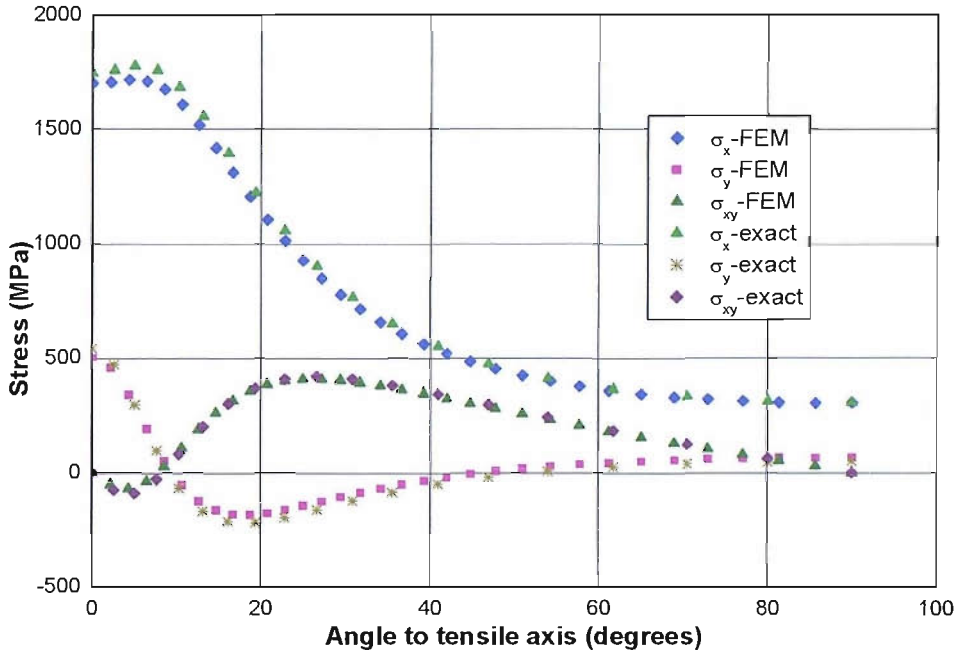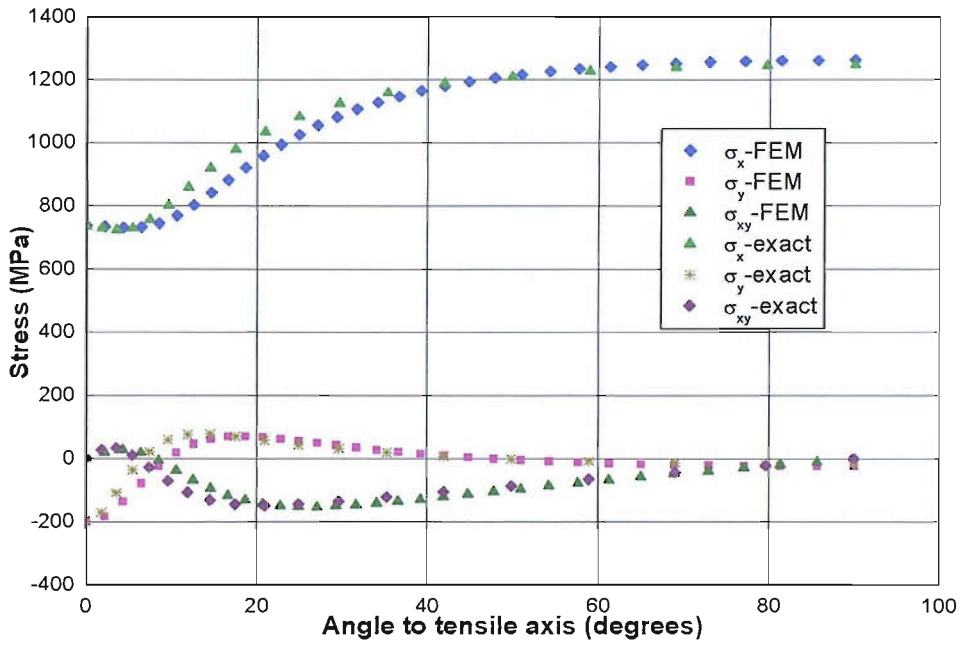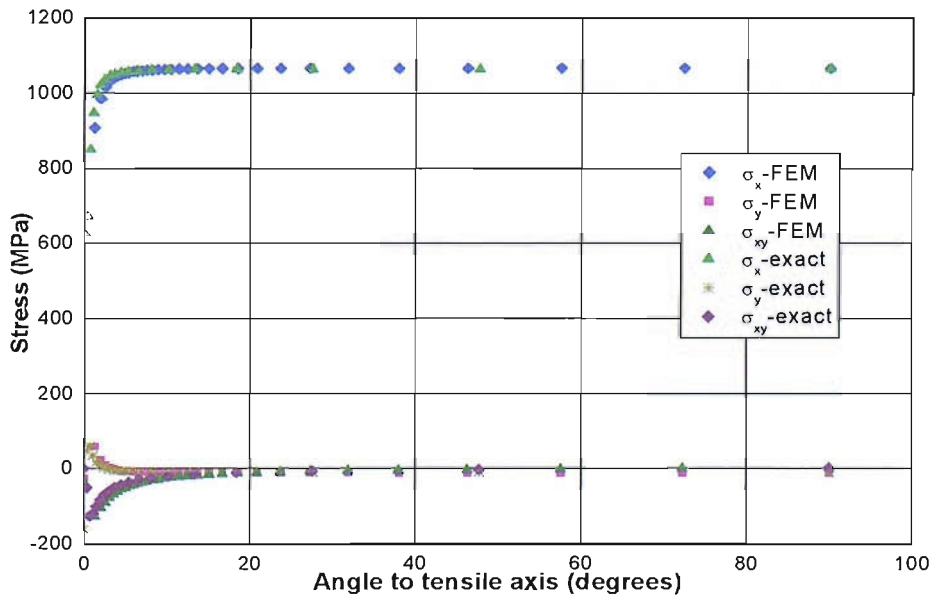
Figure 3-8    Stresses in the matrix along its interface with the hard particle from

FEM and exact solution for $c$=0.5

Figure 3-9 shows stresses for another comparison when the ratio $b/a$ equals to 0.1, obtained by assigning a value of 0.2 mm to the minor semi-axis $b$. Again, the same good agreement is achieved with a maximum error of $-7.73\%$ for $\sigma_x$. The maximum error in this case is higher than that obtained for $b/a$=0.5 since the smaller aspect ratio causes a higher stress concentration and a similar uniform mesh along the interface was adopted in both cases. A refined mesh in the high-stress region would help to reduce the error. Stress concentration and hence FE error is thus expected to be minimum in the case of circular particles.
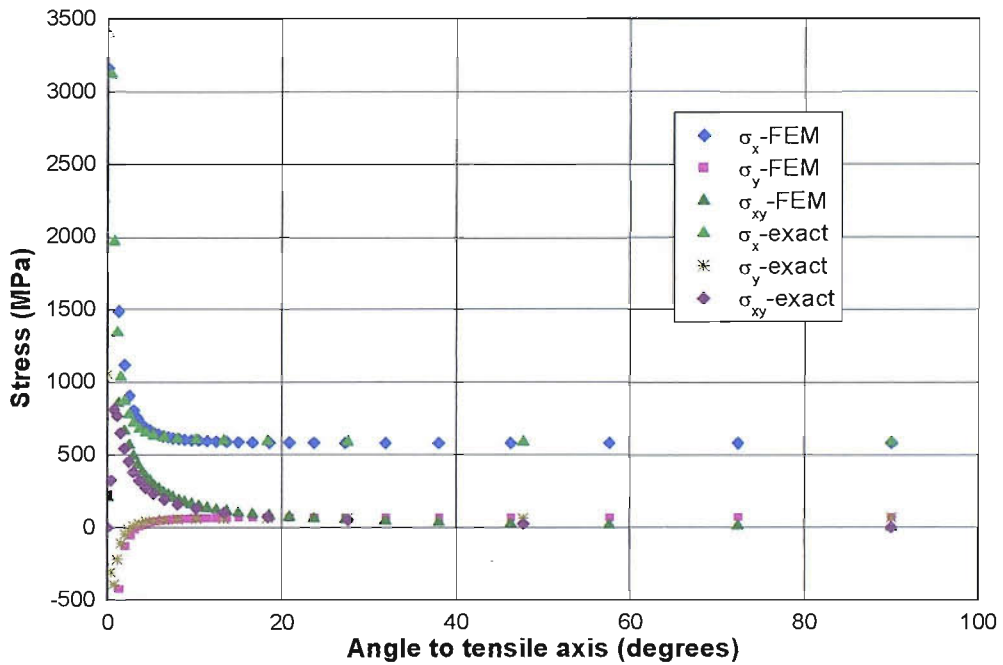
Figure 3-9    Stresses in the matrix along its interface with the hard particle from

FEM and exact solution for $c$=0.1

### 3.3.3    Soft inclusion

The same modelling approach was applied in the case of a soft inclusion and good agreement between numerical and exact solutions was obtained. The results are shown in Figure 3-10 and Figure 3-11 for $c$=0.5 and $c$=0.1, respectively.

Figure 3-10    Stresses in the matrix along its interface with the soft particle from

FEM and exact solution for *c*=0.5



Figure 3-11    Stresses in the matrix along its interface with the soft particle from

FEM and exact solution for *c*=0.1

731.005      849.069      967.133      1085      1203     MPa
     790.037      908.101      1026      1144      1262
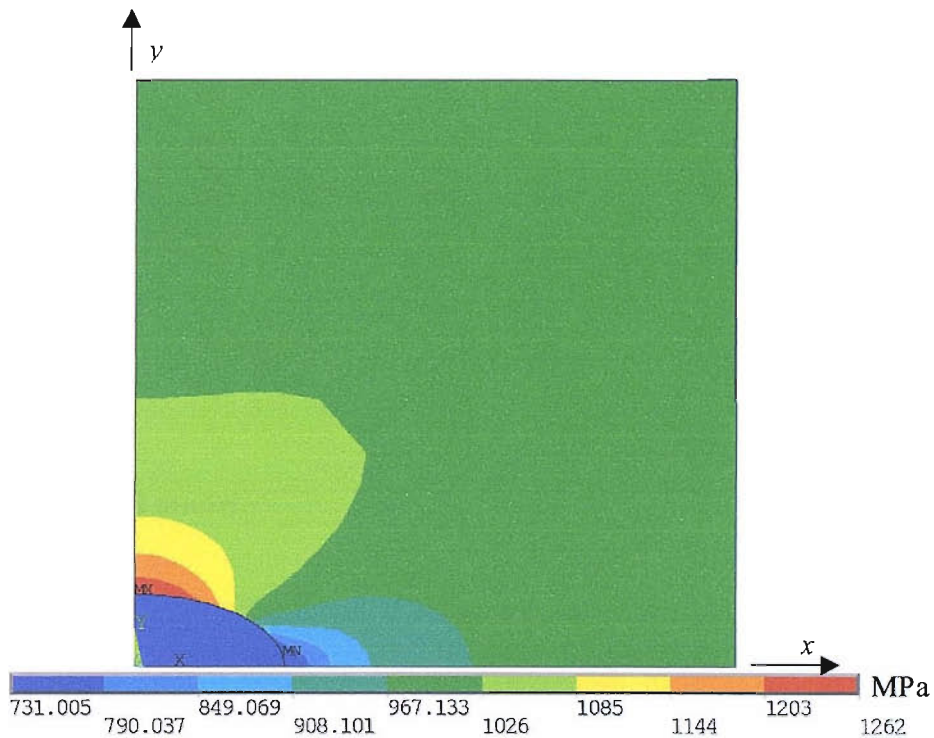
Figure 3-12     $\sigma_x$ distribution in both inclusion and matrix under uniform tension in
$x$-direction

In contrast to the hard inclusion model, Figure 3-12 shows that the maximum $\sigma_x$ in the matrix is at the end of minor semi-axis perpendicular to the tensile axis. As expected, a soft inclusion has an effect similar to that of a hole.

## 3.4 Multi-particle analysis

The elastic analysis of a single particle gives a degree of confidence in the performance of the FE microstructure model beyond the elastic limit. For most of the loading range during fatigue bending tests, the lining undergoes elasto-plastic deformation. For this reason, elasto-plastic material properties were used for matrix and soft inclusions in the FE microstructure model. A 2D embedded cell model was used in this analysis to simulate a group of particles of the whole microstructure. Before the FE analysis of the real microstructure was performed, FE models of regular particle patterns were developed to investigate the effect of certain critical

geometric parameters on stresses and strains used in initiation criteria. Convergence tests were performed to select a minimum representative number of particles in this regular particle pattern using an ANSYS program which automatically expands the pattern through a parameter controlling the number of layers. This model was eventually applied to provide information on how possible initiation parameters, i.e. the maximum hydrostatic stress and the maximum plastic shear strain, are affected by variation of geometric parameters of a real microstructure.

### 3.4.1 Embedded cell model

Following a similar methodology to that of Dong *et al*[10], a 2D embedded cell model with a multi-particle pattern within a cell was developed to represent part of the lining's stretched surface so that a reasonable representation of the local microstructure effect on initiation could be obtained without excessive computational effort. The basic assumptions on which this model have been presented in Section 1.3.4. A typical embedded cell model is shown schematically in Figure 1-6. The core region containing the secondary phase particles is surrounded by a considerably larger region to provide appropriate constraint. In the present application of this model, the core region is circular with radius $D$ and the surrounding region is a square with side length $L$. The ratio $L/D$=5 was adopted. In order to simulate the lining material response, the core region was modelled as an elasto-plastic material with properties close to those of the matrix of the lining, while the larger surrounding region was modelled as an elasto-plastic material representing the aggregate mechanical behaviour of the lining.

### 3.4.2 Material properties

In the microstructure modelling of the AS1241 flat strip lining, the surrounding region was modelled using the $\sigma$-$\varepsilon$ curve for AS1241 flat strip lining obtained from hardness data through material characterisation analysis as shown in Figure 2-50. The core region should have the properties of the matrix of the AS1241 flat strip lining, which can be considered as an Al-Sn alloy. Removing the Si content from the AS1241

lining, the nominal composition of its Al-Sn matrix becomes 87.5% Al and 12.5% Sn, which is comparable to the composition of AS16 lining (80% Al and 20% Sn). The $\sigma$-$\varepsilon$ curve of AS16 flat strip lining, shown in Figure 2-50, which was obtained from hardness data through material characterisation analysis, was therefore adopted to model the core region. It is understood that the actual matrix would be slightly harder but this is not expected to have a significant qualitative effect on the results. The Young's moduli of both AS1241 and AS16 were taken equal to 70 GNm$^{-2}$, and the Poisson's ratios equal to 0.33. Si is a brittle material and it is assumed that its fracture limit is not reached at maximum applied load. The Si particle in the AS1241 model was therefore assumed to be elastic with a Young's modulus of 112 GNm$^{-2}$ and the Poisson's ratio is 0.28[11].

For the modelling of the AS16 lining, the $\sigma$-$\varepsilon$ curve of AS16 flat strip lining obtained by material characterisation analysis was used to model the surrounding region. The matrix of AS16 lining is mainly Al, it may be considered similar to a supplied Al/Mn 3003 alloy. Therefore the $\sigma$-$\varepsilon$ curve of that alloy obtained from tensile tests[1] was used to model the core region. Its Young's modulus was taken equal to 70 GNm$^{-2}$, and its Poisson's ratio equal to 0.33. Tensile tests[1] were also performed on pure Sn specimens provided by sponsoring company. The obtained $\sigma$-$\varepsilon$ curve was used to model the elasto-plastic response of Sn particles in the AS16 model. The Young's modulus and Poisson's ratio of Sn were taken equal to 40.4 GNm$^{-2}$ and 0.3, respectively. The $\sigma$-$\varepsilon$ curves of Si, Sn, and Al/Mn 3003 alloy are shown in Figure 3-13.
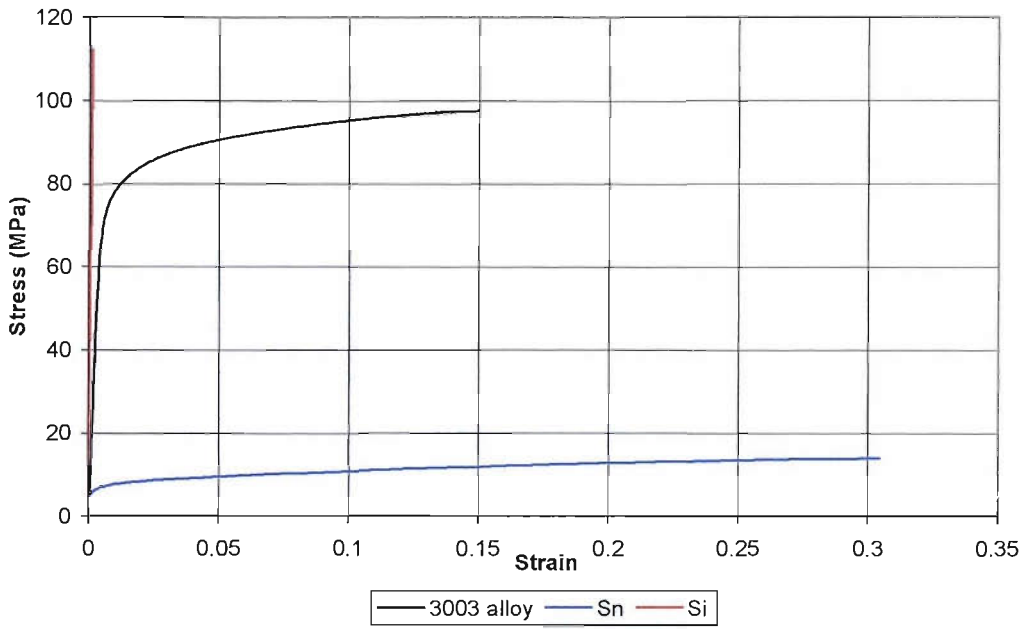
Figure 3-13    σ-ε curves used in multi-particle models

### 3.4.3    Hexagonal pattern

### 3.4.3.1    Model description

Initially a regular hexagonal pattern of constant-diameter particles was generated. The adopted scheme and its tessellation are shown in Figure 3-14.
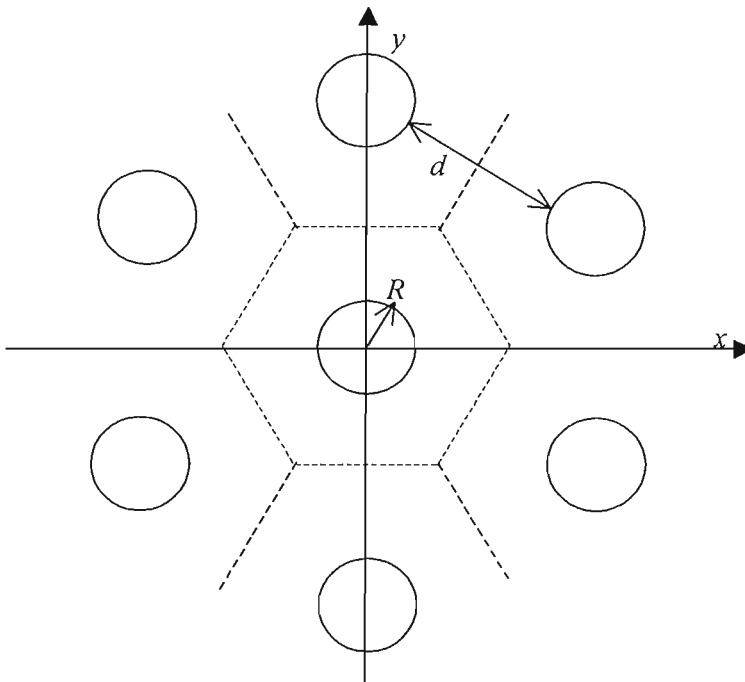


Figure 3-14    Scheme of hexagonal pattern

118

The size of each particle is controlled by its radius $R$. The distance between two particles $d$ is constant and thus equals both nearest ($d_{min}$) and mean near neighbour ($d_{mean}$) distances among the tessellation parameters. The parameter local area fraction ($LAF$) defined in the tessellation program can also be easily obtained. The following relation between the three parameters exists:

$$LAF = 0.9069 \left( \frac{1}{1 + \dfrac{d}{2R}} \right)^2 \qquad (3.1)$$

It can be seen that if the particle size is kept constant, $LAF$ will increase when $d$ decreases. It is very important to consider the interdependence of these values because an effect which may be attributed to the variation of one may actually be due to the variation of the other. The present parametric study allows the investigation of the effect of those geometric parameters of the microstructure on critical stresses and strains associated with initiation behaviour.

Since the hexagonal pattern model simulates a global periodical microstructure, the stress and strain around each particle should be the same under far field uniform load. It is important to ensure that this requirement is satisfied by the results of the embedded cell model. It is sufficient to show that a group of particles in the central part of the core region have and are surrounded by almost identical stress and strain distribution. A sensitivity analysis was performed to determine the minimum number of particles to be modelled in the core region so that the central particle could be accepted as a representative particle of the whole domain and the size of FEM model could be limited. A control parameter was used in the ANSYS program to generate easily models with different number of particles. The scheme for increasing particles number is illustrated in Figure 3-15. Starting from a single central particle, the model is gradually expanded with one more layer of hexagonal pattern of particles added to the previous model. For each model, the stresses in the core region, around the central particle are calculated. These stresses are compared with those of the nearest two particles (Cp1 and Cp2).
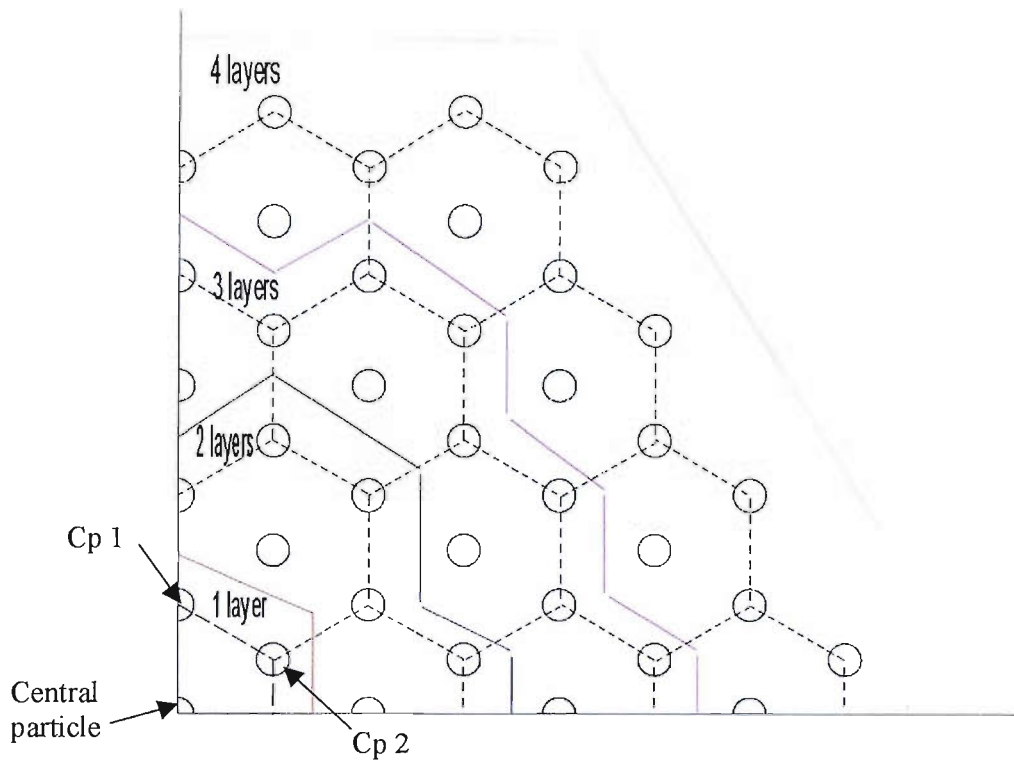
Figure 3-15     Scheme of expanding particles pattern by adding layers

### 3.4.3.2   Sensitivity tests

Due to symmetry, only one quarter of the adopted hexagonal pattern needs to be modelled as indicated in Figure 3-15. Figure 3-16 gives an example of mesh and boundary conditions for a typical model. The whole model is a square with dimensions 500 μm×500 μm. The core region has a radius of 100 μm.

Free edge

Plane of
symmetry

Loaded
edge

Plane of symmetry
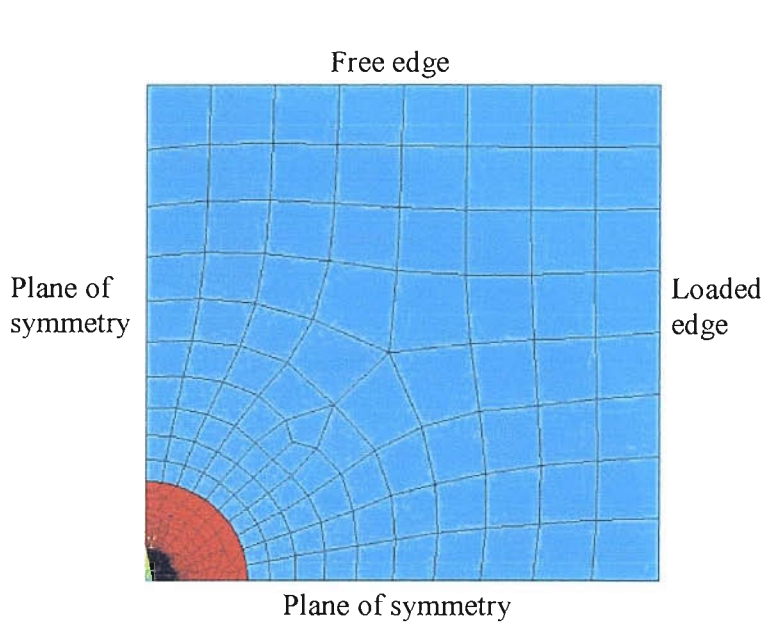
Figure 3-16    Whole model and boundary conditions

All regions are modelled using PLANE82 element. In this typical model corresponding to two layers of hexagonal pattern (Figure 3-15) the embedding region contains 105 elements. The core region contains 3278 elements. Refinement was performed along the periphery of each particle and in total 704 elements were used to simulate all particles in this model. Enlarged plots of the mesh in the core region and its central part containing the particles are shown in Figure 3-17 and Figure 3-18 respectively. Monotonic loading was applied via a uniform nodal displacement with a maximum value of 1 μm, which is equivalent to a total strain of 0.2%.
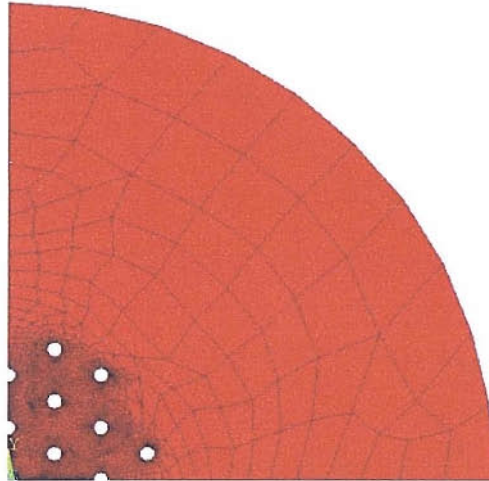
Figure 3-17    Mesh in the core region
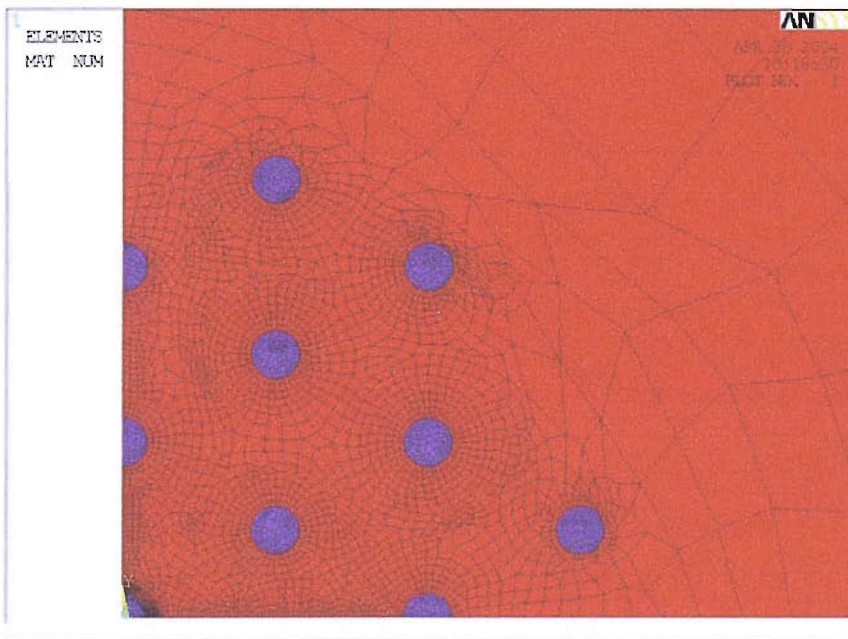


Figure 3-18    Enlarged view of the mesh in central part of the core region

Figure 3-19 to Figure 3-21 show the stress results in the matrix for comparison while increasing particle number for the AS1241 lining model. It should be noted that in all these models the number of particles quoted is the total number accounting for the symmetry condition.
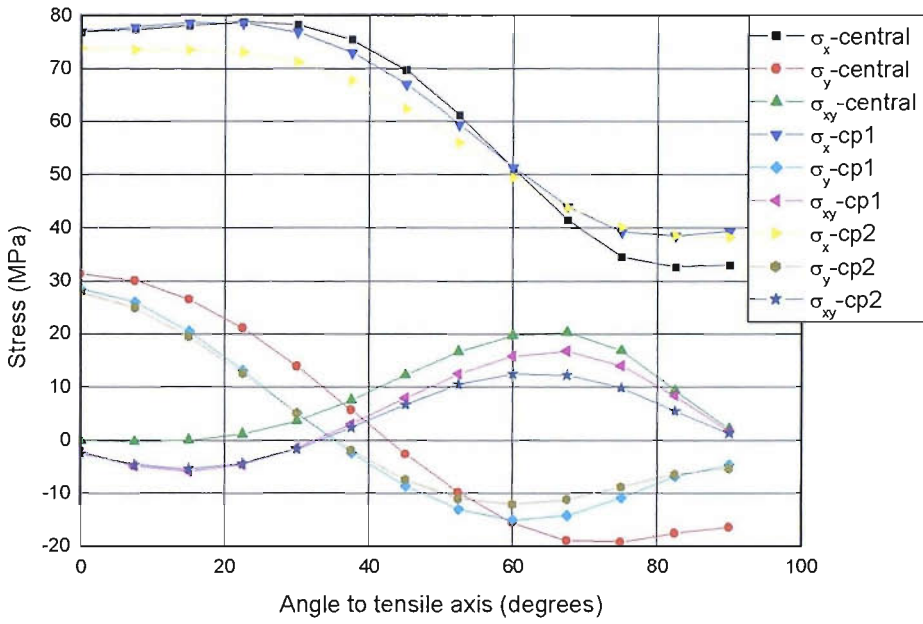
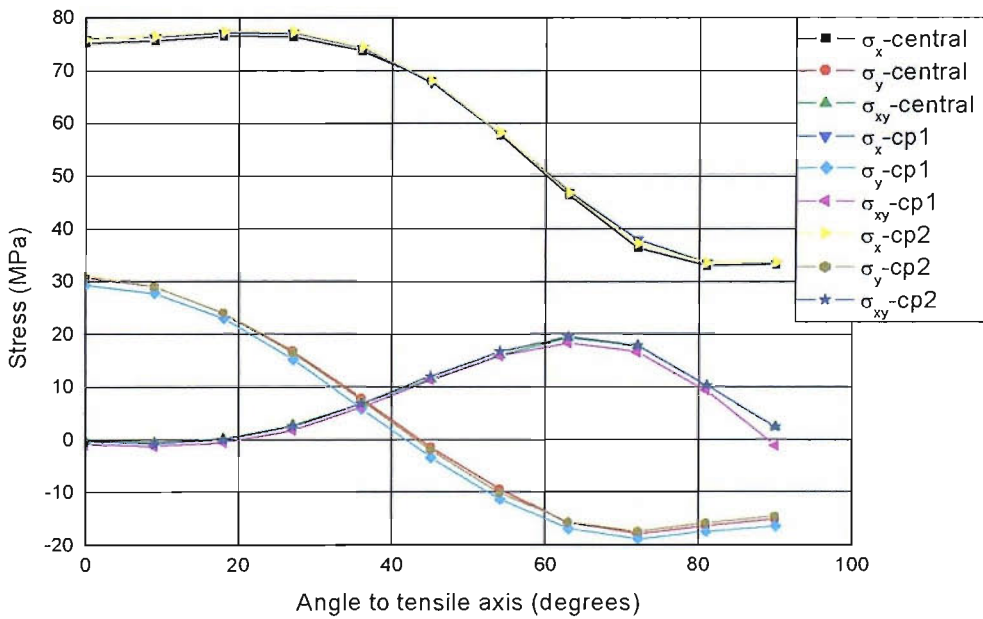Figure 3-19    Stress comparison for one layer particles model (7 particles)



Figure 3-20    Stress comparison for two layers particles model (31 particles)
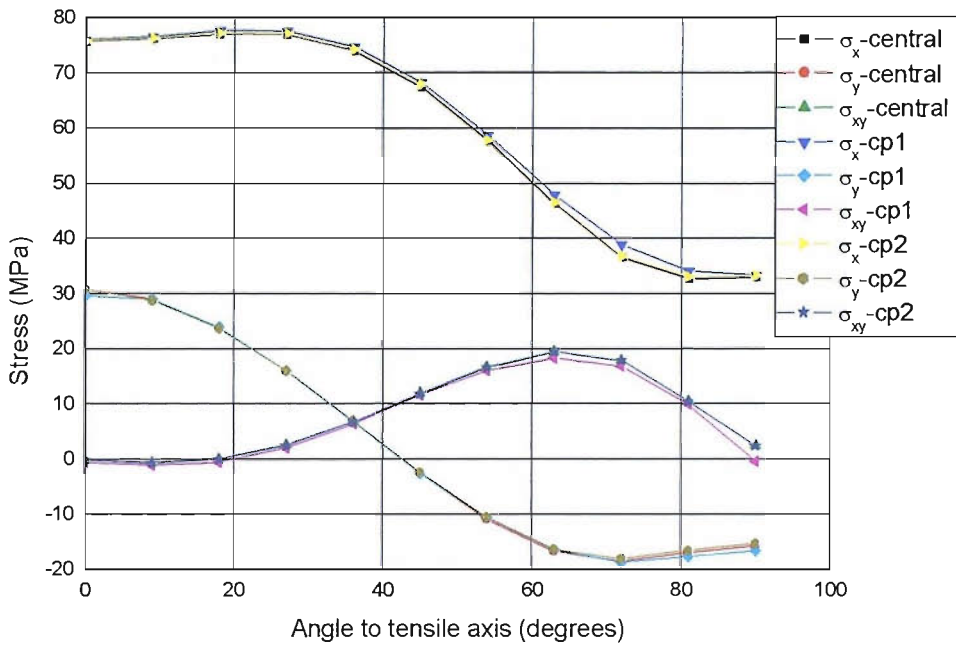
Figure 3-21    Stress comparison for three layer particles model (73 particles)

It can be seen that when the number of modelled particles is more than 31, that is, the particle pattern consists of at least two layers, good agreement is obtained between stresses around the central particle and the nearest two particles. This indicates that the solution around the central particle gives a good representation of the stress distribution around any particle in this multi-particle model. Increasing further the number of particles in FE modelling could increase only slightly the accuracy of calculated stress as shown in Figure 3-21. Considering the computation time, it was decided that a two layer multi-particle model with 31 particles provides sufficient accuracy for further investigation on the effects of microstructural parameters.

Figure 3-22 gives a comparison of the stress development surrounding the central particle for models with different layers. A quick convergence of results could be seen for models with more than two layers. This gives further confidence in the two-layer multi-particle model.
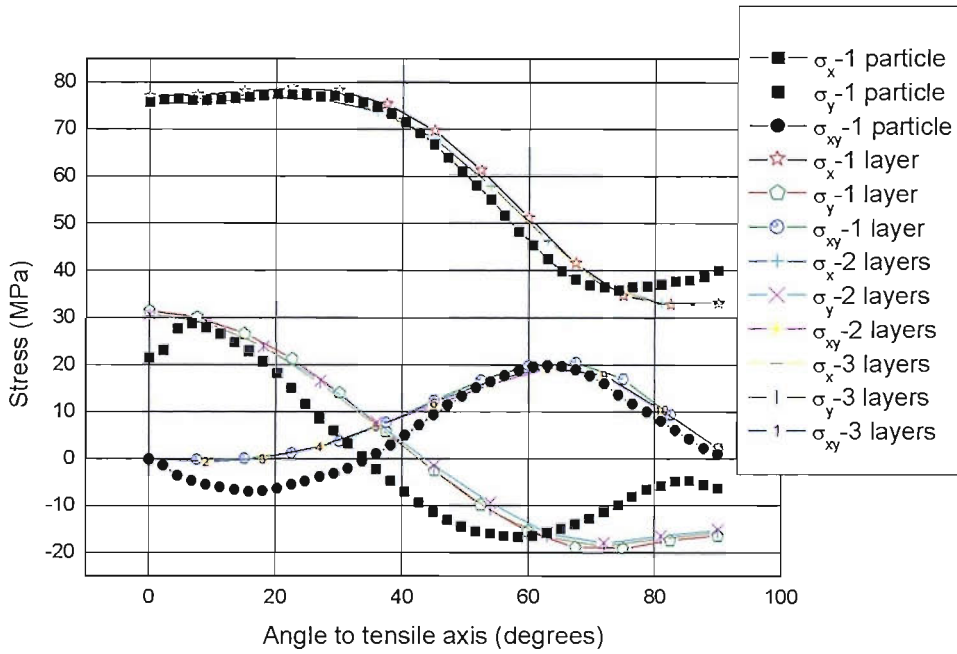
Figure 3-22    Stresses around central particle for models with different layers

### 3.4.4    Effect of microstructure parameters

From the sensitivity test presented in the previous section, it was seen that a two-layer multi-particle embedded cell model gives a good representation of stress and strain distribution around and within a particle in a hexagonal-pattern microstructure. The ultimate purpose of this modelling was to investigate the variation of the maximum plastic shear strain and maximum hydrostatic stress surrounding the central particle in embedded cell models when the particle size or distance changes. This may give an understanding of critical parameter ranges for fatigue crack initiation in a real microstructure.

As pointed out in Section 3.4.3.1, in the regular hexagonal pattern, both $d_{min}$ and $d_{mean}$ are the same equalling the distance $d$ between any two particles. $OA$ is determined from the radius $R$ and $LAF$ can be calculated from (3.1). Thus, varying $d$ and $R$ in the FEM program, it is possible to investigate the effect of tessellation parameters $d_{min}$, $d_{mean}$ and $LAF$. Since $CA$ is related to $OA$ and $LAF$, its effect would be related to that

125

of *OA* and *LAF*. Tessellation parameters *OAspRat*, *OAng*, *CAspRat*, *CAng*, will not be investigated here since their variation requires patterns of ellipses rather than the circular particle shape adopted at this stage. For the investigation of *No. NNs*, a number of alternative regular particle patterns needs to be considered.

### 3.4.4.1 AS1241 lining

To achieve the most meaningful results, the AS1241 lining model uses similar ranges of dimensions as the real microstructure. Useful tessellation data for Si particles in the AS1241 flat strip lining[3] are listed in Table 3–1. The respective histograms can be found in Figure 3-4, D-1, D-2 and D-3.

**Table 3–1 Some tessellation data for Si particles in the lining of AS1241 flat strip lining**

| | $OA$ ($\mu m^2$) | $LAF$ (%) | $d_{min}$ ($\mu m$) | $d_{mean}$ ($\mu m$) |
|---|---|---|---|---|
| Mean value | 7.20 | 7.63 | 2.23 | 8.05 |
| Standard deviation | 6.08 | 5.69 | 2.10 | 3.32 |
| Significant range | 1.12-13.28 | 1.94-13.32 | 0.13-4.33 | 2.73-11.37 |

In this parametric study, the particle radius varies from 0.75 $\mu m$ to 2 $\mu m$ with a mean value of 1.375 $\mu m$ corresponding to particle area range from 1.77 $\mu m^2$ to 12.57 $\mu m^2$ with a mean value of 7.16 $\mu m^2$.

This model is the same as that adopted for the sensitivity study described in Section 3.4.3.2. The mesh of the original two-layer, 31-particle model was further refined with regular shape elements around the central particle as shown in Figure 3-23. The elasto-plastic material inputs for AS1241 and AS16 have been given in Figure 2-50. Again a monotonic load is applied via a uniform nodal displacement reaching the maximum value of 1 $\mu m$, which is equivalent to a total strain of 0.2%.
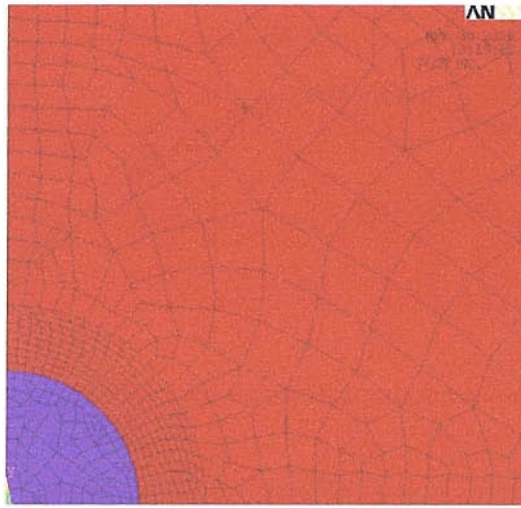
Figure 3-23    Refined mesh surrounding central particle

For a given particle radius, $d$ is varied from 1 µm to 18 µm to give a range of *LAF* between approximately 2% and 40%. Contour plots indicated that both maximum plastic shear strain and hydrostatic stress attain their maximum values at the particle-matrix interfaces. Thus, for each combination of *LAF*, $d$ and $R$ values, the variation of these two variables in the Al-Sn matrix along the periphery of the central Si particle is examined and their maximum values recorded. The results are given in Figure 3-24 and Figure 3-25.
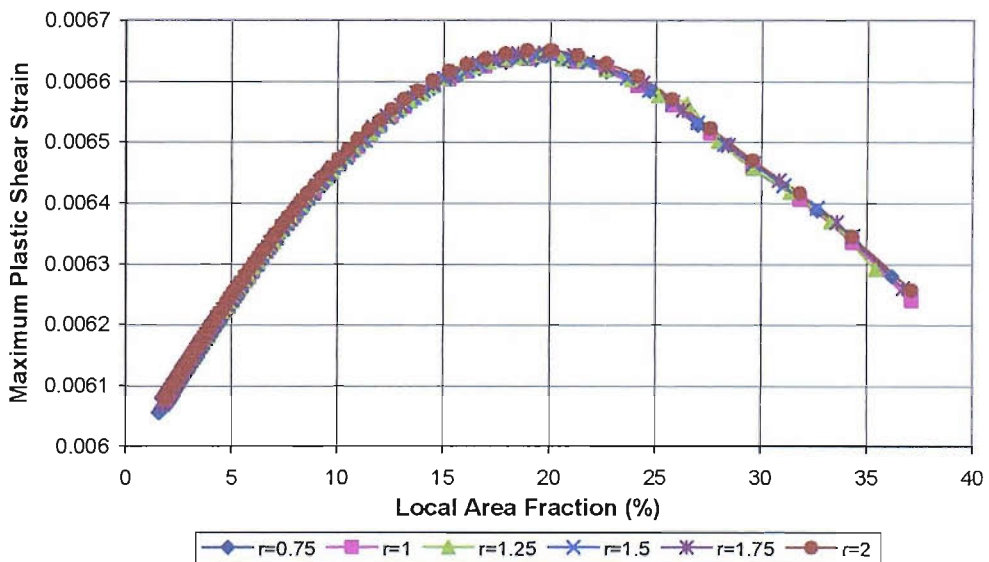


Figure 3-24    Maximum plastic shear strain on the periphery of the central Si particle versus *LAF*

127
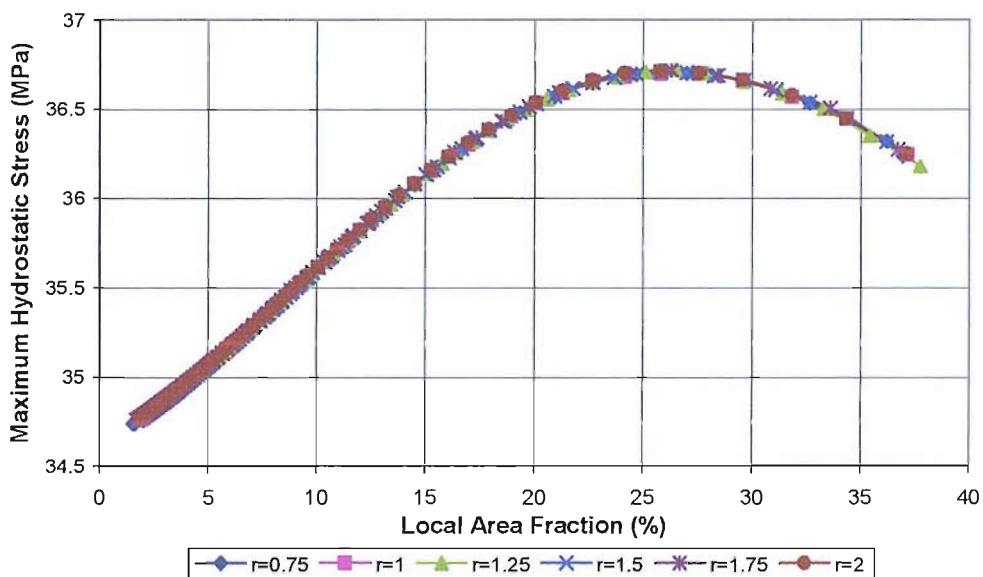
Figure 3-25     Maximum hydrostatic stress on the periphery of the central Si particle

versus *LAF*

In Figure 3-24, it could be seen that maximum plastic shear strain increases with *LAF* (increasing particle density) for the range between approximately 1.8% and 20%, then decreases. A similar trend is observed in Figure 3-25 for maximum hydrostatic stress with a transition point of 25% of *LAF*. Within the significant range of *LAF* (between 1.94% and 13.32%) of real microstructure (see Table 3–1), both maximum plastic shear strain and maximum hydrostatic stress increase with *LAF*. It is also noted that the particle size has very little effect on both these relations. The FEM results indicate that microstructures with high *LAF* (up to 20%) are more likely to initiate fatigue failure. The frequency histogram of *LAF* of Si particles in AS1241 flat strip lining for initiating cells, bordering cells and background cells, shown in Figure D-4, suggests the same trend, that is, a higher possibility of initiation for higher *LAF*. There is, therefore, qualitative agreement between FBT and FEM results.

The FEM results of maximum plastic shear strain versus *d* and maximum hydrostatic stress versus *d* are given in Figure 3-26 and Figure 3-27.
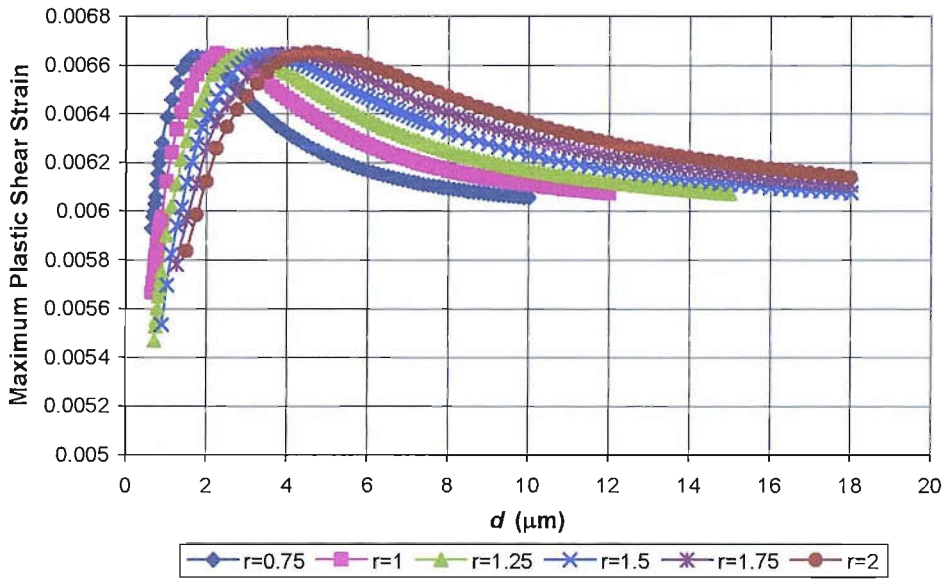
Figure 3-26    Maximum plastic shear strain on the periphery of the central Si particle versus $d$
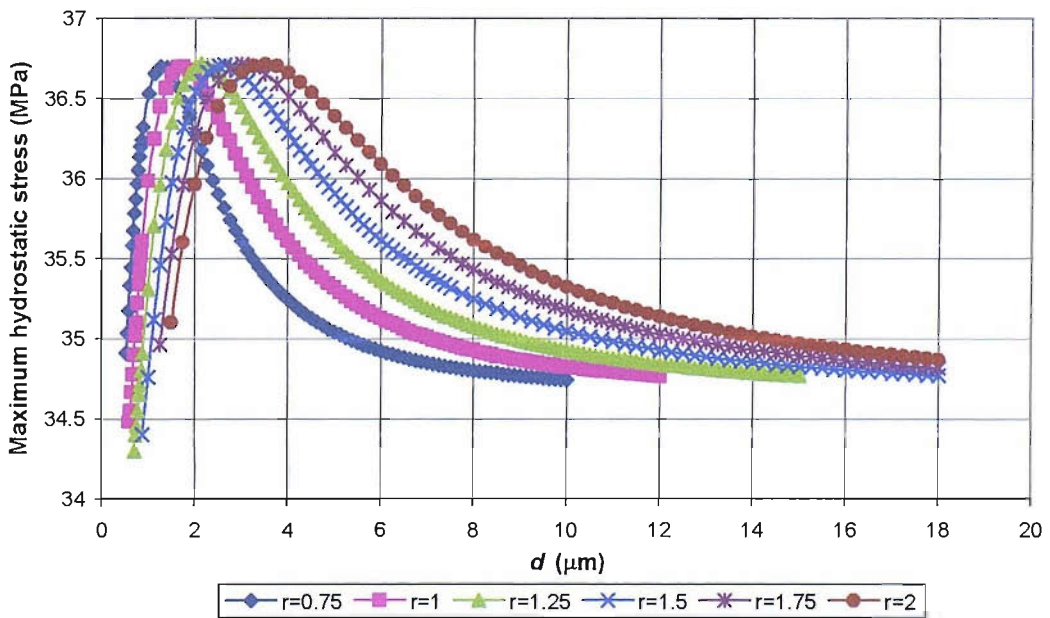


Figure 3-27    Maximum hydrostatic stress on the periphery of the central Si particle versus $d$

From these figures, it can be seen that both the maximum plastic shear strain and maximum hydrostatic stress rise over a lower range of $d$ and then fall over a higher

range. The transition point between these ranges depends on the particle size. Since $d_{min}$ equals $d_{mean}$ in the regular hexagonal pattern, $d$ could represent either $d_{min}$ or $d_{mean}$. $d_{min}$ in the real microstructure has a significant range between 0.46 μm and 3.29 μm (see Table 3–1 and Figure D-2), which predominantly lies within the range of $d$ for which maximum plastic shear strain and maximum hydrostatic stress rise. This indicates that increasing $d$ increases the likelihood of initiation, which is consistent with the observation from the FBT frequency histogram of $d_{min}$ of Figure D-5, which shows that a higher percentage of initiating cells than background cells for increasing $d_{min}$.

However, this consistency between FEM and tessellation results is not apparent when $d$ is considered as $d_{mean}$. The significant range of $d_{mean}$ (see Table 3–1 and Figure D-3) in real microstructure covers both rising and falling ranges of FEM results shown in Figure 3-27. The tessellation results, shown in Figure D-6, indicate a higher percentage of initiating cells at higher $d_{mean}$. This trend cannot be verified by the FEM results.

FEM analysis appears to suggest that $d_{min}$ is more critical for initiation than $d_{mean}$. The validity of this conclusion depends on the reliability of the adopted initiation criteria.

### 3.4.4.2 AS16 lining

The same embedded cell model as for AS1241 lining with a two-layer hexagonal particle pattern was adopted for AS16 lining. For materials with a soft inclusion, the initiation might happen in the inclusions or in the matrix. Therefore the maximum plastic shear strain and maximum hydrostatic stress in both Sn and surrounding matrix along their interface are examined.

As with the AS1241 lining model, the AS16 lining model uses dimensions consistent to those observed in the real microstructure. Tessellation analysis for Sn particles in AS16 flat strip lining provided the statistical data listed in Table 3–2.

**Table 3–2 Some tessellation data for Sn particles in the lining of AS16 flat strip lining**

|  | $OA$ ($\mu m^2$) | $LAF$ (%) | $d_{min}$ ($\mu m$) | $d_{mean}$ ($\mu m$) |
|---|---|---|---|---|
| Mean value | 92.43 | 12.70 | 5.14 | 19.05 |
| Standard deviation | 82.25 | 7.78 | 4.67 | 10.61 |
| Significant range | 10.18-174.68 | 4.92-20.48 | 0.47-9.81 | 8.44-29.66 |

It can be seen that the Sn particles in AS16 lining are considerably larger than the Si particles in AS1241 lining. Thus the Sn particle radius in the AS16 lining model varied from 5 $\mu m$ to 6 $\mu m$ with a mean value of 5.5 $\mu m$ corresponding to a mean object area of 96.24 $\mu m^2$. Consequently, the radius of core region $R$ was changed to 300 $\mu m$, with the side length $L$ of the whole embedding region becoming 1.5 mm. A monotonic load was applied via a uniform nodal displacement reaching a maximum value of 3 $\mu m$, which is equivalent to a total strain of 0.2%.

For a given particle radius, $d$ is varied from 3 $\mu m$ to 50 $\mu m$ to give a range of $LAF$ between approximately 3% and 54%. For each combination of $LAF$, $d$ and $R$ values, the maximum plastic shear strain and maximum hydrostatic stress in the Sn particles and the surrounding matrix on the periphery of the central Sn particle are recorded. The results are given in Figure 3-28 to Figure 3-31.
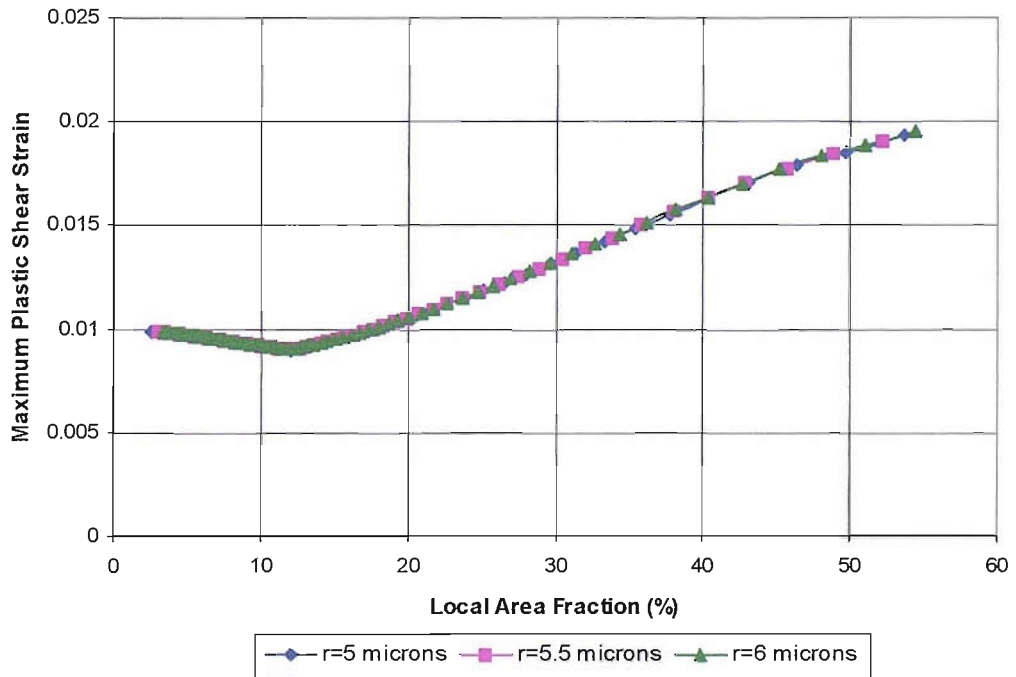
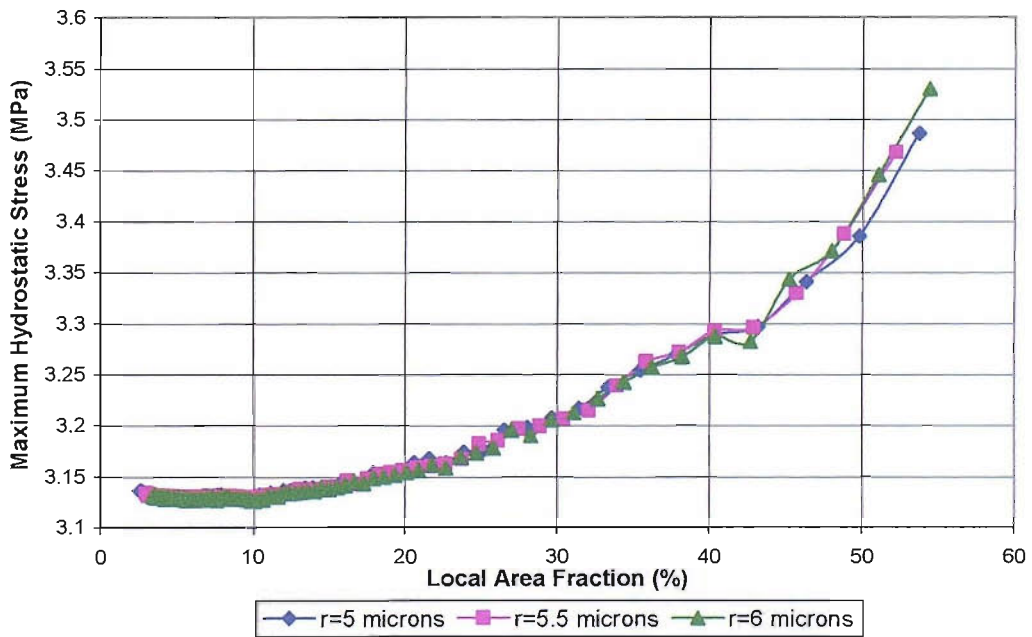Figure 3-28    Maximum plastic shear strain in central Sn particle versus *LAF*



Figure 3-29    Maximum hydrostatic stress in central Sn particle versus *LAF*
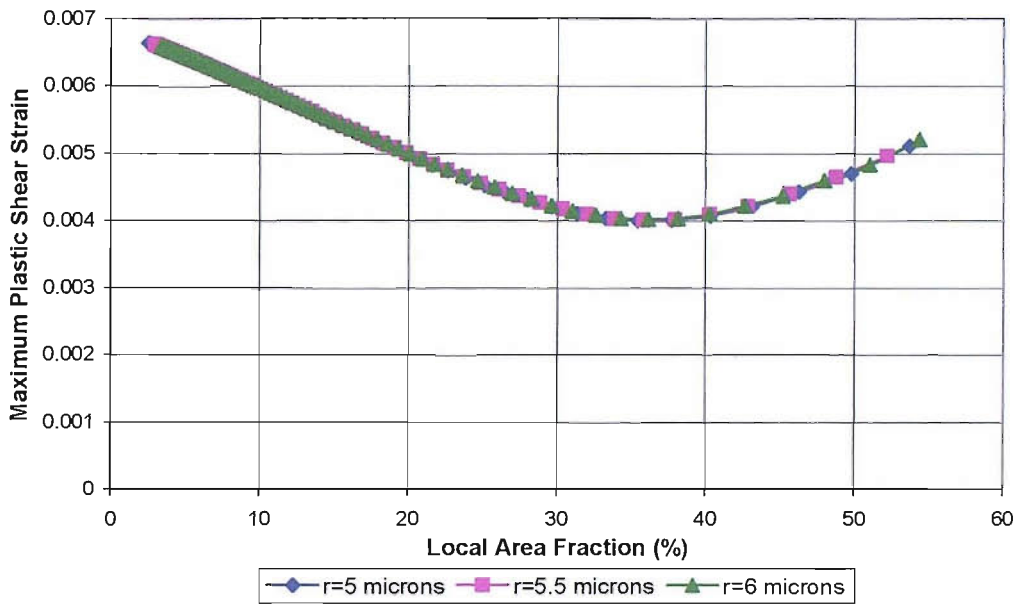
Figure 3-30    Maximum plastic shear strain in Al matrix on the periphery of the central
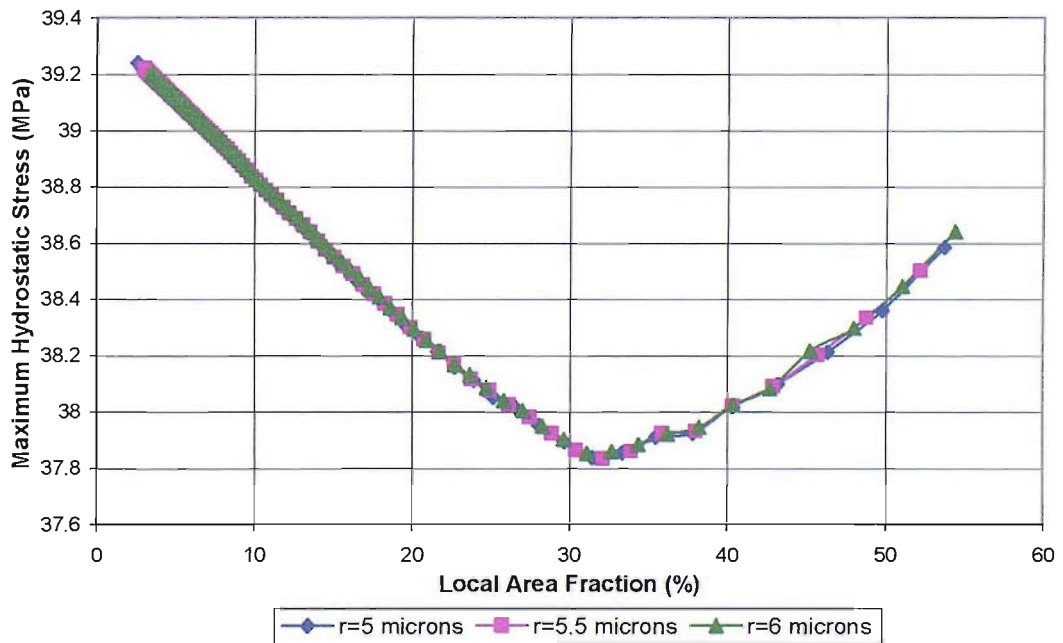
Sn particle versus *LAF*



Figure 3-31    Maximum hydrostatic stress in Al matrix on the periphery of the central

Sn particle versus *LAF*

From Figure 3-28, it can be seen that the maximum plastic shear strain in Sn drops slightly as *LAF* increases up to a limit of 12% and then increases. Since the mean *LAF* value in real microstructure is 12.7%, the results for the maximum plastic shear strain do not lead to an unambiguous conclusion regarding its effect on initiation.

The maximum hydrostatic stress in Sn, as shown in Figure 3-29, increases over the whole range of *LAF* tested. This indicates that initiation becomes most likely in Sn particles for higher *LAF* with the hydrostatic pressure as the critical factor.

Both the maximum plastic shear strain and maximum hydrostatic stress in the Al matrix are falling over a lower range of *LAF* and rising over a higher range as shown in Figure 3-30 and Figure 3-31 with a transition *LAF* value of around 32%. Over the significant *LAF* range in the real microstructure (Table 3–2), the likelihood of initiation is therefore falling with increasing *LAF*. The particle size is found to have very little effect on the relations between possible initiation parameters and *LAF*. The *LAF* histogram for Sn particles in fatigued AS16 flat strip lining shown in Figure D-8 suggests that higher percentage of initiating cells than background cells for increasing *LAF*. For the FEM results to agree with the tessellation results, the initiation should therefore occur in the Sn particles. FEM results in Al also indicate a *LAF* transition value above which the likelihood of initiation increases. As Figure D-8 shows, the very small proportion of *LAF* values lying within that range is associated with initiating particles.

The FEM results for the maximum plastic shear strain versus *d* and the maximum hydrostatic stress versus *d* for Sn particle and Al matrix are given in Figure 3-32 to Figure 3-35.
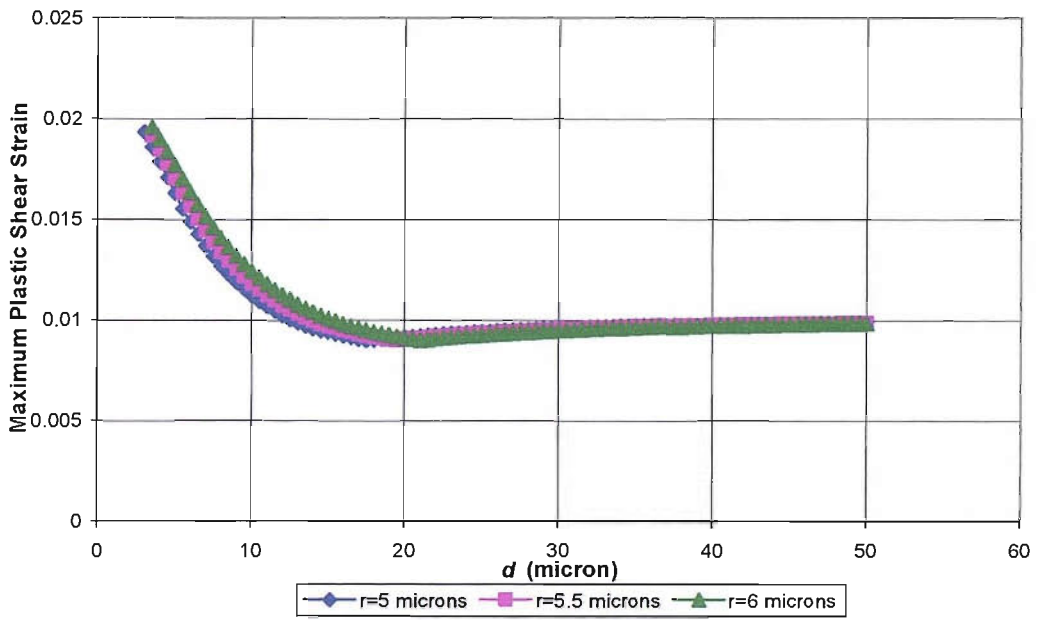
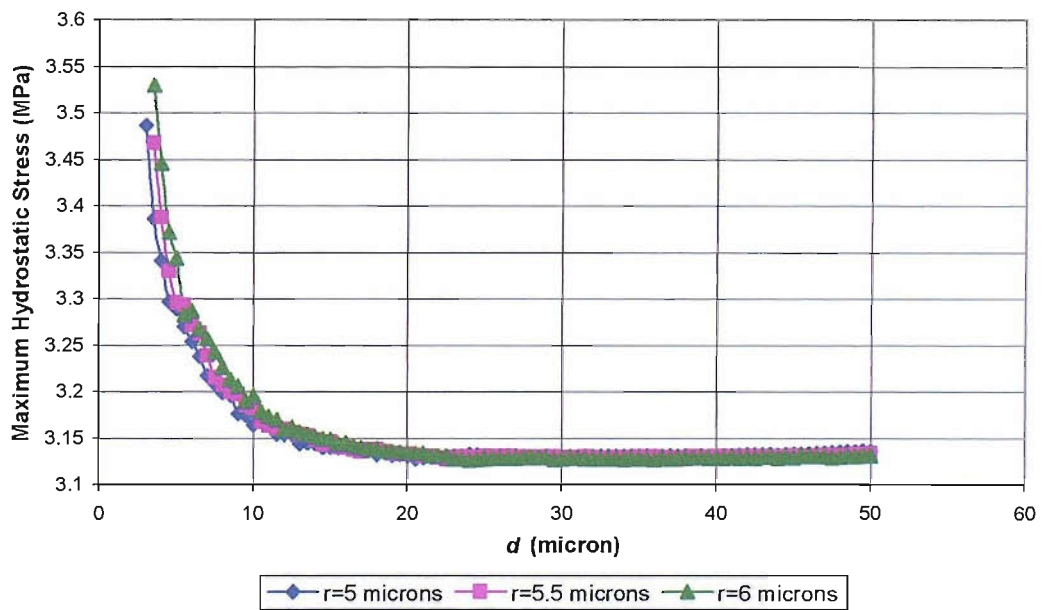Figure 3-32      Maximum plastic shear strain in central Sn particle versus *d*



Figure 3-33      Maximum hydrostatic stress in central Sn particle versus *d*
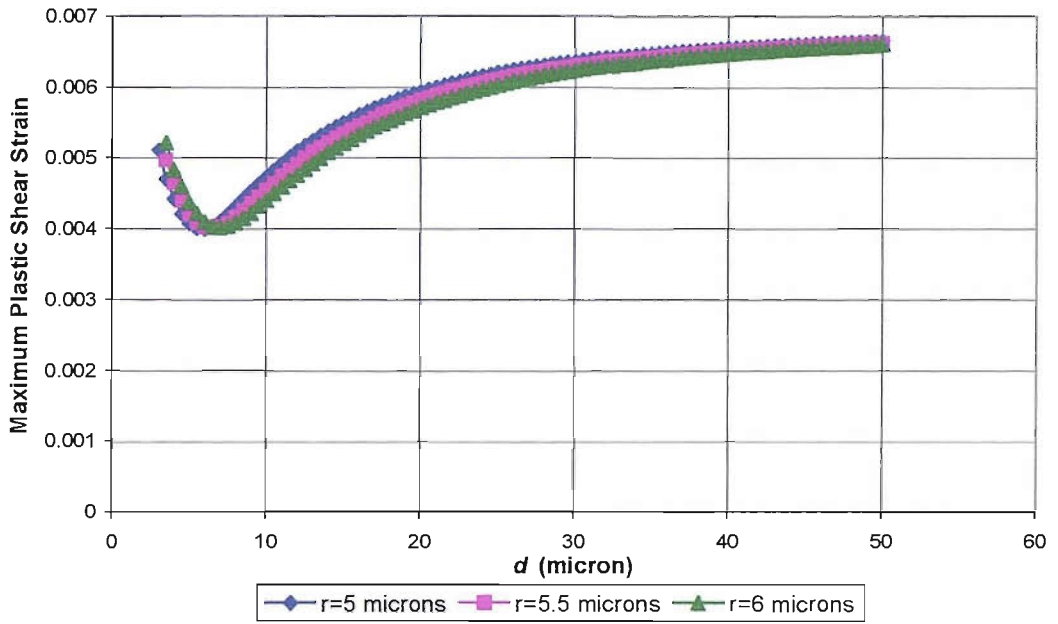
Figure 3-34    Maximum plastic shear strain in Al matrix on the periphery of the central Sn particle versus *d*
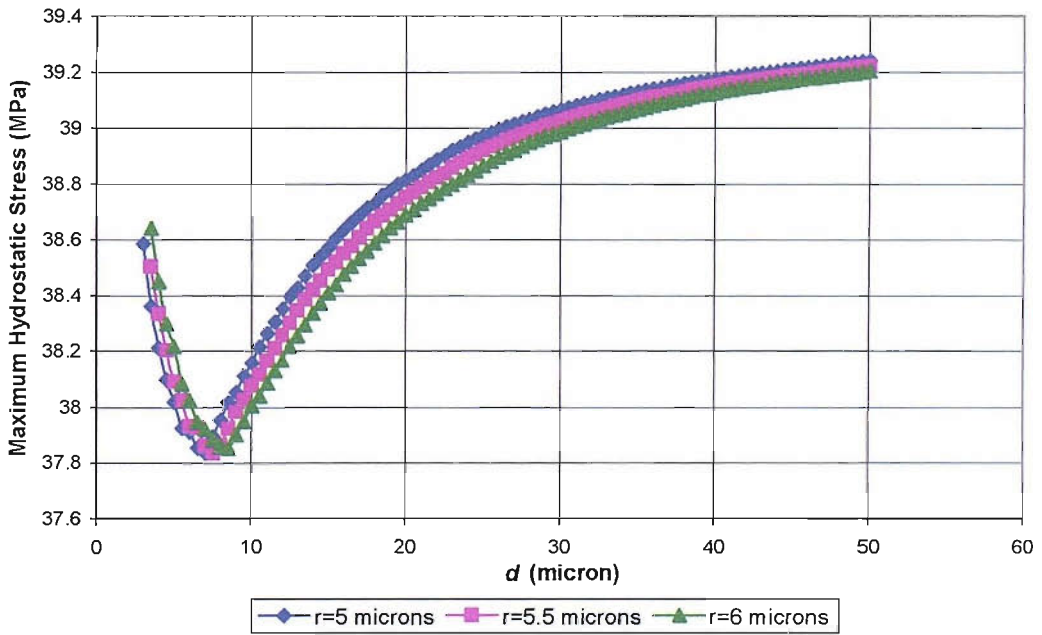


Figure 3-35    Maximum hydrostatic stress in Al matrix on the periphery of the central Sn particle versus *d*

Figure 3-32 and Figure 3-33 show that both the maximum plastic shear strain and the maximum hydrostatic stress in Sn particle are falling over a lower range of $d$ and have not much variation over a higher range. The two parameters in the surrounding Al matrix on the periphery of the central Sn particle, as shown in Figures Figure 3-34 and Figure 3-35, drop first as $d$ increases up to a transition value of around 7.5 μm and then increase. For the selected range of $r$ between 5 μm and 6 μm, which gives a range of particle size between 78.5 μm$^2$ and 113.04 μm$^2$, the FEM results show that the particle size has a small effect on the two initiation parameters.

If $d$ is considered as $d_{min}$, both the maximum plastic shear strain and the maximum hydrostatic stress in Sn particle are falling over the significant range of $d_{min}$ (between 0.47 μm and 9.81 μm) in the real microstructure (see Table 3–2), as shown in Figures Figure 3-32 and Figure 3-33. This indicates that initiation is less likely to occur as $d_{min}$ increases. Over this significant range, there are no clear trends detected for the FEM results of the two parameters in Al matrix as shown in Figure 3-34 and Figure 3-35.

The significant range for $d_{mean}$ in the real microstructure is between 8.44 μm and 29.96 μm. If $d$ is considered as $d_{mean}$, Figure 3-32 and Figure 3-33 show that both initiation parameters in the Sn particle have not much variation as $d$ increases, thus they do not give any clear trends of $d_{mean}$ regarding the effect on initiation. Over the significant range, the FEM results of the two parameters in the Al matrix increase as $d$ increases, as shown in Figure 3-34 and Figure 3-35, which indicate that the likelihood of initiation in Al matrix increases as $d_{mean}$ increases.

Therefore, considering both cases, the FEM results suggest that as $d$ increases (beyond transition point), initiation is likely to occur in Al matrix. When $d$ is small, initiations are most likely to happen in Sn particles. These FEM results appear to suggest that variation of $d_{min}$ and $d_{mean}$ leads to initiation being associated with different material.

The FBT results of $d_{min}$ and $d_{mean}$ are given in Figures D-9 and D-10, respectively. It can be seen that with increasing values of both $d_{min}$ and $d_{mean}$, the percentage of initiating particles appears to increase, with $d_{mean}$ having the stronger effect. For this

to agree with FEM results, the initiation should occur in Al matrix around Sn particles with high $d_{mean}$. This may happen in the real microstructure where decohesion at the Sn/Al matrix has been observed but further detailed microscopic data is needed to detect the failure location.

The tessellation results suggested that the particle size is important in initiation behaviour. However from the analyses of AS1241 and AS16 lining it can be seen that the constant particle size assumption does not really shed light on particle size effects in real microstructure as increasing particle size but keeping *LAF* the same for this geometrical pattern did not show any difference (effectively just a magnification change). It implies that a different particle pattern, e.g., varying particle size within the population, is required to investigate the particle size effect. A method of working towards this model will be proposed later in Section 3.8.

## 3.5   Modelling of real AS16 lining microstructure

The real microstructure of the lining material of AS16 flat strip was modelled to investigate the relation of stress and strain distribution to initiating sites. The replica records of the early fatigue tests were collected and the initiation sites were identified under microscope. A local embedded cell FE modelling of preferential initiation sites was developed. Stress and plastic strain developing in such a realistic representation of microstructure was reproduced in an attempt to identify possible criteria of fatigue crack initiation.

### 3.5.1   Modelling description

The ANSYS-generated embedded cell finite element model was based on Mwanza's[1] tessellation work on the binary image of an AS16 material microstructure obtained from flat strip. Each tessellation cell contains either an initiating particle or a non-initiating particle. Figure 3-36 shows an example of the tessellation results, in which the initiating cells are highlighted by green colour.
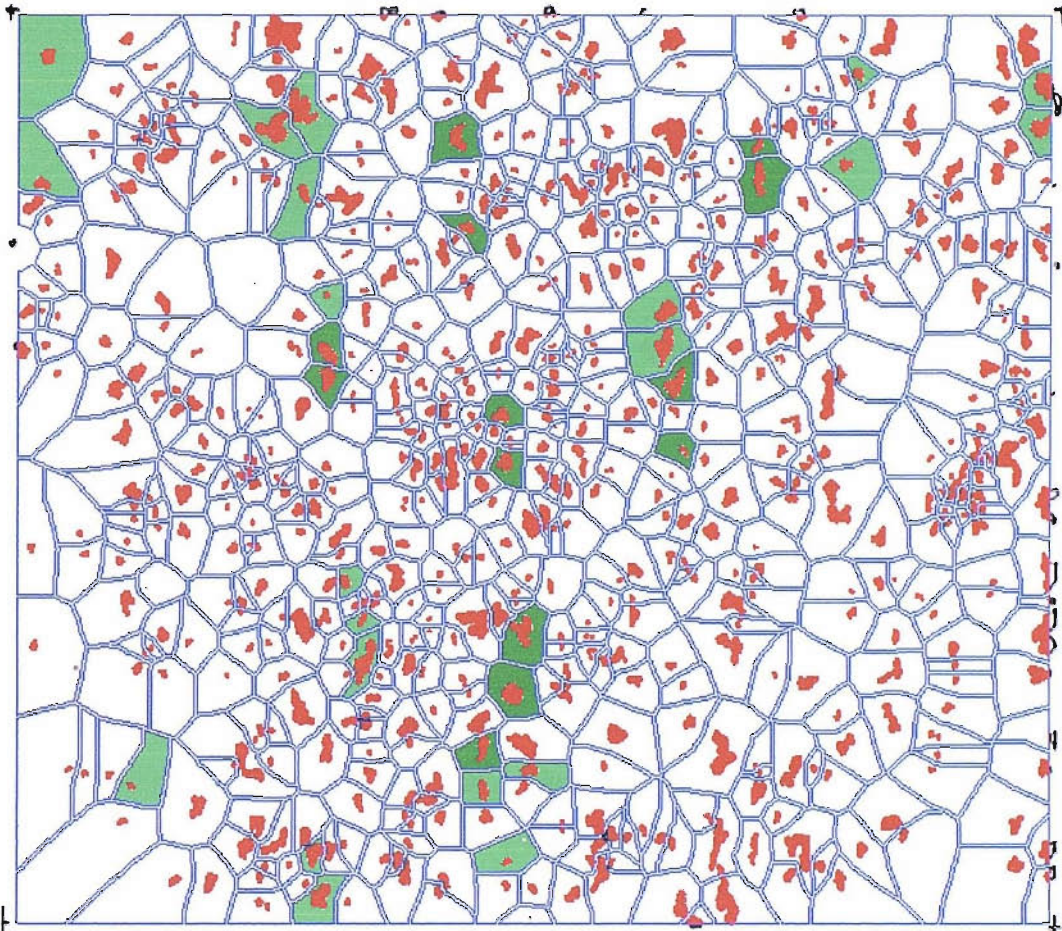
Figure 3-36    AS16 Sn tessellated binary showing initiating cells

The region selected for 2D finite element modelling was a small area containing a few Sn particles associated with several crack initiation sites and approximately 30 surrounding Sn particles. This is used as the core region in the embedded cell model. Following the same approach described in Section 3.4.1, the core region was surrounded by a large embedding region. For comparison some areas with only non-initiating Sn particles were also selected for modelling and analysis. To develop the model in ANSYS, the geometry of the Sn particles was described by polygons based on the Finite Body Tessellation results. Figure 3-37 shows a typical area selected for local microstructure modelling. At this stage only the Sn phases were considered in the model. There is no attempt to model the intermetallic particles (e.g. $CuAl_2$) which are occasionally found in the lining material.
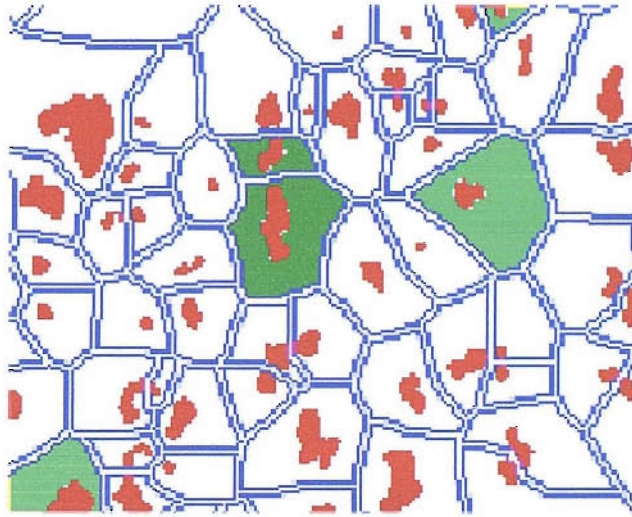
139

Figure 3-37    Typical area selected for microstructure modelling

The core region was modelled as a circle with a radius $R$ of 200 μm. A dimension $L$ of 1000 μm was used for the whole embedding square region. The same material properties as those adopted in the ideal hexagonal particle pattern model for AS16 lining were used here. This elasto-plastic input is described in detail in Section 3.4.2. A monotonic load was applied via a uniform nodal displacement up to a maximum value of 1 μm, which is equivalent to a total strain of 0.1%.

The embedding region was meshed using approximately 210 eight-node quadrilateral elements under plane stress. The core region was meshed using approximately 4750 elements. The Sn particles were meshed using approximately 1440 elements. Perfect bonding between the particles and matrix was assumed and no attempt has been made to model any interface failure effect. The mesh was refined in the regions surrounding the particles since they are sites of interest and likely to be associated with crack initiation. Figure 3-38 shows the mesh of the whole model and the boundary conditions applied. An enlarged view of core region without the meshing of Sn particles is given in Figure 3-39. It can be seen that the mesh in the central area surrounding initiating particle has been refined.
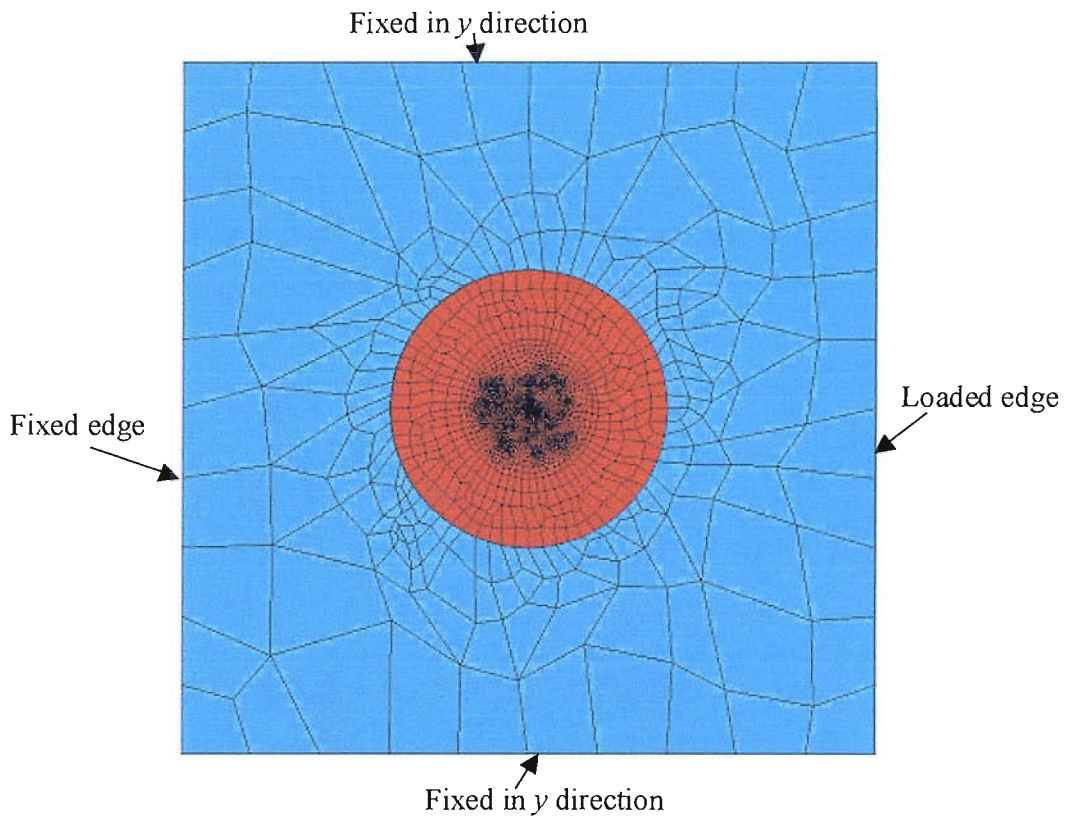
Fixed in *y* direction



Fixed edge

Loaded edge

Fixed in *y* direction

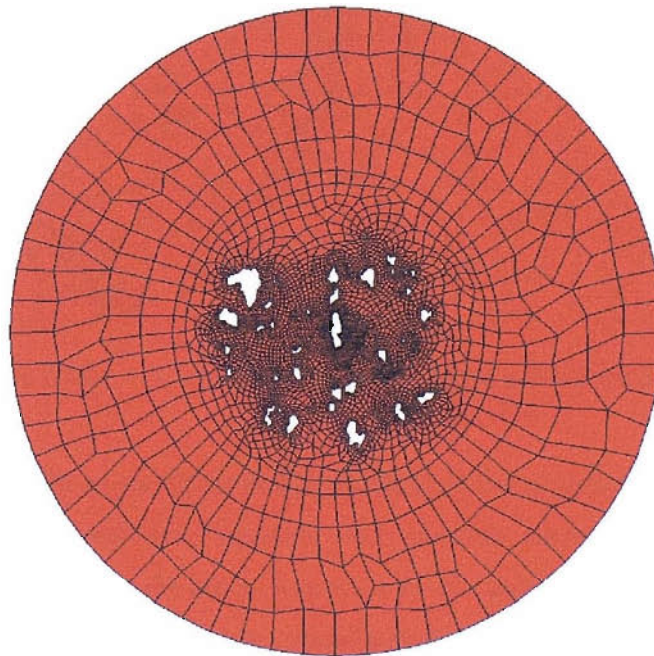Figure 3-38    Mesh of the whole embedded cell FE model



Figure 3-39    Mesh of core region

## 3.5.2    Results

In total 10 typical small areas were selected from Figure 3-36 for modelling as highlighted in Figure 3-40. Areas 1-8 contain at least one initiating particle, while Areas 9 and 10 include only non-initiating particles.
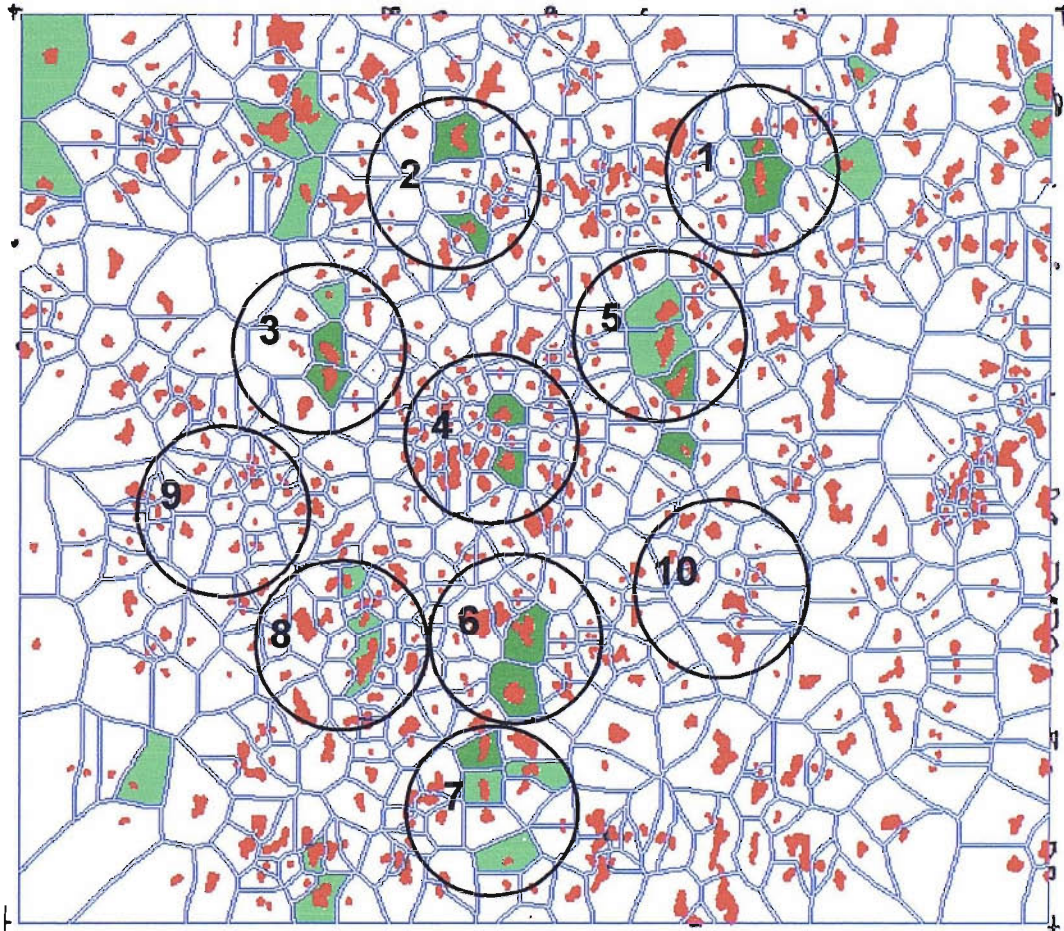


Figure 3-40      Areas selected for embedded cell FE modelling

The maximum plastic shear strain and hydrostatic stress in both Sn and surrounding Al matrix are examined since they are both possible causes of initiation. Some selected contour plots are shown in Appendix E. It can be seen from these contour plots that the particles variable size, shape and distribution generate a highly non-uniform stress and strain field within the matrix alloy material and Sn particles. The concentration of high stress and strain fields appear to be distributed along directions approximately perpendicular to the loading direction, which is consistent with the

effect due to a soft inclusion identified in the analysis of Section 3.3.3. Comparing Figures E-1 (a) and (b) with Figure 3-37, a correlation can be seen between the locations of maximum plastic shear strain and maximum hydrostatic stress and the crack initiation sites. It is also noted that the highest values always appear at or near the boundary between the Sn particles and the matrix, which is consistent with the experimental observations that most of the crack initiation sites were at the Sn-matrix interface. This observation is also confirmed by the hydrostatic stress and maximum plastic shear strain distribution in Sn [see Figures E-1 (c) and (d)].

In order to assess the degree of stress and strain concentration due to the microstructure, two homogeneous FE models with the same boundary conditions were developed to give reference stresses and strains for comparison. The materials used in these two models are shown schematically in Figure 3-41.



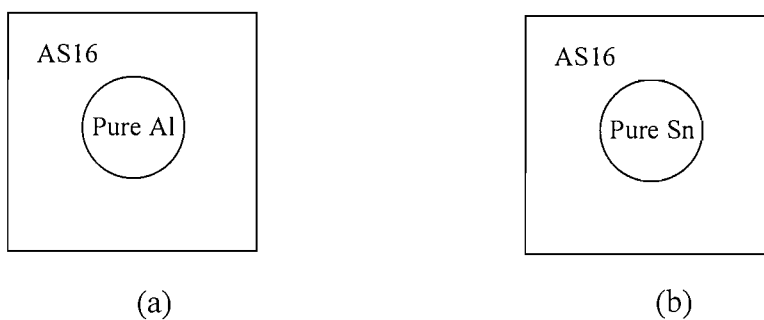(a)                                    (b)

Figure 3-41          Materials used in the two homogeneous FE models

In models (a) and (b) the surrounding regions are modelled as AS16 flat strip lining material and the core regions as pure Al and Sn, respectively. The maximum values of maximum plastic shear strain and hydrostatic stresses for the two models are listed Table 3–3.

**Table 3–3 Maximum values of maximum plastic shear strain and hydrostatic stress in the two homogeneous FE models**

| Model | Maximum Plastic Shear Strain | | | Hydrostatic stress (MPa) | | |
|---|---|---|---|---|---|---|
| | AS16 | Al | Sn | AS16 | Al | Sn |
| (a) | 0.000741 | 0.000589 | N/A | 24.36 | 24.22 | N/A |
| (b) | 0.003147 | N/A | 0.00586 | 26.56 | N/A | 4.07 |

The maximum values of maximum plastic shear strain and hydrostatic stress from the real microstructure modelling of selected areas are recorded and given in Table 3–4.

**Table 3–4 Maximum values of maximum plastic shear strain and hydrostatic stress in selected areas**

| Area | Including initiating sites | Al | | Sn | |
|------|------|------|------|------|------|
| | | Maximum Plastic Shear Strain | Hydrostatic stress (MPa) | Maximum Plastic Shear Strain | Hydrostatic stress (MPa) |
| 1 | Y | 0.030($\sqrt{}$) | 62.25($\sqrt{}$) | 0.090($\sqrt{}$) | 5.31($\sqrt{}$) |
| 2 | Y | 0.048($\sqrt{}$) | 68.76($\sqrt{}$) | 0.095($\sqrt{}$) | 5.44($\sqrt{}$) |
| 3 | Y | 0.060($\sqrt{}$) | 62.92($\times$) | 0.097($\sqrt{}$) | 5.89($\times$) |
| 4 | Y | 0.018($\times$) | 53.88($\times$) | 0.066($\times$) | 5.16($\times$) |
| 5 | Y | 0.036($\sqrt{}$) | 63.76($\sqrt{}$) | 0.101($\sqrt{}$) | 5.42($\sqrt{}$) |
| 6 | Y | 0.021($\times$) | 61.16($\sqrt{}$) | 0.079($\times$) | 5.31($\times$) |
| 7 | Y | 0.055($\sqrt{}$) | 65.83($\sqrt{}$) | 0.072($\times$) | 9.35($\times$) |
| 8 | Y | 0.067($\sqrt{}$) | 72.16($\sqrt{}$) | 0.114($\sqrt{}$) | 5.61($\sqrt{}$) |
| 9 | N | 0.015($\times$) | 55.70($\times$) | 0.031($\times$) | 4.80($\times$) |
| 10 | N | 0.024($\times$) | 62.14($\times$) | 0.068($\times$) | 4.80($\times$) |

($\sqrt{}$): The maximum value is associated with initiating sites.

($\times$): The maximum value is not associated with initiating sites.

It can be seen from Table 3–3 and Table 3–4 that the maximum plastic shear strain and hydrostatic stress in both Sn and matrix Al are magnified by factors as high as 20 and 3, respectively, due to the existence of Sn particles. The results from areas with initiating particles in Table 3–4 also indicate the correlations between the maximum values of the two stress/strain parameters and initiating particles. For areas 1, 2, 5, and 8, the maximum FEM predictions of the two parameters in both Al matrix and Sn particles are associated with initiating particles. For areas 3, 6 and 7, at least one of the maximum values is associated with initiating particles. Area 4 is one exception where none of the maximum values occurs at the initiating particles and the predicted values of initiating parameters are rather low. It is possible that the failure of this

region is due to other causes or that the relevant stress concentration was not captured due to the real microstructure not represented accurately when digitised to generate the FE model. The high hydrostatic stress in Sn of area 7 is believed to be an example of such artificial stress concentration. It should be noted that for the two areas (9 and 10) without initiating particles, the maximum values of maximum plastic shear strain and hydrostatic stress are smaller than most of those of the areas with initiating particles.

## 3.6 Critical assessment of all tessellation results

The modelling of real AS16 lining microstructure shows correlations between the maximum values of the two initiation parameters and initiating particles. Since the stress and strain concentration is due to the complex microstructure, it is necessary to further assess the tessellation results of microstructures to investigate initiation behaviour. As pointed out earlier, the FBT analysis was restricted to the Si phase in AS1241 alloy and the Sn phase in AS16 alloy. The cells produced by the tessellation were then divided into two rather than three populations according to the behaviour of the enclosed secondary particles for the convenience of further analysis: initiating class-cells containing a particle initiating cracks, and non-initiating class-cells containing a non-initiating particle. Each cell of the two populations was then measured using the 11 feature measurements described in Section 3.2. The statistical results from these cells were then collated and the mean values and standard deviations for each population of all cases taken. Table 3–5 shows the average results together with standard deviations of each population for AS1241, AS16 Perp. and the new AS16 Para. data. Rather than just representing the data as mean values, histograms of each of the 11 tessellation measurements were also produced and are presented in Appendix F, in which (a), (b), and (c) in each figure correspond to the frequency distribution of each tessellation measurement for AS1241, AS16 Perp. and AS16 Para. data respectively.

**Table 3–5: AS1241 (Si)[8], AS16 Perp. (Sn)[9] and new AS16 Para. (Sn) mean values and standard deviations of F.B.T. measurements on initiating class and non-initiating class**

| Population | $OA$ (μm$^2$) | | | $OAspRat$ | | |
|---|---|---|---|---|---|---|
| | AS1241 | AS16 Perp. | AS16 Para. | AS1241 | AS16 Perp. | AS16 Para. |
| Overall | 5.23±6.44 | 25.00±41.01 | 24.56±47.59 | 1.49±0.47 | 1.54±0.39 | 1.52±0.39 |
| Initiating | 12.17±11.54 | 47.07±53.87 | 50.84±59.92 | 1.49±0.36 | 1.84±0.48 | 1.70±0.40 |
| Non-initiating | 4.82±5.75 | 23.72±39.79 | 23.66±46.87 | 1.49±0.48 | 1.53±0.38 | 1.51±0.38 |

| Population | $OAng$ (Rad) | | | $CA$ (μm$^2$) | | |
|---|---|---|---|---|---|---|
| | AS1241 | AS16 Perp. | AS16 Para. | AS1241 | AS16 Perp. | AS16 Para. |
| Overall | 0.88±0.41 | 0.98±0.38 | 0.73±0.41 | 72.23±49.49 | 281.44 ±284.74 | 285.40 ±248.85 |
| Initiating | 0.90±0.41 | 1.19±1.31 | 0.92±0.43 | 113.65±58.6 | 40.822 ±362.86 | 442.38 ±322.81 |
| Non-initiating | 0.87±0.41 | 0.97±0.38 | 0.72±0.41 | 69.80±47.81 | 274.07 ±277.90 | 280.00 ±244.25 |

| Population | $CAspRat$ | | | $CAng$ (Rad) | | |
|---|---|---|---|---|---|---|
| | AS1241 | AS16 Perp. | AS16 Para | AS1241 | AS16 Perp. | AS16 Para |
| Overall | 1.67±1.40 | 1.60±0.52 | 1.57±0.52 | 0.78±0.45 | 0.80±0.42 | 0.79±0.43 |
| Initiating | 1.49±0.42 | 1.44±0.33 | 1.45±0.33 | 0.88±0.43 | 0.85±0.36 | 0.83±0.37 |
| Non-initiating | 1.68±1.43 | 1.61±0.53 | 1.58±0.53 | 0.78±0.45 | 0.80±0.42 | 0.79±0.43 |

| Population | $LAF$ (%) | | | No. NNs | | |
|---|---|---|---|---|---|---|
| | AS1241 | AS16 Perp. | AS16 Para. | AS1241 | AS16 Perp. | AS16 Para. |
| Overall | 7.15±5.72 | 9.10±6.51 | 7.82±7.07 | 5.70±1.45 | 5.49±1.45 | 5.55±1.44 |
| Initiating | 10.48±6.42 | 11.62±7.59 | 10.23±8.10 | 6.39±1.39 | 6.28±1.40 | 6.02±1.33 |
| Non-initiating | 6.95±5.62 | 8.96±6.42 | 7.74±7.02 | 5.66±1.44 | 5.44±1.49 | 5.53±1.44 |

| Population | $d_{min}$ (µm) | | | $d_{mean}$ (µm) | | |
|---|---|---|---|---|---|---|
| | AS1241 | AS16 Perp. | AS16 Para. | AS1241 | AS16 Perp. | AS16 Para. |
| Overall | 2.14±1.80 | 3.39±2.94 | 3.99±3.25 | 6.47±2.66 | 11.24±6.18 | 11.95±5.99 |
| Initiating | 2.61±1.87 | 3.54±2.87 | 4.49±3.21 | 7.59±2.50 | 12.85±5.63 | 13.49±5.40 |
| Non-initiating | 2.12±1.79 | 3.39±2.94 | 3.97±3.26 | 6.40±2.65 | 11.14±6.20 | 11.89±6.00 |

| Population | NNAng (Rad) | | |
|---|---|---|---|
| | AS1241 | AS16 Perp. | AS16 Para. |
| Overall | 0.82±0.46 | 0.88±0.47 | 0.73±0.46 |
| Initiating | 0.73±0.44 | 1.08±0.46 | 0.66±0.45 |
| Non-initiating | 0.82±0.46 | 0.87±0.47 | 0.74±0.46 |

First considering the *OA*, the overall mean *OAs* in AS16 Perp. and AS16 Para. data are similar (as expected). In all three cases the mean *OA* of the initiating class is considerably higher than that of the non-initiating class. As shown in Figure F-1, a distinct shift in the frequency distribution towards larger *OA* can be seen for AS1241 and AS16 Perp. data. Although the shift is not so significant for AS16 Para. data, it is notable that a higher frequency distribution of initiating class than that of non-initiating class is observed with increasing *OA*. The high standard deviation of *OA* of AS16 Perp. and AS16 Para. data indicates a wider range in Sn particle sizes. Similar observations can be made for *CA* and *LAF* when the initiating class is compared to the non-initiating class. As indicated earlier, the initiating cells' class values were found to be larger than the non-initiating cells with a higher mean *LAF* value. These trends were also revealed by the discernible shifts in the frequency distribution (Figures F-5 and F-11). As a first approximation therefore, it can be deduced that large Si (or Sn) particles of a high local area fraction show a greater probability of initiating fatigue cracks. However the standard deviations and overlaps in frequency distribution indicate that initiating particles are not separable from non-initiating particles by differences in these values alone.

For both cases of the AS16 alloy, a higher mean value of *OAspRat* of the initiating class is seen than in the non-initiating class, which are shown in Figures F-2 (b) and

(c), indicating a more elongated Sn particle is likely to initiate. However this is not observed for AS1241 alloy where a similar *OAspRat* is seen and the histogram of frequency distribution (Figure F-2 (a)) shows no immediately discernible differences between initiating and non-initiating classes. The *CAspRat* of initiating class in all three cases is observed to be lower than that of the non-initiating class in terms of both mean values and frequency histograms (Figure F-5).

*OAng* is a measurement of the alignment of secondary phases. It is not surprising that the overall mean value of *OAng* of AS16 Perp. is larger than that of AS16 Para. data due to the rolling directionality during rolling process. So a higher proportion of Sn phases at 90° to the tensile axis would be expected in the AS16 Perp. data. For both AS16 Para. and AS16 Perp. data, the *OAng* of the initiating class is higher than that of the non-initiating class, which is not significant in AS1241 data. In Figures F-3 (b) and (c), both figures have a peak frequency distribution at high values (near 90°), indicating that initiating particles tend to have their longest axis aligned almost perpendicular to the global tensile axis direction. This trend is not observed in Figure F-3 (a) for AS1241 data which appears to be more randomly distributed. In comparison with *OAng*, similar observations were made for *CAng* in terms of mean value, however less significant trends were seen in the histograms (Figure F-6).

A distinct shift of frequency distribution of the initiating class towards higher values was observed for all three histograms of *No. NNs*, $d_{min}$ and $d_{mean}$ in Figures F-8 to F-10 (not so significant for $d_{mean}$ of the AS16 Perp. data). The mean values of these three measurements of initiating classes are higher than that of non-initiating classes respectively. This indicates that the secondary phases associated with fatigue crack generally have more near neighbours but are more remote from their immediate neighbours.

The measurement of *NNAng* shows two opposing trends in values of the magnitudes of two classes in the three cases. The *NNAng* of AS1241 and AS16 Para. data in the initiating classes is lower than that of non-initiating classes, whereas in the initiating class of AS16 Perp. data, the *NNAng* is higher than that of non-initiating class, which can be observed from histograms in Figure F-11. A distinct peak of the initiating class

frequency distribution is seen at a high value in the histogram of AS16 Perp. data (see Figure F-11 (b)), however, for the initiating class of AS16 Para. data (see Figure F-11 (c)), peaks are found appearing at both high and low values. For AS1241 data (see Figure F-11 (c)), peaks exist but the frequency is more or less randomly distributed. This indicates that for materials having similar microstructure to AS16 Perp., the Sn particle that has its nearest neighbouring particle positioned along its major axis is likely to cause initiation.

In summary, from the analysis and comparison of the 11 FBT parameters in terms of both mean values and frequency distribution histograms of two populations, it can be deduced that for AS16 Perp. and AS16 Para. data, isolated (remote to their immediate neighbours) large particles having their longest axis aligned almost perpendicular to the global tensile stress field, with a high local area fraction and more near neighbours, show a great probability of initiating particles. In the case of AS16 Perp., having their nearest neighbouring particles positioned along their major axis appears to help particles to initiate cracks. When the secondary phases are Si in the case of AS1241, isolated large particles with high local area fraction and more near neighbours show a great probability of initiating particles.

However, the large standard deviations associated with the mean values indicate that it is not possible to predict whether an individual particle will cause fatigue initiation by simply considering these individual FBT measurements. The physical meaning of the FBT measurements (e.g. *LAF=OA/CA*) means that they are not independent. The complex mechanism of crack initiation is likely to be dependent on combinations of more than one of the FBT measurements. The factors affecting crack initiation in these alloys might be a complex function of multiple measurements. It is thus important to know what combination leads to failure, and thus successfully predict initiation. With 11 tessellation parameters it is not feasible to consider all possible combinations by inspection. Statistical classification techniques that consider all possible combinations of these FBT measurements are thus more appropriate and were used in this analysis. As with the material characterisation problem discussed in Chapter 2, the classification approach used here is a modified Adaptive Numerical Modelling (ANM) approach, based on Support Vector Machines (SVMs) with a parsimonious ANOVA representation (SUPANOVA)[12]. This classification approach

has been successfully adopted in considering fatigue initiating features in austempered ductile iron (ADI)[13] for automotive camshaft application, in AS1241 Al-Si alloys[8], and in AS16 Al-Sn alloys[9] (where previous analysis was performed on AS16 perpendicular data).

## 3.7 SUPANOVA analysis

The general features of SUPANOVA are presented in Chapter 1, Section1.5. As described in Section 1.5, Support vector machines (SVMs) provide a mechanism for choosing optimal model complexity for limited data, thus accurately classifying behaviour (e.g. they might achieve reasonably successful classification of those Sn particles associated with crack initiation). Spline kernels were used in this work due to their ability to approximate arbitrary functions. As mentioned in Section 1.5, SVMs are essentially complex 'black-box' predictive models. They can produce very accurate models, but the relationship between inputs and outputs is difficult to visualise when assessing the physical relationships (e.g. what form and combination of these 11 parameters cause a particle to initiate cracks).

To increase the transparency of this classification problem, a modified SUPANOVA model is used. Therefore, unlike many classification techniques, which place an emphasis on obtaining a good classification rate (e.g. 100% successful classification of those Sn particles associated with crack initiation in the SVM technique), the SUPANOVA approach provides enhanced model transparency whilst retaining predictive accuracy and hence aids model interpretation. In this crack initiation analysis therefore, the result is a predictive model that retains a high degree of interpretability, capable of producing a combination of particle parameters related to crack initiation. Such interpretation should provide a valuable mechanistic insight allowing physically based optimisation of the fatigue process in question.

In applying the SUPANOVA classification in this research, the initiating and non-initiating classes were used, termed "crack" and "non-crack" classes respectively. Since the crack class usually contains less phases compared with the non-crack class, these are imbalanced data sets and require special care in selecting training data when the model is constructed. The SUPANOVA classification avoids a bias operating for

the more heavily represented class by use of differing misclassification costs (effectively weighting the smaller class more heavily) and a Geometric mean ($G_{mean}$), which favours a balanced classification by measuring the square root of the product of the class classification rates. A more detailed description of the approach taken to incorporate the differing misclassification costs and performance criteria for imbalanced data can be found in Lee *et al*[14,15]. The misclassification costs for each class were then tuned to obtain a good classification performance using the pure SVM approach (based on $G_{mean}$ of the unseen test data). This partitioning of the data was repeated ten times with random selection of the training and testing data split each time, thus providing 10 models. Since the SVM classification has no inherent transparency, the sparse ANOVA decomposition was next obtained for each model. The full ANOVA decomposition of the 11 tessellation features had 2048 possible terms ($2^{11}$), but by using the sparse representation approach adopted in SUPANOVA it was possible to reduce the numbers of these terms without greatly compromising overall performance.

The SUPANOVA classification approach has been reported for AS1241 and AS16 (AS16 Perp. data mentioned above) alloys in previous research. The process and results are summarised in this section for comparison with the current work of analysis of the new AS16 Para. data.

### 3.7.1 Data correlation

To apply SUPANOVA, the eleven FBT measurements were normalised between 0 and 1 to avoid bias for any particular feature. Before the analysis was performed, it is important to assess data correlation and input space distribution. Ideally the inputs for SUPANOVA should be independent of each other. Correlation between inputs can prove troublesome for determining classification functions and should be considered when interpreting the relationships generated by the SUPANOVA model. One method to achieve this is to look at pair-wise scatter plots. These are presented for all the FBT parameters of AS16 Para. data in Appendix G. There is obvious clustering of the data in some of the plots such as those including *OA*. This is due to the existence of a few high values in this term. After the input normalisation process, most of the

*OA* values fall in a limited space between 0 and 0.5 in the input space plots. There is observable correlation between a number of the terms as shown in Appendix G (e. g . *OA* vs *LAF*, $d_{min}$ vs $d_{mean}$ and *CA* vs $d_{mean}$). It is noted that the angular parameters (e. g. *OAng*, *CAng*, and *NNAng*) usually are independent of the other parameters while the size and distance parameters show strong correlation in the input space.

The simple 2-D pair-wise scatter plots can give some insight into the data correlations and how the data is distributed in the input space. But this is essentially a qualitative method and does not describe the data correlation quantitatively. There is no intent to apply more complex methods to assess input correlation further in this work. Efforts will focus on the SUPANOVA analysis.

## 3.7.2    Application of SUPANOVA

The applications of SUPANOVA on AS1241 and AS16 (AS16 Perp.)data from previous work are summarised in Table 3–6, as well as results of the analysis on the new AS16 Para. data. To perform SUPANOVA analysis, the normalised input data were partitioned into training and testing data sets. In the new AS16 Para. sampling data, the crack class contained 55 phases associated with crack initiation, and the non-crack class 1599 non-initiating phases. Because there were fewer data in the crack class, c.f. with the previous work, 82% of the crack class was used for training to have enough data to construct the model to ensure reliability of prediction, whilst 44% of the non-crack class was taken for training. The remaining data in both classes were used for testing respectively. This contrasts with the approaches taken by previous researchers. For the AS1241 data, 45% of both classes were used for training and the rest for testing respectively. For the AS16 Perp. data, 30% of both classes were used for training and the rest for testing respectively. The misclassification costs for each class were then tuned to obtain a good classification performance (based on $G_{mean}$ of the unseen test data) using the pure SVM approach. This partitioning was repeated 10 times with random selection of the training and testing data split each time, thus providing 10 models. The full ANOVA decomposition of the 11 tessellation features has 2048 possible terms ($2^{11}$), but by using the sparse representation approach adopted

in SUPANOVA it was possible to reduce these terms without greatly compromising overall performance.

**Table 3–6: Features of AS1241[8], AS16 Perp[9]. and AS16 Para. SUPANOVA models**

|  | AS1241 | AS16 Perp. | AS16 Parallel |
|---|---|---|---|
| Crack Class (data set) | 163 | 90 | 55 |
| Non-crack Class | 2775 | 1550 | 1599 |
| Training Data | 45% | 30% | 82% for crack class, 44% for non-crack class |
| Test Data | 55% | 70% | 18% for crack class, 56% for non-crack class |
| "Crack" Classification | 69% | 58% | 77% |
| "Non-Crack" Classification | 71% | 64% | 52% |
| $G_{mean}$ | 70% | 60% | 62.7% |
| Variance | 1.36% | 0.55% | 0.52% |
| Significant terms selected | 5 | 10 | 29 |

As seen from Table 3–6, in AS1241 the 2048 terms were reduced to just 5 significant terms which were selected most consistently ($\geq$5/10, selected by more than five models out of the ten), with the sparse model giving a successful "crack" classification rate of 69%, a successful "non-crack" classification rate of 71% and an overall classification performance based on mean and variance values of $G_{mean}$ = 70% and 1.36% respectively. In AS16 Perp., the 2048 terms were reduced to 10 significant terms which were selected most consistently ($\geq$5/10), with the models giving a successful "crack" classification rate of 58%, a successful "non-crack" classification rate of 64% and an overall mean and variance value of $G_{mean}$ of 61% and 0.7%

respectively. For AS16 Para. data, the sparse models give a successful "crack" classification rate of 77%, a successful "non-crack" classification rate of 52% and an overall classification performance based on mean and variance values of $G_{mean}$ = 62.7% and 0.52% respectively. The 2048 terms were however reduced to 29 significant consistent terms ($\geq$6/10).

Compared with AS1241 and AS16 Perp, the SUPANOVA model of new AS16 Para. data gives a very good crack classification rate (due to more crack data used to form model), but relatively weak non-crack classification rate. The overall $G_{mean}$ and variance are similar to those obtained for AS16 Perp. data. However, there are many more selected terms of AS16 Para. model than for the AS1241 and AS16 Perp. models, which indicates the complexity of the AS16 Para. model. The selected significant terms of the AS16 Para. model based on the 10 different partitioned data sets are listed in Table 3–7. According to the number of FBT parameters combined in each terms, these terms can be described by univariate (one FBT parameter), bivariate (two FBT parameters) and trivariate (three FBT parameters) terms. Due to random partitioning of the sampling data for training and testing, the selected terms differ between each model. Most of the univariate terms (9 out of 11 possible univariate terms) are selected as significant terms. The occurrence of some univariate terms (e.g. *LAF*) is 10/10 indicating the important role of this parameter in fatigue initiation. It is also noted that most of the bivariate terms and all trivariate terms selected involve the combination of one or more angular parameters (e.g. *OAng* and *CAng*), which indicates the importance of particle directionality to fatigue initiation for AS16 alloy (parallel alignment).

**Table 3–7: Significant terms selected by the ten SUPANOVA data sets of AS16 parallel data**

| Term | Data set 1 | Data set 2 | Data set 3 | Data set 4 | Data set 5 | Data set 6 | Data set 7 | Data set 8 | Data set 9 | Data set 10 |
|---|---|---|---|---|---|---|---|---|---|---|
| *OAspRat* | ● | ● | ● | ● | ● | ● | ● | ● | ● | ● |
| *OAng* | ● | ● | ● | ● | | | ● | ● | ● | ● |
| *CA* | ● | ● | | ● | ● | ● | | | | ● |
| *CAng* | ● | ● | ● | ● | ● | ● | ● | ● | ● | ● |
| *LAF* | ● | ● | ● | ● | ● | ● | ● | ● | ● | ● |
| *No. NNs* | ● | ● | ● | ● | ● | ● | ● | ● | ● | ● |
| $d_{min}$ | ● | ● | | ● | ● | ● | ● | ● | ● | |
| $d_{mean}$ | ● | ● | ● | ● | ● | ● | ● | ● | ● | ● |
| *NNAng* | ● | ● | ● | ● | ● | ● | ● | ● | ● | ● |
| *OAspRat & Ang* | | ● | | ● | ● | ● | ● | ● | ● | ● |
| *OAspRat & CAng* | ● | ● | ● | | ● | ● | ● | ● | | ● |
| *OAng & CAspRat* | ● | ● | | ● | | ● | | | ● | ● |
| *OAng & CAng* | ● | ● | ● | ● | ● | ● | | ● | ● | |
| *OAng & No. NNs* | ● | ● | ● | ● | ● | ● | ● | ● | ● | |
| *OAng & $d_{min}$* | ● | ● | ● | ● | ● | ● | | | ● | |
| *OAng & NNAng* | ● | ● | ● | ● | ● | ● | ● | ● | ● | ● |
| *CA & NNAng* | | | ● | ● | ● | ● | ● | | ● | |
| *CAng & No. NNs* | ● | ● | ● | ● | ● | ● | ● | ● | ● | ● |
| *CAng & $d_{mean}$* | ● | ● | ● | ● | ● | ● | ● | | ● | ● |
| *CAng & NNAng* | ● | | ● | ● | ● | ● | ● | ● | ● | |
| *No. NNs & $d_{mean}$* | ● | ● | ● | ● | ● | ● | ● | ● | | ● |
| *$d_{min}$ & NNAng* | ● | ● | | ● | ● | | ● | | ● | |
| *$d_{mean}$ & NNAng* | ● | ● | ● | ● | ● | ● | ● | ● | ● | ● |
| *OAspRat & CAng & NNAng* | | ● | ● | ● | ● | ● | | | ● | ● |

Microstructure Modelling of the Initiation Sites

| Term | Data set 1 | Data set 2 | Data set 3 | Data set 4 | Data set 5 | Data set 6 | Data set 7 | Data set 8 | Data set 9 | Data set 10 |
|---|---|---|---|---|---|---|---|---|---|---|
| *OAng & CAng & LAF* | ● | ● | ● | ● | ● | ● | ● |  | ● | ● |
| *OAng & CAng & $d_{min}$* |  | ● | ● |  |  | ● | ● | ● |  | ● |
| *OAng & CAng & NNAng* |  | ● | ● | ● | ● | ● | ● | ● | ● | ● |
| *OAng & No. NNs & NNAng* | ● | ● | ● | ● | ● |  | ● |  | ● | ● |
| *CAng & $d_{mean}$ & NNAng* | ● | ● |  | ● | ● |  | ● |  | ● | ● |

### 3.7.3  Interpretation of selected initiation features

Appendix H shows the 29 significant ANM terms (occurrence more than 60%) picked by SUPANOVA decomposition for the AS16 Para. data. These plots show the relationships found between these input terms (*x*-axis or *x*-*y* axes) and the likelihood of cracking (output on the *y* or *z*-axis) in which a decreasing trend in the *y*-axis (2D) or the *z*-axis (3D) indicates increased likelihood of fatigue crack initiation. The selected terms and identified trends are also summarised in Table 3–8.

**Table 3–8: AS16 Para. SUPANOVA terms selected and their occurrence across 10 modelling runs on random partitions of training and test data**

| Term | Occurrence | Component 1 (univariate) | Component 2 (bivariate) | Component 3 (trivariate) | Likelihood of Initiation and Consistency within models |
|------|------------|--------------------------|--------------------------|---------------------------|--------------------------------------------------------|
| 1 | 10/10 | $OAspRat$=High | | | Likely (8/10) |
| 2 | 8/10 | $OAng$=High | | | Likely (6/8) |
| 3 | 6/10 | $CA$=High | | | Likely (6/6) |
| 4 | 10/10 | $CAng$ | | | Not Consistent |
| 5 | 10/10 | $LAF$=High | | | Likely (10/10) |
| 6 | 10/10 | $No.\ NNs$=High | | | Unlikely (10/10) |
| 7 | 8/10 | $d_{min}$=High | | | Likely (8/8) |
| 8 | 10/10 | $d_{mean}$=High | | | Likely (10/10) |
| 9 | 10/10 | $NNAng$=High | | | Unlikely (10/10) |
| 10 | 8/10 | $OAspRat$=High | $OAng$=High | | Likely (8/8) |
| 11 | 8/10 | $OAspRat$=High | $CAng$=High | | Likely (8/8) |
| 12 | 6/10 | $OAng$=High | $CAspRat$=High | | Unlikely (6/6) |
| 13 | 8/10 | $OAng$=High | $CAng$=High | | Unlikely (7/8) |
| 14 | 9/10 | $OAng$=High | $No.\ NNs$=High | | Likely (8/9) |
| 15 | 7/10 | $OAng$=High | $d_{min}$=High | | Unlikely (7/7) |
| 16 | 10/10 | $OAng$=High | $NNAng$=High | | Likely (7/10) |
| 17 | 6/10 | $CA$=High | $NNAng$=High | | Likely (6/6) |
| 18 | 10/10 | $CAng$=High | $No.\ NNs$=High | | Likely (9/10) |
| 19 | 9/10 | $CAng$ | $d_{mean}$ | | Not Consistent |
| 20 | 8/10 | $CAng$=High | $NNAng$=High | | Unlikely (8/8) |

| 21 | 9/10 | *No. NNs*=High | $d_{mean}$=High | | Unlikely (9/9) |
|----|------|------|------|------|------|
| 22 | 6/10 | $d_{min}$=High | *NNAng*=High | | Likely (6/6) |
| 23 | 10/10 | $d_{mean}$=High | *NNAng*=High | | Likely (10/10) |
| 24 | 7/10 | *OAspRat*=High | *CAng*=High | *NNAng*=High | Unlikely (7/7) |
| 25 | 9/10 | *OAng*=High | *CAng*=High | *LAF*=High | Unlikely (9/9) |
| 26 | 7/10 | *OAng*=High | *CAng*=High | $d_{min}$=High | Unlikely (7/7) |
| 27 | 9/10 | *OAng* | *CAng* | *NNAng* | Complex trend |
| 28 | 8/10 | *OAng*=High | *No. NNs*=High | *NNAng*=High | Likely (8/8) |
| 29 | 7/10 | *CAng* =High | $d_{mean}$=High | *NNAng*=High | Unlikely (7/7) |

A total of 29 selected terms and a multiplicity of identified trends indicate the relative complexity of AS16 Para. SUPANOVA model. Term 1 selected by the classifier is a univariate relationship between increasing *OAspRat* and the increasing likelihood of the Sn particle initiating a crack. From Appendix H it is seen that two trends are identified. This is due to the different data-set sampling in training and testing data of the ten models. Based on different populations of input space, different trends might be identified by each model. It is hence necessary to evaluate all ten models and identify the occurrence and consistency of each term. Taking term 1 for example, it was picked by all 10 models, and trend 1 appears 8 times while trend 2 appears only 2 times, so trend 1 can be considered as the most consistent or representative trend of term 1. Trend 1 (consistency 6/8) of term 2 indicates that increasing *OAng* gives increasing likelihood of a Sn particle initiating a crack. Although only 6 models picked up term 3, it shows a consistent relationship between increasing *CA* and the increasing likelihood of a Sn particle initiating a crack. Term 4 relating *CAng*, however, shows 3 inconsistent trends, indicating a complex function of this term in the SUPANOVA model. Other univariate terms 5, 7 and 8 show the increasing probability of a Sn particle initiating a crack with increasing *LAF*, increasing $d_{min}$ and increasing $d_{mean}$. The rest of the univariate terms 6 and 9 picked by the classifier show that increasing *No. NNs* and increasing *NNAng* give lower probability of a Sn particle initiating a crack. The prediction from these univariate terms may be interpreted as:

isolated (increasing *No. NNs*, increasing $d_{min}$ and increasing $d_{mean}$) large (increasing *CA* and increasing *LAF*) elongated (increasing *OAspRat*) particles with longest axis aligned perpendicular to the tensile axis (increasing *OAng*) predominantly act as fatigue initiation sites except when the *NNAng* is high. A large value of *LAF* can be associated with local particle clustering, generally implying low values of $d_{min}$ and $d_{mean}$. However, this condition is contradictory to the condition of $d_{min}$ and $d_{mean}$ for the increasing likelihood of initiation. This implies a more complex function of these terms in predicting initiation, hence the combination of these terms (e.g. bivariate or trivariate) need to be considered.

The bivariate relationships (term 10 – 23) predict the likelihood of crack initiation based on the combination of the angular information (*OAng*, *CAng* and *NNAng*), spatial distributions ($d_{min}$ and $d_{mean}$), particle alignment (*OAspRat*) and the cell measurements (*CAspRat* and *CA*). From terms 10 and 11, it is seen that fatigue initiation is more likely to occur when the *OAspRat* increases with increasing *OAng* or increasing *CAng* respectively, implying that narrow Sn particles, aligned perpendicular to the global tensile axis are most likely to initiate crack growth. However, the relationships revealed by terms 12 and 13 show a low probability of initiation when *OAng* increases and *CAspRat* or *CAng* increases. This condition however involves cell information which is difficult to understand related as it is to complex functions of the local particle arrangements. Terms 14, 15 and 16 are also relationships involving *OAng* information. It is seen increasing *OAng* is likely to cause initiation when *No. NNs* is increasing or *NNAng* is increasing except when $d_{min}$ is increasing. Term 16 implies that particles with their major axis perpendicular to the tensile axis and having their near neighbours in the same alignment as their major axis are more likely to cause initiation. Term 17 shows the increasing likelihood of a Sn particle initiating a crack with both increasing *CA* and increasing *NNAng*. Term 18 shows the increasing likelihood of a Sn particle initiating a crack with both increasing *CAng* and increasing *No. NNs*. Term 19 involves *CAng* again shows inconsistency in its trends as in the univariate term 4. Two trends that are unlikely to cause initiation are seen for bivariate terms 20 and 21, when both *CAng* and *NNAng* increase or both *No. NNs* and $d_{mean}$ increase. Terms 22 and 23 show an increasing likelihood of a Sn particle to initiate a crack when *NNAng* increases with increasing $d_{min}$ or increasing $d_{mean}$. A higher $d_{min}$ or $d_{mean}$ is considered to indicate a relatively unclustered local

microstructure. A higher $d_{min}$ or $d_{mean}$ for an initiating particle implies a greater distance to the neighbours of that initiating particle. These results thus indicate that the spatial distribution of the near neighbours is significant in affecting the local stress distribution that causes crack initiation around a central Sn particle. From these two terms it is concluded that a Sn particle that is isolated from its neighbours and has a high *NNAng* is likely to initiate.

Trivariate term 24, 25, 26, and 29 give consistent trends of what is unlikely to cause initiation. A low probability of a Sn particle to initiate a crack is found when *CAng* increases with both increasing *OAspRat* and increasing *NNAng*, or both increasing *OAng* and increasing *LAF*, or both increasing *OAng* and increasing $d_{min}$, or both increasing *NNAng* and increasing $d_{mean}$. Term 27 shows a complex trend. At high values of *OAng*, *CAng* and *NNAng*, an increasing likelihood of initiating is seen, but the likelihood is not monotonically increasing when the inputs increase. From term 28 it is seen that increasing *OAng*, increasing *No. NNs* and increasing *NNAng* is likely to cause initiation.

It is noted that some of the trends identified are contradictory (or at least in part). For example, the univariate term 8 indicates that increasing $d_{mean}$ is likely to cause initiation, while bivariate term 21 shows that the increasing $d_{mean}$ with increasing *No. NNs* gives a low probability for a Sn particle to initiate a crack. Similar contradictions can be found between terms 9 and 16, terms 8 and 21, terms 11 and 24, etc. This may reflect the fact that each term shows only part of the whole contribution to the likelihood of initiation. When the contribution of one input parameter is positive in one term, it might be negative with the combination of other parameters in another term. It is a reflection of a more complex function that may exist in the SUPANOVA model (which has been constrained to be parsimonious). Another explanation is the random data-set sampling for 10 models. Noted that the selected terms discussed here do not all appear in one model at the same time, therefore they may be contradictory to each other due to different sampling of the data sets used to construct the models.

**Table 3–9: Micromechanical system features suggested by ANM terms selected in AS16 para. model**

| Crack promoted by | Terms related | Micromechanical system |
|---|---|---|
| High Object Aspect Ratio | 1,10,11 except 24 | |
| High Object Angle (close to 90° to tensile axis) | 2,10,14,16,28 except 12,13,15,25,26 | |
| High Object Area (relating to high *LAF* and *CA*) | 3,5,17 except 25 | |
| Far away from Near Neighbours | 7,8,22,23 except 15,21,26,29 | |

Table 3–9 has attempted to group these terms into micromechanical systems that promote or avoid cracks. The complexity of the interactions of each parameter in crack initiation can be seen from this table. The identified parameters can promote or avoid crack initiation when other parameters are considered, e.g., the function of *OAspRat* can be visualised as: if a Sn particle has a high *OAspRat* it initiates a crack, unless it has a high *CAng* and a high *NNAng*. Similarly, if a Sn particle has a high *OAng* (perpendicular to tensile axis) it initiates a crack, unless it has a high *CAspRat*, or a high *CAng*, or a high $d_{min}$, or high values of both *CAng* and *LAF*, or high values of both *CAng* and $d_{min}$; high *OA* also promotes cracks unless the Sn particle has high values of both *OAng* and *CAng*, if the Sn particle is far away from its near neighbours, it initiates a crack unless it has high *OAng*, or it has lots of near neighbours, or it has both high values of *OAng* and *CAng*, or it has both high values of *CAng* and *NNAng*. The table also shows particles with lots of near neighbours and with its nearest neighbour above it avoid crack initiation unless other conditions are considered.

To summarise the interpretations from the ANM's selected features, the Sn particle in the AS16 lining (parallel) most associated with fatigue initiation appear to be larger than average, long, aligned perpendicular to the tensile axis in a relatively unclustered

area of microstructure (far away from its near neighbours). Under this condition, if the nearest neighbour is above and has its long axis aligned to the axis of the Sn particle, it also promotes crack initiation.

For comparison, the ANM terms picked by AS16 (perpendicular)[9] and AS1241[8] alloys, are given and summarised by two tables in Appendix I. Compared with the new AS16 Para. data, the trends revealed by AS16 Perp. model and AS1241 model were much simpler. The Si particles in AS1241 associated with fatigue are found to be larger than average and have their major axis aligned parallel to the tensile axis. In the AS16 Perp. model, the Sn particles most likely to cause crack initiation are larger than average, long and narrow, aligned perpendicular to the tensile axis and have their nearest neighbours aligned with the particles' major axis. As found in AS16 Para., there is indication for both AS16 Perp. and AS1241 that the fatigue cracks initiate at particles in relatively unclustered areas of microstructure.

The complexity of the AS16 Para. model indicates that further methods are required to more fully assess the predicted trends of the SUPANOVA model. One approach would be to apply the SUPANOVA models derived from the experimental data on simulated particle populations (identified from inspection of the critical SUPANOVA terms) to predict possible initiation sites, these can then be compared with the FEM obtained stress and strain results on these simulated particle populations to verify the predicted trends. The next section details a possible approach to this.

## 3.8   Idealised particles

The critical features determining possible initiation sites obtained from the SUPANOVA models generated in the previous section could be further explored and visualised with the help of simulated particle populations. Previous work carried out at Southampton by Yang *et al*[16] using a variety of two-dimensional finite-size particle distributions indicated that increasing inhomogeneity of reinforcement distribution (i.e. particle clustering) may provide easy crack initiation and/or propagation sites. The simulated particle distributions were generated using an in-house Fortran program written by Yang *et al*. This program was able to define and systematically

vary several microstructure characteristics such as the shape, orientation, size and spatial distribution of the particles. In addition to the individual particle morphology parameters, random and clustered populations could also be simulated. Prediction of possible initiation sites in simulated particle populations using SUPANOVA models was performed by Lee[7] based on ADI and AS1241 materials. In this section, a suggested approach to apply this method to the new AS16 Para. data will be discussed.

Since the SUPANOVA model is derived from the experimental AS16 Para data, it is essential to ensure that the area fractions of the particles are the same for both the real microstructure and the simulated particle distributions. Information on the overall particle population of AS16 Para. (see Table 3–5 in Section 3.6) will be used here to identify a set of model particle distributions. The procedure (provided by Lee) and specification to produce these distributions are described in some detail.

1. A two dimensional rectangular field with nominal width of 1014 pixels/units and height of 653 pixels/units was specified.

2. In order to provide a realistic simulated data set, the Volume Fraction ($V_F$) and hence the average Area Fraction ($A_F$) of secondary phase particles found in the original data set and the simulated data set must be consistent. Once the $A_F$ is given, a number of objects can be specified to fit into the simulated area with appropriate radius. For the AS16 Para data set,

$$A_F = \frac{\Sigma O.A.}{\Sigma C.A.} = 0.0861$$

and average radius,

$$R = 2.979 \ \mu m.$$

However, if this small radius is used in the simulation, significant rounding errors due to pixel resolution will be produced. Therefore the scale of radius is effectively magnified by five times ($R=14 \ \mu m$) which will still give a reasonable number of particles in the simulation.

$$\text{Number of Objects in this field} = \frac{1014 \times 653 \times 0.0861}{\Pi \times R^2} = 92$$

3. Once the number of particles in the image area has been defined, the size, shape and distribution of the objects can be varied to give a certain

distribution. Apart from circular objects, elliptical objects can also be generated. For a given area, the circle can be converted to an ellipse shape. This is given as:

$$\text{area of circle } (\Pi \times R^2) = \text{area of ellipse } (\Pi \times A \times B)$$

where *A* and *B* are the length of the major axis and length of the minor axis of an ellipse. *A/B* is the aspect ratio of the ellipse which is a feature obtained from the FBT. When the radii of objects are generated, the mean value of 14 μm and the standard deviation of 17 μm (both are magnified) are used to give a normal distribution.

4. The centroids of the objects are then generated in the form of a random or clustered distribution. It is important to note that a strict constraint is imposed that the objects generated should not overlap with each other. For the random distribution, the centroids of the objects are generated using a random number generated with a repeatable sequence. For the clustered distribution, 9 "parent" centroids are generated randomly which are at least 250 pixels/units away from each other. 10 "children" centroids are then generated randomly for each "parent" centroid within a specified distance to it (here this gives an area with the size of 100 units/pixels ×65 units/pixels). The remaining objects will be generated randomly within the whole image area.

5. The *OAng* can be fixed to be parallel, perpendicular or random with respect to the (horizontal) loading axis.

6. Upon obtaining the relevant parameters (i.e. for circular objects – *x* and *y* coordinates and object radius; for ellipses – *x* and *y* coordinates, *A*, and *B* chord lengths of the ellipse) these values are then digitised to produce the simulated images.

7. The tessellation analysis may then be applied to the simulated images to give the FBT information which can run through the 10 SUPANOVA models to predict possible initiation sites. The consistency of initiation site selection may then be assessed.

Table 3–10 gives the proposed populations variations.

**Table 3–10: Proposed particle population for SUPANOVA analysis**

| | Model | Shape | Object size | Object angle | Distribution | |
|---|---|---|---|---|---|---|
| | | | | | Random | Clustered |
| 1 | 1 | circle | constant | N/A | Y | - |
| | 2 | circle | constant | N/A | - | Y |
| 2 | 3 | circle | varying | N/A | Y | - |
| | 4 | circle | varying | N/A | - | Y |
| 3 | 5 | ellipse | constant | parallel to load direction | Y | - |
| | 6 | ellipse | constant | parallel | - | Y |
| 4 | 7 | ellipse | constant | perpendicular to load direction | Y | - |
| | 8 | ellipse | constant | perpendicular | - | Y |
| 5 | 9 | ellipse | varying | parallel | Y | - |
| | 10 | ellipse | varying | parallel | - | Y |
| 6 | 11 | ellipse | varying | perpendicular | Y | - |
| | 12 | ellipse | varying | perpendicular | - | Y |
| 7 | 13 | ellipse | constant | $\theta$ | Y | - |
| | 14 | ellipse | constant | $\theta$ | - | Y |
| 8 | 15 | ellipse | varying | $\theta$ | Y | - |
| | 16 | ellipse | varying | $\theta$ | - | Y |

Examples of simulated particle populations are given in Figure 3-42 and Figure 3-43.
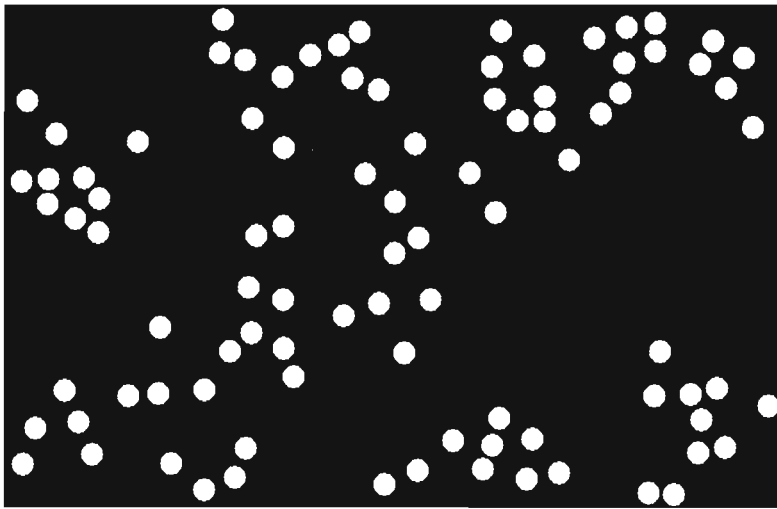
Figure 3-42     Simulated particle population: random object distribution, constant area, circular shapes, clustered distribution (model 2)
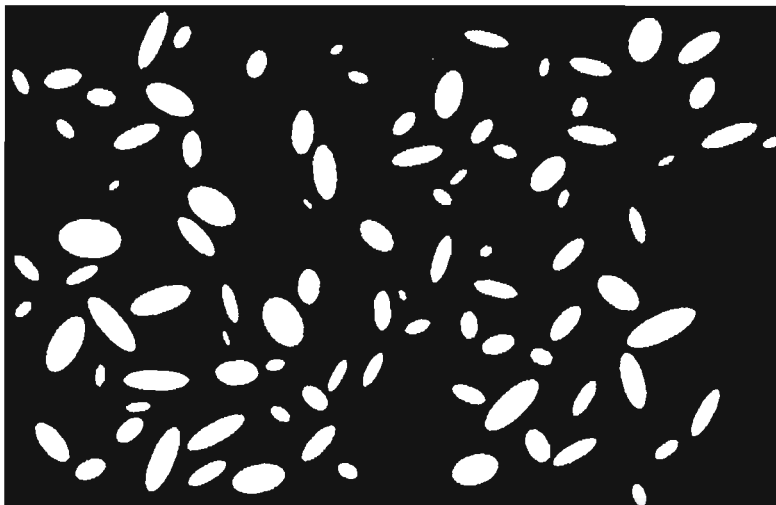


Figure 3-43     Simulated particle population: random object distribution, varying object area ellipse shapes at varying angle θ to the loading axis (model 15)

However, before applying SUPANOVA models to these simulated particle populations, there is a need to reassess the data sampling originally made when generating the SUPANOVA models. Due to the lack of initiation site data, 82% of the crack class was taken for training to provide enough training data sets for initiation class. In an assessment of the SUPANOVA models by applying them to the original real microstructure data set, it was found that the models predicted accurately most of the initiation sites in crack class (54 out of 55 being identified as initiation). However, for a selection of 55 datasets of non-crack class, 43 were identified as possible

initiation sites. This indicates that the models produced show the inability to differentiate the differing features of non-initiation sites from initiation sites.

Referring to Table 3–6, although the overall $G_{mean}$ of 62.7% is reasonable for classification models, the "Non-crack" classification rate of 52% indicates that the models are weak in predicting non-initiation sites. This indicates that $G_{mean}$ might not be able to reflect the balance of prediction between two classes. To increase the "Non-crack" classification rate, a more careful selection of training data and tuning parameters is required to achieve the "best" prediction. Ideally for a good classification model, the data sampling should be an automatic process following certain rules until the best classification rates are obtained. While retaining transparency, the tuning parameter should keep a high performance of the model. In addition to this, the assumption (or criteria) used to identify initiation and non-initiation sites should be under consideration. The current SUPANOVA models calculate and assign for each dataset a numerical value. The corresponding particle is taken as an initiating particle if the value is negative, or a non-initiating particle if it is positive. This assumption however omits the absolute value which might be an indication of possibility of initiating. It would be more reasonable to have this consideration in the models.

However, the work of refining the SUPANOVA models is beyond the scope of current PhD project and will be discussed more in the Further Work section. As a result, the existing SUPANOVA models have not been applied to the simulated particle populations, although this remains an interesting future possibility.

---

[1] M. Mwanza, Microstructural modelling of fatigue in novel plain bearing designs, PhD Thesis, University of Southampton, (2004)

[2] J. Boselli, P.D. Pitcher, P.J. Gregson and I. Sinclair, Secondary phase distribution analysis via finite body tessellation, J Microsc-Oxford, Vol.195, pp. 104-112, (1999)

[3] M.R. Joyce, Fatigue of Aluminium Linings in Plain Automotive Bearings, PhD Thesis, University of Southampton, (2000)

[4] K. Gall, M. Horstemeyer, D.L. McDowell and J.H. Fan, Finite element analysis of the stress distributions near damaged Si particle cluster in cast Al-Si alloys, Mech Mater, Vol. 32, pp. 277-301, (2000)

[5] J.D. Eshelby, The determination of the elastic field of an ellipsoidal inclusion and related problems, P Roy Soc Lond, Vol. A241, pp. 376-396, (1957)

[6] N.J. Hardiman, Elliptic elastic inclusion in an infinite elastic plate, Quart J Mech App Math, Vol. VII, Pt. 2, (1954)

[7] K.K. Lee, Interpretable classification model for automotive material fatigue, PhD thesis, University of Southampton, (2002)

[8] M.R. Joyce, K.K. Lee, S. Syngellakis and P.A.S. Reed, Quantitative assessment of preferential fatigue initiation sites in a multiphase aluminium alloy, Fatigue Fract Eng M, Vol. 27, pp. 1025-1036, (2004)

[9] M.C. Mwanza, M.R. Joyce, K.K. Lee, S. Syngellakis and P.A.S. Reed, Microstructural characterisation of fatigue crack initiation in Al-based plain bearing alloys, Int. J. Fatigue, Vol. 25, September-November, pp. 1135-1145, (2003)

[10] M. Dong and S. Schmauder, Modelling of metal matrix composites by a self-consistent embedded cell model, Acta Mater Vol. 44, pp. 2465-2478, (1996)

[11] J.J. Wortman and R.A. Evans, Young's modulus, shear modulus, and Poisson's ratio in Silicon and Germanium, J of App Phys, Vol 36, pp. 153-156, (1965)

[12] S.R. Gunn and M. Brown, SUPANOVA - a sparse, transparent modelling approach. Proc. IEEE International Workshop on Neural Networks for Signal Processing, (Edited by Y.H. Hu, J. Larsen, E. Wilson and S. Douglas), pp. 21-30, IEEE, Piscataway, NJ, USA, (1999)

[13] P.A.S. Reed, R.C. Thomson, J.S. James, D.C Putman, K.K. Lee and S.R. Gunn, Modelling of microstructural effects in the Fatigue of Austempered Ductile Iron, Mat Sci Eng A-Struct, Vol. 346, pp. 273-286, (2003)

[14] K.K. Lee, C.J. Harris, S.R. Gunn and P.A.S. Reed, Classification of imbalanced data with transparent kernels. Proc. IJCNN, Washington DC, USA, pp. 2410-2415, (2001)

[15] K.K. Lee, C.J. Harris, S.R. Gunn and P.A.S. Reed, Regression models for classification to enhance interpretability. Proceedings of the 3rd international conference on Intelligent Processing and Manufacturing of Materials IPMM, (2001)

[16] N. Yang, J. Boselli J and I. Sinclair, Simulation and quantitative assessment of homogeneous and inhomogeneous particle distributions in particulate metal matrix composites, J Microsc-Oxford, Vol. 201-2, pp. 189-200, (2001)

# CHAPTER 4  Conclusions and Further Work

## 4.1  Material characterisation

### 4.1.1  Summary

As pointed out in the Introduction, AS16 and AS1241 plain bearing systems have multi-layered structures and their linings are multi-phase materials with distinct secondary phase particles (Si in the AS1241 lining, and Sn in the AS16 lining in the absence of Si). Fatigue tests performed on both bearing and flat strip specimens in previous projects showed the effect of microstructure on fatigue crack initiation. In this thesis, the main aim is to investigate this effect further through FEM. To achieve this, it is necessary to determine the elasto-plastic properties of the lining for use in modelling in order to identify accurately the stress and strain fields in the surface region where crack initiation has been observed.

Since it is hard to apply traditional tensile test method to thin layers, a methodology was proposed here for obtaining elasto-plastic material properties via simple, non-instrumented Vickers micro-hardness test data. This methodology involves a combination of various experimental and numerical techniques: tensile tests, Vickers micro-hardness tests, FEA, adaptive numerical modelling and a genetic optimisation algorithm. The success of the process depends on reliable outputs from all the techniques.

1) Tensile tests

Tensile tests were performed on several available Al alloys (control materials) and pure Sn by the sponsor company and colleagues in the Engineering Materials Group, University of Southampton. The obtained nominal stress-engineering strain curves of these materials were then converted into true stress-logarithmic strain curves. Five basic material parameters were adopted to describe a full $\sigma-\varepsilon$ curve: the Young's modulus $E$, the proportional limit $\sigma_{el}$, the 0.2% proof stress $\sigma_{0.2}$, the hardening coefficient $A$ and the hardening exponent $n$. Based on the limits of the material

parameters of control materials, ranges of the five material parameters were identified for use later in adaptive numerical modelling as values of these parameters for AS16 and AS1241 linings are likely to be found within these ranges.

2) Vickers micro-hardness tests

The Vickers micro-hardness technique was used in this project because the small size of its indentation is more suitable to the thin lining layers of bearings and flat strips than that of the traditional Vickers hardness technique, and it can be more accurately measured than that of a spherical indenter. The micro-hardness tests were carried out on control materials and various lining materials for which stress-strain data were not available. During the micro-hardness tests for each material the applied load was varied and the diagonal size of the indentation for corresponding applied load was recorded. For each load five readings were made to generate a load-average indent size (*P-l*) curve.

3) FE modelling

FE models were developed to simulate accurately the micro-hardness process so that reliable load-indentation size relations could be generated. The modelling process started from the generation of a 3D FE model. Subsequently axi-symmetric models with rigid indenter and deformable indenter were developed and the FEM results were compared. All three models are in good agreement with the input of experimentally obtained $\sigma$–$\varepsilon$ curve. The axi-symmetric model with rigid indenter was chosen for further FE analysis due to its obvious advantage in reducing the model complexity and computation time. Various factors that could possibly affect the performance of the axi-symmetric model were investigated to further refine the model. For validation purposes, this model was applied to all control materials and the FEM results were compared with the corresponding *P-l* curves obtained from micro-hardness tests. Good agreements were achieved for the soft control materials (VQ1B and AS1241) while discrepancies were found for hard materials (B1Q2, B1Q3, and RTWQ).

4) Adaptive numerical modelling

Since it is impossible to guess correctly the $\sigma-\varepsilon$ curve for the materials of interest to produce satisfactory agreement between FE and experimental *P-l* curves, iterations are necessary to achieve a solution. Due to the limitation of FE analysis of indentation being time consuming for a large number of modelling runs, adaptive numerical modelling was used to interpolate between the FEM results accurately and quickly. The SUPANOVA technique was used since it is able to provide transparency without sacrificing predictive accuracy compared with many other adaptive numerical methods, which may offer good predictive accuracy but little insight into the underlying process being modelled.

FE analyses were performed on artificial $\sigma-\varepsilon$ curves to provide well-distributed and plentiful data for the generation of SUPANOVA models. The artificial $\sigma-\varepsilon$ curves were generated randomly from the five material parameters within the realistic ranges of interest. A total of 150 material inputs (five material parameters for each) and corresponding FEM *P-l* curves were produced. Each dataline for the SUPANOVA training dataset includes four inputs and one input. Considering the correlations between the five material parameters and assuming $E$ to be constant for Al alloys, $P$, $\sigma_{el}$, $\sigma_{0.2}$, and $n$ were used as inputs, and $l$ was used as an output. Four SUPANOVA models were generated based on different selections of training datasets. The output $l$ can be considered as a function of the respective load $P$ and material parameters $\sigma_{el}$, $\sigma_{0.2}$, and $n$ in the SUPANOVA models. The performance of each SUPANOVA model was examined and for all of them good agreements were achieved between SUPANOVA and FEM obtained *P-l* results. Model 4 was found to give the minimum rms error among the four models and it was chosen for further optimisation analysis.

5) Optimisation

A Genetic Algorithm (GA) was used in the optimisation process. The GA searches the solution space while evaluating the simulated solution, which can be obtained from SUPANOVA model 4, to give a best guess of material inputs for a given *P-l* data set. It achieves this by minimising the rms error between input *l* and the SUPANOVA-

generated $I^S$ with consideration of the constraints (ranges of material inputs) in the form of penalty functions. Finally, the optimisation process was performed on both artificial data (training data and unseen data) and control materials. Satisfactory agreements were achieved although some discrepancies exist between original and predicted material inputs. As a result, the predicted stress-strain curves of lining materials of AS16 and AS1241 were used in flat strip and bearing modelling for fatigue analysis and microstructure modelling to investigate initiation behaviour.

### 4.1.2   Conclusions and discussion

The characterisation methodology described in this thesis was developed for thin layer materials for which traditional tensile tests could not be performed. The thin layer materials of interest in this project are Al bearing lining alloys, but it is possible for the methodology to be easily expanded to other materials. To achieve this for other materials of interest such as steel, a new SUPANOVA model based on FEM results for similar artificial materials is required since the data used to construct current SUPANOVA model has rather specified ranges for Al alloys. The indentation FE model needs to be re-evaluated for new materials. Due to the generic nature of the methodology, the characterisation procedure could be easily repeated for new materials. The respective ANSYS program and MATLAB scripts are described and given in Appendix J to allow future access.

1) Tensile tests

The stress-strain curves obtained from tensile tests on control materials help to establish key material parameters and realistic ranges of these parameters for Al alloys. They are also used for validation of FEM simulation of indentation. It is notable that these tensile tests were performed by other colleagues due to the limitation of available alloys. Thus, lack of full control of the test conditions and doubt about the quality of the stress-strain curves obtained, has affected the evaluation of the indentation FE modelling. Ideally all control materials should be in similar condition, i.e., either annealed or work-hardened. In this project elasto-plastic properties of work-hardened materials are of more interest since the bearing linings

experience a significant work-hardening process. It will be helpful to have systematic generation of data with full control of conditions during the tensile tests. Multiple tensile tests should be performed on the same material to increase the accuracy of tensile test data. More materials are needed for tensile test data. This will also help to identify a more rational spread of experimental (tensile) data. It can also enrich the knowledge of the nature of elasto-plastic properties, from which the selection of key material parameters could be improved. The stress-strain curves described by the five material parameters used currently in the characterisation analysis could not exactly match those from experiments. It is possible to add additional parameters, e.g., a characteristic strain and/or stress, to avoid the mismatch, hence to improve the performance of the whole methodology. Increasing the number of inputs the SUPANOVA model will require a much amplified dataset. Typically at least $2^n$ datalines are required where $n$ is the number of inputs. The datalines used in current SUPANOVA model are more than the requirement (16) for 4 inputs.

2) Vickers micro-hardness tests

*P-l* curves of control materials and linings were obtained from Vickers micro-hardness tests. The results of hardness tests for control materials are consistent with the relative trends of the $\sigma$-$\varepsilon$ curves, which implies that a relation between the *P-l* curve and the $\sigma$-$\varepsilon$ curve exists. This possibility is confirmed by the extraction of elasto-plastic properties from micro-hardness tests. The error ranges of the five readings made for each applied load in the micro-hardness tests of this project are acceptable. However the reliability of obtained data could be improved by increasing the number of readings per load, hence improving the quality of predicted $\sigma$-$\varepsilon$ curve.

The Vickers micro-hardness test is chosen here because it is simple and easy to apply. However it should be noted that there is a limitation of the test for characterisation. Since the indentation made from Vickers hardness test corresponds to essentially a flow strain value in the materials, the elasto-plastic information included the *P-l* curve, such as Young's modulus, may not be complete. It is therefore probably difficult to fully determine the $\sigma$-$\varepsilon$ curve from Vickers micro-hardness tests. The relationship between *P-l* curves and $\sigma$-$\varepsilon$ curve should be examined carefully in

further work, with the use of different shaped indenters (e.g., spheres) assessed, as these may evaluate more of a range in flow stress values as load is increased.

## 3) FE modelling

The axi-symmetric FE model with rigid indenter was developed to simulate the micro-hardness process. The FEM results for control materials show that this model gives good agreements when the materials are soft, and discrepancies exist when the materials are hard. However, since this project focuses on soft materials such as the linings of AS16 and AS1241 bearings and flat strips, and the axi-symmetric model shows good prediction ability with materials similar ranges of interest, it should be sufficient for the subsequent modelling for the use of material characterisation process. It may also be helpful to further refine the choice of various parameters (e.g., contact stiffness) towards improving the axi-symmetric model.

## 4) Adaptive numerical modelling

Four SUPANOVA models were developed and their performances were evaluated by considering rms error between the input indentation size vector $l$ (from FEM) and predicted $l^S$. The training dataset used for SUPANOVA models consist of artificial stress-strain curves within the realistic ranges and FEM results. For both training dataset and test dataset (unseen by the SUPANOVA model) there is a discrepancy between predicted $l^S$ and input $l$. This error is due to averaging over a number of interpolations and is greater at low load levels, which can be attributed to the higher relative error in FEM results at these load levels. Setting aside the inaccuracy due to SUPANOVA approximation itself, the only way to reduce this error is to improve the performance of the indentation FE modelling. It is shown that increasing the number of datasets used for training can improve the performance of the generated SUPANOVA models by giving smaller rms error. Well-distributed training datasets in the input space will also improve the performance of SUPANOVA models. The criteria for prediction accuracy need to be carefully evaluated in further work.

5) Optimisation

Initially optimisation was performed on both training and test datasets of SUPANOVA models using a GA. Discrepancies within acceptance ranges exist between the original material parameters inputs $\mathbf{x}^{exact}$ and predicted $\mathbf{x}^{op}$, which produced almost identical load-indentation size curves. It is noted that the rms error of $\mathbf{I}^S(\mathbf{P}, \mathbf{x}^{op})$ is smaller than that of $\mathbf{I}^S(\mathbf{P}, \mathbf{x}^{exact})$, which means that the stress-strain curve found by GA is indeed the "optimum" solution for the specified objective function and the parameter ranges and constraints. The discrepancy between $\mathbf{x}^{exact}$ and $\mathbf{x}^{op}$ seems to contradict the purpose of optimisation in finding a stress-strain curve as close as possible to the actual one and it is due to the inherent non-zero error of $\mathbf{I}^S(\mathbf{P}, \mathbf{x}^{exact})$. Ideally the SUPANOVA model should give the same $\mathbf{I}^S(\mathbf{P}, \mathbf{x}^{exact})$ as the FEM. Since $\mathbf{I}^S(\mathbf{P}, \mathbf{x}^{exact})$ is not zero, there is a chance for a GA to find a better solution $\mathbf{x}^{op}$, which produces the minimum rms error of $\mathbf{I}^S(\mathbf{P}, \mathbf{x}^{op})$ among all possible $\mathbf{x}$. This can be illustrated schematically in Figure 4-1 where material properties are represented by a single parameter $x$.
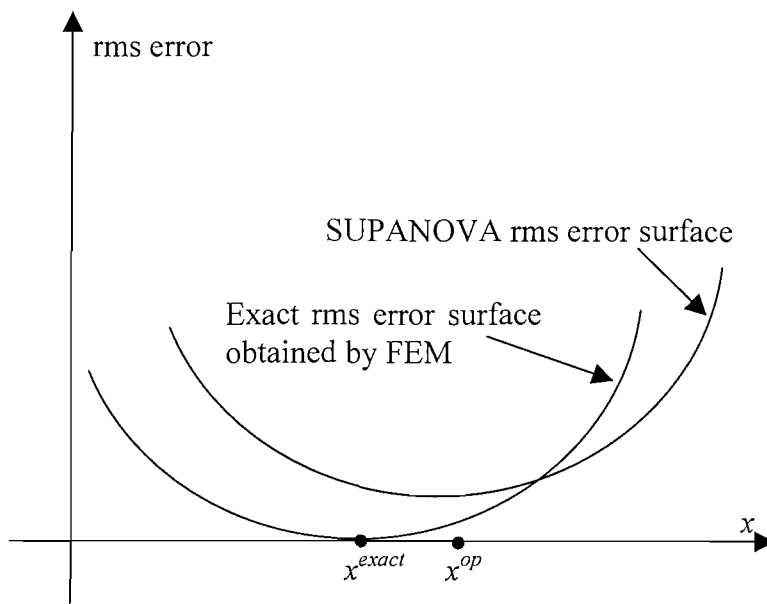


Figure 4-1: Schematic diagram of rms error surface

As seen from Figure 4-1, for a given load set, the rms error surface due to a perturbation around $x^{exact}$ should be tangent to the $x$ axis. However, due to the numerical error of the SUPANOVA calculation, the respective rms error surface is not tangent to the $x$ axis and its minimum is displaced to the left or to the right of $x^{exact}$.

This error surface was numerically found to be rather "flat", that is, the error is not particularly sensitive to the perturbation of $x$. For this reason, the discrepancy between $x^{op}$ and $x^{exact}$ was found to be considerable in certain cases. By further consideration of the definition of rms error and improving SUPANOVA model, it should be possible to reduce the discrepancy caused and therefore improve the performance of material characterisation.

## 4.2 Microstructure modelling

### 4.2.1 Summary

The microstructure modelling aims to investigate the role of the microstructure of the lining material in controlling fatigue crack initiation based on evidence from finite body tessellation (FBT) of polished sections. Fatigue tests on AS1241 and AS16 show that most of the crack initiations occur due to the debonding of particles, which indicates that the high stress and strain in the interface between particles and matrix are most susceptible to cause initiation. The maximum hydrostatic stress and maximum plastic shear strain in particles or in the matrix adjacent to the periphery of a particle were adopted as possible causes of initiation behaviour as suggested by previous researches on AS1241 and AS16 linings. FE analyses were performed on both idealised multi-particle models and simulations of real microstructure. Tessellation results obtained from AS16 flat strip lining with the load parallel to the rolling direction (designated AS16 Para.) were systematically investigated using a classification SUPANOVA model to identify a number of microstructure parameters and their combination that were important to crack initiation.

1) FE validation analysis and multi-particle analysis

In order to assess the reliability of the developed FE two-phase models, the benchmark problem involving a single elliptical elastic particle in an infinite plate with different elastic properties under far field load was analysed for both hard and soft inclusions. In both cases good agreement was achieved between FEM results and analytical solutions.

A 2D embedded cell model consisting of regular hexagonal particle patterns was developed to investigate the effect of several tessellation parameters on hydrostatic stress and maximum plastic shear strain. Sensitivity analysis showed that a two-layer hexagonal particle pattern is sufficient for obtaining a good representation of stress and strain distribution around the central particle in such a periodical microstructure. The material properties predicted by the material characterisation method developed earlier were used in the modelling of flat strip linings. In the modelling, the particle size and the distance between particles $d$ were allowed to vary independently to reflect the range of respective tessellation parameters so that the results could be compared with information obtained from FBT.

The FEM results from the analysis of the idealised AS1241 microstructure show that both maximum plastic shear strain and maximum hydrostatic stress in the Al matrix on the periphery of the central Si particle increase with $LAF$ within the significant range of $LAF$ according to FBT evidence from the real microstructure. The particle size has very little effect on both relations. Similar trends were observed when $d$ was varied.

In the case of the idealised AS16 microstructure, the stress and strain in both Sn particle and Al matrix were examined with varied $LAF$ or $d$. In Sn the predicted maximum plastic shear strain drops slightly as $LAF$ increases and then increases while the maximum hydrostatic stress was found to increase over the whole range of $LAF$ tested. In the Al matrix, both initiation parameters are falling over a lower range of $LAF$, within which the significant range of $LAF$ in real microstructure lies. In Sn both initiation parameters are mainly falling over a lower range of $d$ and then increasing slightly (or remain constant) while in the surrounding Al matrix, they drop first as $d$ increases then increase.

2) Modelling of real AS16 lining microstructure

From replica records with identified initiation sites of the early fatigue tests on AS16 flat strip, local embedded cell FE modelling was developed to investigate the development of stress and strain in the real microstructure. Among the areas selected for modelling, some contain at least one initiating particle, and others include only

non-initiating particles. Contour plots of FEM results show highly non-uniform stress and strain distributions within the matrix and Sn particles due to the Sn particle variable size, shape and irregular pattern. From the modelling of areas with initiating particles, it is found that the high stress and strain is distributed along directions approximately perpendicular to the loading direction at the boundary of Sn particles and matrix as implied by the analysis of a single soft inclusion. Correlations were seen between the locations of high stress and strain of both Al and Sn and the crack initiation sites of the replica record. From the comparison of the maximum values of maximum plastic shear strain and hydrostatic stress in the modelling of real microstructure and in a similar modelling of homogeneous materials, a significant magnification of these values were found in the real microstructure. Also, the results from most areas with initiating particles indicated a strong correlation between the maximum values of the two critical stress and strain parameters and initiating particles. It is noted that for the two areas without initiating particles, the obtained maximum values are lower than those for most of the areas with initiating particles.

3) Assessment of tessellation results and classification analysis

The real microstructure modelling however does not provide much information on how the microstructure parameters affect the initiation behaviour. It is therefore important to apply other methods to investigate the effect of microstructure on fatigue initiation. A detailed assessment of tessellation results was performed on AS16 Para. data and comparisons with AS16 Perp. and AS1241 data were made. The cells produced by the tessellation were divided into two populations according to the behaviour of the enclosed secondary particles: initiating class and non-initiating class. Due to the rolling directionality introduced during the rolling process, the AS16 Para. data has a lower *OAng* than AS16 Perp. data. For AS16 Para. data, the observation shows that the initiating class has a higher *OA*, *CA*, *LAF*, *OAspRat*, *OAng*, *CAng*, *No. NNs*, $d_{min}$ and $d_{mean}$ and a lower *CAspRat* than non-initiating class, which is confirmed by both the statistical results and frequency distribution histograms. Similar observations were made for both AS16 Perp. and AS1241 data except that AS1241 data shows a similar *OAspRat* in both classes. More complex trends were observed for the measurement of *NNAng*. The mean values of *NNAng* of AS1241 and AS16 Para. data in the initiating classes are lower than that of non-initiating classes, whereas the

opposite trend was found for AS16 Perp. data. However the trends observed in AS16 Para. data and AS16 Perp. data are not totally contradictory. Instead of a single distinct peak of the initiating class frequency distribution at a high value in the histogram of AS16 Perp. data, peaks are found appearing at both high and low values for the initiating class of AS16 Para. data. This probably indicates a more complex effect of *NNAng* on initiation in the microstructure of AS16 Para. lining than in AS16 Perp. lining. The more or less randomly distributed frequency of *NNAng* of AS1241 data indicates a lesser effect of *NNAng* in the case of Si secondary phases.

This assessment is based only on individual tessellation measurements. It is likely that the complex mechanism of crack initiation is dependent on combinations of more than one of the measurements. SUPANOVA was then applied as a classification technique to investigate possible combinations leading to failure thus helping to predict initiation. A total of 29 significant terms (individuals or combinations of the 11 FBT parameters) were selected in the AS16 Para. SUPANOVA models, indicating complex effects of FBT parameters on the initiation behaviour. The interaction of these terms were grouped and summarised in Table 3-7 according to their contribution to initiation.

The critical features determined by SUPANOVA analysis could be further explored and visualised with the help of simulated particle populations, for which the distribution of critical stress and strain fields could be assessed by FEM and then compared with the location of likely initiating particles predicted by SUPANOVA. The procedure of this method was presented but not applied because a further refinement of the SUPANOVA model is required.

### 4.2.2   Conclusions and discussion

1) FE validation analysis and multi-particle analysis

Over the significant range of *LAF* in the real microstructure of AS1241 flat strip lining, the FE results indicate that microstructures with high *LAF* are more likely to initiate fatigue failure, which agrees with the tessellation results on initiating Si

particles. It is also evident from FE results that above a certain limit this trend is reversed, that is, very high *LAF* would prevent initiation. It is more difficult to establish a clear relation between particle distance $d$ and initiation trends because of the dual interpretation of d as both $d_{min}$ and $d_{mean}$ in the real microstructure. If $d$ is considered as $d_{min}$, FEM and tessellation results agree that the likelihood of initiation increases for a higher $d$. This consistency is not however apparent when $d$ is considered as $d_{mean}$, which appears to suggest that $d_{min}$ may be a more critical parameter for initiation than $d_{mean}$ under the adopted initiation criteria.

In the case of the AS16 lining, the possibility of failure in either Sn or Al is examined. Over the significant range of *LAF* in the real microstructure, the FEM results agree with tessellation results that initiation is more likely for higher *LAF* if the hydrostatic stress is accepted as the critical factor and failure occurs in Sn rather than Al. Over the significant range of $d_{min}$, the FEM results for both initiation parameters do not indicate trends consistent with tessellation results. When $d$ is considered as $d_{mean}$, both initiation parameters in Sn particles show little variation as $d$ increases, thus they do not give any clear trends of $d_{mean}$ on initiation. Over the significant range of $d_{mean}$, the FEM results agree with tessellation results that the likelihood of initiation increases as $d_{mean}$ increases provided failure occurs in Al. Failure in Sn would therefore seem to be associated with high *LAF* while failure in Al with high $d_{mean}$. However it should be noted that the current FE model does not simulate interfacial failure (the interface is assumed to be perfectly bonded). Further investigation of interfacial failure modes through varying the interfacial bond strength is a possible area of further work.

2) Modelling of real AS16 lining microstructure

Due to the limitation in the resolution of microscopes and in the size of the FE model that can be generated, it is not possible to reproduce the exact shapes of particles in the modelling of a real microstructure. This may reduce or amplify stress/strain concentration in the analysis results. However, obvious correlations were still observed between initiating particles and maximum plastic shear strain and hydrostatic stress for most of the regions modelled. This indicates that these two parameters are important in the investigation of initiation behaviour. Areas without initiating particles gave smaller maximum values for maximum plastic shear strain

and hydrostatic stress than those obtained from the areas with initiating particles. If all areas are considered together, this suggests that the predictions have been consistent with experimental observations. Another limitation that may explain discrepancies between analysis and experiment is that the current FE model is two-dimensional, based on replicas of one section of specimens, while the microstructure is three-dimensional in reality. Thus the modelling results may not always reflect the actual stress and strain fields. A 3D model would have provided more global information for assessing initiation behaviour, although gathering the relevant experimental data would have been challenging.

3) Assessment of tessellation results and classification analysis

From the analysis and comparison of the 11 individual FBT parameters of AS16 Para., and AS16 Perp. data, it suggests that isolated (remote from their immediate neighbours) large particles having their longest axis aligned almost perpendicular to the global tensile stress field, with a high local area fraction and more near neighbours, show a great probability of initiating cracks. In the case of AS1241 lining materials for which the secondary phases are Si, isolated large particles with high local area fraction and more near neighbours show a great probability of initiating particles.

The SUPANOVA analysis of AS16 Para. data shows much more complex trends in classification and prediction of initiation particles. It shows that the Sn particle in the AS16 lining (parallel) most associated with fatigue appear to be larger than average, long, aligned perpendicular to the tensile axis in a relatively unclustered area of microstructure (far away from its near neighbours). This conclusion agrees with the observation from individual tessellation measurements and their frequency histograms, but apparently more complex relationships are involved, e.g., if the nearest neighbour is above and has its long axis aligned the axis of the Sn particle, it also promotes cracks. Similar conclusion was obtained for AS16 Perp. data. The SUPANOVA analysis of AS1241 data suggests that the Si particles associated with fatigue appear to be larger than average and have their major axis aligned parallel to the tensile axis of loading. The opposite alignment behaviours between AS16 and AS1241 data agree with the FEM results of the single particle analyses, which show

that the maximum stress/strain occurs at different positions for soft and hard inclusions.

## 4.3 Further work

The current study includes the methodology development of material characterisation and microstructure modelling on initiation behaviour. Several suggestions have already been made in discussions of results for improvements to these methodologies. Both of them could be refined to enhance current understanding. A summary of possible directions for further work is given below:
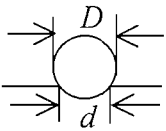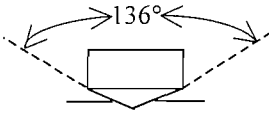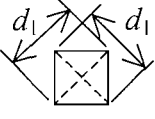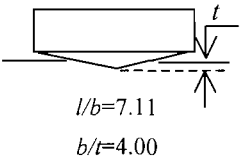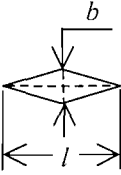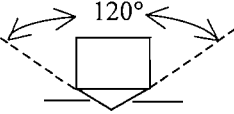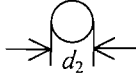
- Material characterisation
  - More tensile tests on various alloys (or other materials) should be performed. The analysis of obtained stress-strain curves will help to define more reasonable key material parameters.
  - More readings of micro-hardness tests for each applied load may be taken. This should provide a more accurate load-indentation size curve.
  - Other hardness techniques could be considered to apply, e.g., a spherical indenter can give information on plastic deformation of materials, and instrumented nano-hardness tests provide information on local microstructures such as Sn secondary phase.
  - FE modelling of simulation of indentation should be further refined. This should improve the FEM prediction, which will reduce possible error in the SUPANOVA analysis.
  - More and better-distributed training datasets should be generated to build SUPANOVA models. This will help to improve the prediction accuracy of SUPANOVA model.
  - The definition of rms error in the SUPANOVA model and optimisation should be re-considered. For example, it is noted that the definition of rms error does not consider the weight of different load levels, for which the FEM results have been already shown to have different accuracies. This will certainly affect the selection of the optimised material parameters in following process. Doing this will help to reduce the discrepancy between

predicted material property and actual properties, therefore improving the predictions.

- FE modelling of microstructure

  - FE models on different particle patterns, particle shapes and orientations could be developed. This would allow investigation of other tessellation parameters using FEA.

  - Interfacial failure between particles and the matrix should be considered in FE models. This would help to investigate the initiation behaviour in a more realistic situation.

  - More data on initiating and non-initiating particles should be obtained to improve classification models (SUPANOVA). The current model shows an inability to differentiate the differing features of non-initiation particles from initiation particles; with more data it is expect to improve the prediction.

  - FE modelling on idealised particle distributions should be performed. Once the SUPANOVA model is improved, the modelling of idealised particle distribution will help to more fully elucidate the effect of microstructure on the initiation behaviour, with critical population parameters differences being identified from the SUPANOVA model and then systematically investigated via FE.

# Appendix A: Hardness Test Techniques

Hardness is a measure of a material's resistance to localised plastic deformation (e.g., a small dent or a scratch). Quantitative hardness techniques use a small indenter which is forced into the surface of a material to be tested, under controlled conditions of load and rate of application. The depth or size of the indentation is then measured and related to a hardness number. A higher hardness index number is related to a larger and deeper indentation, which means a relatively softer material. According to the indenter shape and load applied, the most common hardness test techniques can be clarified as: Brinell hardness test, Vickers micro-hardness test, Knoop micro-hardness test and Rockwell hardness test, etc. The details of these hardness test techniques are listed below.

| Test | Indenter | Shape of Indentation | |
|---|---|---|---|
| | | Side View | Top View |
| Brinell | 10 mm sphere of steel or tungsten carbide |  |  |
| Vickers micro-hardness | Diamond pyramid |  |  |
| Knoop micro-hardnesst | Diamond pyramid |  $l/b=7.11$ $b/t=4.00$ |  |
| Rockwell | Diamond cone |  |  |

# Appendix B: SUPANOVA Indentation Models

This Appendix provides detailed information on the four SUPANOVA indentation models generated from FE-simulated data. All the "training data" properties as well as the rms error of the corresponding SUPANOVA indentation prediction are listed in Tables B-1 to B-4, for models SA1 to SA4, respectively.

**Table B-1: RMS error of each x in SA1**

| Material | $\sigma_{el}$ (MPa) | $\sigma_{0.2}$ (MPa) | $n$ | rms error ($\mu$m) |
|---|---|---|---|---|
| A1 | 90.9 | 193.8 | 0.1143 | 1.2252 |
| A2 | 230.4 | 279.7 | 0.0800 | 0.7930 |
| A3 | 239.9 | 312.4 | 0.0566 | 0.7446 |
| A4 | 70.0 | 131.3 | 0.1787 | 1.4508 |
| A5 | 220.5 | 285.5 | 0.1415 | 0.7907 |
| A6 | 255.7 | 346.9 | 0.0937 | 0.5249 |
| A7 | 149.4 | 179.7 | 0.1117 | 1.3069 |
| A8 | 250.7 | 335.3 | 0.0790 | 0.5460 |
| A9 | 111.3 | 176.5 | 0.2082 | 1.1449 |
| A10 | 79.3 | 151.6 | 0.1976 | 1.1799 |
| A11 | 198.4 | 243.8 | 0.0652 | 1.1012 |
| A12 | 47.5 | 96.6 | 0.2534 | 1.4607 |
| A13 | 282.8 | 340.1 | 0.1009 | 0.5241 |
| A14 | 53.2 | 136.5 | 0.1710 | 1.3712 |
| A15 | 53.5 | 108.8 | 0.1993 | 1.6860 |
| A16 | 57.1 | 162.0 | 0.1738 | 1.1625 |
| A17 | 267.4 | 316.8 | 0.0938 | 0.5687 |
| A18 | 174.8 | 288.4 | 0.1026 | 0.7066 |
| A19 | 290.2 | 317.6 | 0.0561 | 0.7254 |
| A20 | 81.6 | 131.3 | 0.1532 | 1.6632 |
| A21 | 265.7 | 374.0 | 0.0790 | 0.4757 |
| A22 | 115.0 | 154.6 | 0.1347 | 1.4251 |
| A23 | 74.2 | 162.2 | 0.1409 | 1.2734 |
| A24 | 67.1 | 127.3 | 0.2232 | 1.2138 |
| A25 | 175.7 | 247.3 | 0.0502 | 1.1580 |
| A26 | 182.0 | 219.9 | 0.0619 | 1.3383 |
| A27 | 203.0 | 265.5 | 0.0739 | 0.8920 |
| A28 | 285.3 | 330.0 | 0.1010 | 0.5073 |
| A29 | 283.3 | 391.5 | 0.0824 | 0.4668 |
| A30 | 249.9 | 330.8 | 0.0661 | 0.6031 |

## Table B-2: RMS error of each x in SA2

| Material | $\sigma_{el}$ (MPa) | $\sigma_{0.2}$ (MPa) | $n$ | rms error ($\mu$m) |
|---|---|---|---|---|
| A31 | 50.0 | 163.85868 | 0.1931 | 1.3392 |
| A32 | 232.7 | 312.88606 | 0.0559 | 1.1936 |
| A33 | 192.1 | 259.45752 | 0.0609 | 1.3398 |
| A34 | 296.1 | 368.16725 | 0.0825 | 0.7236 |
| A35 | 259.4 | 286.06468 | 0.0925 | 0.9655 |
| A36 | 123.9 | 217.38199 | 0.1507 | 1.1092 |
| A37 | 150.5 | 187.12957 | 0.1738 | 1.1243 |
| A38 | 179.4 | 263.15212 | 0.1077 | 1.0175 |
| A39 | 83.6 | 135.89429 | 0.2495 | 1.4403 |
| A40 | 234.3 | 311.32427 | 0.0734 | 0.9578 |
| A41 | 147.6 | 261.05915 | 0.0844 | 1.1781 |
| A42 | 272.9 | 303.03676 | 0.1206 | 0.7546 |
| A43 | 234.2 | 291.62163 | 0.1380 | 0.8001 |
| A44 | 136.8 | 181.2856 | 0.1949 | 1.1820 |
| A45 | 51.7 | 143.00771 | 0.2338 | 1.4787 |
| A46 | 110.7 | 213.91374 | 0.1057 | 1.3932 |
| A47 | 197.1 | 289.45427 | 0.0823 | 1.0138 |
| A48 | 276.4 | 348.77583 | 0.1069 | 0.7090 |
| A49 | 296.6 | 384.83028 | 0.0543 | 1.2046 |
| A50 | 144.5 | 207.10498 | 0.1074 | 1.4395 |
| A51 | 139.8 | 226.04609 | 0.0783 | 1.4743 |
| A52 | 106.9 | 166.01924 | 0.1267 | 1.6557 |
| A53 | 43.3 | 73.880632 | 0.2437 | 2.5337 |
| A54 | 219.0 | 265.77774 | 0.1354 | 0.8873 |
| A55 | 208.3 | 274.81918 | 0.1476 | 0.8848 |
| A56 | 297.1 | 402.92397 | 0.0782 | 0.7291 |
| A57 | 87.2 | 159.14513 | 0.1191 | 1.9210 |
| A58 | 262.1 | 315.79422 | 0.1248 | 0.7548 |
| A59 | 218.2 | 261.61863 | 0.1495 | 0.8348 |
| A60 | 70.3 | 111.92058 | 0.1925 | 1.8747 |

## Table B-3: RMS error of each x in SA3

| Material | $\sigma_{el}$ (MPa) | $\sigma_{0.2}$ (MPa) | $n$ | rms error ($\mu$m) |
|---|---|---|---|---|
| B1 | 90.9 | 193.8 | 0.1143 | 0.7660 |
| B2 | 70.0 | 131.3 | 0.1787 | 0.9161 |
| B3 | 149.4 | 179.7 | 0.1117 | 0.8665 |
| B4 | 53.2 | 136.5 | 0.1710 | 0.8847 |
| B5 | 53.5 | 108.8 | 0.1993 | 1.0064 |
| B6 | 81.6 | 131.3 | 0.1532 | 1.0562 |
| B7 | 115.0 | 154.6 | 0.1347 | 0.9397 |
| B8 | 74.2 | 162.2 | 0.1409 | 0.8109 |
| B9 | 110.7 | 213.9 | 0.1057 | 1.1676 |
| B10 | 197.1 | 289.5 | 0.0823 | 0.9043 |
| B11 | 144.5 | 207.1 | 0.1074 | 1.2262 |
| B12 | 106.9 | 166.0 | 0.1267 | 1.4436 |
| B13 | 43.3 | 73.9 | 0.2437 | 1.9612 |
| B14 | 87.2 | 159.1 | 0.1191 | 1.6872 |
| B15 | 70.3 | 111.9 | 0.1925 | 1.5601 |
| B16 | 98.6 | 178.1 | 0.1113 | 1.2003 |
| B17 | 172.8 | 219.8 | 0.1312 | 0.9027 |
| B18 | 56.0 | 87.8 | 0.2392 | 1.3214 |
| B19 | 122.2 | 199.1 | 0.1327 | 0.9180 |
| B20 | 59.4 | 102.2 | 0.2139 | 1.2334 |
| B21 | 67.7 | 171.4 | 0.1620 | 1.0082 |
| B22 | 58.7 | 121.4 | 0.1626 | 1.4294 |
| B23 | 126.3 | 178.7 | 0.1441 | 0.9803 |
| B24 | 98.7 | 158.9 | 0.1345 | 1.1707 |
| B25 | 147.9 | 235.3 | 0.0613 | 1.0965 |
| B26 | 96.2 | 148.9 | 0.1680 | 1.0524 |
| B27 | 197.9 | 223.4 | 0.1254 | 0.8607 |
| B28 | 146.6 | 223.5 | 0.1239 | 0.8643 |
| B29 | 180.3 | 231.7 | 0.1141 | 0.8386 |
| B30 | 172.4 | 217.4 | 0.1218 | 0.8858 |
| B31 | 59.7 | 104.7 | 0.1968 | 1.3179 |

## Table B–4: RMS error of each x in SA4

| Material | $\sigma_{el}$ (MPa) | $\sigma_{0.2}$ (MPa) | $n$ | rms error ($\mu$m) |
|----------|------------|-------------|--------|------------|
| B1 | 90.9 | 193.8 | 0.1143 | 0.7060 |
| B2 | 70.0 | 131.3 | 0.1787 | 0.8588 |
| B3 | 149.4 | 179.7 | 0.1117 | 0.7924 |
| B4 | 53.2 | 136.5 | 0.1710 | 0.8321 |
| B5 | 53.5 | 108.8 | 0.1993 | 0.9231 |
| B6 | 81.6 | 131.3 | 0.1532 | 0.9559 |
| B7 | 115.0 | 154.6 | 0.1347 | 0.8535 |
| B8 | 74.2 | 162.2 | 0.1409 | 0.7387 |
| B9 | 110.7 | 213.9 | 0.1057 | 1.0800 |
| B10 | 197.1 | 289.5 | 0.0823 | 0.8420 |
| B11 | 144.5 | 207.1 | 0.1074 | 1.1375 |
| B12 | 106.9 | 166.0 | 0.1267 | 1.3308 |
| B13 | 43.3 | 73.9 | 0.2437 | 1.7712 |
| B14 | 87.2 | 159.1 | 0.1191 | 1.5585 |
| B15 | 70.3 | 111.9 | 0.1925 | 1.4230 |
| B16 | 98.6 | 178.1 | 0.1113 | 1.1108 |
| B17 | 172.8 | 219.8 | 0.1312 | 0.8553 |
| B18 | 56.0 | 87.8 | 0.2392 | 1.2272 |
| B19 | 122.2 | 199.1 | 0.1327 | 0.8603 |
| B20 | 59.4 | 102.2 | 0.2139 | 1.1348 |
| B21 | 67.7 | 171.4 | 0.1620 | 0.9598 |
| B22 | 58.7 | 121.4 | 0.1626 | 1.2989 |
| B23 | 126.3 | 178.7 | 0.1441 | 0.9153 |
| B24 | 98.7 | 158.9 | 0.1345 | 1.0751 |
| B25 | 147.9 | 235.3 | 0.0613 | 1.0307 |
| B26 | 96.2 | 148.9 | 0.1680 | 0.9838 |
| B27 | 197.9 | 223.4 | 0.1254 | 0.8127 |
| B28 | 146.6 | 223.5 | 0.1239 | 0.8153 |
| B29 | 180.3 | 231.7 | 0.1141 | 0.7862 |
| B30 | 172.4 | 217.4 | 0.1218 | 0.8318 |
| B31 | 59.7 | 104.7 | 0.1968 | 1.1880 |
| B32 | 57.7 | 99.3 | 0.2029 | 1.2226 |
| B33 | 109.7 | 149.7 | 0.1422 | 1.1116 |
| B34 | 72.5 | 157.2 | 0.1620 | 0.9785 |
| B35 | 72.8 | 120.7 | 0.1722 | 1.1766 |
| B36 | 168.9 | 234.8 | 0.0850 | 0.8855 |
| B37 | 53.6 | 81.1 | 0.2388 | 1.2793 |
| B38 | 99.5 | 137.9 | 0.1512 | 1.1667 |

# Appendix C: FE Modelling of Flat Strips

The flat strips of AS16 and AS1241 were subjected to fatigue tests by Mwanza to obtain the fatigue performance data. Three-point bending fatigue tests were performed on the specimens. Since the specimens contain three different material layers, it is difficult to apply analytical methods to work out the stress and strain fields in the aluminium lining. Thus FE models of the three-point bending tests were developed using ANSYS to calculate the top surface stresses and strains of the aluminium lining which were used to generate the appropriate S-N curves for the bearing and flat sheet strip.

Due to the symmetric geometry and loading condition of the flat strip tests, only half of the specimen was modelled as shown in Figure C-1. The whole two-dimensional FE model had 1680 8-node quadrilateral structural solid elements (PLANE82) and were solved in plane strain to simulate the material behaviour along a plane through the centre of the specimen. Elasto-plastic material models* were used for each layer to give a more thorough representation of the experimental tests. The load range applied was from 10N to 1000N. For each step loading of 10N the maximum top surface stresses and strains were calculated.
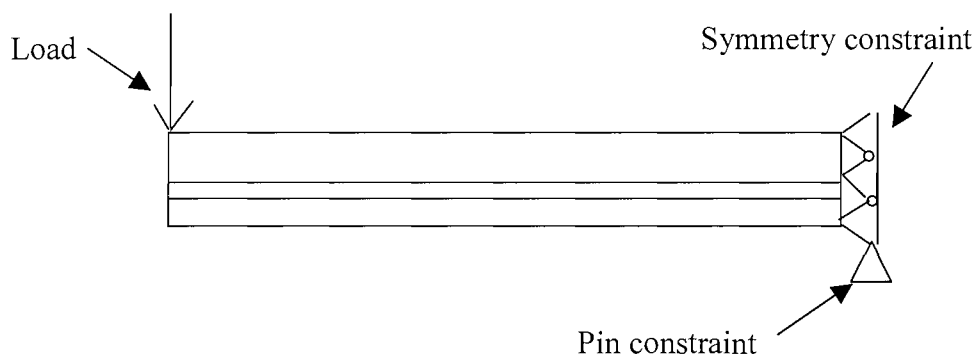


Figure C-1: Flat strip model geometry and loading conditions

---

* Thus the requirement for accurate elasto-plastic materials models is established, which is the focus of Chapter 2.

# Appendix D: Selected Histograms of AS1241 and AS16 Perp. Materials

In Appendix D, selected frequency histograms of AS1241 material systems and AS16 from previous projects are presented. Figures D-1 to D-3 show histograms for Si particles in the lining alloy of three AS1241 material systems of bearing, flat strip and monolithic alloy. The histograms in Figures D-4 to D-6 give the comparison of histograms for Si particles in initiating cells, bordering cells, and background cells of AS1241 flat strip. Figures D-7 to D-10 shows the comparison of Sn particles in initiating cells, bordering cells and background cells of AS16 flat strip.
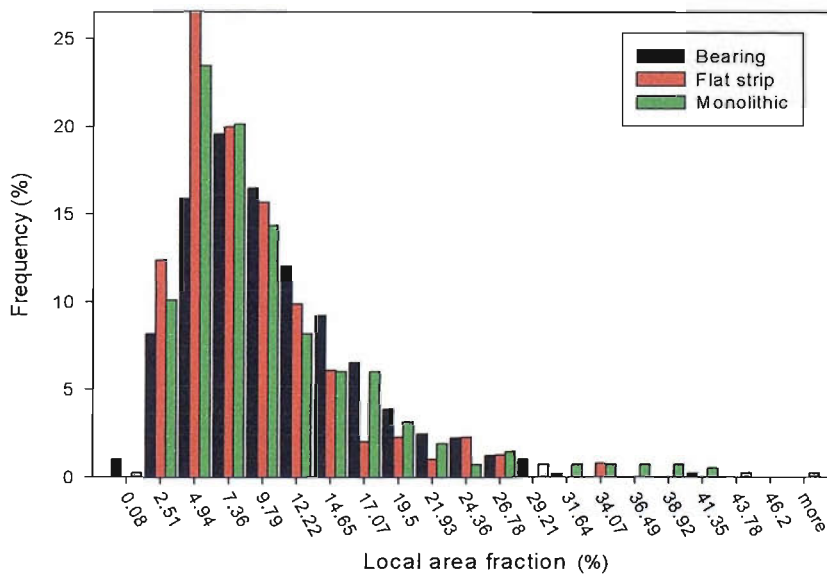


Figure D-1: Local area fraction histogram for Si particles in AS1241 material systems
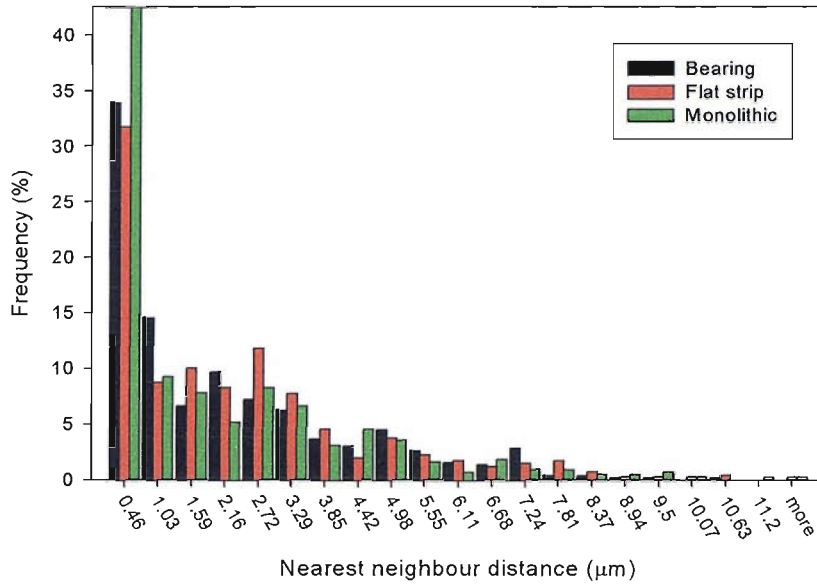
Figure D-2: Nearest neighbour distance histogram for Si particles in AS1241 material systems
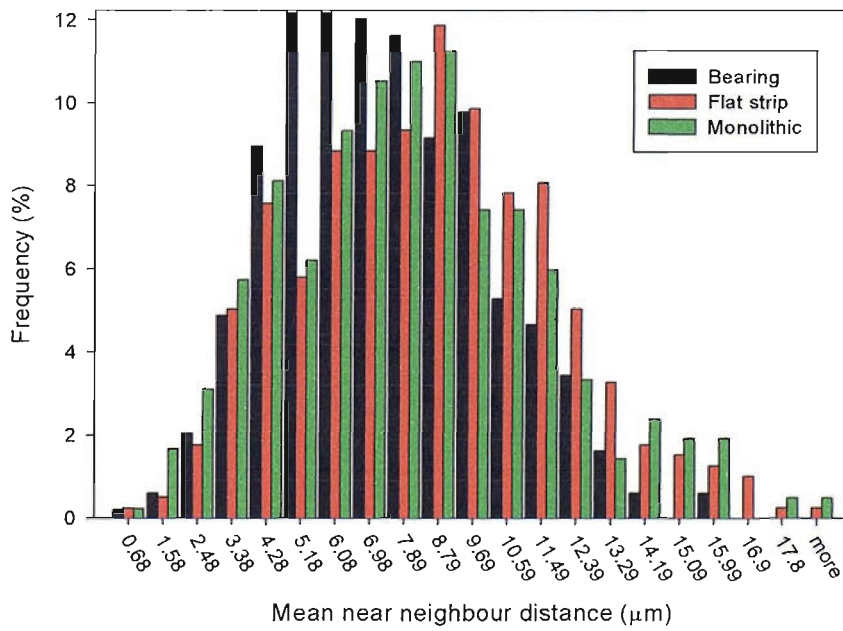


Figure D-3: Mean near neighbour distance histogram for Si particles in AS1241 material systems
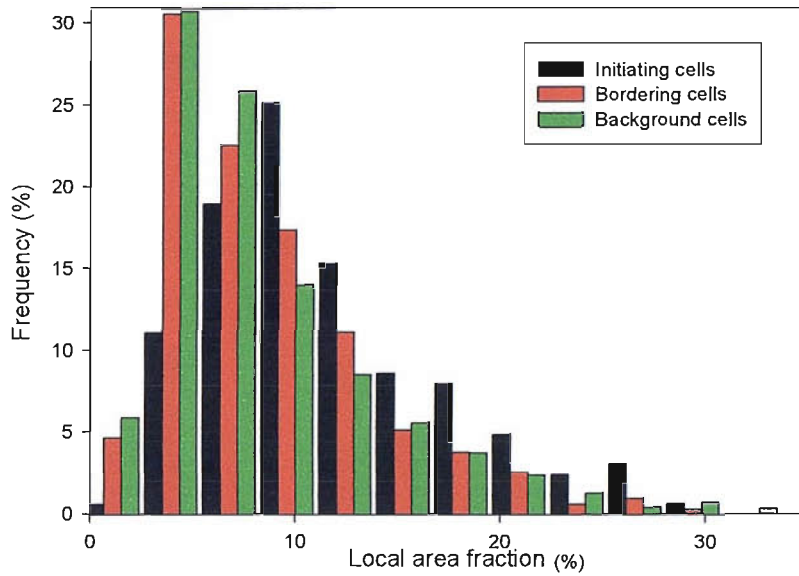
Figure D-4: Local area fraction histogram for Si particles in fatigued AS1241 flat strip
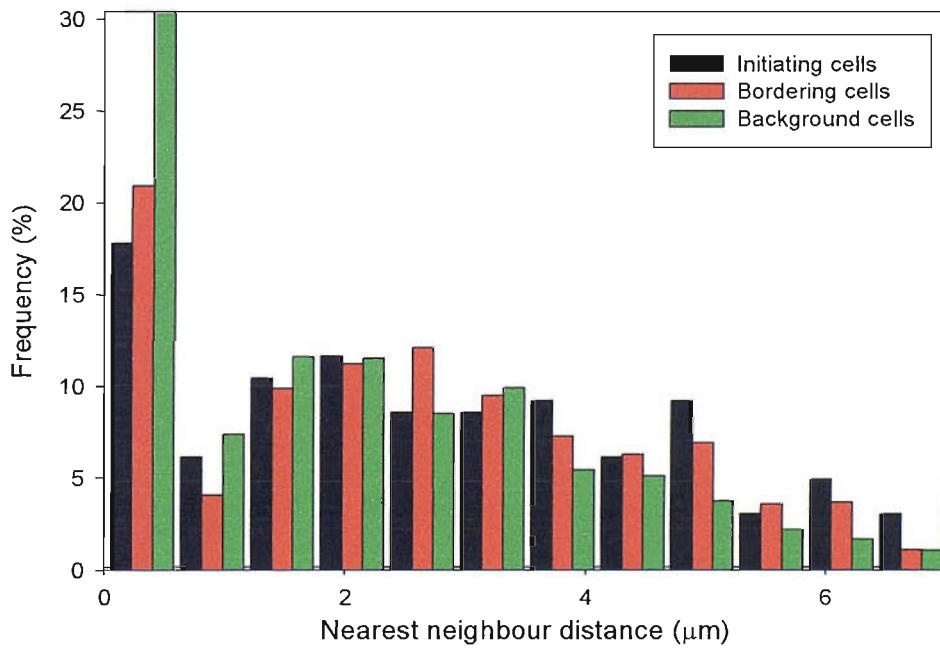


Figure D-5: Nearest neighbour distance histogram for Si particles in fatigued AS1241
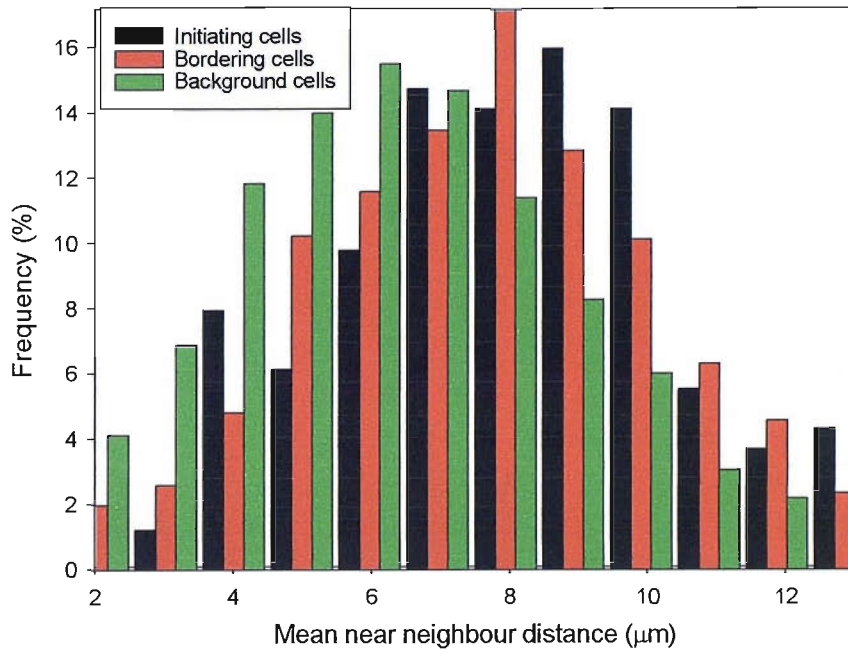
flat strip

Figure D-6: Mean near neighbour distance histogram for Si particles in fatigued AS1241 flat strip
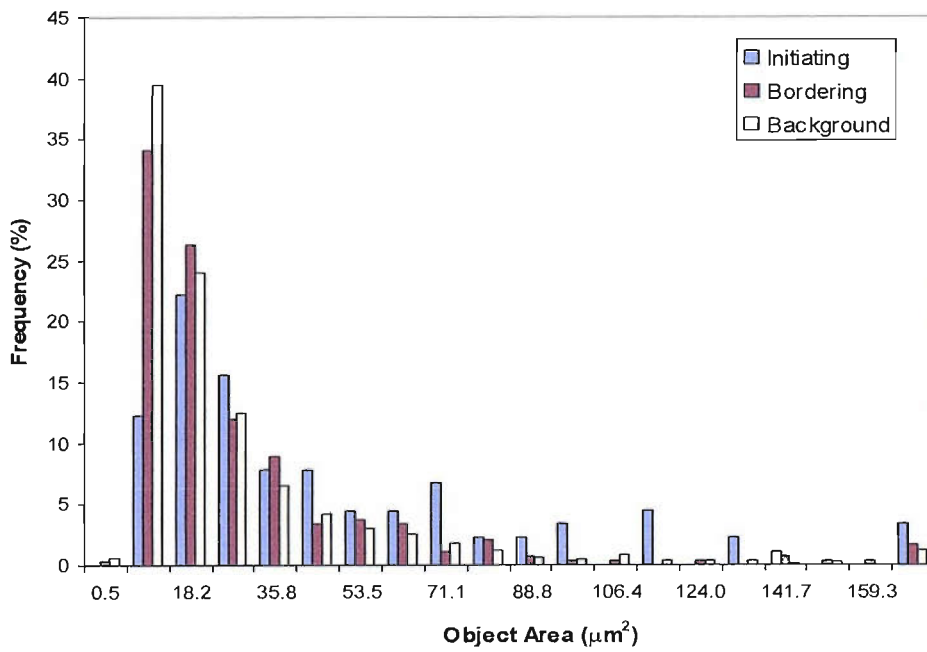


Figure D-7: Object area histogram for Sn particles in fatigued AS16 flat strip
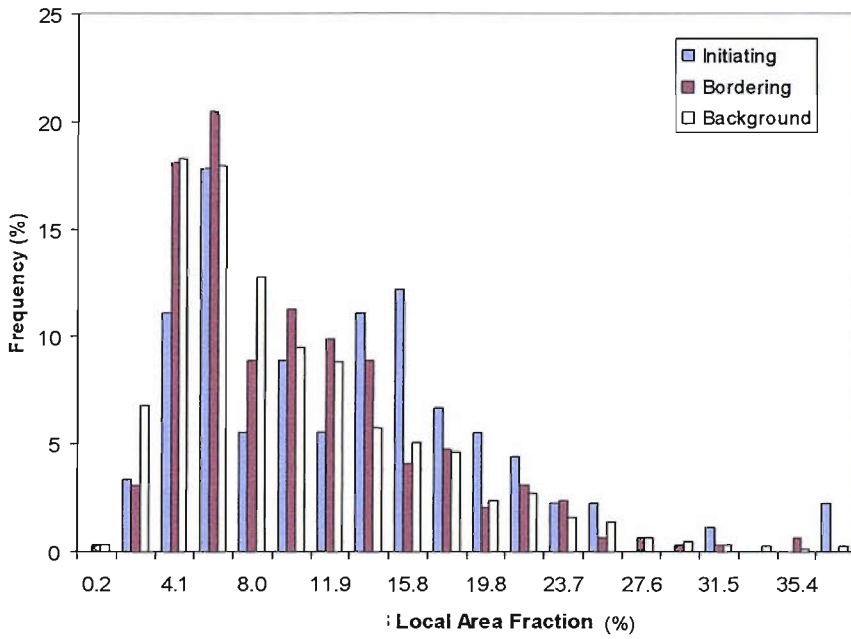
Figure D-8: Local area fraction histogram for Sn particles in fatigued AS16 flat strip
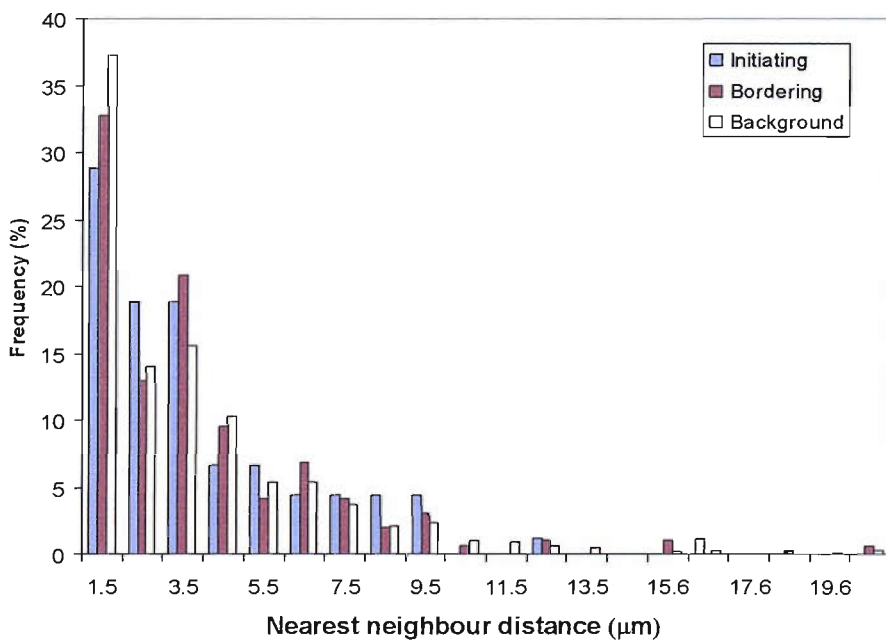


Figure D-9: Nearest neighbour distance histogram for Sn particles in fatigued AS16 flat strip
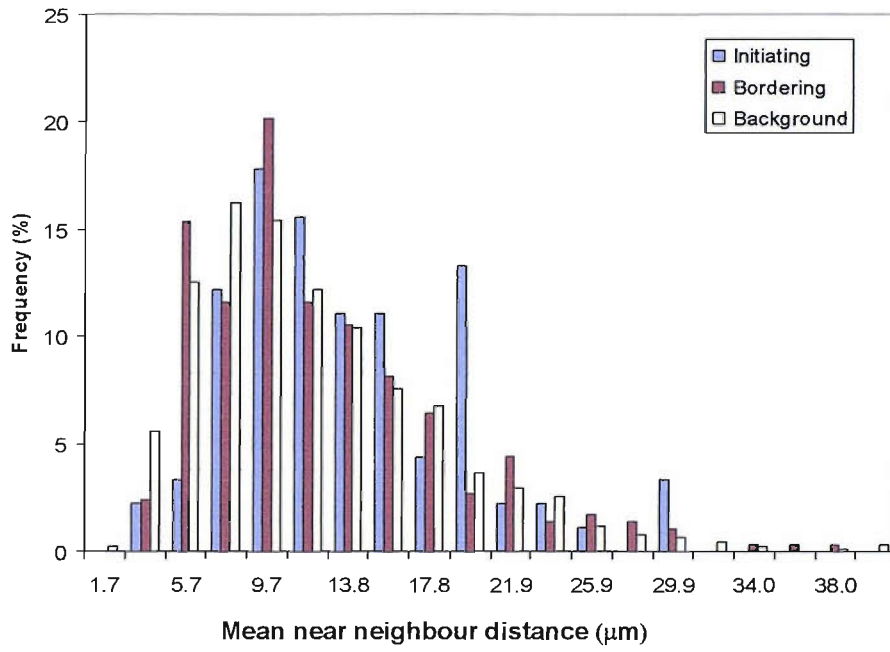
Figure D-10: Mean near neighbour distance histogram for Sn particles in fatigued AS16 flat strip

# Appendix E: Contour Plots of FEM on Real Microstructure of AS16 Flat Strip Lining

The real microstructure of the lining material of AS16 flat strip was modelled and selected contour plots of FEM results are presented in this appendix. Figures E-1 to E-4 are corresponding to the selected areas of real microstructure (see Figure 3-40) 1, 3, 4 and 9, respectively. Areas 1, 3 and 4 contain at least one initiating particle, while Area 9 includes only non-initiating particle.



Figure E-1 (a): Maximum plastic shear strain within Al matrix for Area 1
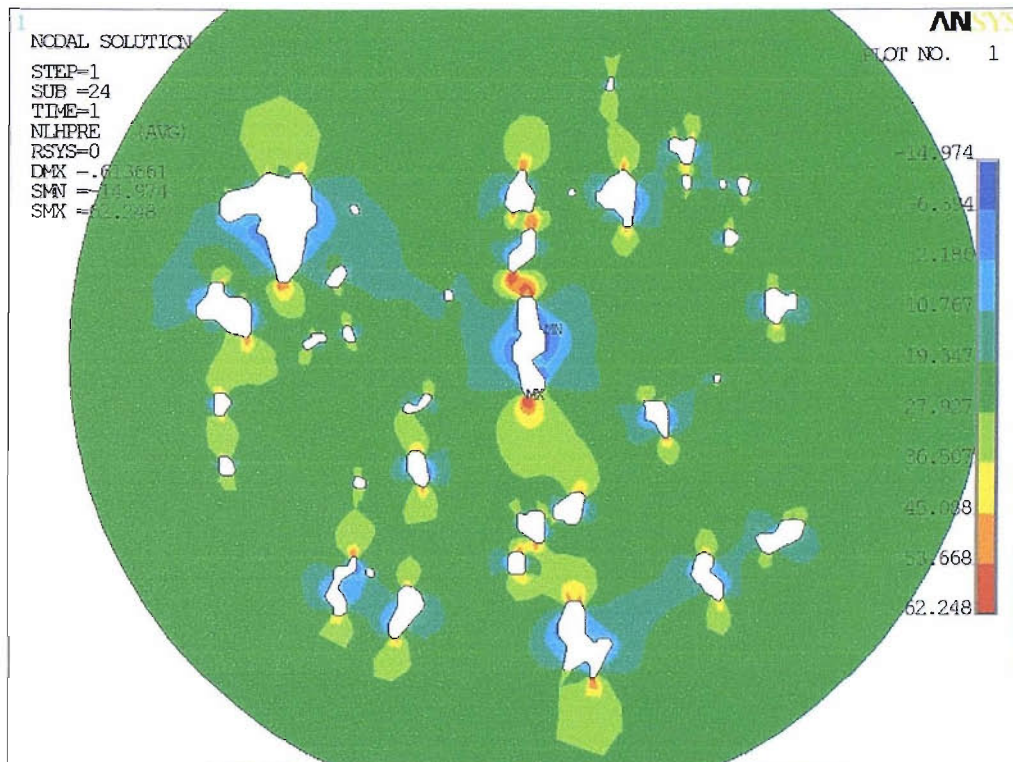
Figure E-1 (b): Hydrostatic stress within Al matrix for Area 1
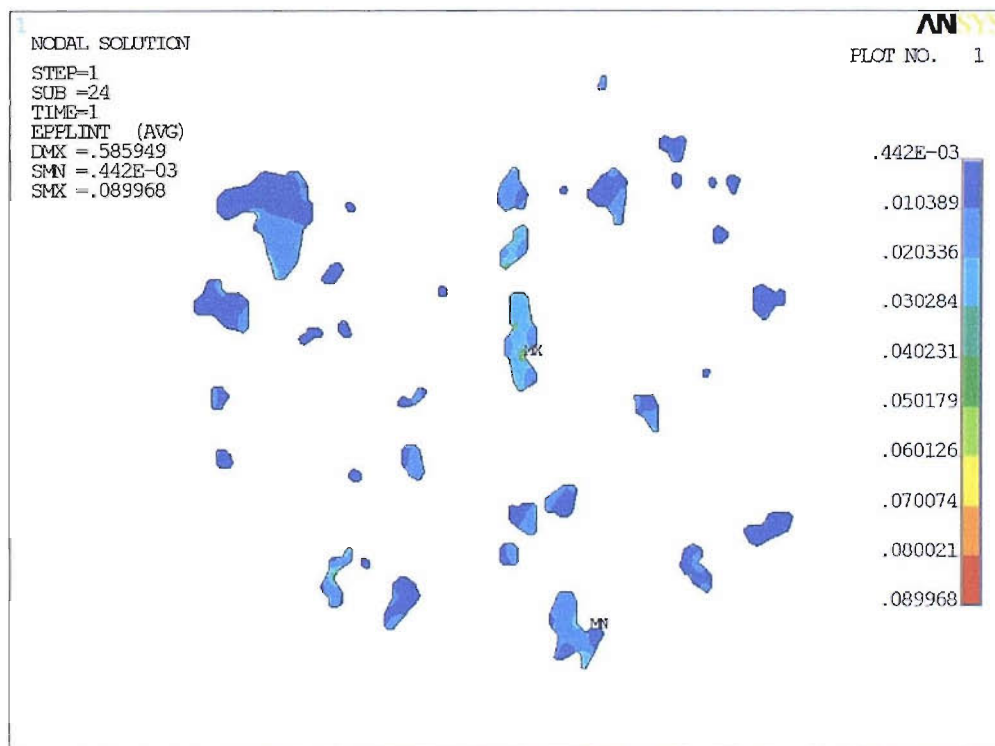


Figure E-1 (c): Maximum plastic shear strain within Sn particles for Area 1
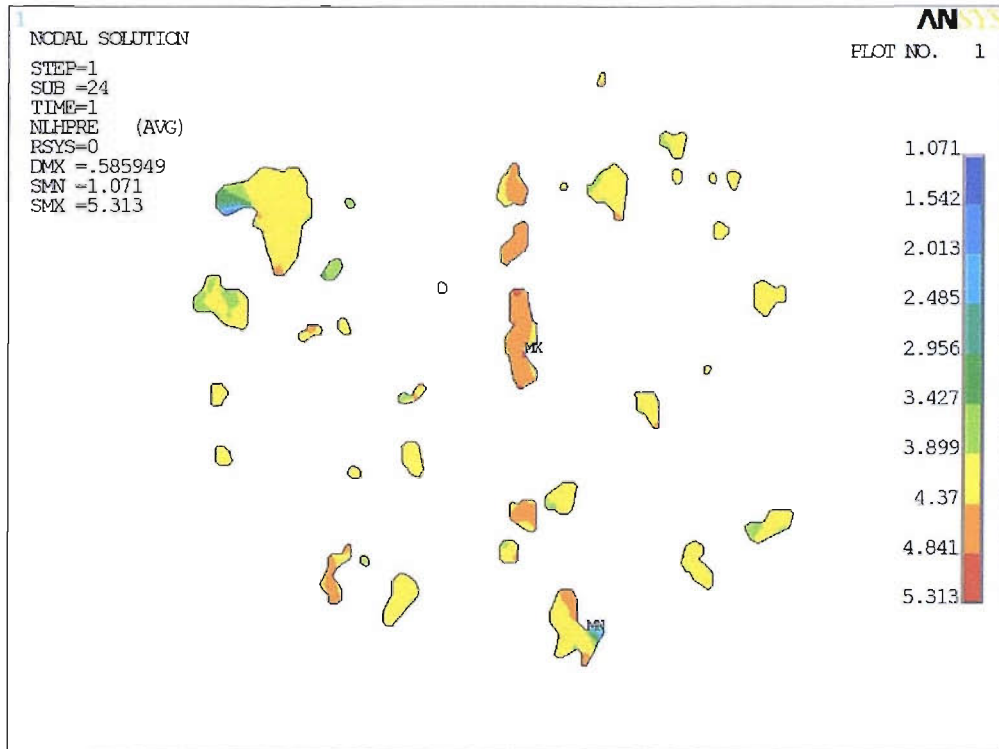
Figure E-1 (d): Hydrostatic stress within Sn particles for Area 1



Figure E-2 (a): Maximum plastic shear strain within Al matrix for Area 3
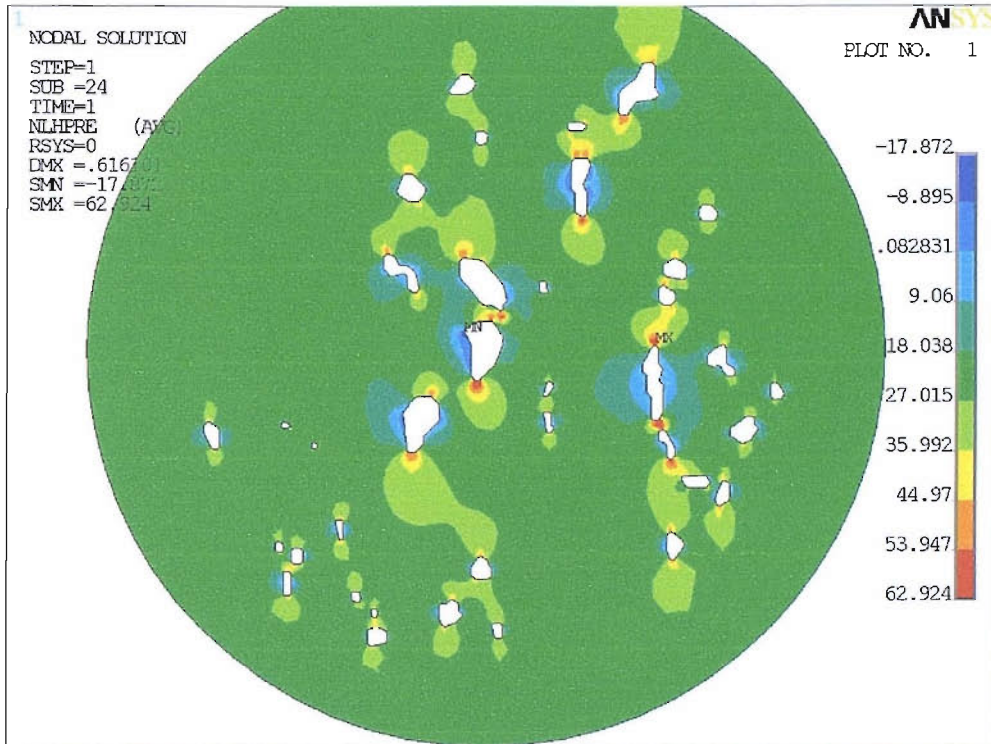
Figure E-2 (b): Hydrostatic stress within Al matrix for Area 3
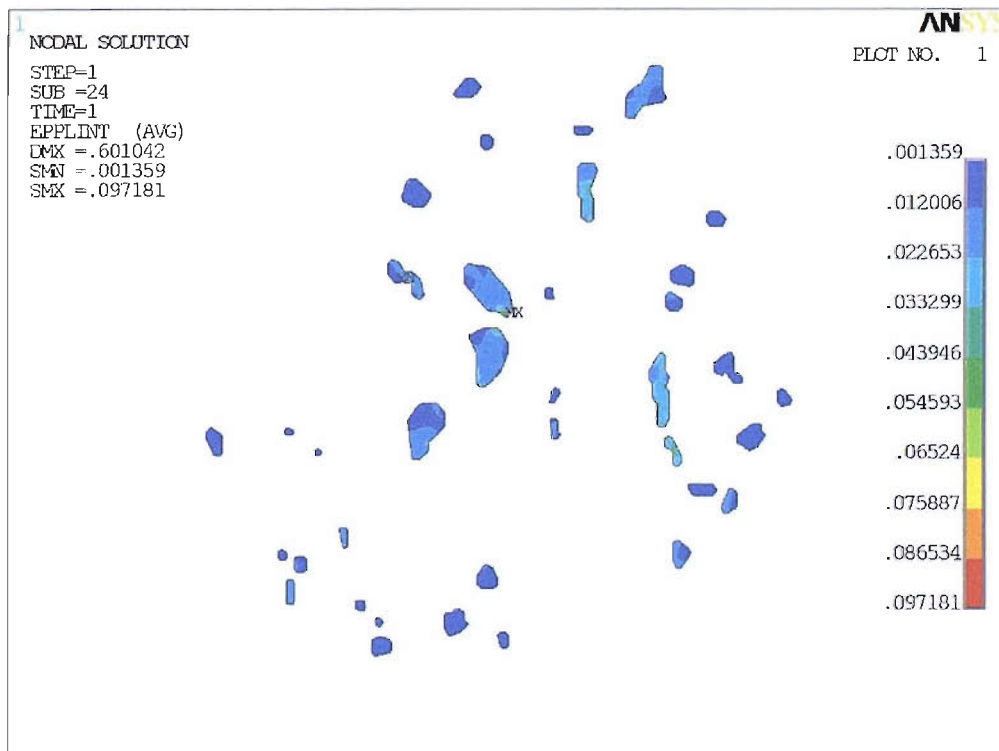


Figure E-2 (c): Maximum plastic shear strain within Sn particles for Area 3
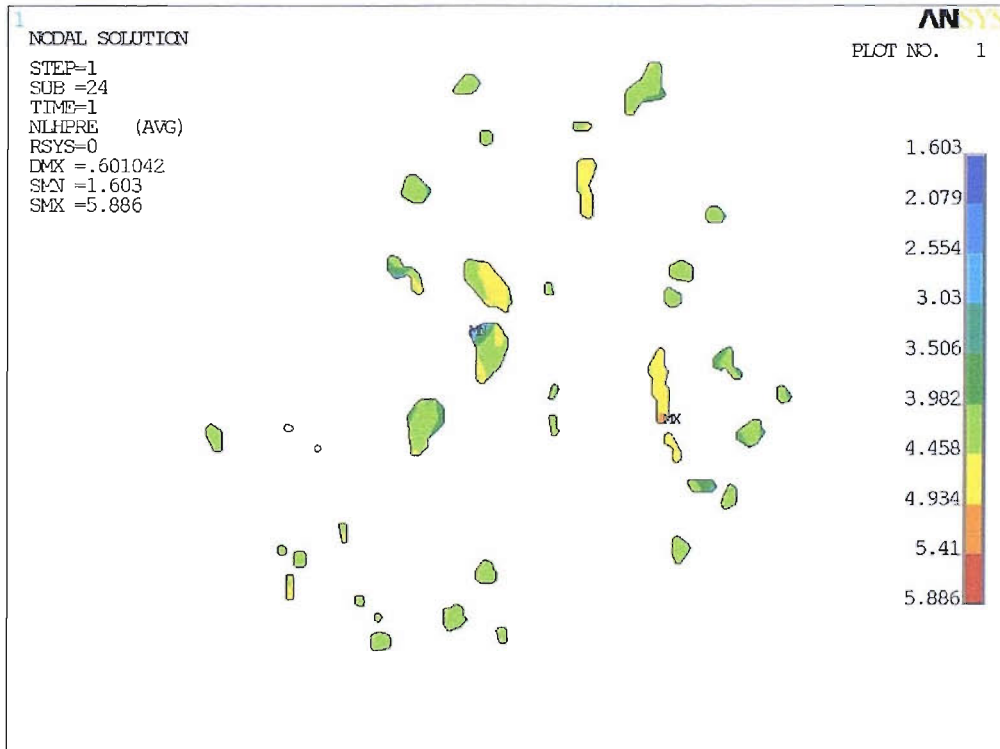
Figure E-2 (d): Hydrostatic stress within Sn particles for Area 3
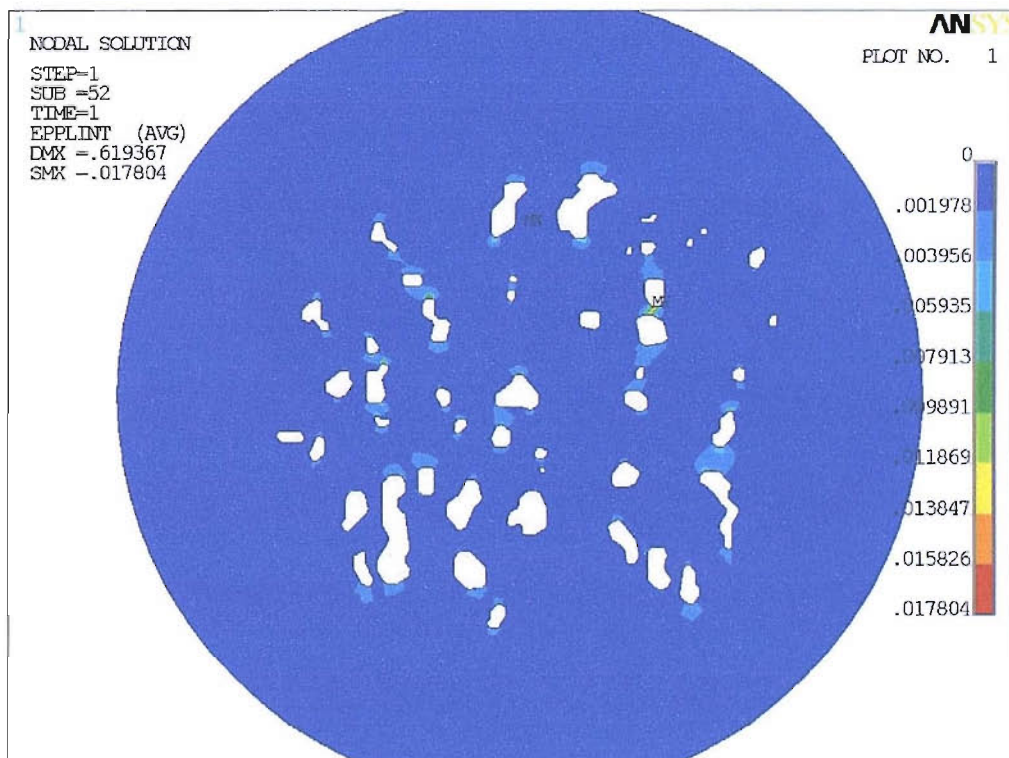


Figure E-3 (a): Maximum plastic shear strain within Al matrix for Area 4
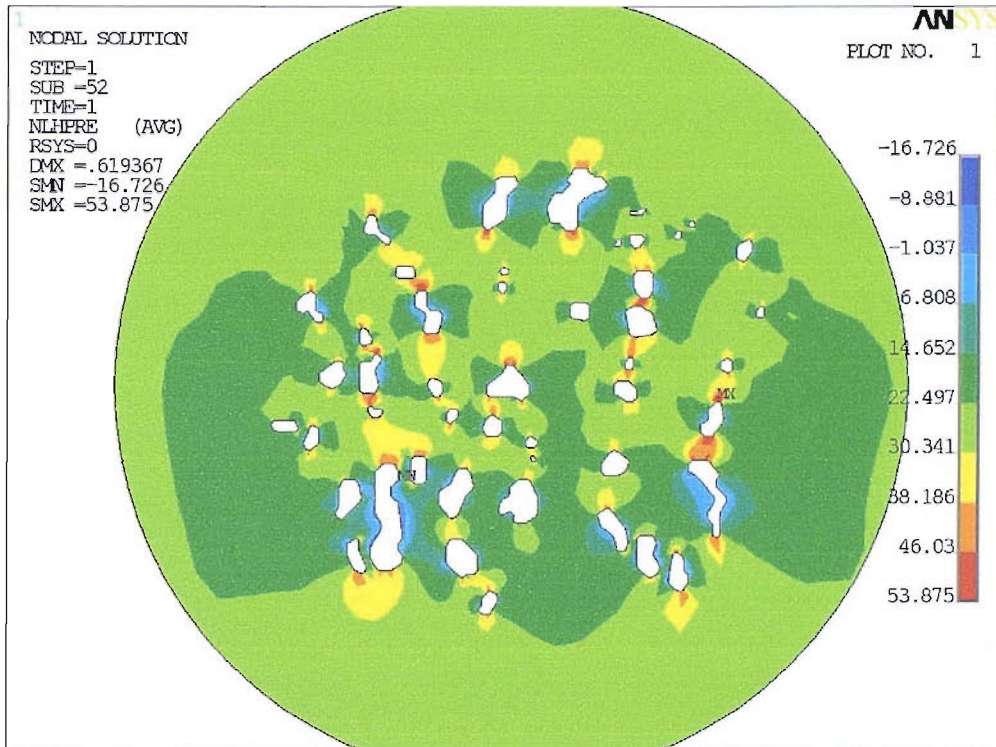
Figure E-3 (b): Hydrostatic stress within Al matrix for Area 4
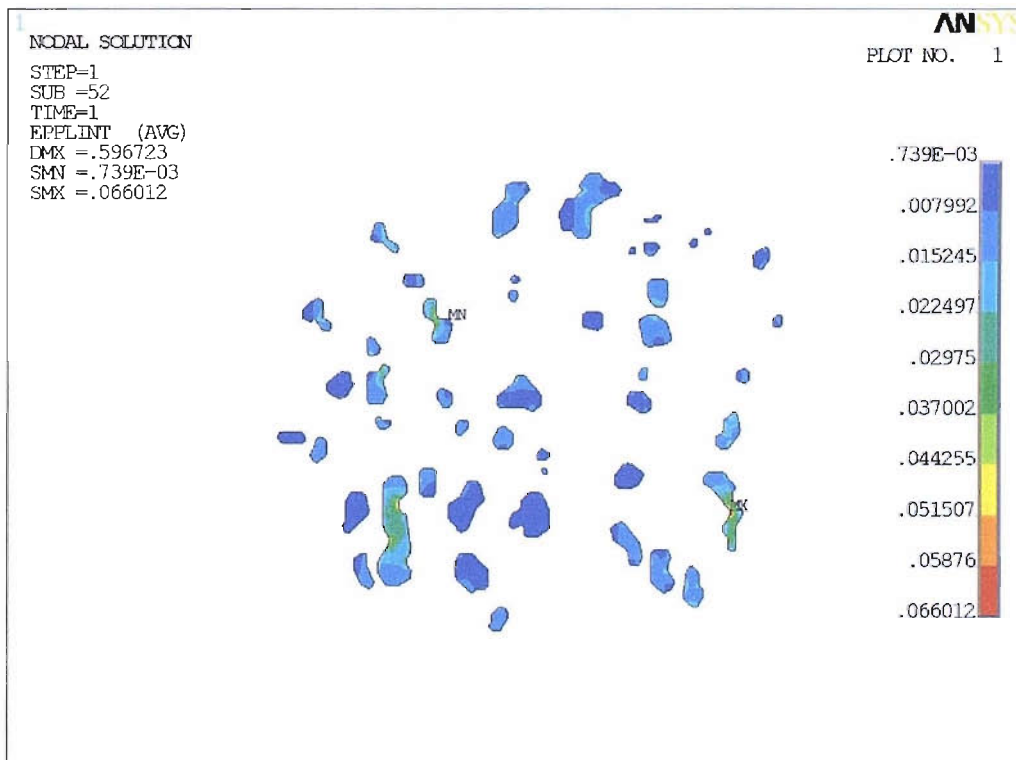


Figure E-3 (c): Maximum plastic shear strain within Sn particles for Area 4
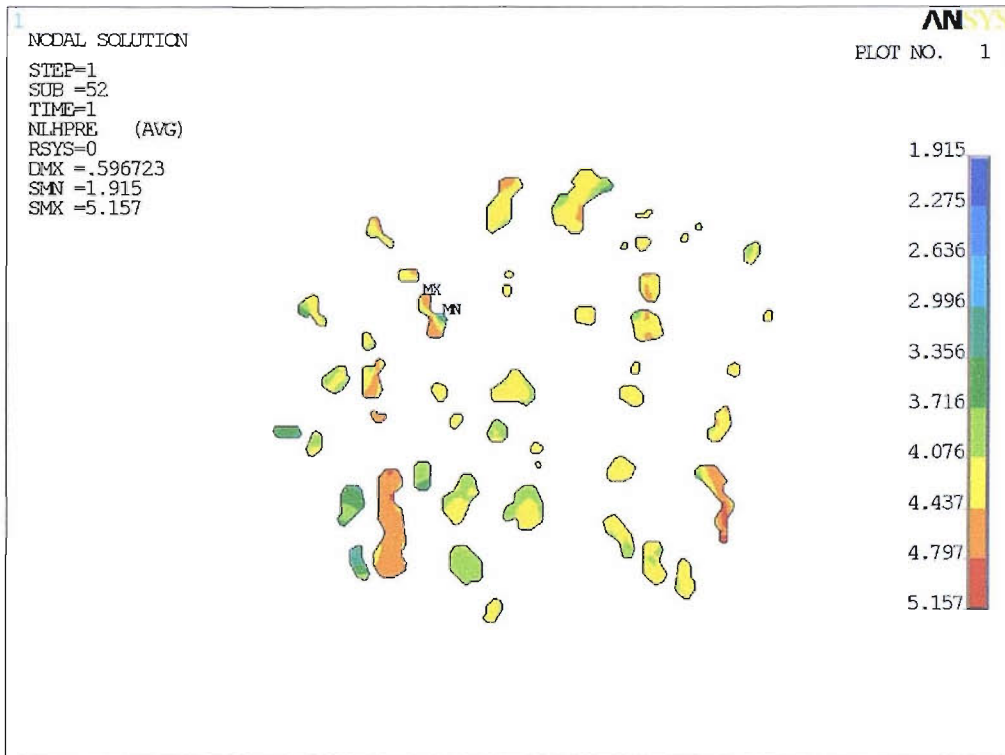
Figure E-3 (d): Hydrostatic stress within Sn particles for Area 4
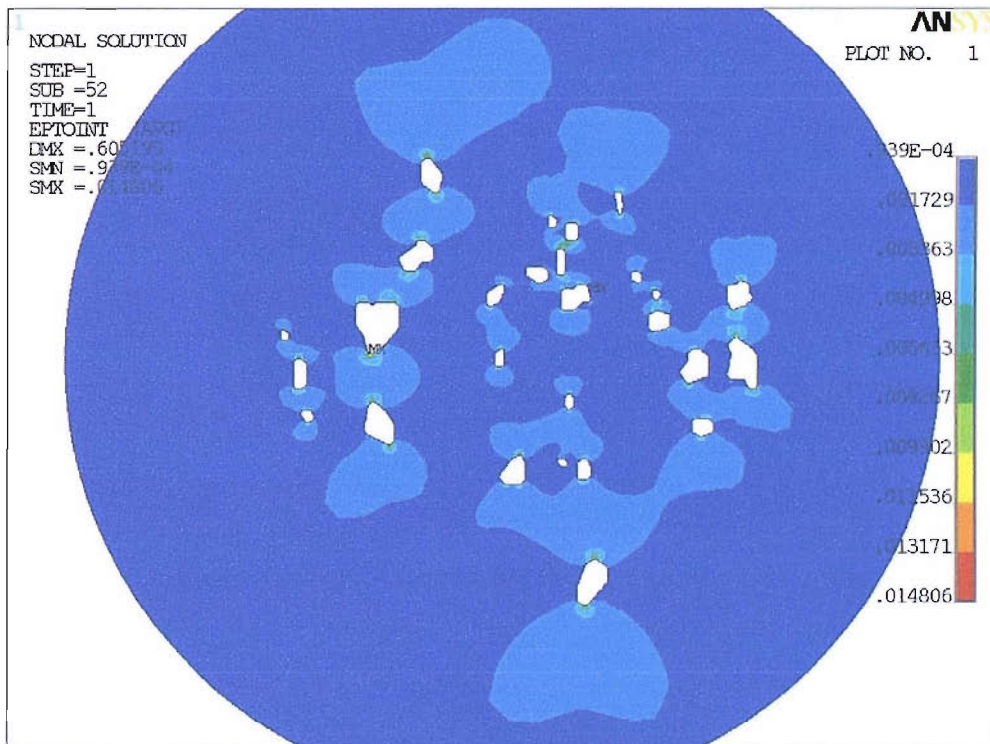


Figure E-4 (a): Maximum plastic shear strain within Al matrix for Area 9
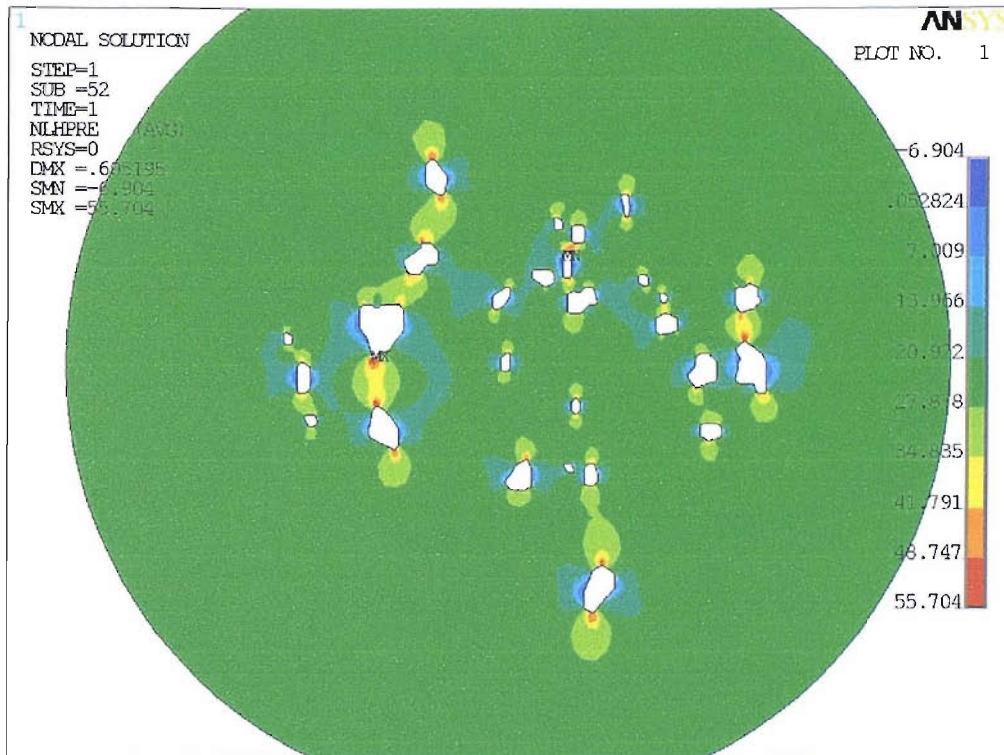
Figure E-4 (b): Hydrostatic stress within Al matrix for Area 9
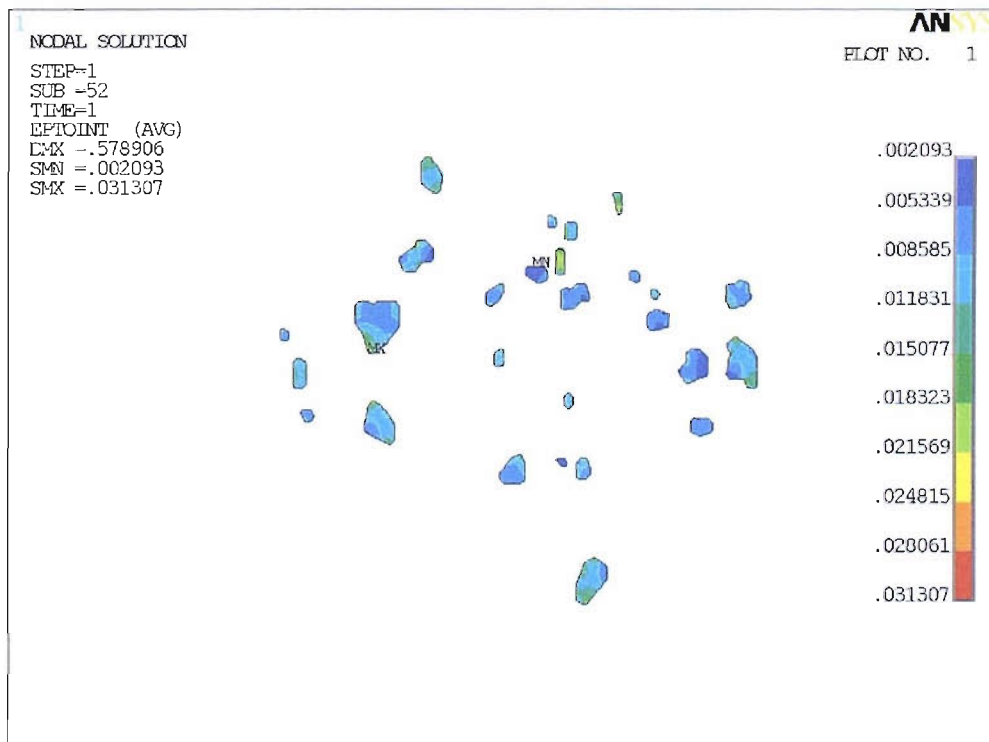


Figure E-4 (c): Maximum plastic shear strain within Sn particles for Area 9
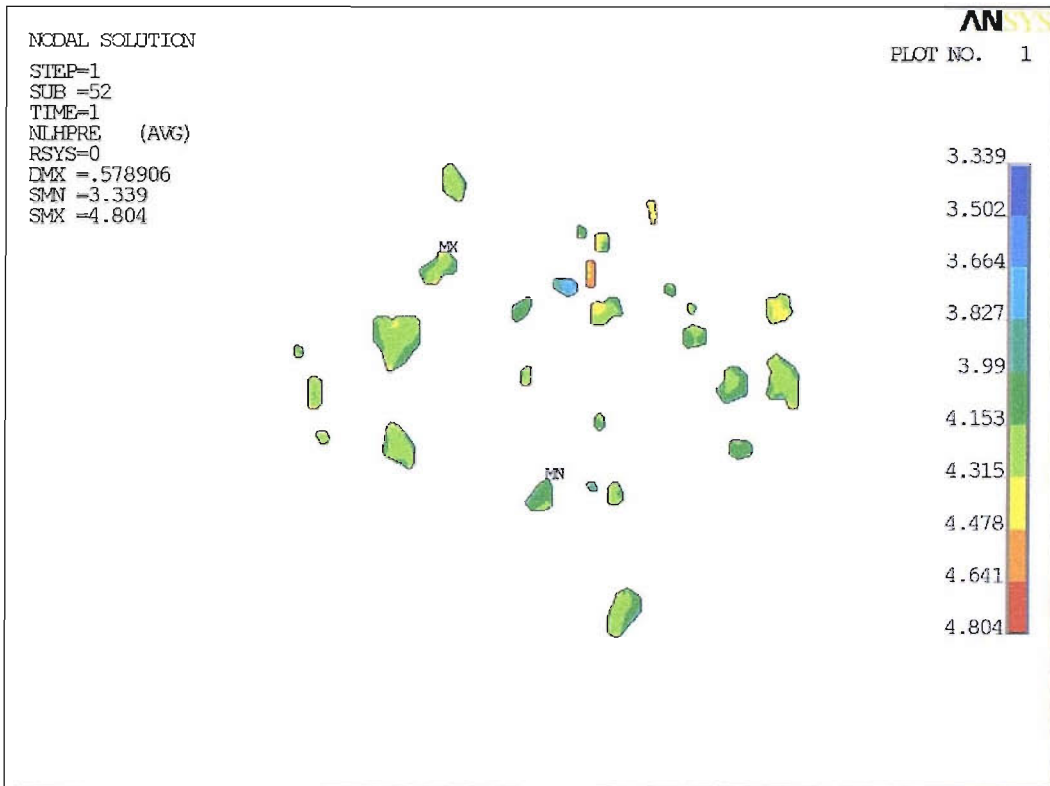
Figure E-4 (d): Hydrostatic stress within Sn particles for Area 9

**Appendix F: Histograms of FBT Measurements Frequency Distribution of AS1241, AS16 Perp. and AS16 Para**
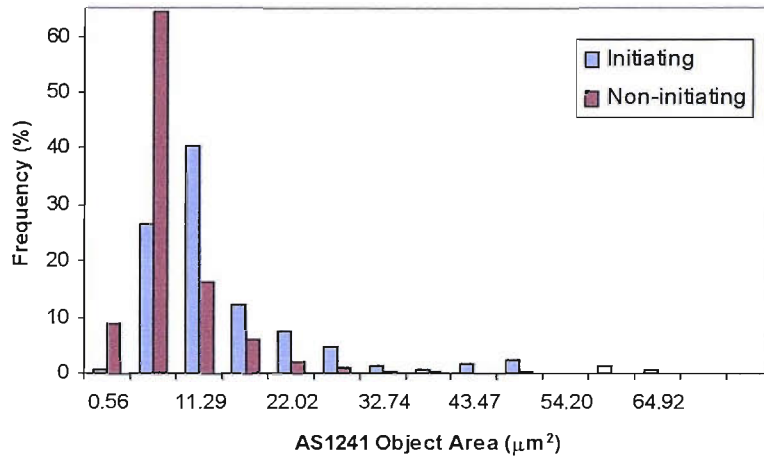


(a)
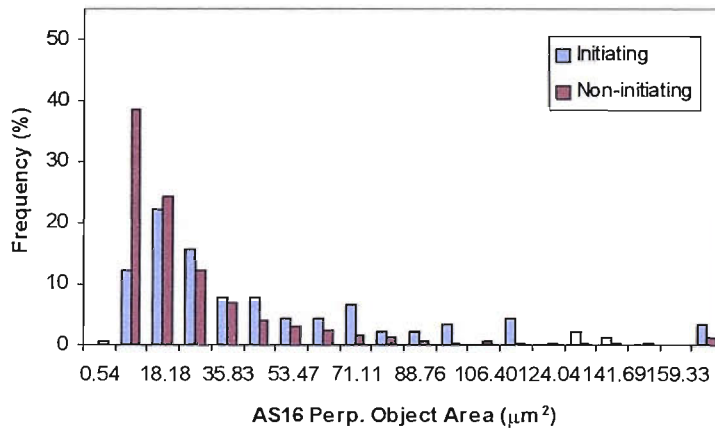


(b)
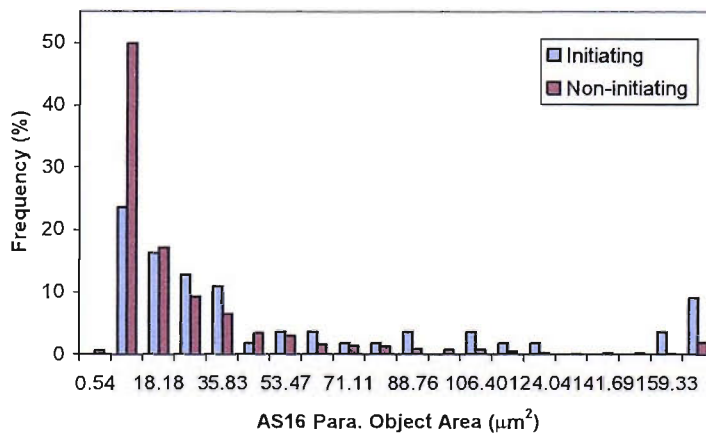


(c)

Figure F-1: Histograms of Object Area

(a)



(b)



(c)
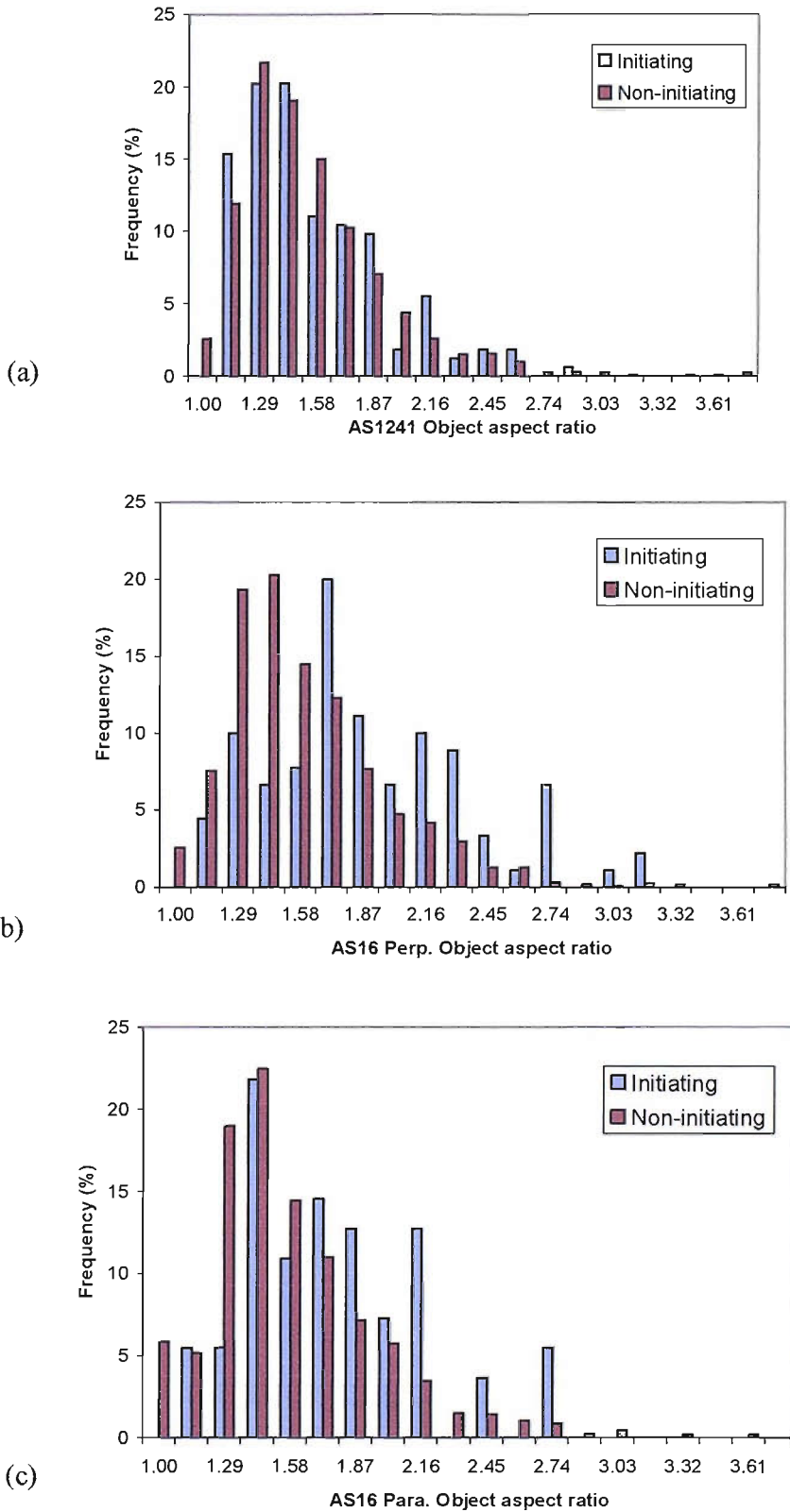
Figure F-2: Histograms of Object Aspect Ratio

(a)



(b)



(c)
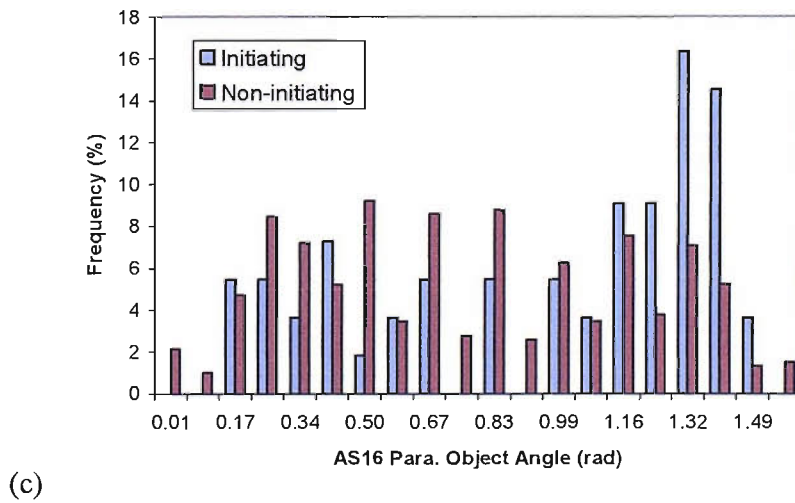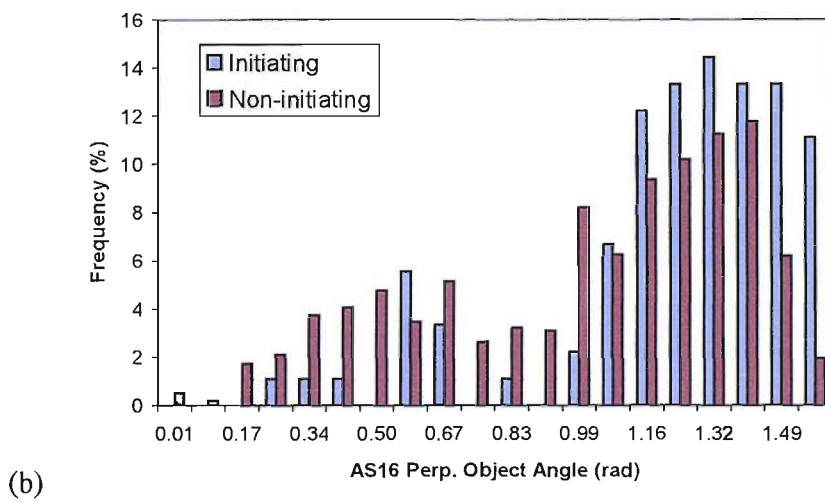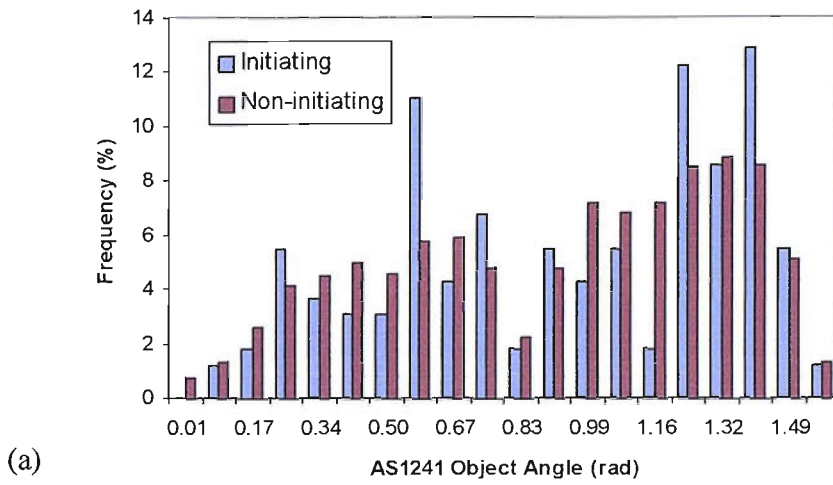
Figure F-3: Histograms of Object Angle

(a)



(b)



(c)
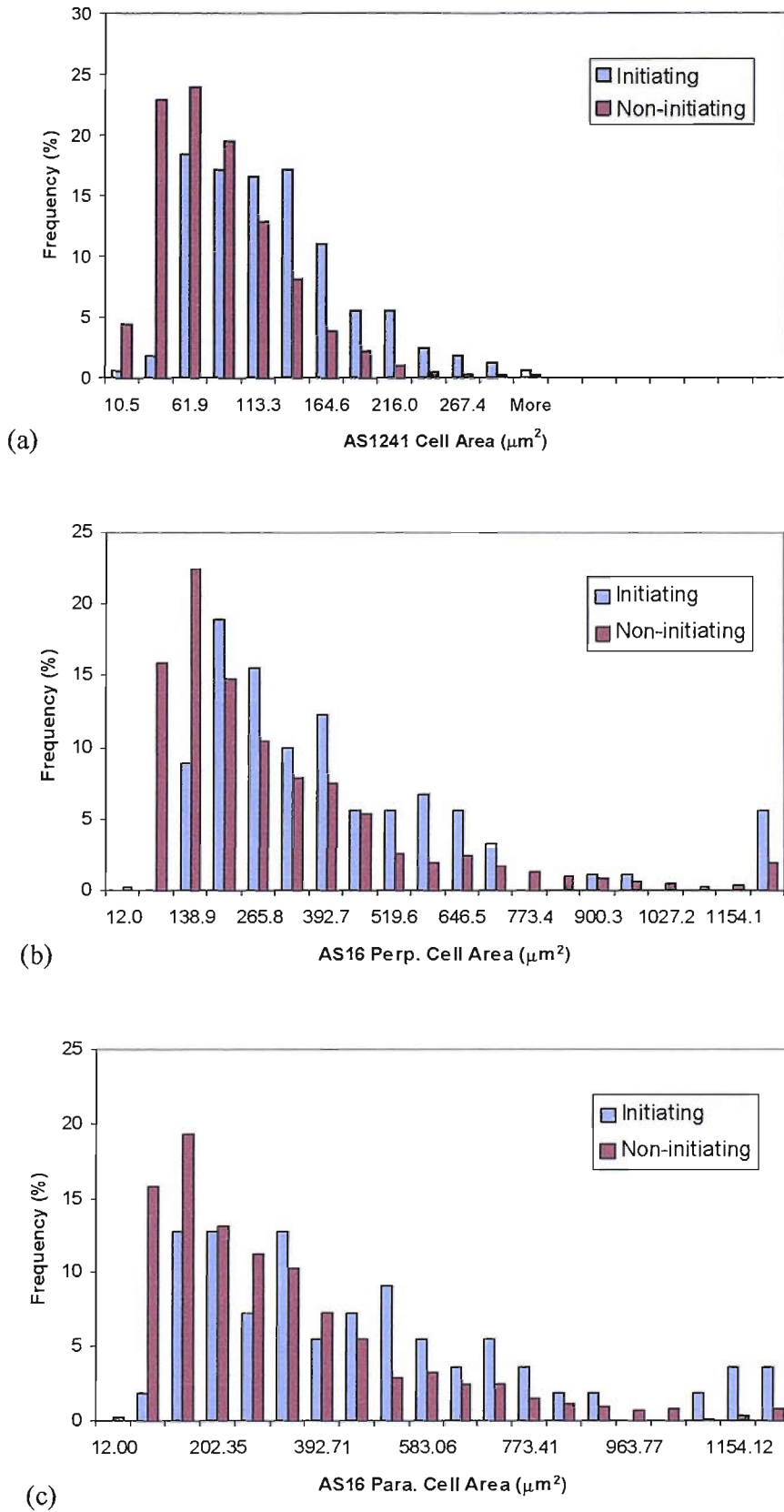
Figure F-4: Histograms of Cell Area

(a)



(b)



(c)
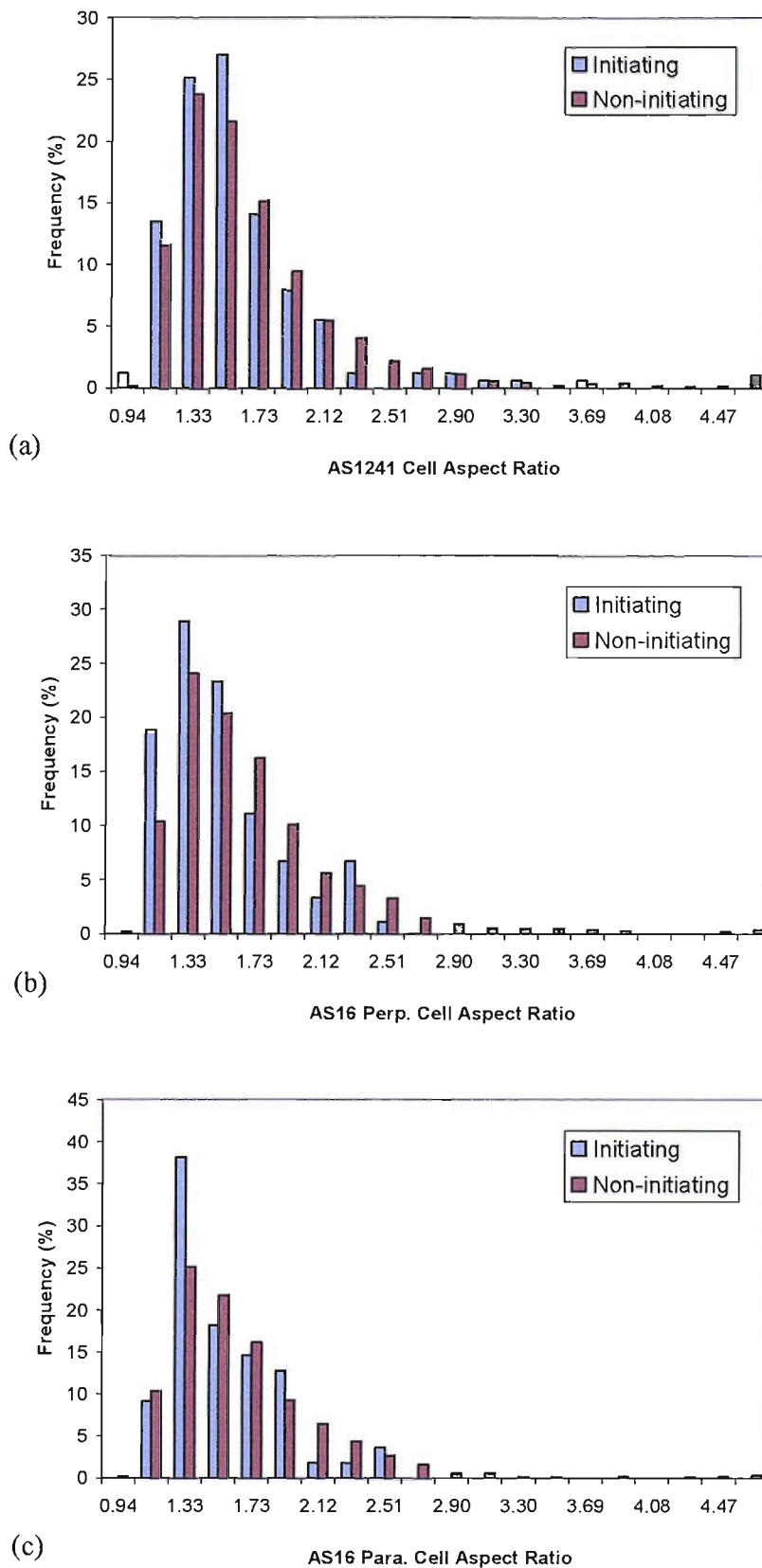
Figure F-5: Histograms of Cell Aspect Ratio
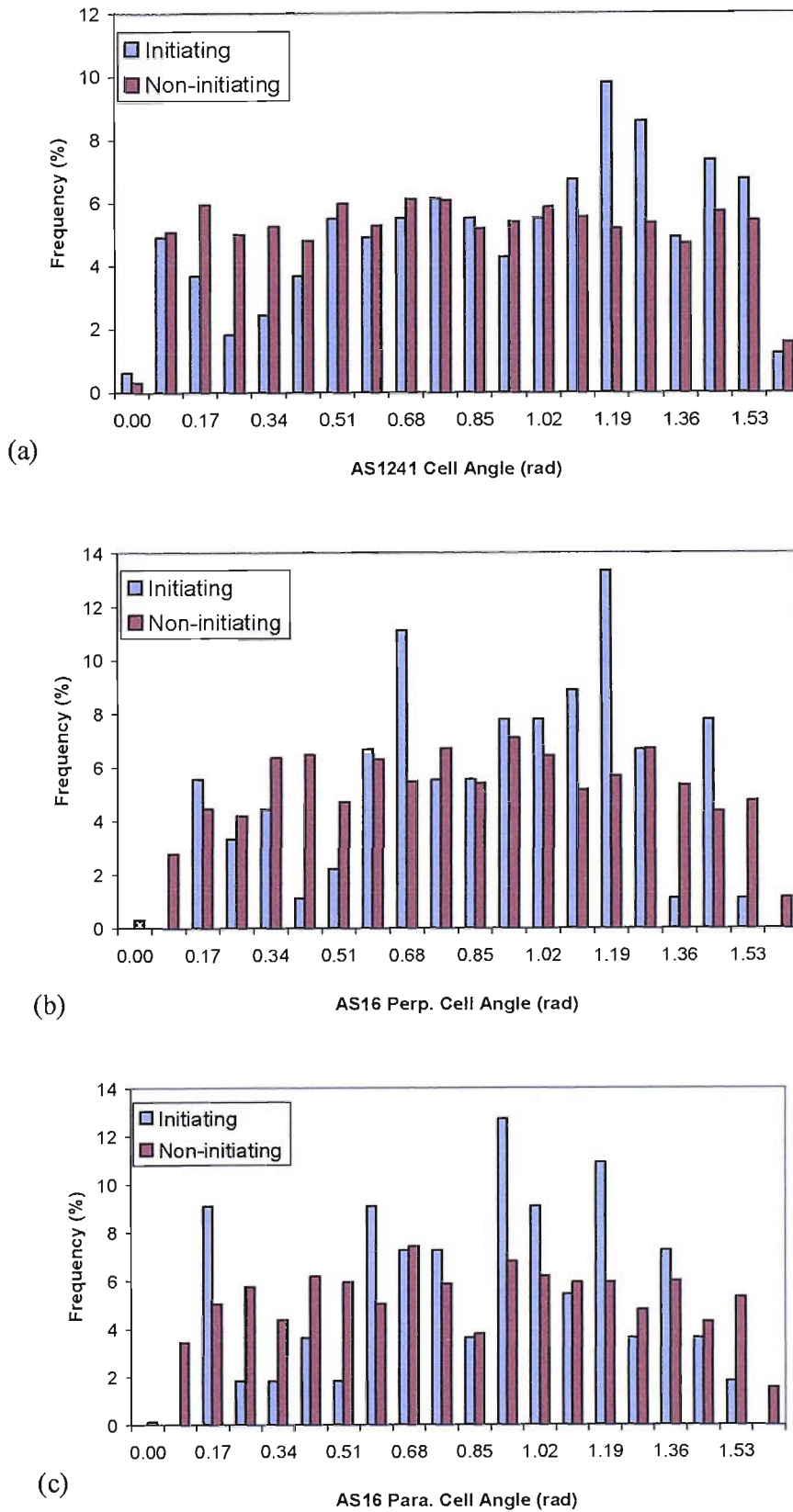
Figure F-6: Histograms of Cell Angle

(a)



(b)



(c)
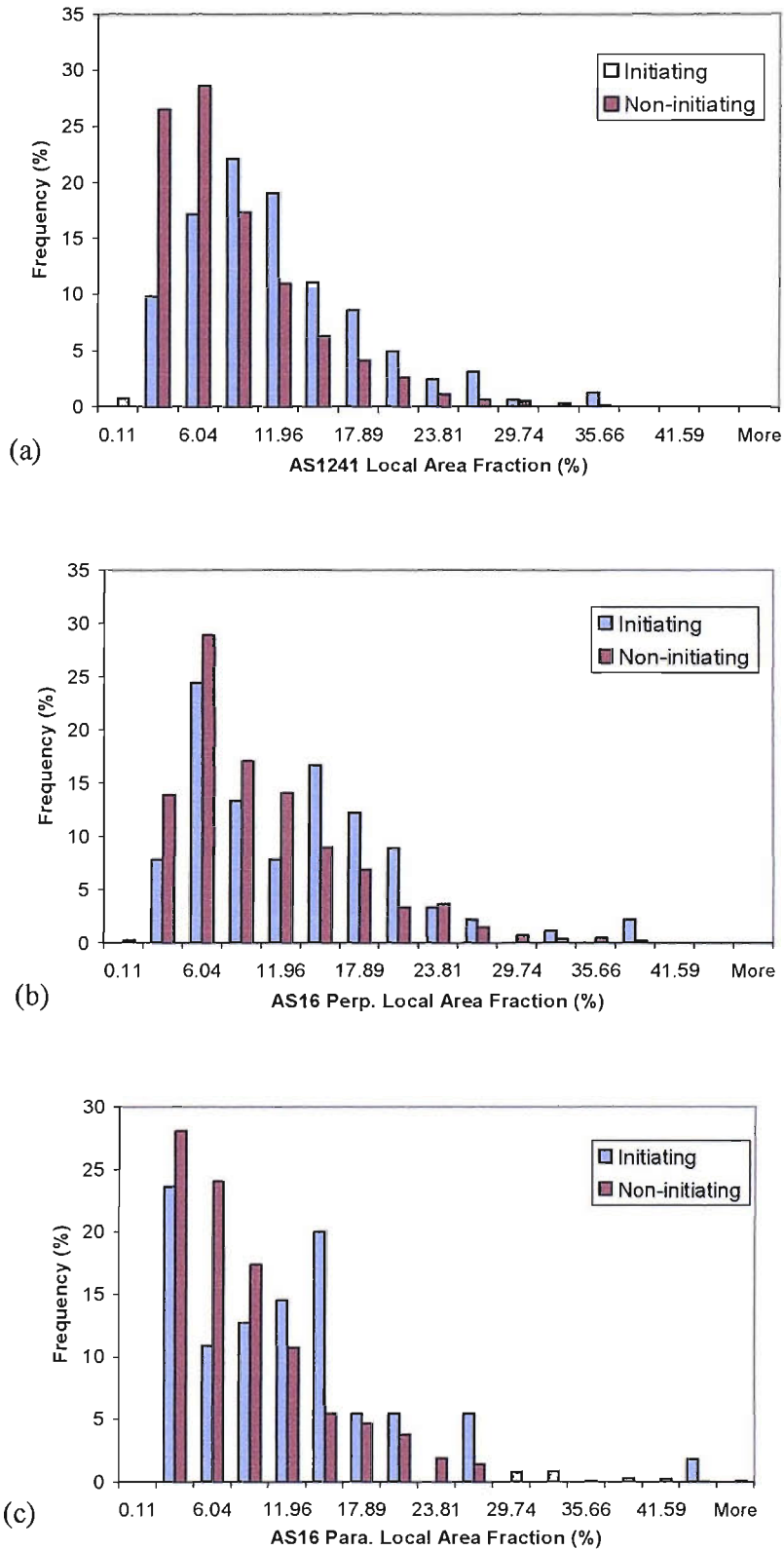
Figure F-7: Histograms of Local Area Fraction

(a)



(b)



(c)
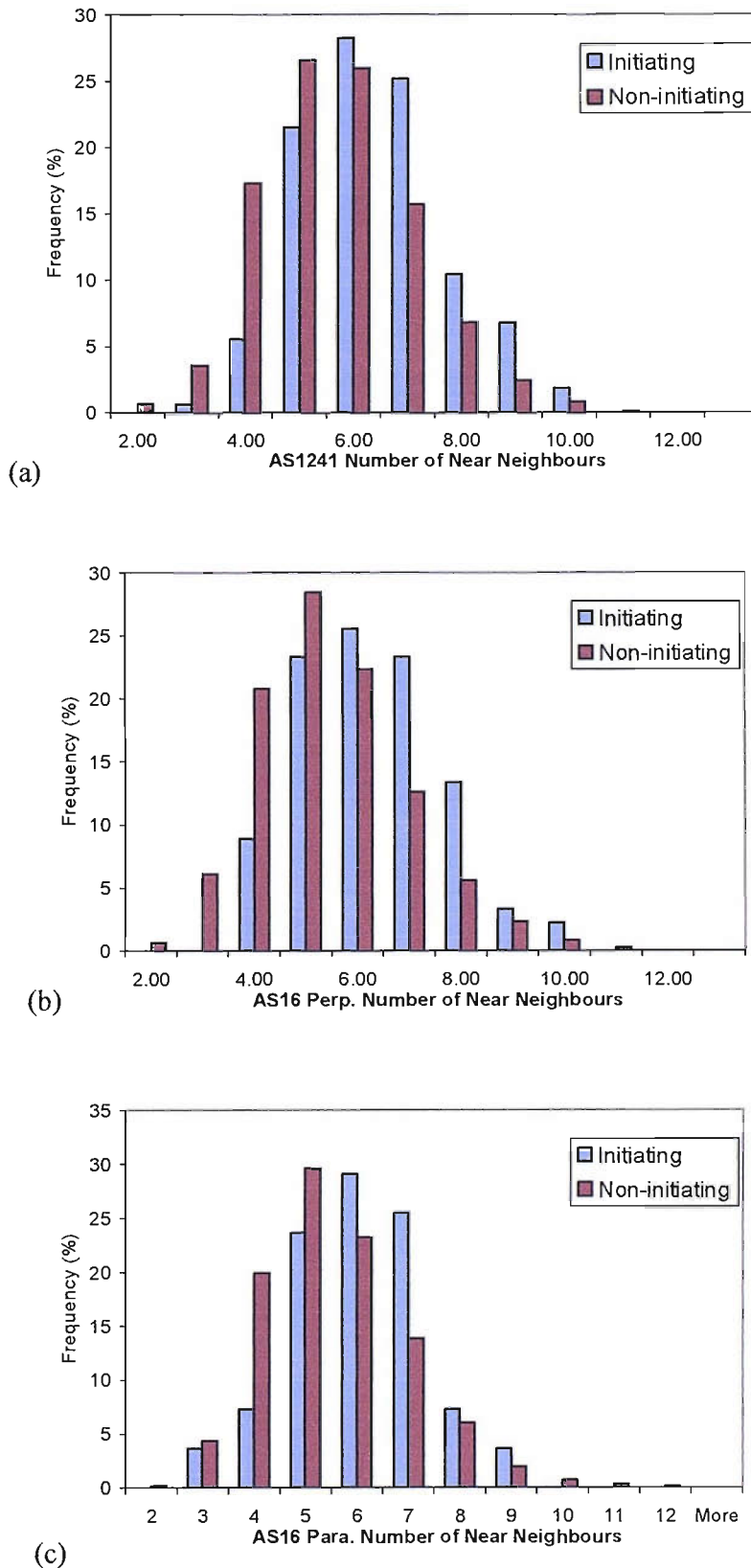
Figure F-8: Histograms of Number of near neighbours

(a)



(b)



(c)
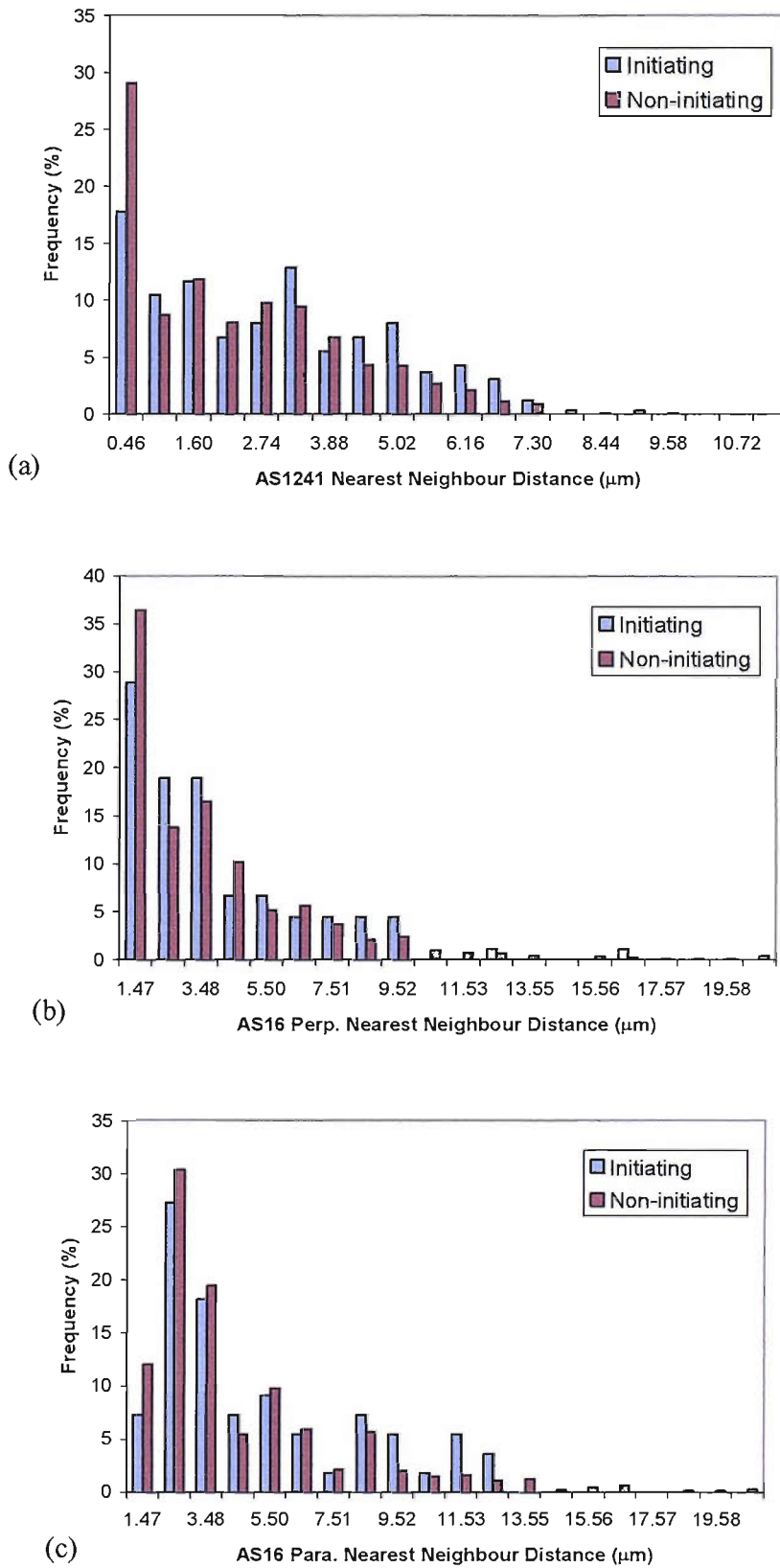
Figure F-9: Histograms of Nearest neighbour distance

(a)



(b)



(c)
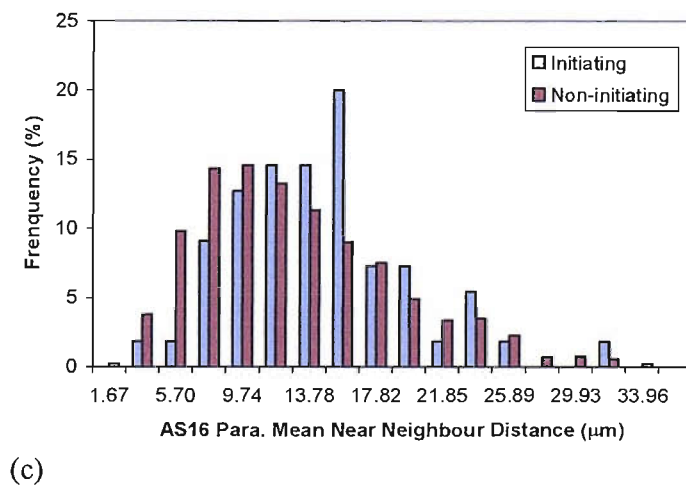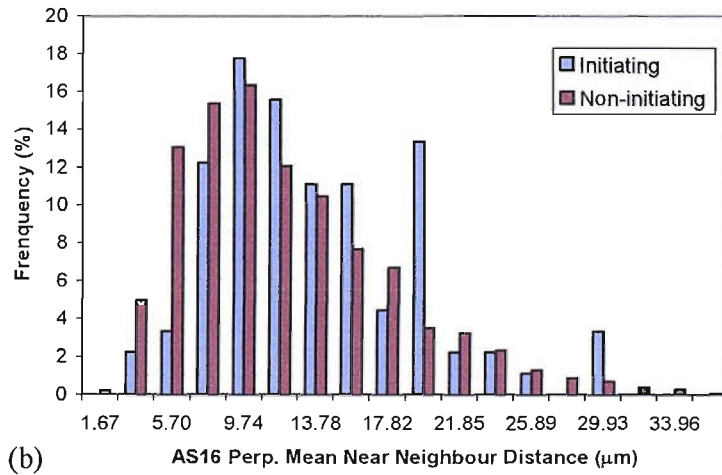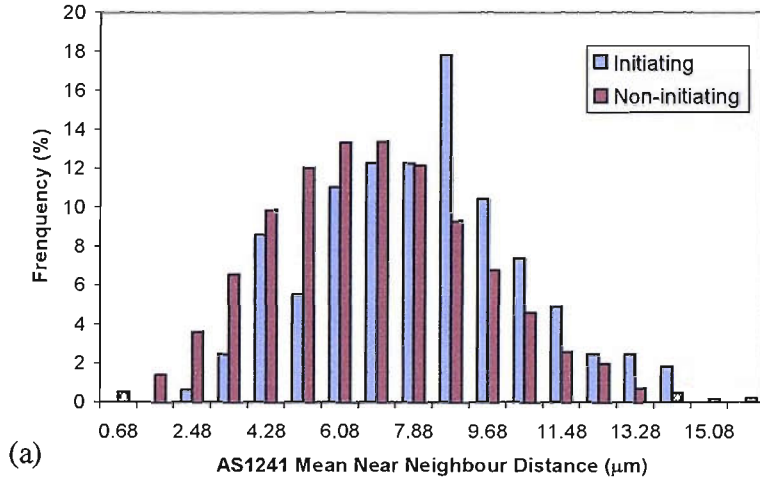
Figure F-10: Histograms of Mean near neighbour distance

(a)



(b)



(c)
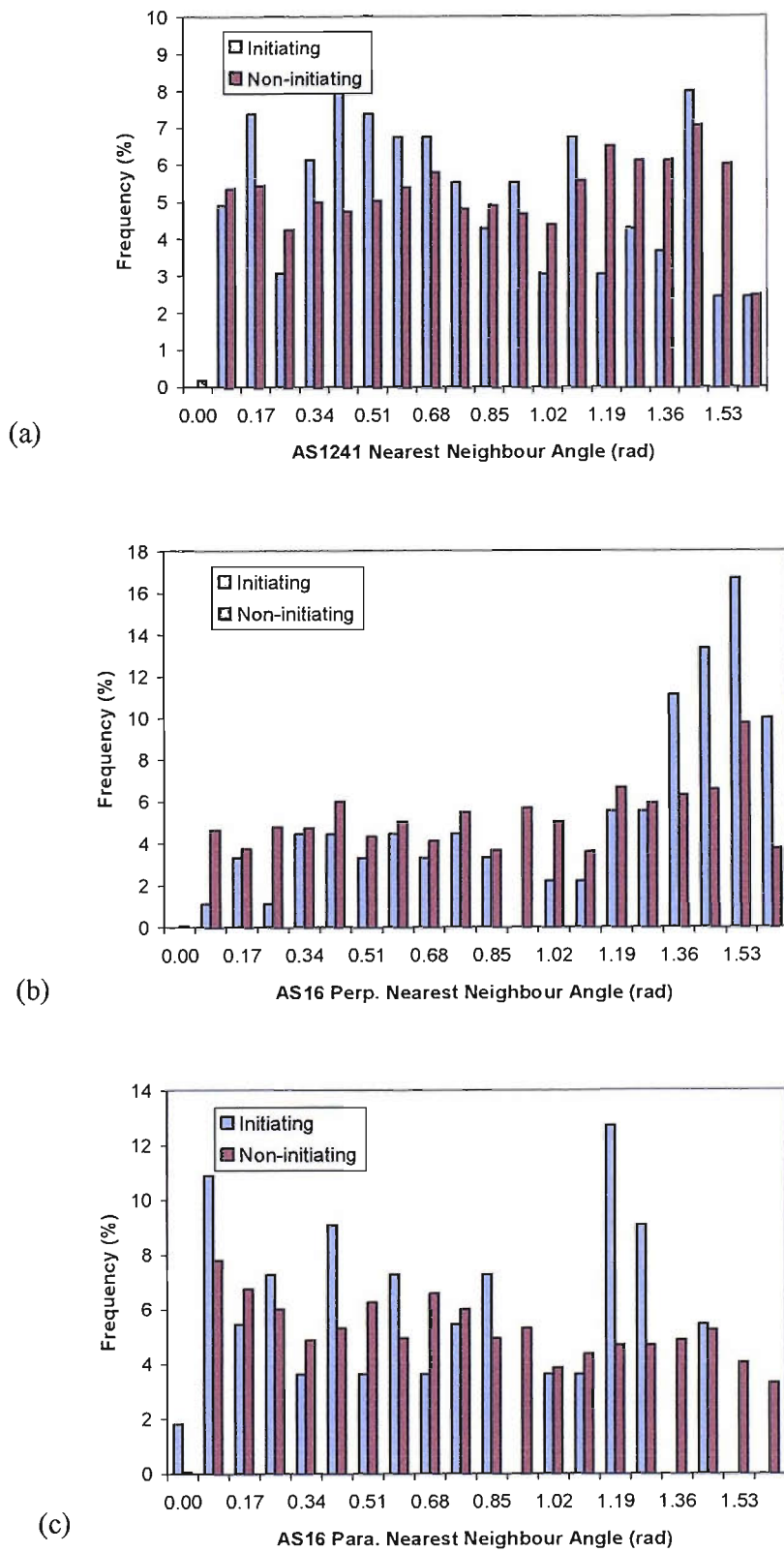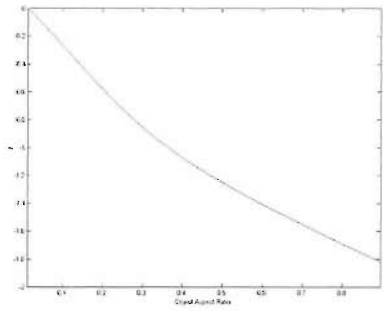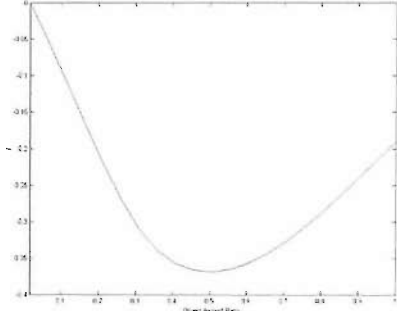
Figure F-11: Histograms of Nearest neighbour angle
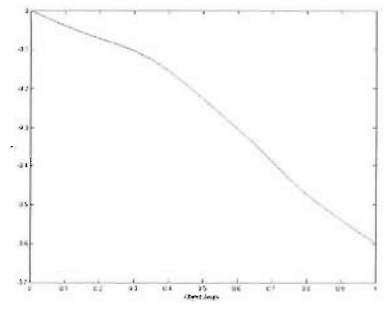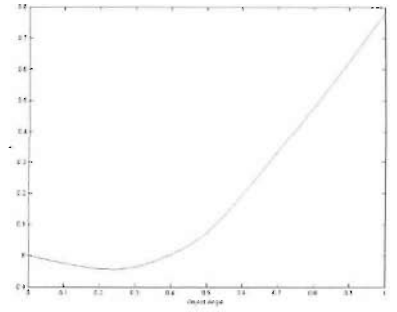
# Appendix G: Pair-wise Scatter Plots of FBT Parameters of AS16 Para. data

*LAF*

*No. NNs*

$d_{min}$

$d_{mean}$

*NNAng*

*CAng*  *LAF*  *No. NNs*  $d_{min}$  $d_{mean}$
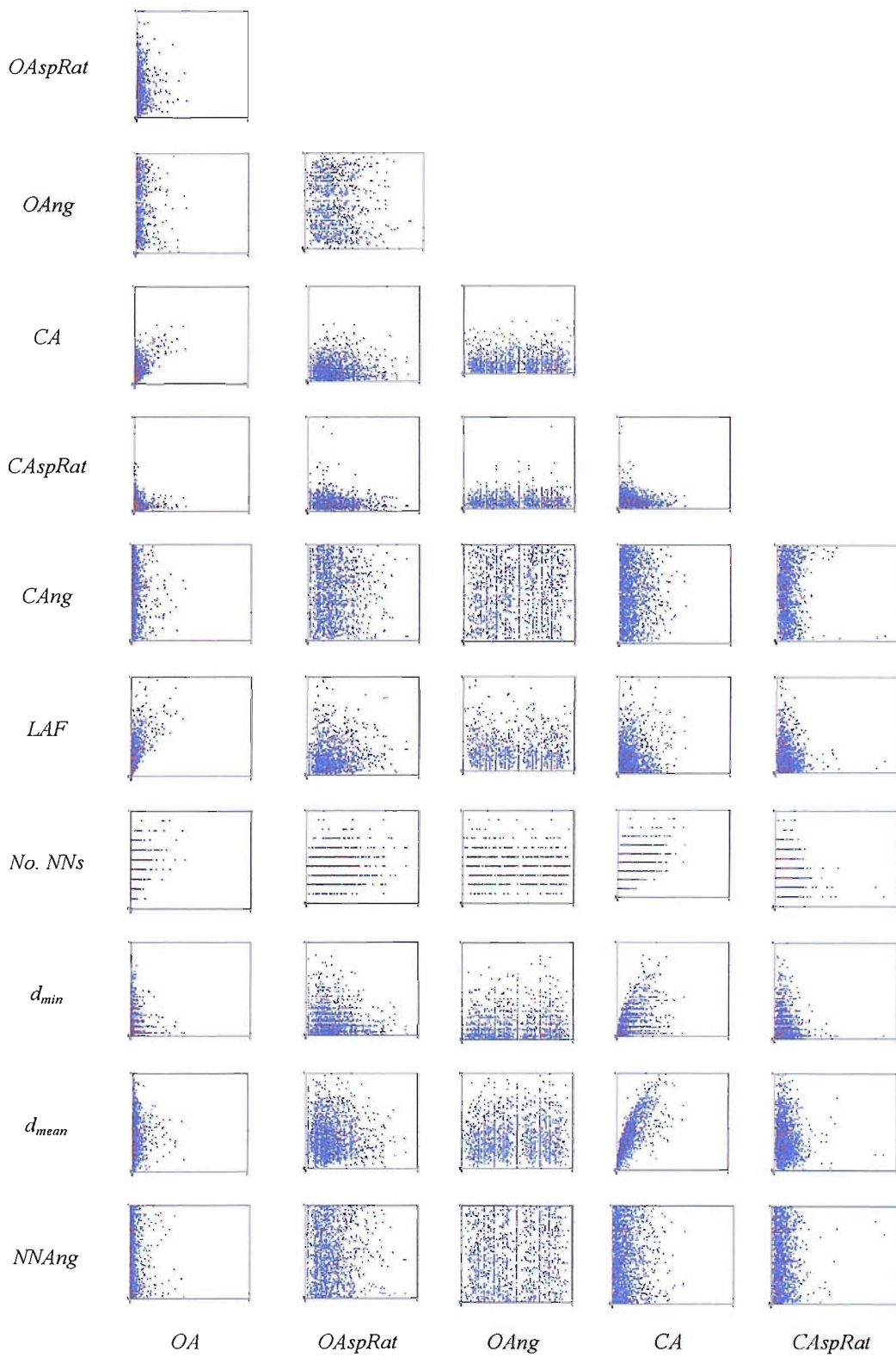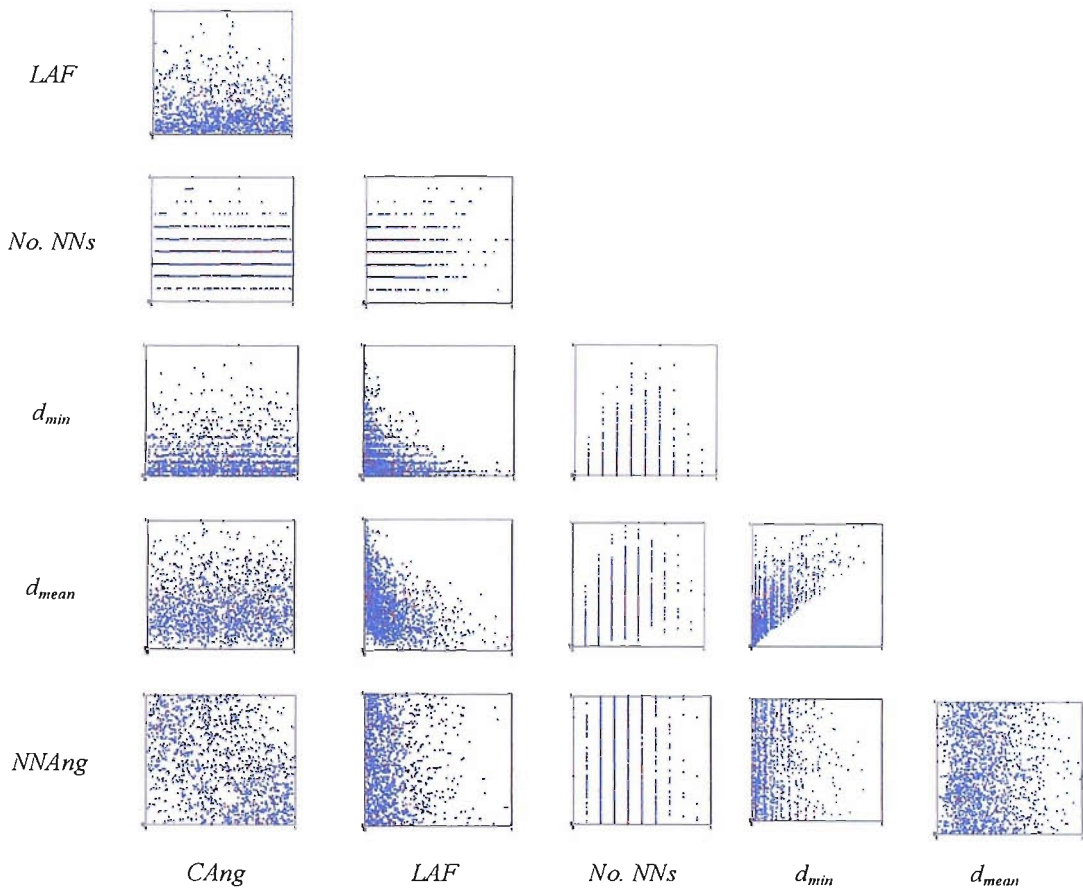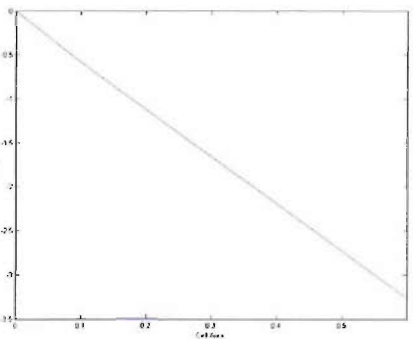
# Appendix H: Selected ANM Terms by SUPANOVA for AS16 Para. Data

| Term 1 | Trend 1 | Trend 2 |
|---|---|---|
| *OAspRat* |  |  |
| Consistency | 8/10 | 2/10 |

| Term 2 | Trend 1 | Trend 2 |
|---|---|---|
| *OAng* |  |  |
| Consistency | 6/8 | 2/8 |

| Term 3 | Trend 1 |
|---|---|
| *CA* |  |
| Consistency | 6/6 |

| Term 4 | Trend 1 | Trend 2 |
|---|---|---|
| *CAng* |  |  |
| Consistency | 5/10 | 4/10 |

| Term 4 | Trend 3 |
|---|---|
| *CAng* |  |
| Consistency | 1/10 |

| Term 5 | Trend 1 |
|---|---|
| *LAF* |  |
| Consistency | 10/10 |

| Term 6 | Trend 1 |
|--------|---------|
| *No. NNs* |  |
| Consistency | 10/10 |

| Term 7 | Trend 1 |
|--------|---------|
| $d_{min}$ |  |
| Consistency | 8/8 |

| Term 8 | Trend 1 |
|--------|---------|
| $d_{mean}$ |  |
| Consistency | 10/10 |

| Term 9 | Trend 1 |
|---|---|
| *NNAng* |  |
| Consistency | 10/10 |

| Term 10 | Trend 1 |
|---|---|
| *OAspRat & OAng* |  |
| Consistency | 8/8 |

| Term 11 | Trend 1 |
|---|---|
| *OAspRat & CAng* |  |
| Consistency | 8/8 |

| Term 12 | Trend 1 |
|---------|---------|
| *OAng & CAspRat* |  |
| Consistency | 6/6 |

| Term 13 | Trend 1 | Trend 2 |
|---------|---------|---------|
| *OAng & CAng* |  |  |
| Consistency | 7/8 | 1/8 |

| Term 14 | Trend 1 | Trend 2 |
|---------|---------|---------|
| *OAng & No. NNs* |  |  |
| Consistency | 8/9 | 1/9 |

| Term 15 | Trend 1 |
|---|---|
| *OAng* & $d_{min}$ |  |
| Consistency | 7/7 |

| Term 16 | Trend 1 | Trend 2 |
|---|---|---|
| *OAng* & *NNAng* |  |  |
| Consistency | 7/10 | 2/10 |

| Term 16 | Trend 3 |
|---|---|
| *OAng* & *NNAng* |  |
| Consistency | 1/10 |

| Term 17 | Trend 1 |
|---|---|
| *CA & NNAng* |  |
| Consistency | 6/6 |

| Term 18 | Trend 1 | Trend 2 |
|---|---|---|
| *CAng & No. NNs* |  |  |
| Consistency | 9/10 | 1/10 |

| Term 19 | Trend 1 | Trend 2 |
|---|---|---|
| *CAng & d_{mean}* |  |  |
| Consistency | 4/9 | 4/9 |

| Term 19 | Trend 3 |
|---|---|
| *CAng* <br> & *d_{mean}* |  |
| Consistency | 1/9 |

| Term 20 | Trend 1 |
|---|---|
| *CAng* <br> & *NNAng* |  |
| Consistency | 8/8 |

| Term 21 | Trend 1 |
|---|---|
| *No. NNs* <br> & *d_{mean}* |  |
| Consistency | 9/9 |

| Term 22 | Trend 1 |
|---|---|
| $d_{min}$ & *NNAng* |  |
| Consistency | 6/6 |

| Term 23 | Trend 1 |
|---|---|
| $d_{mean}$ & *NNAng* |  |
| Consistency | 10/10 |

| Term 24 | Trend 1 |
|---|---|
| *OAspRat* & *CAng* & *NNAng* |  |
| Consistency | 7/7 |

| Term 25 | Trend 1 |
|---------|---------|
| *OAng* <br> *& CAng* <br> *& LAF* |  |
| Consistency | 9/9 |

| Term 26 | Trend 1 |
|---------|---------|
| *OAng* <br> *& CAng* <br> *& $d_{min}$* |  |
| Consistency | 7/7 |

| Term 27 | Trend 1 | Trend 2 |
|---------|---------|---------|
| *OAng* <br> *& CAng* <br> *& NNAng* |  |  |
| Consistency | 7/9 | 2/9 |
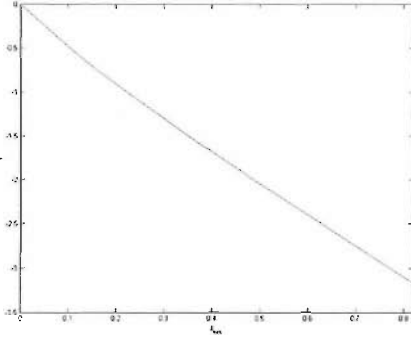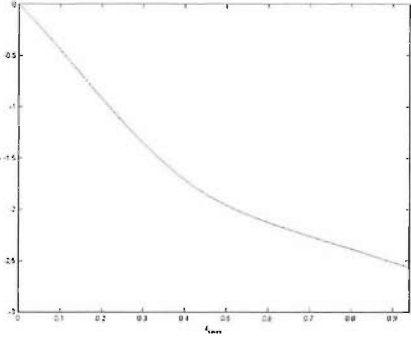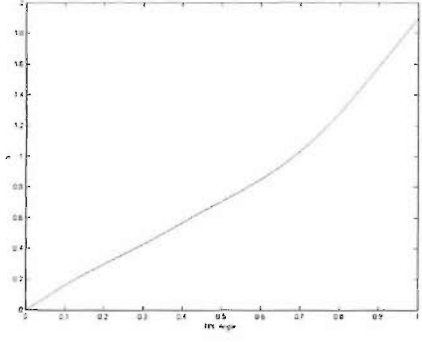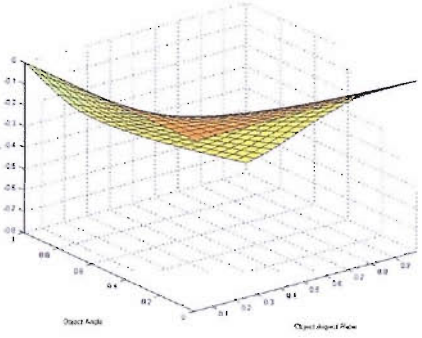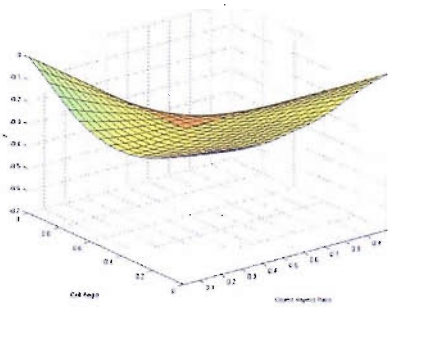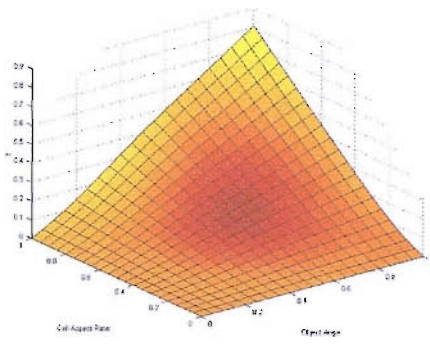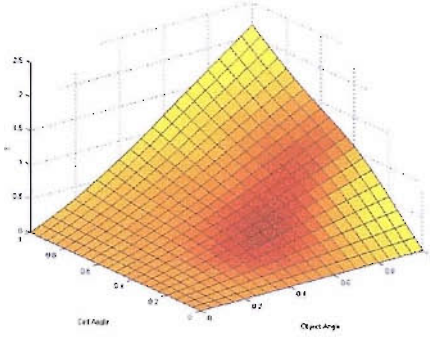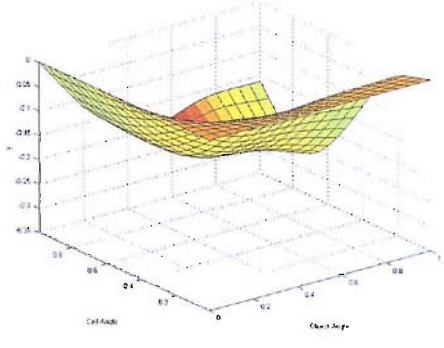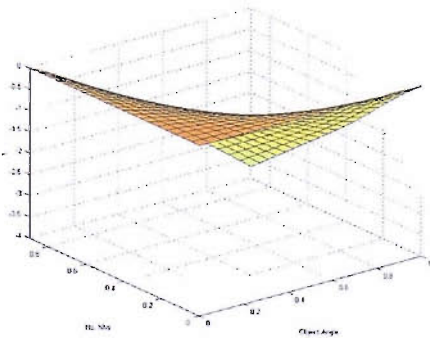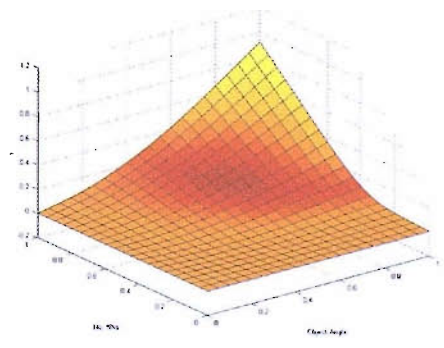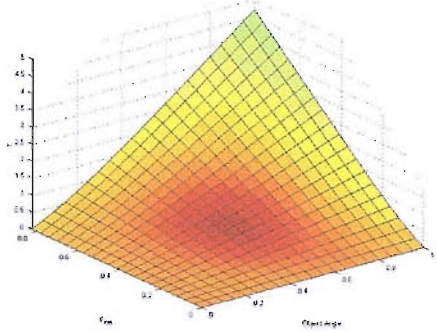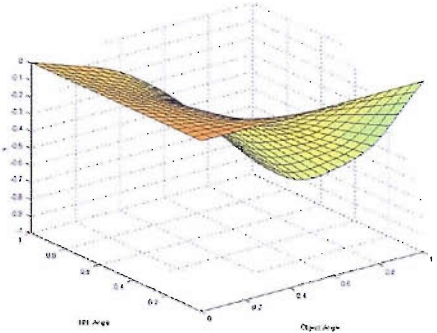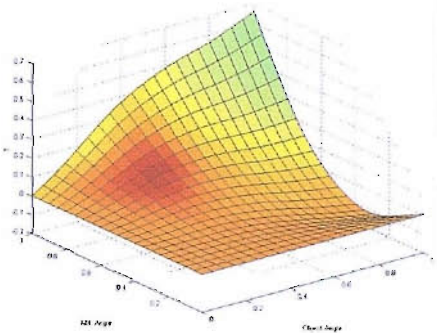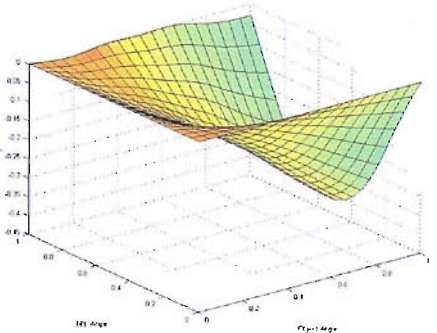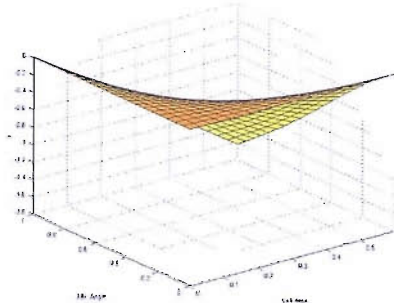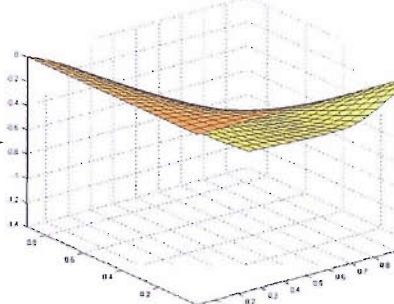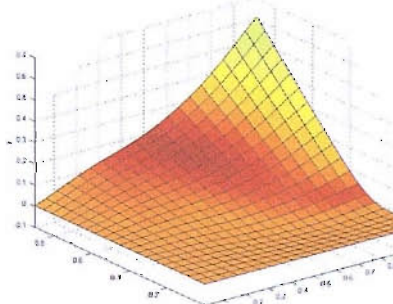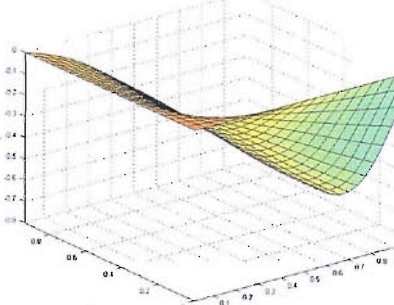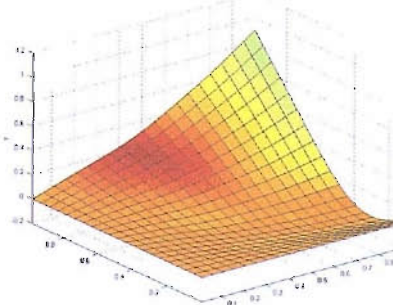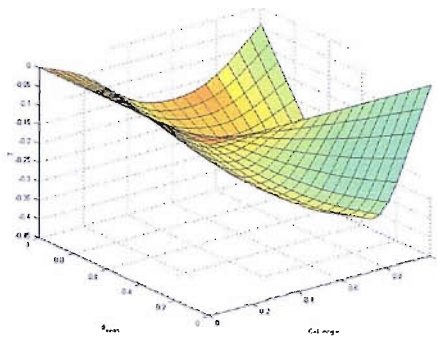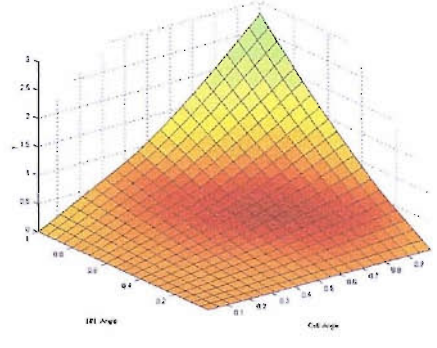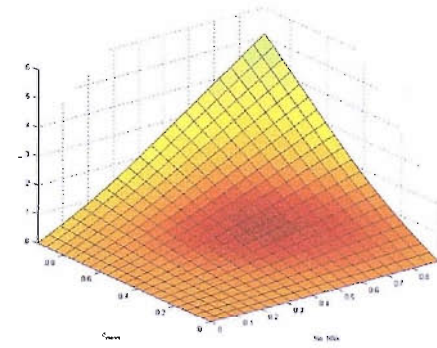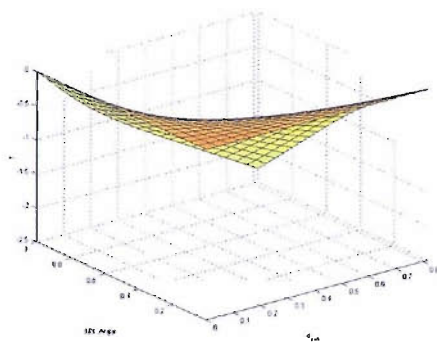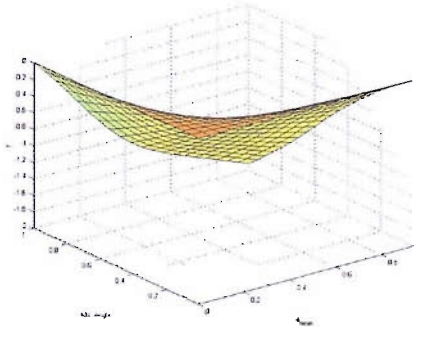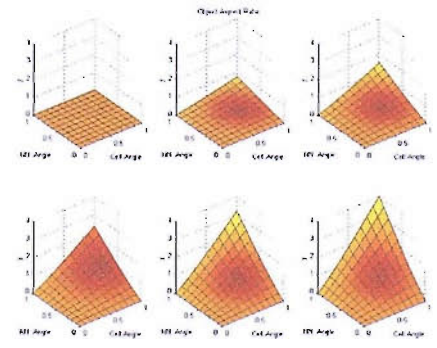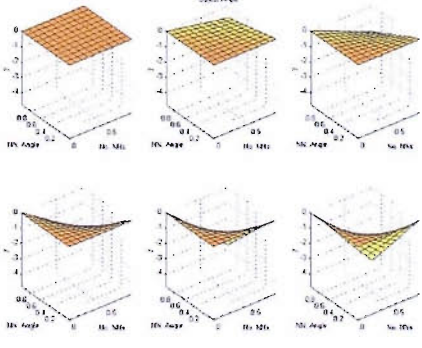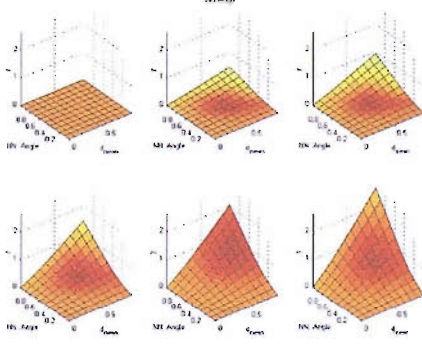
228

| Term 28 | Trend 1 |
|---------|---------|
| *OAng*<br>*& No. NNs*<br>*& NNAng* |  |
| Consistency | 8/8 |

| Term 29 | Trend 1 |
|---------|---------|
| *CAng*<br>*& d_{mean}*<br>*& NNAng* |  |
| Consistency | 7/7 |

# Appendix I: ANM terms picked by SUPANOVA model for AS16 Perp. and AS1241 data

This appendix shows the picked ANM terms and trends by SUPANOVA for both AS16 Perp. and AS1241 data.

**Table I-1: AS16 Perp. SUPANOVA terms selected and their occurrence across 10 modelling runs on random partitions of training and test data[1]**

| Term | Occurrence | Component 1 (univariate) | Component 2 (bivariate) | Likelihood of Initiation |
|------|-----------|--------------------------|-------------------------|--------------------------|
| (i) | 70% | $OA$=High | | Likely |
| (ii) | 50% | $CAspRat$=High | | Unlikely |
| (iii) | 70% | $CAng$=High | | Unlikely |
| (iv) | 70% | $OAng$=High | $OAspRat$=High | Likely |
| (v) | 50% | $OAng$=High | $LAF$=High | Likely |
| (vi) | 50% | $OA$=High | $NNAng$=High | Likely |
| (vii) | 60% | $LAF$=High | $NNAng$=High | Likely |
| (viii) | 60% | $CAng$=High | $NNAng$=High | Likely |
| (ix) | 60% | $CAng$=High | $d_{mean}$=High | Likely |
| (x) | 80% | $CAng$=High | $NNAng$=High | Unlikely |

**Table I-2: AS1241 SUPANOVA terms selected and their occurrence across 10 modelling runs on random partitions of training and test data[2]**

| Term | Occurrence | Component 1 (univariate) | Component 2 (bivariate) | Component 3 (trivariate) | Likelihood of Initiation and Consistency within models |
|------|-----------|--------------------------|-------------------------|--------------------------|-------------------------------------------------------|
| (i) | 100% | $CA$=High | | | Likely |
| (ii) | 100% | $LAF$=High | | | Likely |
| (iii) | 60% | $LAF$=High | $d_{mean}$=High | | Likely |
| (iv) | 80% | $OAng$=Low | $CAng$=Low | | Likely |
| (v) | 80% | $OAng$=Low | $NNAng$=Low | $d_{min}$=High | Unlikely |

Figure I-1 (*a* to *e*): ANM terms (i) to (vi) picked up by the SUPANOVA classifer for AS16 Perp. data[1]

g).

h).

i).
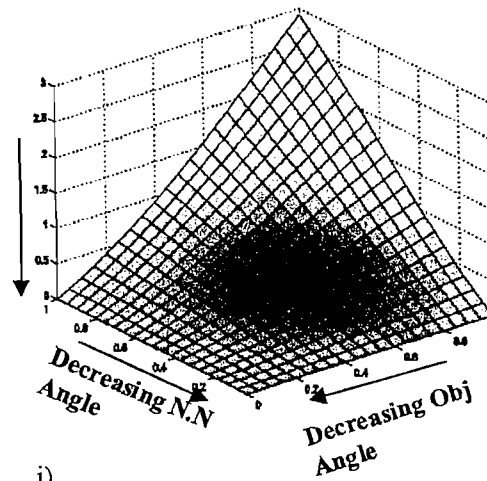
j).

Figure I-2 (*g* to *j*): ANM terms (vii) to (x) picked up by the SUPANOVA classifer for AS16 Perp. data[1]
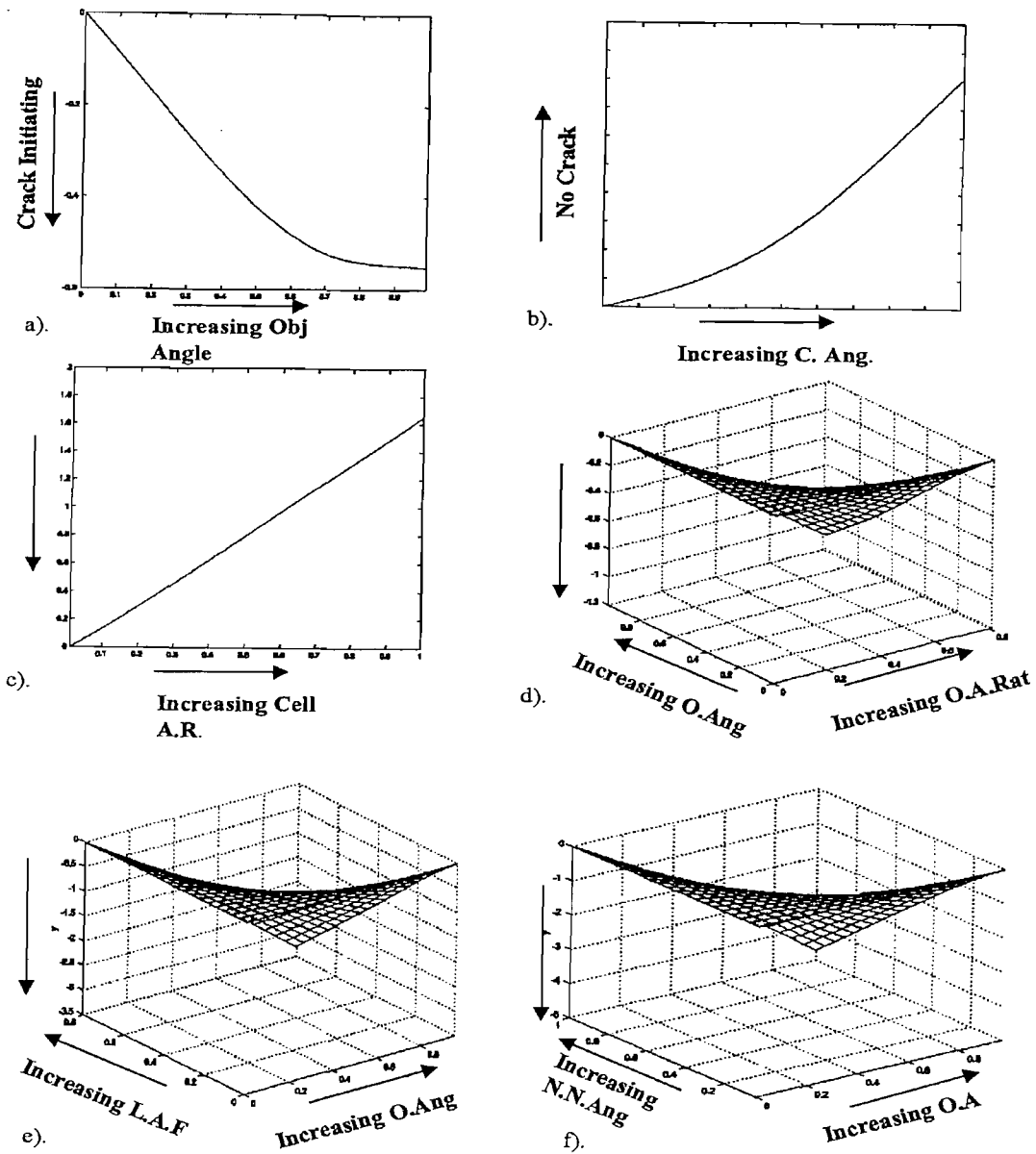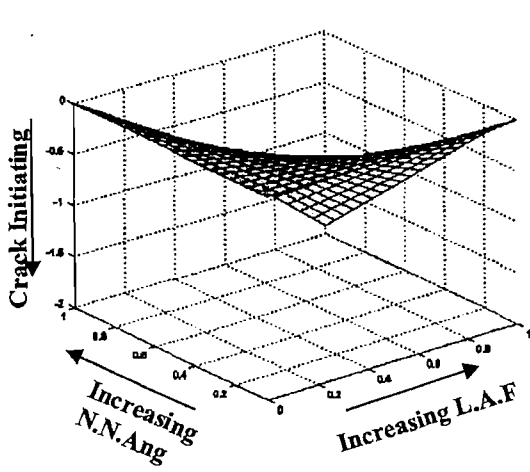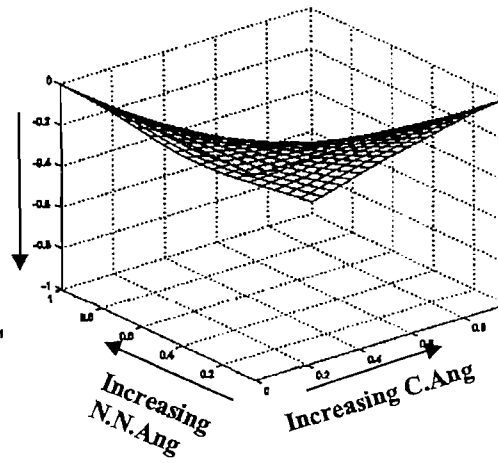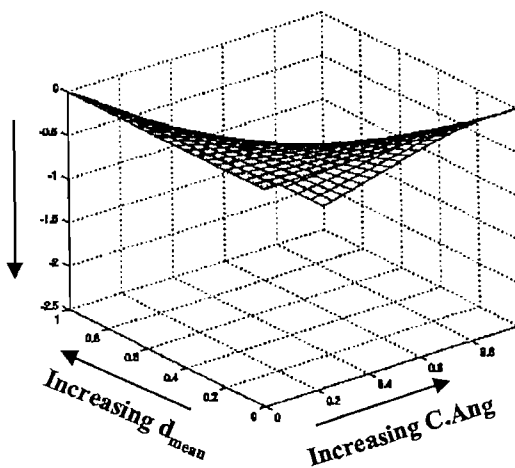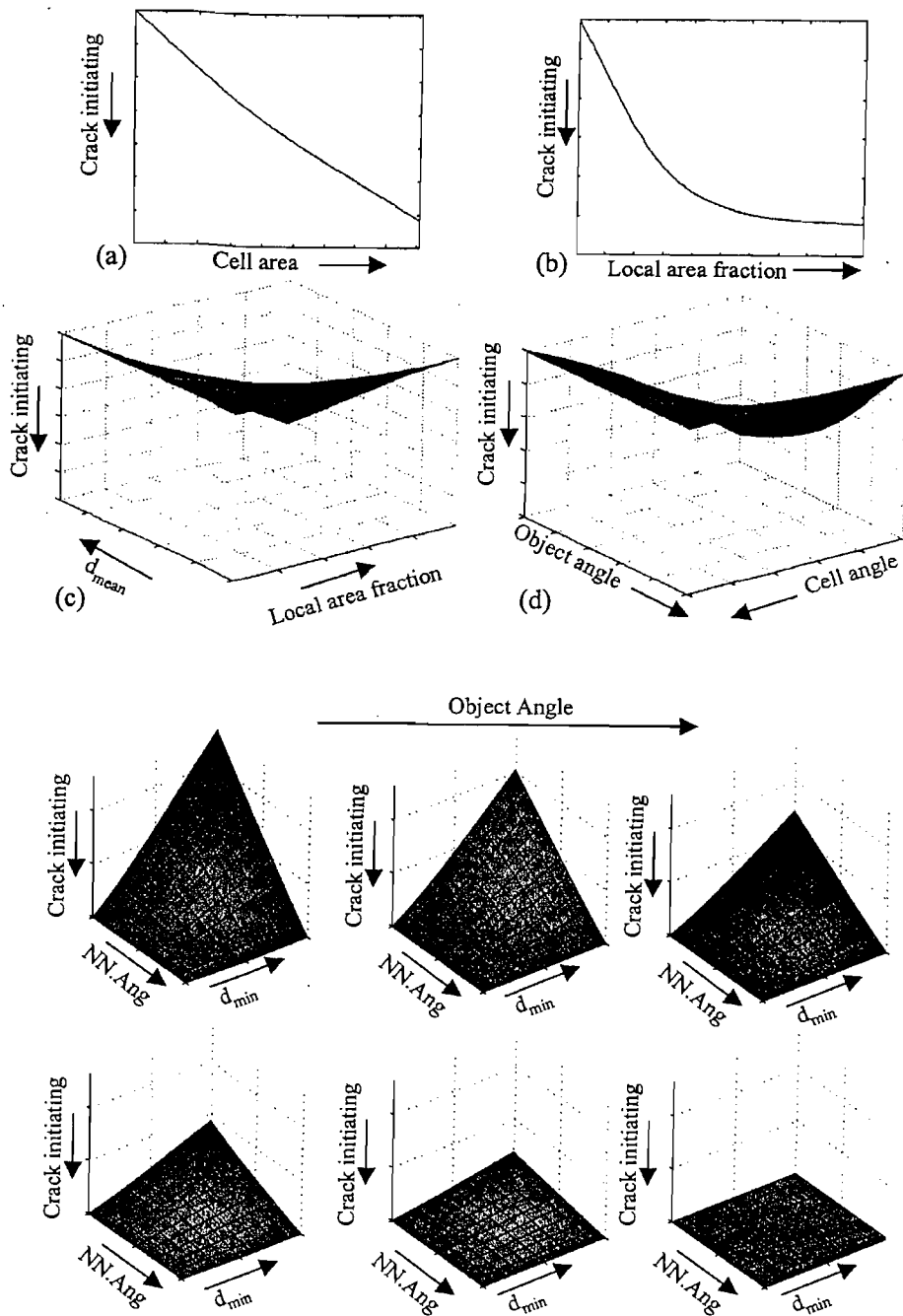
Figure I-3 (*a* to *e*): ANM terms (i) to (v) picked up by the SUPANOVA classifer for AS1241 data[2]

[1] M.C. Mwanza, M.R. Joyce, K.K. Lee, S. Syngellakis and P.A.S. Reed, Microstructural characterisation of fatigue crack initiation in Al-based plain bearing alloys, International Journal of Fatigue, Vol. 25, Issues 9-11, pp. 1135-1145, September, (2003)

[2] M.R. Joyce, K.K. Lee, S. Syngellakis and P.A.S. Reed, Quantitative assessment of preferential fatigue initiation sites in a multi-phase aluminium alloy, Fatigue Fract Engng Mater Struct, Vol. 27, pp. 1025-1036, (2004)

# Appendix J: ANSYS and MATLAB Files Used in Material Characterisation

This appendix lists the ANSYS input file and some MATLAB scripts used in the material characterisation procedure. The ANSYS input file "Vickers_simulation.log" was used to simulate the indentation process. Two MATLAB scripts were used to produce the artificial stress strain curves for the use of FE simulation program. The script "randomdataset.m" produces the artificial material parameters within predefined constraints. Then the obtained ascii file containing artificial material parameters were loaded in "producecurve.m" to generate a number of ascii files of proper format used in FEM as material model input files. The FE indentation results and artificial material parameters were colleted together and used to generate a SUPANOVA model through a SUPANOVA software, which is accessible from the Image, Speech and Intelligent Systems Research Group, University of Southampton. The SUPANOVA model obtained are in form of MATLAB data file. It was then loaded in optimisation process for iterations to give indentation sizes for any material parameters and a set of loads. The optimisation process used a Genetic Algorithm Optimisation Toolbox, which is available from the website http://www.ie.ncsu.edu/mirage/GAToolBox/gaot/. Two MATLAB scripts were written to perform optimisation using this toolbox. The script "supanovaga.m" specified a solution space and called the GA toolbox to search the best solution. The script "supanovaeva.m" returned a rms error of each material inputs set as a criterion for the GA toolbox to perform further searching in the solution space.

# Vickers simulation.log

```
! Vicker hardness simulation program using
! Axi-symmetric model with a rigid indenter

/batch
/filnam,vq1b
/title,Simulation of Vickers hardness test

!Save the loop index into a file loopindex.txt
*do,loopdepth,1,19,1
parsav,,loopindex,txt
/clear,all
parres,,loopindex,txt

!clear database then start analysis
/prep7
/uis,msgpop,3

!Element Types
et,1,42,,,1
et,2,169
et,3,171
r,1,,,1,0.1,0.01
rmore,,0.001

!Material Properties
! Stress [MPa]
! Length [mm]
! Force [N]
!=================
!Specimen to be tested
!
uimp,1,ex,,,74629.91287
 !Mpa
uimp,1,nuxy,,,0.33
*ulib,feb1q2,txt
*use,alloy,1
!fevq1b.txt contains the stress-strain
information
!

!Geometry model generation and parameters
diagonal=0.01*loopdepth     !diagonal size
measured in vickers pyramid hardness test
tancone=2.792836442     !degree of conical
indenter is 70.29964031, tan value
factor=0.142844842
!factor=ctan68*sqrt(2)/4, to get conical
indenter depth
depth=-factor*diagonal     !applied conical
indenter depth
modelratio=1          !model size ration, basic
model size is 0.4 mm
lblock=modelratio*0.4   !model size
k,1,0,0
k,2,lblock,lblock/tancone
k,3,0,0
k,4,lblock,0
```

```
k,5,lblock,-lblock
k,6,0,-lblock
k,7,lblock/2
k,8,,-lblock/2
k,9,lblock/2,-lblock/2
k,10,lblock,-lblock/2
k,11,lblock/2,-lblock
l,1,2
l,3,7
l,7,4
l,8,9
l,9,10
l,6,11
l,11,5
l,3,8
l,8,6
l,7,9
l,9,11
l,4,10
l,10,5
al,2,10,4,8
al,3,12,5,10
al,4,11,6,9
al,5,13,7,11

!Meshing
div1=60
div2=20
div3=10
lesize,2,,,div1
lesize,4,,,div1
lesize,8,,,div2
lesize,10,,,div2
lesize,6,,,div1
lesize,9,,,div3
lesize,11,,,div3

lesize,3,,,div3,3
lesize,5,,,div3,3
lesize,7,,,div3,3
lesize,12,,,div3
lesize,13,,,div3

type,1
mat,1
amesh,1
amesh,2
amesh,3
amesh,4

! flexible contact elements
type,3
mat,1
real,1
lmesh,2
lmesh,3
```

```
esel,s,type,,3
esurf,,reverse
! rigid target elements
type,2
real,1
lmesh,1
kmesh,1
finish
allsel

!Solve
!
/solu
dl,8,,symm
dl,9,,symm
dl,6,,symm
dl,7,,symm
dk,1,uy,depth
allsel
antype,stat
nlgeom,1
kbc,0
time=1
autots,on
nsubst,50,5000,20
solcontrol,on,1

solve

!get reaction and save results
!
yforce=0
ytemp=0
lsel,s,,,2
esll,s
nsll,s,1

!element and node number
*get,elemmx,elem,0,num,max
*get,elemmn,elem,0,num,min
*get,nodemx,node,0,num,max
*get,nodemn,node,0,num,min

ksel,s,kp,,1
nslk,s
*get,indenttip,node,0,num,min
allsel

!reaction on contact elements
*do,step,elemmn,elemmx,1
*get,ytemp,elem,step,nmisc,22
*if,ytemp,le,0,cycle
yforce=yforce+ytemp
*enddo
vload=yforce*1000/9.8

!numerical error of indenter tip
*get,ntipdis,node,indenttip,u,y
*get,nconerdis,node,nodemn,u,y
tiperror=nconerdis-ntipdis!
```

```
!unload process
dk,1,uy,0
time,1
autots,on
allsel
solve
finish
/post1

!load against diagonal size file
*cfopen,invq1b,txt,,append
*get,pdepth,node,1,u,y
dd=-pdepth*1000/factor
ddcorrect=-(pdepth-tiperror)*1000/factor
*vwrite,ddcorrect,vload
(f10.4,f10.4,)
*cfclos

finish
*enddo
/exit
```

# randomdataset.m

```
% To generate random material parameters set for artificial alloys,
%random values are elastic limit (sel)
% 0.2% proof stress (s02), and n. A will be
%determined by n and s02 0.2.
clear all
format long;

rand('state',615141)
% the random data set depends on initial condition,
%Change the state number if you want to generate another set of Data
temp=[ ];
result=[ ];
E=70000;
N=30; % number of curves to generate
Bsel=200;          % Boundary of Sigma el
Smsel=35;          % Boundary of sigma el
Bs02=300;          % Boundary of sigma 0.2
Sms02=65;          % Boundary of sigma 0.2
Bn=0.3;            % Boundary of n
Smn=0.08;          % Boundary of n
Ba=450;            % Boundary of A
Sma=300;           % Boundary of A
x=1;
i=0;
j=0;
while i<N;
j=j+1; % to record how many sets of data have been tried
sel=Smsel+rand(1)*(Bsel-Smsel);
s02=Sms02+rand(1)*(Bs02-Sms02);
n=Smn+rand(1)*(Bn-Smn);
% generate sel,s02 and n

eps02=0.002+s02/E;
epsel=sel/E;
A=s02/(eps02^n);
E1=(s02-sel)/(eps02-epsel);
E2=A*n*eps02^(n-1);
%calculate related values for constrains

if sel<s02 & A>Sma & A<Ba & E2>2500 &
E2<6500 & E1>12000 & E1<30000 &
E2/E1<0.55 & E2/E1>0.1 & E1/E<0.45
&E1/E>0.15
  i=i+1;
  temp=[sel s02 n A epsel eps02 E1 E2];
  result=[result;temp];
end
end

save result.txt result -ascii;
```

# producecurve.m

```
% this matlab program generate the stress strain curve for indenation simulation.
% it reqires the result.txt file generated by randomdataset.m

clear;
format long;
load result.txt
[NUM NUM2]=size(result);
%NUM gives the number of curves in result.txt

sel=result(1:NUM,1);
s02=result(1:NUM,2);
n=result(1:NUM,3);
A=result(1:NUM,4);
epsel=result(1:NUM,5);
eps02=result(1:NUM,6);
grad2=result(1:NUM,7);
grad=70000;
total=[ ];
for i=1:NUM
M=[epsel(i)^2,epsel(i),1;eps02(i)^2,eps02(i),1;
2*eps02(i),1,0];
B=[sel(i);s02(i);grad2(i)];
% 2nd order polynomial are used to connect elastic limit and yield point
N=inv(M);
X=N*B;
pointsnum=7;
  for j=1:(pointsnum-1)
  ep(j)=epsel(i)+j*(eps02(i)-
epsel(i))/pointsnum;
  end

EE=[ep(1)^2,ep(1),1;ep(2)^2,ep(2),1;ep(3)^2,e
p(3),1;ep(4)^2,ep(4),1;ep(5)^2,ep(5),1;ep(6)^2,
ep(6),1];

sprey=EE*X;
% 6 points are generated. ep is strain, sprey is stress

ssprey=[ep',sprey];
ssel=[epsel(i),sel(i)];
ss02=[eps02(i),s02(i)];
ssprey=[ssel;ssprey];
ssprey=[ssprey;ss02];

% below is to generate the whole curve and save to a txt file
for k=1:20
epposty(k)=eps02(i)+0.001*k;
sposty(k)=A(i)*epposty(k)^n(i);
end

for m=1:20
epposty(20+m)=epposty(20)+0.01*m;
```

```
sposty(20+m)=A(i)*epposty(20+m)^n(i);
end


for t=1:10
epposty(40+t)=epposty(40)+0.1*t;
sposty(40+t)=A(i)*epposty(40+t)^n(i);
end
ssposty=[epposty' sposty'];
ss=[ssprey;ssposty];


name1='fealloy';
name2=int2str(i);
name3='.txt';
name=[name1,name2,name3];
fid=fopen(name,'w+');
fprintf(fid,'alloy\n');
fprintf(fid,'tb,miso,arg1,,%2i\n',58);
fprintf(fid,'tbpt,defi,%d,%d\n',ss');
fprintf(fid,'/eof\n');
fclose(fid);
total=[total,ss];
end


save totalalloy.txt total -ascii;
```

## supanovaga.m

```
% This script calls GA toolbox to search the
best solution
clear all;
echo off;
%bounds is the solution space
bounds=[35 200;65 300;0.08 0.3];
[x,endPop,bestSols,trace]=ga(bounds,'supanov
aeva');
save x.txt x -ascii -double;
```

## supanovaeva.m

```
% This script is a function file used in
supanovaga.m
function [sol,val]=supanovaeva(sol,options)
load
artificial02.supanova.quadratic.trivariate.mat;
data1=artificial02;
inputScale=data1(1).data.inputScale;
inputOffset=data1(1).data.inputOffset;
sige=sol(1);
sigy=sol(2);
neva=sol(3);
tstX=[ ];
load loadv.txt;
[msize nsize]=size(loadv);
ansY=loadv(:,1);
for i=1:msize
   tstX(i,1)=sige;
   tstX(i,2)=sigy;
   tstX(i,3)=neva;
end
```

```
tstX=[tstX loadv(:,2)];
for j=1:4
tstX(:,j)=tstX(:,j)*inputScale(j)+inputOffset(j);
end % calculate test data
tstYgns = 0;
ker = 'ANOVA';
for n=1:10
       trnX = data1(n).data.X;
       comp                              =
data1(n).model.stageIII.kernel.comp;
       beta = data1(n).model.stageIII.beta;
       bias = data1(n).model.stageIII.bias;
       tstY                              =
anovasvroutput(trnX,tstX,comp,ker,beta,bias);
       tstYgns = tstYgns+tstY;
end
tstYgns = 0.1*tstYgns;
tstY=tstYgns;
exY=loadv(:,1);
%val=-sqrt(dot(exY-tstY,exY-tstY));
%boundary constraint
E=70000;
epsigy=0.002+sigy/E;
epsige=sige/E;
Aeva=sigy/(epsigy^neva);
E1=(sigy-sige)/(epsigy-epsige);
E2=Aeva*neva*epsigy^(neva-1);
if sige>sigy   g1=((sige-sigy)/sigy)^2;
elseif sige==sigy   g1=0.1;
else   g1=0;
end
if Aeva>450   g2=((Aeva-450)/450)^2;
elseif Aeva<300   g2=((Aeva-300)/300)^2;
else   g2=0;
end
if E2/E1>0.55   g3=((E2/E1-0.55)/0.55)^2;
elseif E2/E1<0.1   g3=((E2/E1-0.1)/0.1)^2
else    g3=0;
end
if E1/E>0.45   g4=((E1/E-0.45)/0.45)^2;
elseif E1/E<0.15   g4=((E1/E-0.15)/0.15)^2;
else   g4=0;
end
if E2>6500   g5=((E2-6500)/6500)^2;
elseif E2<2500   g5=((E2-2500)/2500)^2;
else   g5=0;
end


if E1>30000   g6=((E1-30000)/30000)^2;
elseif E1<12000   g6=((E1-12000)/12000)^2;
else   g6=0;
end


c=(tstY-ansY);
r=10;
val=-sqrt(dot(c,c)/msize)-
r*sqrt(g1+g2+g3+g4+g5+g6);


screen=[sol val]
```